

HAFNIUM ALKYLAMIDES AND ALKOXIDE ADSORPTION  
AND REACTION ON HYDROGEN TERMINATED  
SILICON SURFACES IN A FLOW REACTOR

by

KEJING LI

A DISSERTATION

Submitted in partial fulfillment of the requirements for the  
degree of Doctor of Philosophy in the Department  
of Chemical and Biological Engineering  
in the Graduate School of  
The University of Alabama

TUSCALOOSA, ALABAMA

2010

Copyright Kejing Li 2010  
ALL RIGHTS RESERVED

## ABSTRACT

This work is a study of the gas phase and surface chemistry of three metalorganic Hf (IVB) precursors – tetrakis(dimethylamido) hafnium (TDMAH), tetrakis(ethylmethylamido) hafnium (TEMAH), and hafnium tert-butoxide (HTB) adsorption and reaction onto hydrogen terminated Si(100), Si(111) and Ge surfaces during low pressure chemical vapor deposition (CVD) in a temperature range of 25 °C to 300 °C in a flow reactor. The main methods used include *in-situ* attenuated total reflectance Fourier transforms infrared spectroscopy (ATR-FTIR), transmission IR, quadrupole mass spectrometer (Q-MS), *ab initio* density functional theory (DFT), photoelectron spectroscopy (XPS), finite element analysis (FEA), computational fluid dynamics (CFD), and atomic force microscopy (AFM).

Possible gas phase decomposition and surface adsorption reactions were surveyed. Reaction energies, vibrational spectra and transition states were calculated for the three precursors and especially the two alkylamido hafnium precursors to support experimental observations. Interfacial bonding and surface catalyzed reaction processes initiated by the adsorption of precursors were detected. For TDMAH and TEMAH,  $\beta$ -hydride elimination and insertion reactions were calculated to be not favorable thermodynamically at these low experimental temperatures. Interfacial bonding during adsorption between the Si was through N-Si and/or C-Si. Decomposition products containing Hf-H species were observed on the surface at room temperature and 100 °C and the peak assignment was confirmed by deuterated water experiments. The gas phase by-products were mostly dimethylamine (DMA) and a small amount of methylmethleneimine (MMI) or ethylmethylamine (EMA) and methylethyleneimine (MEI). A surface three-member cyclo species was tentatively identified.

For HTB, interfacial bonding was Si-O or Ge-O. Another  $\beta$ -hydride elimination generated Hf-OH on the surface and t-butene in the gas phase. A monodentate and bidentate model was proposed for chemisorption of HTB with different concentration on two Si surface orientations at temperatures below 150 °C. Carbonate was found to form in the film at higher temperatures.

The effect of HTB buoyancy driven flow in the ATR flow through cell on thin film topography was observed using AFM of thin films deposited from HTB at 250 °C. The images showed a wavy surface at the downstream end of the substrate due to roll-type flow predicted by CFD calculations.

## LIST OF ABBREVIATIONS AND SYMBOLS

ALD	Atomic layer deposition
ATR	Attenuated total reflectance
C	Capacitance
CAE	Constant analyzer energy mode
CB	Conductance band
CFD	Computational fluid dynamics
CRR	Constant retard ratio
d	Film thickness
$d_p$	Depth of penetration
DTGS	Duterated triglycine sulphate
e	Electron charge
EBE	Binding energy
EF	Evanescent field
$E_g$	Band gap
$E_{KIN}$	Kinetic energy
EOT	Equivalent oxide thickness
EPL	Effective path length
ESCA	Electron spectroscopy for chemical analysis
ESI	Electron spray ionization
FEA	Finite element analysis
GGA	Generalized gradient approximation

Gr	Grashof number
GTO	Gaussian type orbital
HTB	Hafnium tert-butoxide
IRE	Internal reflectance element
ISD	Source drain current
ITRS	International technology roadmap for semiconductors
$\kappa$	Dielectric constant
k	Conductivity coefficient
Kn	Knudsen number
L	Channel length
LCAO	Linear combination of atomic orbitals
LDA	Local density approximation
MEI	Methylethyleneimine
MMI	Methylmethylenimine
MOSFET	Metal oxide semiconductor field effect transistor
N	Number of molecular orbitals
n	Number of electrons in a molecule
N-S	Navier-Stokes equation
PDA	Personal digital assistant
RBS	Rutherford backscattering
PPM	Parts per million
Ra	Raleigh number
Re	Reynolds number
RMS	Root-mean-square
SCF	Self-consistent field

SLD	Soft laser desorption
STO	Slater type orbital
S/N	Signal to noise ratio
ss	Stainless steel
TDEAT	Tetrakis(dimethylamido) hafnium
TDMAH	Tetrakis(dimethylamido) hafnium
TEMAH	Tetrakis(methylethylamido) hafnium
TM	Transition metal
UHV	Ultra high vacuum
VB	Valence band
$C_v$	Constant volume heat capacity
$m$	Reduced ion mass
MS	Mass spectrometry
$N$	Number of ions per unit volume
$n$	Refractive index
<b><math>P</math></b>	Polarization
$t$	IRE thickness
$V_D$	Voltage between source and drain
$V_G$	Gate voltage
$V_{FB}$	Flat band voltage
$V_{Th}$	Threshold voltage
$ZT^*$	Ion's transverse effective charge
$\epsilon$	Absorption coefficient
$\omega_{TO}$	Frequency of the transverse optical phonon
$\hat{H}$	Hamiltonian

$\eta$  Plank constant

$\chi_\mu$  Contracted Gaussian basis functions

## ACKNOWLEDGEMENTS

I am grateful to have been admitted to the Chemical & Biological Engineering Department in The University of Alabama four and half a year ago where I spent a very meaningful journey during which I owe my sincere gratitude to many persons. They have accompanied me and helped me through achieving this thesis. This is one of the most beneficial fortunes that God has blessed in my life. It is a privilege for me to acknowledge these people and wish I have listed all of them.

I would like to thank my advisor Dr. Tonya Klein for her passionate guidance, training, and support in my work. She has trained me in every aspect from a very dependent fresh undergraduate with bare idea about research to a self-motivated Ph.D who is willing to devote to this field. I appreciate the open opportunities she granted me to dig in subjects that I felt interested in. The subconscious beneficial learning from her is tremendous. She has taught me knowledge, creative way of thinking, techniques and skills that would be useful in my career; and she also taught me the optimistic philosophy to life and people. Her independence, persistence, confidence, patience and sense of humor have enlightened her students including me, with feeling full of hope and not running away from problems. I still remember the day when I first got frustrated with some experimental results and we were leaving after talking a long time in the late afternoon, she turned around and said to me across the hall way, “do you know what does Ph.D. stand for?” she asked and then stood there, answered her question loudly “P means persistency.” I remember these words when I really felt lost in solving these mechanism puzzles and got the courage to persist, never give up. Without her guidance and help, this journey would be a very high mountain for me to climb.

I would like to thank Dr. David Dixon and Dr. Shengang Li for training me half core

of this thesis in density functional theory and hands-on teaching in many ways one page may not be enough. I feel fortunate to have met them and benefited from their smartness, solid chemistry knowledge, critical way of thinking, and preciseness in study. I always breathed a lot of inspiration after talking with them and felt learnt a lot. I really appreciate their continuous offering of guidance and help in this work and my improvement as a researcher. I will always remember Dr. Dixon's advice – "it is this tiny thing that makes a difference." Without their positive catalytic help, this thesis would be taking much longer.

I would like to express my gratitude to my committee and members in their groups who have added indispensable bricks to this thesis work. Dr. Alan Lane and his student Dr. Wei Li have helped a lot in the mass spectrometry work. Dr. Lane was my teaching assistant advisor for two semesters and I was impressed by his leading style. I was also encouraged when Wei toured us passionately about his laboratory and his work; Dr. C. Heath Turner and his student Dr. Zheng Hu has led my way in using Gaussian software and intrigued my interest in modeling. I also thank his later post doc associates Dr. Wei An and Dr. Xian Wang for their friendship and beneficial discussion about chemistry. Dr. Shane Street and his students Dr. Litao Bai and Mr. Clifton Watkins helped me with the transmission IR in their lab and they were very patient and we had pleasant discussions about IR every time.

I can't forget my appreciation to my labmates Shilpa Dubey, Ning Li, Gihan Kwon, and Jinwen Wang. Shilpa spent half a year with me before graduation, who taught me step by step about manipulating instruments and handling experiments. Her detail oriented style has laid the basis of my experimental attitude a lot. Ning is a diligent co-worker and quick learner with whom I got much encouragement in solving problems professionally and had fun in the lab when we discussed our projects from different perspectives. Gihan had four years here as my labmate and officemate. He was like a big brother in the lab who was willing to offer assistance. I was amazed about the complex Matilda he built and his instrumental sense is the

best I have ever seen. Jinwen was also like a big brother who worked very diligently from morning until midnight almost every day, which was somewhat a little pressure for me but has been a role model for all of us. I would also like to thank two earlier labmates Harish Bhandari and Lucas Falco for their friendship. I feel proud to have ever worked with these people and in this lab.

I also would like to thank Dr. Alfred Waterfeld and Dr. Joseph Thrasher who several times provided me with materials that I was in dire need of, which have been so important to accomplish this thesis. The help from Dr. Huzhen Zhu, Mr. David Drab, Mr. Scott Brown, Dr. Kevin Shaughnessy, Dr. Myrna Hernandez and Dr. Ken Belmore with the X-ray crystallography, discussions about transition states and Khimera, and NMR analysis is greatly appreciated.

Special thanks to Dr. David Young in Alabama Super Computer Center, Susan Berets in Harrick Scientific Inc., Dr. Christopher. L. Platt in Seagate, Dr. Elizabeth Moore, Dr. Jim Maslar and Dr. Will Kimes in NIST, and Mr. Zhang Lin in Harbin Institute of Technology for their help and collaborative work on the computation source, transmission cell setup, TDMAH mechanism discussions, and fluid dynamic calculations. The occasional but very beneficial discussions and guidance from Dr. Yuping Bao (ChE, UA), Dr. Peter Clark (ChE, UA), Dr. Stephen M.C. Ritchie, Dr. Muhammad Sharif (ME, UA), Dr. Gary Mankey (PHY, UA), Dr. Greg Szulczewski (CH, UA), Dr. Carolyn J. Cassady (CH, UA), Dr. James Western (MINT, UA), Dr. Subhadra Gupta (MTE), Dr. Theodosia Gougousi about (UMD), and Dr. Yves Chabal (RU) about my research as well as research philosophy are greatly appreciated.

I gratefully acknowledge the departmental administrative staff Mrs. Inge Archer and Mrs. Susan Noble for their kindness and assistance in making my graduate life easier and more convenient. I would like to thank Mr. James Hill and the MINT center staff for assistance in the laboratory and office setup. I also thank professors in Chemical Engineering

Department Dr. John Wiest and Dr. David Arnold in whose courses I felt happy as an engineering student. I also would like to thank my friends and people in Calvary church for their friendship and help that accompanied me through.

Finally, I want to dedicate my dissertation to my dearest parents and grandmother for their continuous support and love behind this work. I would also like to dedicate this dissertation in remember of my grandfather in heaven who would be happy to see my accomplishment in this degree and his granddaughter's growth in pursuing her dreams.

This work was supported by NSF CAREER award # 0239213 to Tonya M. Klein. I would also like to acknowledge the University of Alabama Graduate School for Graduate Council Research and Creativity Fellowship.

“Everything should be made as simple as possible, but not simpler.”

– Albert Einstein

“三人行必有我师焉。默而识之，学而不厌，诲人不倦。”

–《论语》

## CONTENTS

ABSTRACT.....	ii
LIST OF ABBREVIATIONS AND SYMBOLS.....	iv
ACKNOWLEDGEMENTS.....	viii
LIST OF TABLES.....	xvii
LIST OF FIGURES.....	xviii
Chapter 1 MOSFET and High- $\kappa$ Dielectric.....	1
1.1 MOSFET Introduction.....	1
1.1.1 MOSFET Operation.....	2
1.1.2 MOSFET Scaling Down.....	3
1.2 High- $\kappa$ Dielectric Introduction.....	4
1.3 High- $\kappa$ Dielectric Figure of Merits.....	7
1.3.1 Dielectric constant $\kappa$ .....	7
1.3.2 Band Gap $E_g$ .....	8
1.3.3 Band Offset.....	10
1.3.4 Interface Bonding.....	11
1.3.5 Flat Band and Threshold Voltage.....	12
Chapter 2 HfO <sub>2</sub> Thin Film Development.....	14
2.1 Atomic Layer Deposition.....	14
2.2 Reactors.....	16
2.3 HfO <sub>2</sub> and On-going Studies.....	17
2.4 Precursor Decomposition Chemistry.....	19
2.5 Electronic Studies of alkylamide precursor surface reaction in ALD.....	24
Chapter 3 Experimental Characterization Methods.....	26

3.1	Summary of Characterization Techniques .....	26
3.2	Infrared Spectroscopy .....	26
3.2.1	Background.....	26
3.2.2	History of ATR.....	26
3.2.3	ATR-FTIR Instrumentation and Basic Theory .....	27
3.3	Scanning Force Microscopy .....	30
3.3.1	History of AFM .....	30
3.3.2	AFM Instrumentation and Basic Principles.....	31
3.4	Photoelectron Spectroscopy.....	32
3.4.1	Introduction .....	32
3.4.2	History of XPS.....	32
3.4.3	XPS Instrumentation.....	33
3.4.4	XPS Physics.....	34
3.5	Quadrupole Mass Spectrometer .....	36
3.5.1	Background and History .....	36
3.5.2	Quadrupole MS Instrumentation and Basic Theory .....	36
3.6	Thickness and Pressure Measurement .....	38
3.6.1	Thickness Measurement .....	38
3.6.2	Pressure Measurement .....	40
Chapter 4	Density Functional Theory & Infrared Spectroscopy Calculation .....	41
4.1	Chapter Summary .....	41
4.2	Quantum Mechanics Theoretical Background.....	41
4.2.1	The Schrödinger Equation .....	41
4.2.2	The Molecular Hamiltonian.....	42
4.2.3	Hartree-Fock Theory .....	43

4.2.4	Density Functional Theory .....	46
4.3	<i>Ab initio</i> Applications in Vibrational Spectroscopy .....	49
4.3.1	Harmonic Oscillator .....	49
4.3.2	Vibrational Calculation .....	51
4.3.3	Vibrational Anharmonicity .....	52
4.4	Computational Methods.....	53
Chapter 5	TDMAH Adsorption and Reaction on H-Si(100) Surface .....	55
5.1	Introduction .....	55
5.2	Experimental and Computational Methods.....	55
5.2.1	Experimental Methods.....	56
5.2.2	Computational Methods .....	60
5.3	Results and Discussion.....	61
5.3.1	Bulk FTIR Thermal Analysis.....	64
5.3.2	Gas Phase FTIR Analysis .....	67
5.3.3	Surface FTIR Analysis of TDMAH and D <sub>2</sub> O or H <sub>2</sub> O ALD on H-Si(100) .....	71
5.3.4	Surface Adsorption/Desorption FTIR Analysis on Ge and ZnSe .....	81
5.3.5	Residual Gas Analysis .....	81
5.4	DFT Calculations of Gas Phase Reactions .....	83
5.4.1	Calculations of Surface Reactions .....	86
5.5	Chapter Summary .....	94
Chapter 6	TEMAH Adsorption and Reaction on H-Si(100) Surface .....	96
6.1	Chapter Introduction.....	96
6.2	Results and Discussion.....	96
6.2.1	Experimental and Computational Spectra Comparison.....	96
6.2.2	Gas Phase FTIR Analysis .....	98

6.2.3	Surface Adsorption/D <sub>2</sub> O/H <sub>2</sub> O FTIR Analysis .....	103
6.3	Calculations of Reaction Mechanisms.....	106
6.4	Chapter Conclusions.....	109
Chapter 7	HTB Adsorption and Reaction on Si (100) and Si(111) Surfaces.....	111
7.1	Chapter Introduction.....	111
7.2	Experiments .....	111
7.2	Results and Discussion .....	113
7.3	Kinetic Calculations .....	127
7.3.1	Adsorption Energy.....	127
7.3.2	Decomposition and Hydrolysis Reaction .....	129
7.4	XPS Study.....	130
7.5	Chapter Summery .....	132
Chapter 8	ATR-FTIR Flow Through Meso-Reactor.....	134
8.1	Chapter Introduction.....	134
8.2	Experimental Setup and Meso-Reactor .....	135
8.3	Temperature Profile of the Meso-Reactor .....	137
8.3.1	Temperature Modeling.....	137
8.3.2	FEA Model and Formulation .....	138
8.3.3	Experiment Temperature Measurement.....	139
8.4	Fluid Behavior Model.....	141
8.4.1	CFD Formulation and Simulation .....	143
8.4.2	Flow Rates and Pressure Drop.....	145
8.4.3	Film Thickness.....	148
8.4.4	Velocity Field and Flow Patten.....	151
8.5	Chapter Summary .....	157

Chapter 9	Conclusion and Future Work.....	158
9.1	Conclusions.....	158
References	.....	163
Appendix A	Experimental Configurations and Thermal Transfer Meterial Properties...	173
Appendix B	DFT Caluated Geometries and Energies for Selected Models.....	185
Appendix C	Copyright Release.....	196

## LIST OF TABLES

Table 1-1. Further Downscaling Physical and Technological Limitations. [Ref.].....	6
Table 1-2. Static Dielectric Constant ( $\kappa$ ), Experimental Band Gap and Conductance Band Offset on Si of the Candidate Gate Dielectrics [Ref. 6] .....	7
Table 2-1. Precursor Properties .....	20
Table 5-1. Band Positions ( $\text{cm}^{-1}$ ) and Assignments for the Experimental IR Spectra of TDMAH and DMA from the Unscaled Calculated B3LYP/BS1 Values .....	64
Table 5-2. Peak positions ( $\text{cm}^{-1}$ ), IR Intensities ( $\text{km/mol}$ ), and Assignments for the Characteristic Experimental IR Peaks from the Calculated B3LYP/BS1 Values. ....	74
Table 5-3. Relative Energies from the Reactants at 0 K in kcal/mol for the Gas Phase Reactions Calculated with the B3LYP Functional and the BS1 and BS2 Basis Sets. ....	84
Table 5-4. Relative Energies from the Reactants at 0 K in kcal/mol for the Surface Reactions Calculated with the B3LYP Functional and the BS1 and BS2 Basis Sets. ....	87
Table 6-1. TEMAH Liquid Drop IR Spectrum and B3LYP/BS1 Calculated Vibrational Assignments at 25 °C, 1 atm. Without Scaling Factor (wavenumbers in $\text{cm}^{-1}$ ). ....	98
Table 6-2. Energetic Data for Gas Reactions(kcal/mol) <sup>c</sup> .....	108
Table 6-3. Energetic Data for Surface Reaction of Gas Phase Products (kcal/mol) <sup>c</sup> .....	108
Table 7-1. HTB Related Infrared Spectra (Gas Phase not Shown, and HTB Liquid Drop on Ge) and DFT Calculated Vibrations Assignments (in $\text{cm}^{-1}$ ). ....	115
Table 8-1. Estimated Fluid Mechanics Parameters for 60 °C HTB at 0.3 Torr. ....	143
Table B-1. Thermal Conductivity of Flow Through Cell Component Materials.....	184

## LIST OF FIGURES

Figure 1-1. MOSFET types.....	1
Figure 1-2. Schematic of an n-channel enhancement-type MOSFET structure .....	2
Figure 1-3. (a) Molecular orbital energy level diagram for a group IV transition metal in an octahedral bonding arrangement with six oxygen neighbors; (b) Bands and density of states of cubic HfO <sub>2</sub> . .....	9
Figure 1-4. Schematic of band offsets determining carrier injection from intrinsic-Si into oxide band states. ....	10
Figure 1-5. Schematic of bands in the depletion region. ....	11
Figure 1-6. Various calculated configurations of (100) Si:ZrO <sub>2</sub> interface: (a) O <sub>4</sub> , (b) O <sub>3</sub> , (c) O <sub>3T</sub> , (d) O <sub>3B</sub> , (e) O <sub>2A</sub> , (f) Zr <sub>6</sub> , and (g) Zr <sub>10</sub> . ....	12
Figure 2-1. (a) Selective adsorption and (b) adsorbate-inhibition mechanism.....	15
Figure 2-2. Multiple-wafer-in-tube type reactor. ....	16
Figure 2-3. Flow behavior in a horizontal reactor with isothermal side wall. ....	17
Figure 2-4. Arrhenius plot for ZrO <sub>2</sub> growth rate vs. 1/T for ZTB from First Reaction (A) and Aldrich (B). ....	21
Figure 2-5. Degradation of TEMA during isothermal TGA (120 °C and 150 °C).....	23
Figure 2-6. Infrared absorption spectra of TEMAT, TEMAZ, and TEMA in both liquid (left panel) and gas (right panel) phases. ....	24
Figure 3-1. Schematic apparatus of infrared spectrometry Michelson interferometer. ....	28
Figure 3-2. Internal reflectance element and evanescent wave. ....	29
Figure 3-3. Atomic force microscopy apparatus schematic drawing.....	31
Figure 3-4. X-ray photoelectron spectroscopy excitation of electrons. ....	34
Figure 3-5. Mass spectrometer with electron ionization source and quadrupole analyzer. ....	37
Figure 3-6. U-V diagram for quadrupole control line of operation. ....	38
Figure 3-7. Light interference in a three-layer model.....	39
Figure 5-1. (A) FTIR schematic. (B) Transmission gas cell cross-section. (C) Attenuated total	

reflectance compartment. (B) and (C) are interchangeable in the middle component space of FTIR. (B) and (C) are permitted to reprint from HarrickScientific. ....	56
Figure 5-2. Pressure change as a function of bubbler equilibrium time at a bubbler temperature of 65 °C. The pressure behaved similarly for the same bubbler temperature and different gas cell temperatures below 150 °C. ....	57
Figure 5-3. (A) Structure of model of THE surface. H <sub>14</sub> Si <sub>9</sub> cluster representing H-Si(100). (B) Structure and highest occupied molecular orbital (HOMO) of TDMAH. ....	60
Figure 5-4. Top: infrared spectrum of TDAMH in gas phase in flow mode at room temperature. Bottom: Calculated IR spectrum at the DFT/BS1 level with scaling factor 0.9408 applied to the region of C-H stretches for TDAMH. ....	62
Figure 5-5. IR spectra for a liquid drop of TDMAH on Si and raised to (a) 30 °C, (b) 150 °C, (c) 150 °C under vacuum. The temperature ramping rate was 50 °C/min. Spectra were reprocessed with bare Si backgrounds at their corresponding temperature. ....	65
Figure 5-6. Gas phase TDMAH reactions 1 to 5: (1) dimerization; (2) β-hydride elimination reaction; (3) intramolecular insertion reaction leading to TI-3; (4) intramolecular insertion reaction leading to TI-4; and (5) 1,2-β-hydride elimination reaction. ....	66
Figure 5-7. IR spectra at 100 °C of gas phase TDMAH in a closed gas cell with Si windows using a resolution of 2 cm <sup>-1</sup> as a function of time. ....	68
Figure 5-8. Gas phase TDMAH IR spectra at different temperatures in flow mode at 5 min. and 0.6 Torr. ....	69
Figure 5-9. Reactions (6) to (8): first step surface reaction from TDMAH forming different interfacial bonds: (6) L <sub>3</sub> Hf-Si, (7) L <sub>3</sub> HfN-Si, and (8) L <sub>3</sub> HfNC-Si. ....	71
Figure 5-10. IR spectra for TDMAH/D <sub>2</sub> O adsorption on H-Si(100) at room temperature. In sequence: (a) 3.5×10 <sup>8</sup> L TDMAH; (b) desorption under vacuum for 10 min. (c) 5.0×10 <sup>7</sup> L dose of TDMAH; (d) 1.0×10 <sup>8</sup> L of D <sub>2</sub> O cycle; (e) 5.0×10 <sup>7</sup> L dose of TDMAH; (f) 5.0×10 <sup>7</sup> L dose of D <sub>2</sub> O. ....	72
Figure 5-11. IR spectra for the H-Si and H-Hf stretching regions for TDMAH followed by H <sub>2</sub> O adsorption at room temperature, sequentially: (a) 3.5×10 <sup>8</sup> L TDMAH; (b) desorption under vacuum for 10 min.; (c) 5.0×10 <sup>7</sup> L dose of TDMAH; (d) 1.0×10 <sup>8</sup> L of H <sub>2</sub> O cycle; (e) 5.0×10 <sup>7</sup> L dose of TDMAH; (f) 5.0×10 <sup>7</sup> L dose of H <sub>2</sub> O; (g) desorption under vacuum for 10 min. ....	76
Figure 5-12. IR spectra for the H-Si and H-Hf stretching regions for TDMAH followed by D <sub>2</sub> O or H <sub>2</sub> O adsorption on H-Si(100) at 100 °C, sequentially: (a) 3.5×10 <sup>8</sup> L TDMAH; (b) desorption under vacuum for 10 min. (c) 5.0×10 <sup>7</sup> L dose of TDMAH; (d-1) 1.0×10 <sup>8</sup> L of D <sub>2</sub> O cycle; (d-2) 1.0×10 <sup>8</sup> L of H <sub>2</sub> O cycle. (d-1) is after baseline correction. ....	78
Figure 5-13. Reactions (9) and (10): Proton exchange reaction and hydroxyl substitution reaction for Hf-H with D <sub>2</sub> O (9) or H <sub>2</sub> O (10). ....	79

Figure 5-14. IR spectra for TDMAH followed by D <sub>2</sub> O adsorption on Ge and ZnSe IRE for the lower wavenumber region. (a) 3.5×10 <sup>8</sup> L dose of TDMAH on ZnSe at 100 °C; (b) 3.5×10 <sup>8</sup> L dose of TDMAH on Ge at room temperature; (c) 3.5×10 <sup>8</sup> L dose of TDMAH on Ge at 100 °C; (d) D <sub>2</sub> O cycle after TDMAH cycle on Ge at 100 °C.....	80
Figure 5-15. Q-MS spectra. Background (a) at room temperature; (b) TDMAH effluent from the flow through cell at (b) room temperature, (c) 150 °C and (d) 250 °C. ....	83
Figure 5-16. Reactions (11) and (12): first step surface reaction from possible gas phase intermediates. Reaction (11) from TI-4, and reaction (12) from T-en. ....	89
Figure 5-17. Reactions (13) to (17): second step surface reactions from L <sub>3</sub> Hf-Si. ....	90
Figure 5-18. Reactions (18) and (19): second step surface reactions bridged on Si dimer from L <sub>3</sub> Hf-NSi. ....	91
Figure 5-19. Reactions (20) and (21): proposed mechanisms to form Hf-H and TI-3 on Si surface. ....	92
Figure 5-20. Reactions (22) and (23): silylation reactions from MMI to H-Si surface. ....	93
Figure 5-21. Reactions (24) and (25): hydroxylation of L <sub>2</sub> Hf-Si. ....	94
Figure 6-1. Top: Liquid drop of TEMAH on Ge IRE; Bottom: Calculated TEMAH gas vibrational spectrum at B3LYP/6-31+G(d,p), applied with a scaling factor of 0.9398 for the 3100-2700 cm <sup>-1</sup> region. ....	97
Figure 6-2. Spectra of (a) gas phase TEMAH, (b) liquid drop of TEMAH on Ge IRE, (c) gas phase TDMAH, (d) liquid drop of TDMAH on Ge IRE. All spectra were taken at room temperature. Gas phase spectra (a) and (c) were recorded at 1 min. after introducing sample into the gas cell. ....	99
Figure 6-3. 100 °C gas phase infrared monitoring for introducing TDMAH into the gas cell. (a) - (d) were using Si windows, and (e) was using KBr windows. (a) - (c) were in the flow mode for 1, 5, and 10 min. (d) was under closed system mode for 5 min. (e) was in the flow mode for 1 min using KBr windows. (f) was the calculated vibrational spectrum for ethylmethylamine with scaling factor of 0.9557 and FWHM of 10 applied to the C-H stretching region between 3400 and 2600 cm <sup>-1</sup> . ....	100
Figure 6-4. Pressure drop vs. time for TEMAH gas in a closed gas cell mode at different temperatures. ....	102
Figure 6-5. Infrared spectra of TEMAH/D <sub>2</sub> O or H <sub>2</sub> O on Ge. The bottom was a 4.0×10 <sup>8</sup> L dose of TEMAH. The top two were 2.0×10 <sup>8</sup> L H <sub>2</sub> O or D <sub>2</sub> O after the TEMAH cycle. ....	103
Figure 6-6. Integrated peak area as a function of exposure time of TEMAH to H-Si(100) for the C-H stretch, 1640, 1600 and 1379 cm <sup>-1</sup> peaks. The C-H stretch region 3048-2730 cm <sup>-1</sup> is to the left axis, and the other three to the right axis. ....	104
Figure 6-7. In vacuo XPS spectrum of TEMAH adsorption at room temperature on H-Si(100)	

wafer.....	106
Figure 6-8. Decomposition of TEMAH: (1) Insertion reaction with H from 2-ethyl; (2) $\beta$ -hydride elimination for EMI; (3) Insertion reaction with H from methyl; (4) $\beta$ -hydride elimination for MEI. ....	107
Figure 6-9. Reactions (6)-(8): TEMAH intermediates surface reaction on H-Si(100).....	109
Figure 7-1. 3D Atomic groups for calculated spectra (a) bridged HTB on a H terminated Si cluster; (b) monodentate HTB on H terminated Si with one O-H termination; and (c) the HTB molecule.....	113
Figure 7-2. Top: liquid drop of HTB on Ge IRE. Bottom: calculated HTB vibrational spectrum, using scaling factor of 0.9545. ....	114
Figure 7-3. OH stretch region for different temperatures at saturation on (a) Si (100) and (b) Si (111). No film is spectrum of a clean ATR crystal after 24 hours in atmosphere at room temperature. ....	116
Figure 7-4. O-H, C-H and C-O stretching regions for (a) liquid HTB at 25 °C; (b) adsorbed HTB at 60 °C; (c) adsorbed HTB at 250 °C; and (d) liquid tert-butanol at 25 °C on Si (100). ....	117
Figure 7-5. HTB spectra given by (a) monodentate model; (b) bridged model; (c) liquid HTB on Ge; (d) adsorbed HTB on Ge. (a), (b) are at 0°C, (c) is at 25°C, and (d) is at 100°C. ....	118
Figure 7-6. (a) C-H stretch of adsorbed HTB on Si (111) at 60°C, showing Fourier self-deconvoluted peaks. (b) and (c): Deconvoluted C-H stretching at various temperatures on Si (100) and Si (111) respectively. ....	120
Figure 7-7. Spectra of adsorbed HTB at saturation for different substrate temperatures on (a) Si(100) and (b) Si(111). ....	122
Figure 7-8. Growth of OH group, CH stretching, CH bending, and characteristic bridged bond grows with time at 60°C on (a) Si(100) and (b) Si(111). The solid lines are primary axis, the dashed are secondary axis. ....	124
Figure 7-9. Peak area of the peak between 3118-2763 $\text{cm}^{-1}$ (CH stretch absorbance peak area) plotted with time for varying crystal temperatures. (a) Si(100) and (b) Si(111). ....	126
Figure 7-10. Arrhenius plot from 60°C to 185°C CH stretching peak area vs. temperature on Si(100) and Si(111). ....	127
Figure 7-11. ZPE-corrected PES for the HTB $\beta$ -hydride elimination: a) HTB molecule; (b) beta-hydride elimination transition state; (c) products: 2-butene and OH-terminated HTB. Electron Energies in kcal/mol: (a) 0 (b) 57.9 (c) 9.98 ....	129
Figure 7-12. ZPE-corrected PES for the hydrolysis of HTB: (a) separate HTB and water molecule; (b) H-bonded HTB and water adsorption; (c) transition state; (d) products: Hydroxyl terminated HTB and tert butyl alcohol. ZPE Energies in kcal/mol: (a) 0 (b) -4.56 (c) 3.27 (d) -3.45.....	130

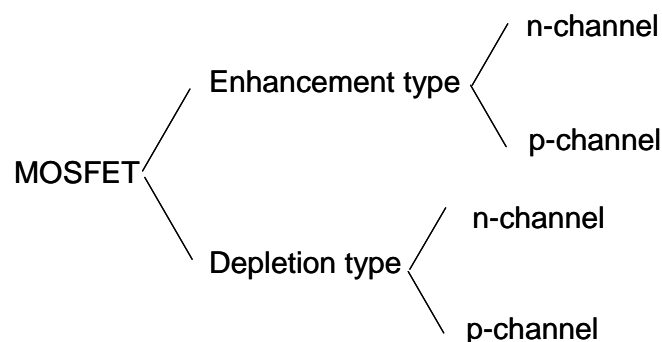
Figure 7-13. <i>ex-situ</i> XPS spectra for HTB adsorption on H-Si(100) at different temperatures. ....	131
Figure 7-14. Deconvoluted O 1s and Hf 4f peak for 1 hr. HTB adsorption on H-Si(100) at 250 °C.....	131
Figure 7-15. Ratio of O:Hf and C:Hf at different tepeatures.....	132
Figure 7-16. <i>ex-situ</i> XPS spectra for HTB adsorption on H-Si(111) at 250 °C. ....	132
Figure 8-1. Fluid Dyanmics Study Experimental Setup .....	136
Figure 8-2. AutoCAD schematic drawing of the flow through cell with dimmensions. ....	137
Figure 8-3. (a) temperature distribution on the Si surface with power 80W; (b) temperature profile on the flow through cell cross section with a power of 80W. ....	139
Figure 8-4. Measured temperatures on ss sheet at the back of Si substrate.....	140
Figure 8-5. Pressure difference between P1 and P2 as a function of time.....	146
Figure 8-6. Pressure at P1 and P2 as a function of different bubbler temperatures.....	146
Figure 8-7. Pressure difference between P1 and P2 as a function of different crystal temperatures.....	147
Figure 8-8. Pressure difference as a function of flow rate.....	148
Figure 8-9. Thickness along axis with different bubbler temperature while the crystal temperature was 250 °C. ....	150
Figure 8-10. Thickness along axis with different crystal temperature, 1 hour HTB adsorption with bubbler temperature of 65 °C.....	150
Figure 8-11. Thickness along the axis for HTB deposited on H-Si(100) crystal with bubbler at 65 °C and crystal setting temperature at 250 °C.....	151
Figure 8-12. Velocity profile of the flow.....	152
Figure 8-13. Mixed convection and film morphology with bubbler at 50 °C and HTB deposition on H-Si(100) for 1 hr. ....	154
Figure 8-14. (a) AFM images at the end of the substrate for 1 hour HTB deposition with 65 °C bubbler temperature on 250 °C hydrogen terminated Si(100) crystal (left column) or with 50 °C bubbler temperature on 250 °C n-Si(100) wafer (right column). (b) 3-D AFM image for comparison between surface morphology before and after HTB adsorption on the H-Si(100) at the end side.....	155
Figure 8-15. Roughness with different bubbler temperatures on native Si wafer.....	156

Figure 9-1. Thickness variation along axis for TDMAH/H <sub>2</sub> O ALD.....	161
Figure 9-2. Experimental setup for IR monitoring of the whole process. ....	162
Figure B-1. Omnic Macro program for auto spectra processing and analysis.....	174
Figure B-2. The MKS Piani gauge readout electronic connection with a serial port. ....	175
Figure B-3. Voltage-Pressure Measure LabView Front Panel .....	176
Figure B-4. Voltage-Pressure Measure LabView Block Diagram .....	177
Figure B-5. Pressure recorded as a function of time at temperatures from 25 to 200°C for TDMAH in a closed cell. ....	178
Figure B-6. Gas phase HTB at 5 min. after opening the bubbler in flow mode for 50 °C and 100 °C.....	179
Figure B-7. Models that have triplet peaks around 1200 cm <sup>-1</sup> .....	180
Figure B-8. TDMAH/H <sub>2</sub> O ALD process pattern. ....	181
Figure B-9. ALD Programming Logic Design with Omron Zen 10 C1**-A.....	182
Figure B-10. MFC flow rate calibration from the reading of down stream piani gauge. ....	183

# Chapter 1 MOSFET and High- $\kappa$ Dielectric

## 1.1 MOSFET Introduction

The first metal oxide semiconductor field effect transistor (MOSFET) was produced in the late 1960s,<sup>1</sup> and is currently the most widely used FETs. Depending on the kind of channel, the MOSFET is divided into p-type (PMOSFET) and n-type (NMOSFET). A MOSFET can be manufactured as enhancement-type or depletion-type. The type division is shown as Figure 1-1. The depletion-type MOSFET is different from the enhancement-type in that it has physically implanted channel, and thus can operate at either depletion mode or enhancement mode depending on the sign of applied gate voltage or threshold voltage. For a general discussion in this chapter, an n-channel enhancement-type MOSFET is given for demonstration.



**Figure 1-1.** MOSFET types.

The MOSFET is the primary building block of a complementary metal oxide semiconductor (CMOS) device which is a fast, common device for dynamic read-and-write and data saving in the volatile memory. CMOS digital logic circuits are a complimentary combination of n-type and p-type MOSFET's and have the advantage that they allow

virtually no current to pass through if the current path includes at least one series connection of both PMOSFET and NMOSFET. This results in larger circuits to be made by choosing n type or p type MOSFET combinations with lower power consumption.

### 1.1.1 MOSFET Operation

The structure of an n-MOSFET is shown as Figure 1-2. It is composed of a gate, source, drain, channel, body and gate insulator oxide. The surface channel is formed near the interface between the semiconductor body and the gate oxide when the direct current (DC) gate voltage  $V_G$  applied is greater than the threshold voltage  $V_{Th}$ . Threshold voltage is a very important figure-of-merit (FOM) that affects the standby power and leakage current which is dependent on the dopant level of the body.<sup>2</sup> It can be extracted by several models from the intercepts in the source-drain current vs. gate voltage ( $I_{SD}-V_G$ ) curves.

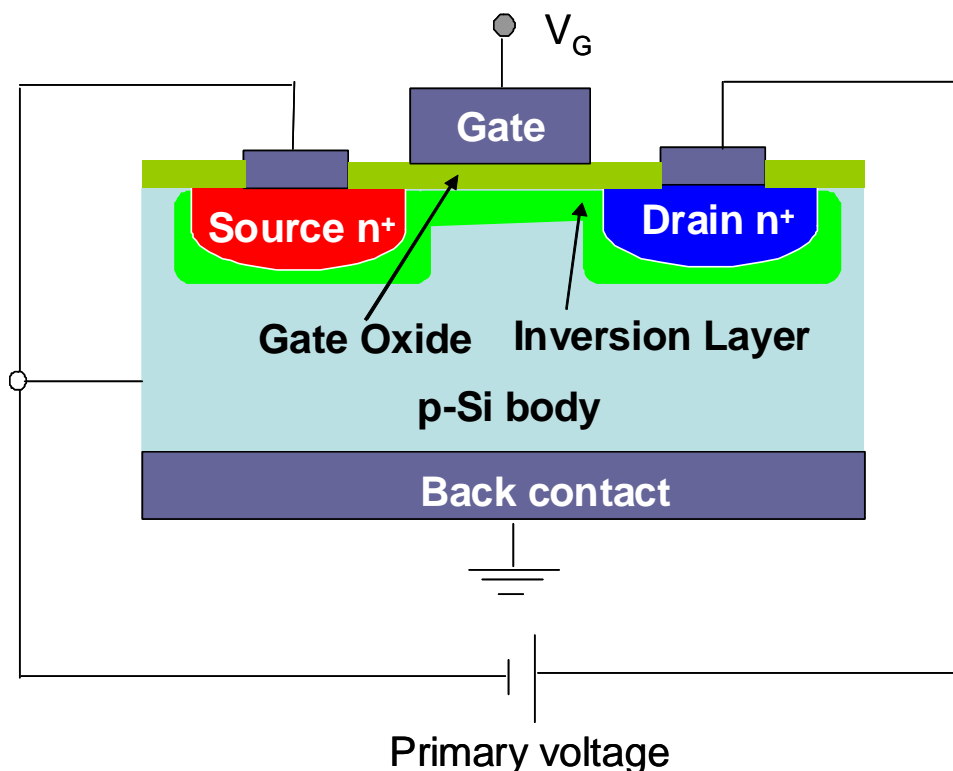


**Figure 1-2.** Schematic of an n-channel enhancement-type MOSFET structure

For the p type MOSFET as shown in Figure 1-2, when positive  $V_G$  applied on the gate is smaller than  $V_{Th}$ , a depletion layer forms to balance the gate charge by repelling the majority

carriers (holes in p-Si body). If a negative  $V_G$  is applied on the gate, an accumulation layer forms. When  $V_G$  is equal or greater than  $V_{Th}$ , an inversion layer or channel forms and turns the MOSFET on.

By increasing either gate voltage  $V_G$  or the voltage between source and drain ( $V_D$ ), the current between source and drain,  $I_{SD}$  initially increases linearly like a resistor obeying Ohm's Law and the carrier transport mechanism is dominated by phonon scattering. It saturates at higher  $V_D$  values due to a finite carrier concentration and speed. Carrier transport mechanism is mainly at the oxide/channel interface where surface scattering decreases carrier mobility. The characteristic equations for the drain current  $I_{SD}$  in NMOS with source connected to body can be described in three operation stages:

Cut-off:  $V_G < V_{Th}$ ,  $I_{SD} = 0$  for any  $V_D$

Ohmic:  $V_G > V_{Th}$ ,  $I_{SD} = (W/L) \cdot C \cdot (V_G - V_{Th} - V_D/2) \cdot V_D$  for  $V_D < V_{GS} - V_{Th}$

Active or Saturation:  $V_G > V_{Th}$ ,  $I_{SD} = (W/L) \cdot C \cdot (V_G - V_{Th})^2$  for  $V_D > V_{GS} - V_{Th}$

where the symbols has definitions:  $V_G$  the gate voltage,  $V_{Th}$  the threshold voltage,  $V_D$  the source to drain voltage,  $I_{SD}$  the current between source and drain, and  $C$  the dielectric capacitance.

### 1.1.2 MOSFET Scaling Down

The famous Moore's law<sup>3</sup> quantifies that the number of transistors placed on integrated circuits is to double every two years and the minimum feature size in a transistor decreases exponentially each year. On the International Technology Roadmap for Semiconductors (ITRS) the gate length is 45 nm in 2009 and will be 22 nm in 2016.<sup>4</sup> More MOSFETs placed on the same sized integrated circuit achieves unprecedented gains in productivity and lower cost per chip. Shorter MOSFET needs smaller supply voltage which ideally conserves more power that meets the requirement of low power dissipation and high throughput portable applications such as notebook computers, portable communication

devices and personal digital assistants (PDAs).

To scale down the MOSFET channel length without excessive short-channel effect which is the decrease of threshold voltage due to electrostatic charge sharing between the gate and the source–drain regions, both the oxide thickness and the gate-controlled depletion width in silicon must be reduced in proportion to channel length  $L$ .<sup>5</sup> However, when the physical thickness of the traditional  $\text{SiO}_2$  gate oxide films becomes less than  $\sim 2$  nm, the conventional scaling methodology cannot further satisfy the power limit for high-performance MOSFET ICs and low stand-by (direct tunneling) leakage current for low-power applications. The answer to solve this problem is to use higher permittivity materials in addition to 3D designed stacked and trenched capacitors. The high- $\kappa$  materials facilitate both an increased physical thickness and a reduction in the electrical equivalent oxide thickness (EOT) to maintain the required scaling. Equivalent oxide thickness is to convert the physical thickness of high- $\kappa$  to an equivalent thickness of  $\text{SiO}_2$  that would have the same capacitance.

$$EOT = \frac{k_{\text{SiO}_2}}{k_{\text{high-}\kappa}} \cdot t_{\text{high-}\kappa}$$

The capacitance per area of the high- $\kappa$  dielectric layer  $C/A$  is a useful FOM. It can be measured using a LCR meter at spot frequencies.

$$C / A = \frac{k_{\text{ox}}}{t_{\text{ox}}}$$

A summary of further downscaling technique limitations is listed in Table 1-1.<sup>8</sup>

## 1.2 High- $\kappa$ Dielectric Introduction

The gate dielectric has emerged as one of the most difficult challenges in further device scaling. The consideration of choosing a high  $\kappa$  oxide includes: the  $\kappa$  value, thermodynamic stability on Si, stability above 1000 °C for 5 s, band offset with Si of over 1 eV, electrical interface with Si, bulk defects, etc.<sup>6</sup> The dielectric constant  $\kappa$  value,

experimental band gap, and conductance band offset on Si of candidate gate dielectrics are listed in Table 1-2.<sup>6</sup>

On the ITRS for EOT scaling in the 2.0 – 1.0 nm region, silicon oxynitride  $\text{SiO}_x\text{N}_y$  was utilized in lieu of  $\text{SiO}_2$ . The  $\text{SiO}_2$  film can be nitrated by ammonia at 700 – 800 °C by controlling the ratio of water to ammonia.<sup>7</sup> In the EOT region of 1.0 nm to 0.7 nm for the 45 nm node,  $\text{HfO}_2$  has been employed based on the consideration of its high  $\kappa$  value (25), wide band gap (5.8), and thermal stability on Si. Long term scaling of the high  $\kappa$  stack below 0.7-0.6 nm EOT for the 22 nm node remains a major challenge. New promising materials such as  $\text{LaAlO}_3$  are still under investigation.

**Table 1-1.** Further Downscaling Physical and Technological Limitations [Ref.8]

Parameter	Constant field scaling factor	Generalized scaling factor	Limiting factors	Possible solutions
Voltage, $V_{DD}$	$1/\kappa$	$\epsilon/\kappa$	Thermal voltage, confinement, quantum	Low operation temperature
Electric field	1	$\epsilon$		
Channel length $L$	$1/\kappa$	$1/\kappa$	Lithography accuracy	
Drain current $I_D$	$1/\kappa$	$\epsilon/\kappa$	Punch through (tunneling between source and drain)	Double gate structure (DG FET)
Gate capacitance $C_{ox}$	$\kappa$	$\kappa$	Physical thickness limit, non-scalabilities, leakage current	Oxynitride/high- $\kappa$ stack, atomic layer deposition (ALD)
Gate propagation delay $t_{pd} \propto CV/I_D$	$1/\kappa$	$1/\kappa$	Nonscalable $V_{DD}$	High mobility materials, improved process
System clock frequency $f_c$	$\kappa$	$\kappa$	Parasitic capacitance, interconnect R and C, EMI	Low- $\kappa$ insulator, copper wire
Chip area	1	1	Yield, delay	Multi-chip module
# of Transistor per chip $n$	$\kappa^2$	$\kappa^2$	Interconnect complexity, yield	Serial signal communication between blocks
Power density $P \propto f_c n C_{ox} V_d^2$	1	$\epsilon^2$	Gate leakage, frequency, # of transistor, over heating	Smart system power management, physically thicker gate dielectric

**Table 1-2.** Static Dielectric Constant ( $\kappa$ ), Experimental Band Gap and Conductance Band Offset on Si of the Candidate Gate Dielectrics [Ref. 6]

	$\kappa$	Gap (eV)	CB offset (eV)
Si		1.1	
SiO <sub>2</sub>	3.9	9	3.2
Si <sub>3</sub> N <sub>4</sub>	7	5.3	2.4
Al <sub>2</sub> O <sub>3</sub>	9	8.8	2.8
Ta <sub>2</sub> O <sub>5</sub>	22	4.4	0.35
TiO <sub>2</sub>	80	3.5	0
SrTiO <sub>3</sub>	2000	3.2	0
ZrO <sub>2</sub>	25	5.8	1.5
HfO <sub>2</sub>	25	5.8	1.4
HfSiO <sub>4</sub>	11	6.5	1.8
La <sub>2</sub> O <sub>3</sub>	30	6	2.3
Y <sub>2</sub> O <sub>3</sub>	15	6	2.3
a-LaAlO <sub>3</sub>	30	5.6	1.8

### 1.3 High- $\kappa$ Dielectric Figure of Merits

#### 1.3.1 Dielectric constant $\kappa$

In dielectrics, polarization  $\mathbf{P}$  is a vector defined as the net electric dipole moment per unit volume with response to an electric field.  $\mathbf{P}$  is proportional to  $\kappa$ , and there are five major microscopic mechanisms of polarization including electronic (related to optical dielectric constant, resonant frequency  $\sim 10^{15}$  Hz), ionic (lattice contribution, resonant frequency  $\sim 10^{13}$  Hz), orientational (dipolar), interfacial (space charge) and ferroelectric.<sup>9</sup> Electronic and ionic are the two most important ones in most dielectrics. Total dielectric constant is dependent on the electric field frequency and temperature. In high- $\kappa$  dielectrics, the main contribution for

the static  $\kappa$  value arises from the lattice contribution  $\kappa_{\text{lattice}}$ .<sup>6</sup>

$$\kappa_{\text{lattice}} = \kappa - n^2 = \sum \frac{Ne^2 Z_T^{*2}}{m\omega_{TO}^2}$$

Here,  $N$  is the number of ions per unit volume,  $e$  is the electron charge,  $Z_T^*$  is the ion's transverse effective charge,  $m$  is the reduced ion mass,  $\omega_{TO}$  is the frequency of the transverse optical phonon,  $n$  is the refractive index of the dielectric.  $\kappa$  needs to be at least 4~5 times bigger than that of SiO<sub>2</sub> to avoid quantum tunneling.

### 1.3.2 Band Gap $E_g$

The bonding in high- $\kappa$  metal oxides is mostly ionic. The structure and symmetry dependent band gap,  $E_g$ , is the energy difference between the conduction band and valence band. A material is insulating if  $E_g$  is big enough and the Fermi level is within the gap.  $E_g$  depends on the crystal orientations as well. The schematic molecular orbital energy level diagram for a group IVB metal oxide MO<sub>2</sub> for octahedral structure (transition metal (TM) in an octahedral bonding arrangement with six oxygen neighbors) is shown as Figure 1-3 (a). Each oxygen atom is assumed to provide one  $\sigma$  and two  $\pi$  2p electrons to bond with the metal atom which contributes four additional electrons. The  $n$  d,  $n+1$  s, as well as empty  $n+1$  p orbitals in TM are all considered to contribute to bond formation. There are several aspects of the energy band scheme: 1) the top of the valence band (VB) is associated with non-bonding  $\pi$  orbitals of oxygen 2p, it is approximately equal to the energy of O 2p state; 2) the first two conduction bands (CB) are associated with transition metal  $n$  d states. The weak  $\pi$ -bonding of the TM establishes that the lowest anti-bonding state is close in energy to the transition metal atomic  $n$  d state; 3) in the order of increasing energy, the conduction bands have the  $t_{2g}(\pi^*)$  and  $e_g(\sigma^*)$  symmetries from the octahedral bonding arrangement; 4) the next conduction band is from the TM  $n+1$  s states with  $a_{1g}(\sigma^*)$  character. The energy separation between the  $n$  d and  $n+1$  s derived anti-bonding states is correlated with the difference between the atomic  $n$  d and

$n+1$  s states. The energy separation between the top of the valence band and the  $a_{1g}(\sigma^*)$  band edge defines the band gap  $E_g'$  which increases in the sequence from Ti, Zr to Hf. However, the lowest conduction band states are associated with  $d^*$ -orbitals of the TM as shown in the Figure 1-3 (b) for density of states in cubic  $\text{HfO}_2$  as an example.

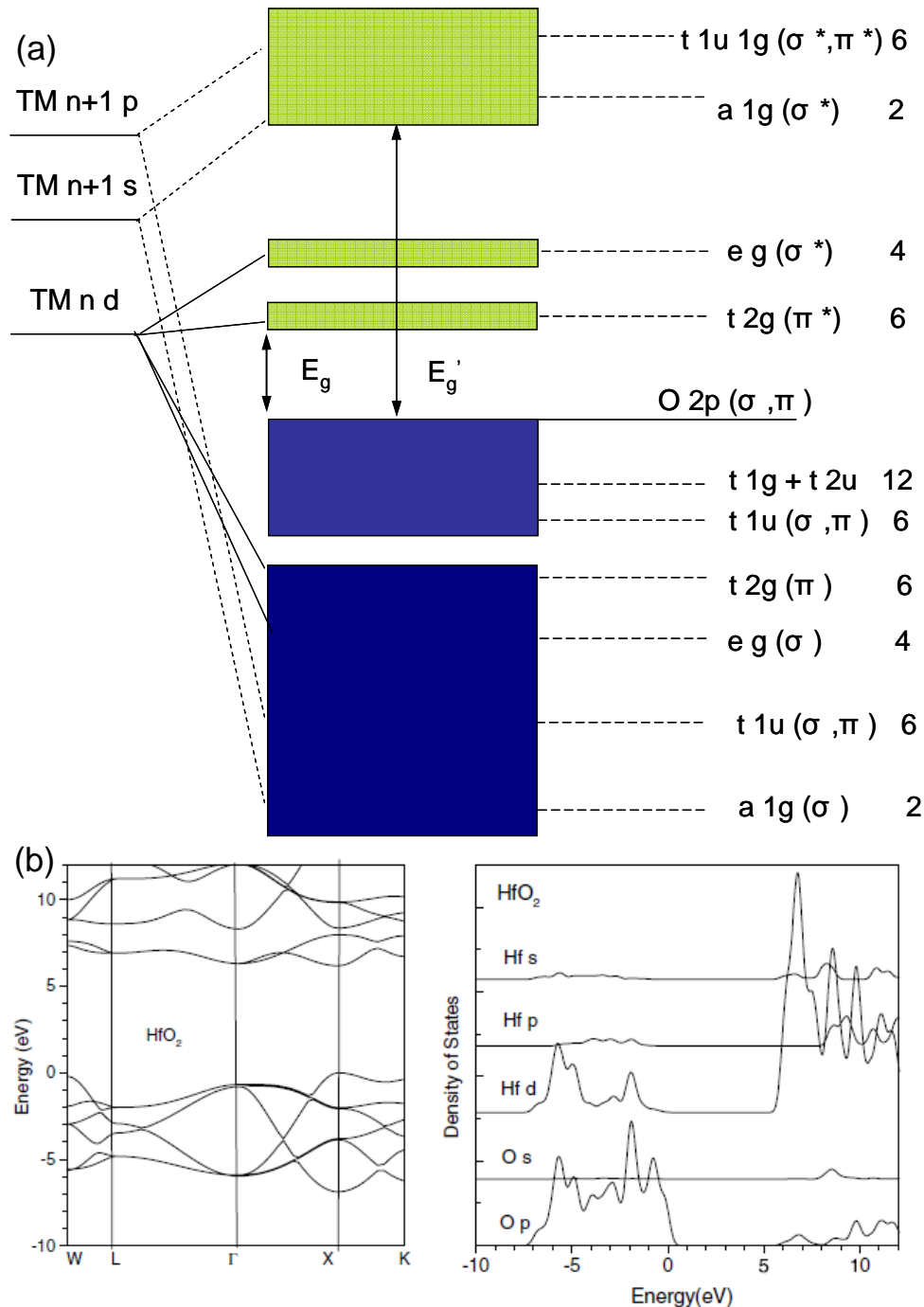


**Figure 1-3.** (a) Molecular orbital energy level diagram for a group IV transition metal in an octahedral bonding arrangement with six oxygen neighbors. [Ref.10]; (b) Bands and density of states of cubic  $\text{HfO}_2$ . [Ref. 6]

### 1.3.3 Band Offset

The band offset between the oxide and Si substrate requires over 1 eV for low leakage current as shown in Figure 1-4. A band offset lower than this barrier would result in injection of electrons or holes from the Si CB/VB into the oxide CB/VB bands.

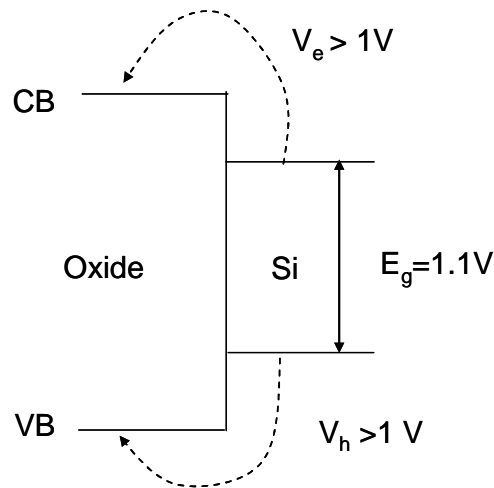


**Figure 1-4.** Schematic of band offsets determining carrier injection from intrinsic-Si into oxide band states.

The conductance band offset, CB, is usually the smaller one of the two. The band offset for two non-interacting surfaces is caused by the chemical potential difference between the high- $\kappa$  and Si (Schottky limit). While for two interacting surfaces, the interface dipole is modified by charge transfer (Bardeen limit).<sup>11</sup> The band line-up at the interface then depends on the dipole that includes two components: one intrinsic to the bulk oxide and one from interfacial bonding.

During p-type MOSFET depletion, the positive charge ( $V_G > 0$  and  $V_G > V_{FB}$ ) on the gate pushes the mobile holes into the substrate, and the semiconductor is depleted of mobile carriers at the interface which bends the bands down (Figure 1-5). The CB and VB are shifted up compared to the oxide bands, thus the CB offset is smaller than the flat band condition when  $V_G = 0$ . When the bias is big enough or the oxide thickness is too thin, the bend-down tunneling in device occurs.

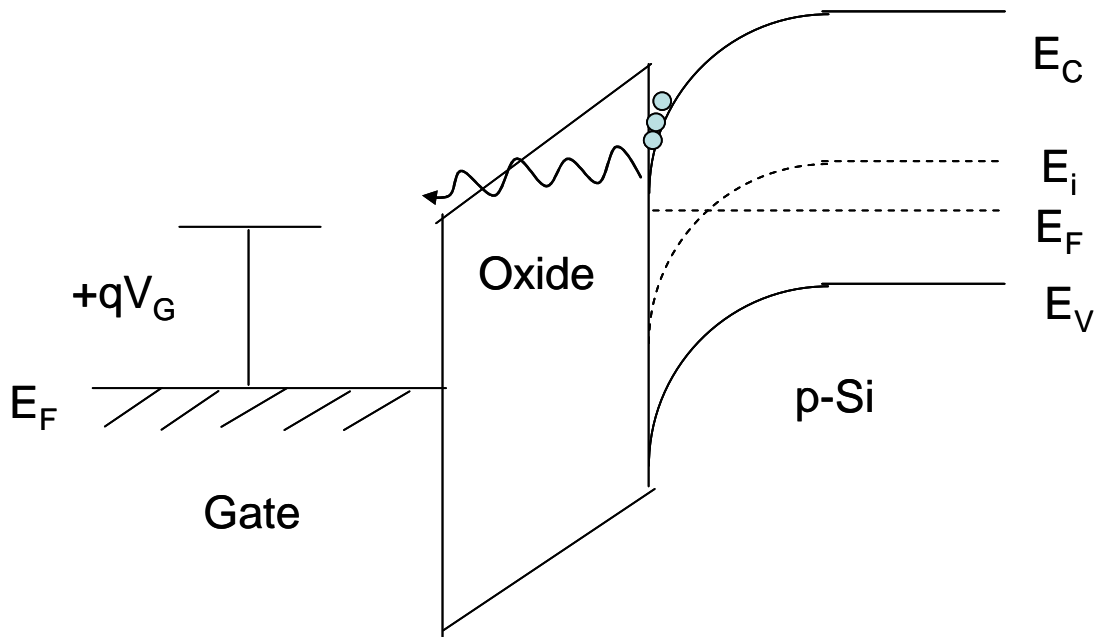


**Figure 1-5.** Schematic of bands in the depletion region.

#### 1.3.4 Interface Bonding

Thermally grown SiO<sub>2</sub> on Si has provided a kinetically stable, and device quality Si–SiO<sub>2</sub> interface with excellent electrical isolation properties over the past twenty years. In state-of-the-art CMOS processing, defect densities are on the order of 10<sup>10</sup>/cm<sup>2</sup>, mid-gap interface state densities are ~10<sup>10</sup>/cm<sup>2</sup> eV, and hard breakdown fields are in excess of 10 MV/cm.<sup>5</sup> The high- $\kappa$  material has to have comparable electrical properties that are compatible with the processing requirement standards such as 1000 °C during dopant activation. The main challenge is in the interface layer control: 1) the lattice between the high- $\kappa$  with crystal structure and the Si substrate has to match; 2) the interface has to avoid gap states and have a large enough band offset. The HfO<sub>2</sub>-Si(100) or ZrO<sub>2</sub>-Si(100) interface for example is modeled by GGA of the LDA method to have seven possible configurations shown as Figure 1-6.<sup>6</sup>

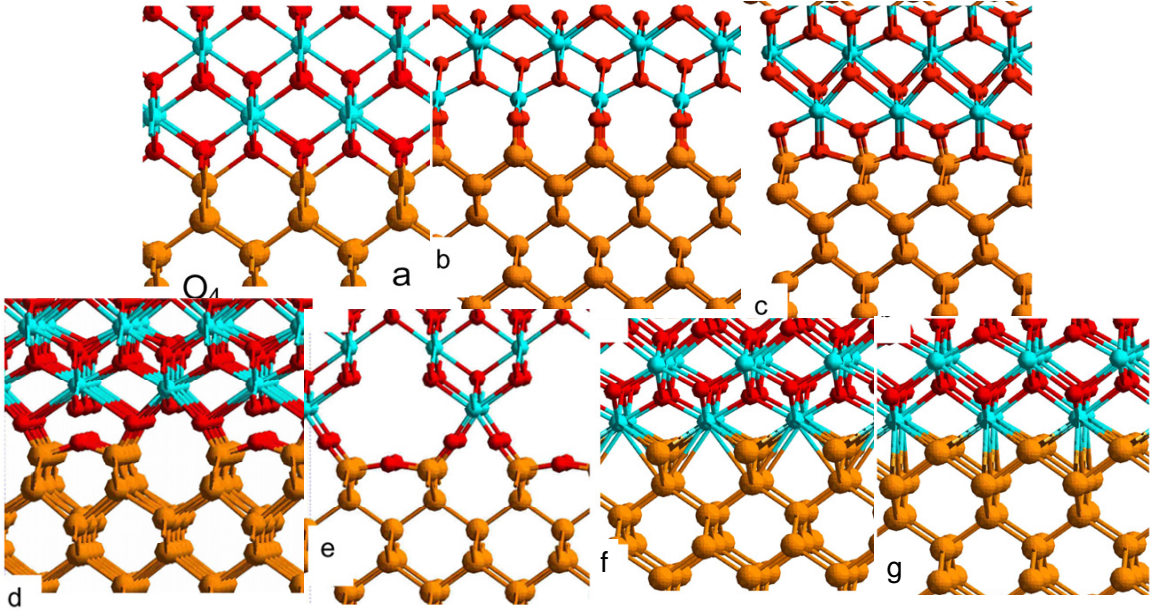


**Figure 1-6.** Various calculated configurations of (100) Si:ZrO<sub>2</sub> interface: (a) O<sub>4</sub>, (b) O<sub>3</sub>, (c) O<sub>3T</sub>, (d) O<sub>3B</sub>, (e) O<sub>2A</sub>, (f) Zr<sub>6</sub>, and (g) Zr<sub>10</sub>. [Ref. 6]

The lattice for ZrO<sub>2</sub> or HfO<sub>2</sub> matches Si(100) substrate well. The interfaces O<sub>4</sub>, O<sub>3</sub>, O<sub>3T</sub>, O<sub>3B</sub> and Zr<sub>6</sub> are insulating, while the Zr<sub>10</sub> interface is metallic.

### 1.3.5 Flat Band and Threshold Voltage

Although threshold voltage  $V_{TH}$  is a figure of merit for the whole MOSFET, it is with related to the gate oxide to a big degree in the flat band voltage  $V_{FB}$ . For an ideal metal-oxide-semiconductor structure, the work function difference between metal and semiconductor is zero.

$$\text{n-type semiconductor substrate: } \Phi_{MS} = \Phi_M - \left( \chi + \frac{E_g}{2q} - \Psi_B \right)$$

$$\text{p-type semiconductor substrate: } \Phi_{MS} = \Phi_M - \left( \chi + \frac{E_g}{2q} + \Psi_B \right)$$

where  $\Phi_M$  is the metal work function,  $\chi$  is the semiconductor electron affinity,  $E_g$  is the semiconductor band gap,  $\Psi_B$  is the potential difference between the metal Fermi level  $E_F$

and the intrinsic Fermi level  $E_i$ , and  $\Psi_B = \frac{kT}{q} \ln\left(\frac{N_D}{n_i}\right)$  depends on the thermal voltage and

doping concentration  $N_D$  of the semiconductor.

There are mainly three types of defects in the dielectric: mobile ionic charges, oxide-trapped charges, fixed charges. Assuming no trapped the charges in the gate oxide, the flat band voltage  $V_{FB} = 0$ . However, many dielectrics contain fixed space charges  $Q_f$  (either positive or negative,  $Q_f = \pm\sqrt{4k_{Si}qN_D\Psi_B}$ ) that has to be accounted in the flat band voltage.

$$V_{FB} = \Phi_{MS} + \frac{Q_f}{C_{accumulation}}$$

The capacitance per unit area is measured in accumulation mode at certain frequencies discussed in the previous MOSFET introduction part. This equation can be used for determining the fixed charge density with the other three measurable values.

The threshold voltage is expressed as:

$$V_{Th} = V_{FB} + 2\Psi_B + \frac{Q_f}{C_{inversion}}$$

For a thinner oxide layer with other fixed parameters, the capacity is bigger and thus a smaller  $V_{Th}$ , while more fixed charges result in higher  $V_{Th}$ .

## Chapter 2 HfO<sub>2</sub> Thin Film Development

### 2.1 Atomic Layer Deposition

Thin high- $\kappa$  film production processes must be reliable to produce controllable thin film properties such as purity, composition, thickness, adhesion, crystalline structure, and surface morphology. Chemical vapor deposition (CVD) and physical vapor deposition (PVD) are the two main traditional thin film deposition methods in industry over the last several decades. CVD has advantages such as the formation of dense, smooth, homogeneous, and conformal isotropic films even in high aspect ratio trenches for micro electro-mechanical systems (MEMS). Some disadvantages are difficulty in controlling film thickness and the possibility of rough and discontinuous thin films due to nucleation and three-dimensional island growth.

Atomic layer deposition (ALD) is currently on the International Technology Roadmap for Semiconductor (ITRS) for high- $\kappa$  dielectric gate oxides and diffusion barriers for backend interconnects. It was initially developed by Suntola and coworkers in 1974 for improved epitaxial growth of ZnS:Mn semiconductor polycrystalline thin film sandwiched by dielectric layers for use in thin film electroluminescent (TFEL) flat panel displays.<sup>12</sup> More recently in the mid 1990's, ALD has been attracting interest from Si-based integrated circuits (IC) industry because of its advantages of self-limiting deposition per cycle resulting in a superior thickness control and excellent conformality.<sup>13</sup> In addition, it can yield pin-hole free insulating films, grow conformal thin film in arbitrarily high aspect ratio trenches,<sup>14</sup> and can produce smooth films with more uniform chemical compositions over larger areas than CVD.<sup>15,16,17</sup> Its limitation is slow film deposition rate<sup>18</sup> and thus is not very suitable for thick films but is good for the current trend toward thinner films.

The CVD or ALD process includes several steps: 1) the precursor is transported to the

reaction zone; 2) the precursor encounters gas phase decomposition or remains intact; 3) the decomposed or intact precursor molecules adsorb onto the surface; 4) the molecules can either physisorb or chemisorb, diffuse across or react with other surface molecules, decompose, or desorb into the gas phase; 4) the chemisorption and/or decomposition of the precursor usually produces by-products which either desorb into the gas phase or remain in the film as contaminants; 5) the precursor and by-products outflow is transported from the reaction zone. Critical ALD processes that influence the film composition include: the substrate deposition temperature  $T_s$ , precursor selection, and the amount of dosage per cycle.<sup>14</sup> Adsorption and desorption are required in film growth. Ideally the sticking coefficient is 1 initially and 0 when the surface is saturated. However, practically this is not always true. There are two adsorption mechanisms: selective adsorption (a) and adsorbate-inhibition (b) as shown in Figure 2-1. For adsorbate inhibition, self-limiting growth layer by layer with alternating cycles is observed within a certain substrate temperature range –  $T_s$  window. Too low of a temperature will cause the precursor to condense without saturation, while too high of a temperature causes part of the adsorbed monolayer to re-evaporate resulting in less than one monolayer per cycle.

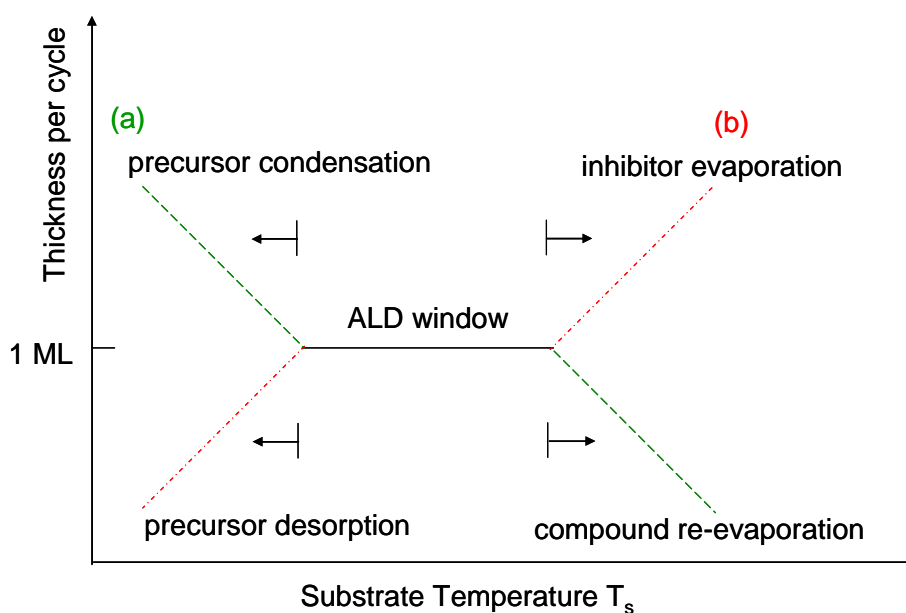


**Figure 2-1.** (a) Selective adsorption and (b) adsorbate-inhibition mechanism Ref. [19].

## 2.2 Reactors

There are three common types of CVD reactors used by industry: stagnation flow reactors, horizontal reactors, and low pressure multi-wafer barrel-type reactors. A horizontal multiple-wafer-in-tube type reactor shown in Figure 2-2 is the main production tool for growing polycrystalline Si, dielectric materials, and passivating films used in Si integrated-circuit manufacturing.<sup>20</sup> The substrates are heated in response to the external inductively coupled radio-frequency (RF) power.

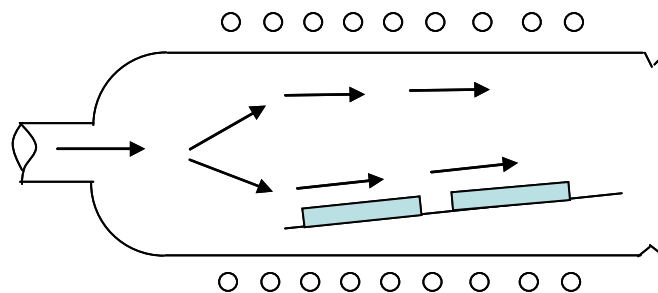


**Figure 2-2.** Multiple-wafer-in-tube type reactor. [Ref.19]

The precursor flows from the source to the substrate by a pressure gradient generated using a vacuum pump downstream. The flux of the precursor is perpendicular to the imposed temperature gradient. It is a classical configuration and has the advantage of high throughput. Concerns about reactant depletion and stagnant eddies due to the geometry and wall-substrate temperature difference driven buoyancy in the cold wall horizontal reactor has been a concern. The flow in a CVD reactor has three regimes determined by Knudson number  $Kn$ : molecular flow ( $Kn > 1$ ), transition regime ( $0.01 \leq Kn \leq 1$ ), and fluid flow regime ( $Kn < 0.01$ ). Simulations for fluid flow in a CVD reactor were developed using finite difference (2D) or finite element (3D) methods, and for molecular flow, line-of-sight computations or Monte Carlo methods have been used.<sup>20</sup> Design of reactors and visualization of CVD-reactor flows have been performed.<sup>21,22</sup>

The mixed complex flow in a rectangular duct representing a horizontal CVD reactor was reproduced as Figure 2-3. The conditions are:  $H_2$  carrier gas with an inlet velocity 58

mm/s, 700 °C substrate, 25 °C cold top wall, and a reactor 30 mm in height and 60 mm in width.<sup>23</sup>

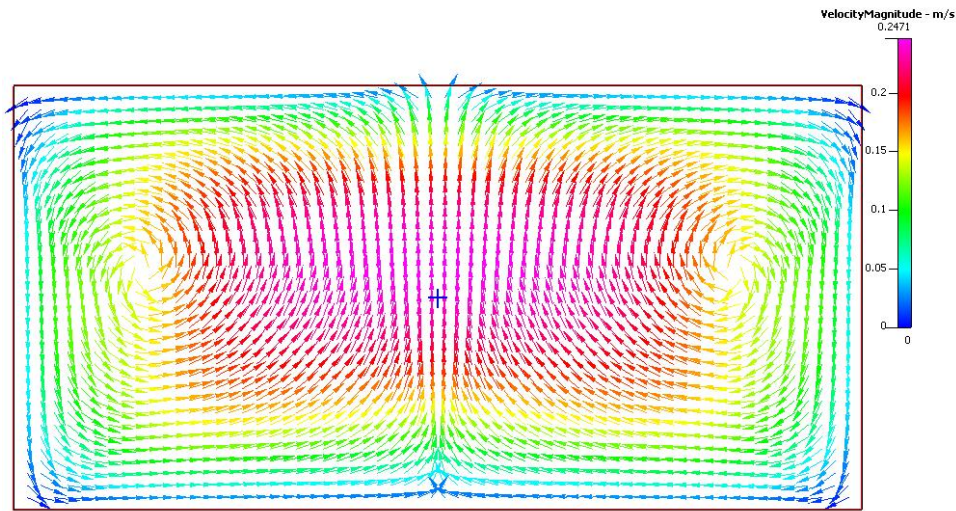


**Figure 2-3.** Flow behavior in a horizontal reactor with isothermal side wall. Reproduced using conditions in Ref. [23].

### 2.3 HfO<sub>2</sub> and On-going Studies

As mentioned in the previous chapter, among all the high  $\kappa$  candidates, HfO<sub>2</sub> is generally accepted as the material for current applications due to its relatively large high  $\kappa$  value, wide band gap and thermodynamic stability on Si.<sup>6</sup> Besides being a gate insulator in MOSFETs, HfO<sub>2</sub> has been studied widely for potential applications such as a tunnel dielectric in nanocrystalline nonvolatile memory devices,<sup>24</sup> a porous support in catalytic oxidative dehydrogenation,<sup>25</sup> variable capacitor in RF MEMS shunt switches,<sup>26</sup> gate insulator in the new-device-architecture double-gate transistors such as FinFET,<sup>27</sup> and crystalline HfO<sub>2</sub> with its high refractive index has led to its application in optical coatings for laser mirrors.<sup>28</sup> Various methods have been used to deposit HfO<sub>2</sub> by chemical solution deposition,<sup>29</sup> electron beam physical vapor deposition,<sup>28</sup> sol-gel method,<sup>30</sup> molecular-beam epitaxy (MBE),<sup>31</sup> chemical vapor deposition (CVD),<sup>32</sup> and atomic layer deposition (ALD).<sup>33</sup> Previous work has focused on implementation aspects such as its electrical properties,<sup>34,35</sup> chemical

composition,<sup>36,37,38</sup> and interfacial properties,<sup>4,39,40</sup> and also deposition processes and growth modes<sup>41,42,43,44</sup> including gaseous precursor reactions during CVD processing.<sup>45</sup> Several groups have reported the formation of an undesirable interfacial layer before or after post-deposition annealing for HfO<sub>2</sub> grown on Si, which depends on the starting surface and deposition methods.<sup>46,47,48</sup>

Most HfO<sub>2</sub> work has been done using hydrogen terminated Si surfaces as substrates which are the most commonly used in industrial electronic devices. Passivation with buffered hydrofluoric acid of the Si(100) surface results in an atomically rough 2×1 reconstructed monohydrogen surface (2×1 H-Si(100)),<sup>49</sup> while Si(111) forms a flat unreconstructed monohydrogen surface (1×1 H-Si(111)).<sup>50,51</sup> The dihydrogen terminated 1×1 Si(100) surface also forms,<sup>52</sup> but it is not as stable as the 3×1 H-Si(100) surface with four hydrogen atoms on three Si atoms.<sup>53</sup> Due to the presence of O<sub>2</sub> and H<sub>2</sub>O in the solutions used for producing these materials, a small number of Si centers terminated with =O or –OH may exist on these hydrogen terminated Si surfaces.<sup>54</sup> HfO<sub>2</sub> on a thermally oxide grown with low and high OH surface concentrations, and compared to H-terminated surface lead to different nucleation and growth characteristics. It has been found that hydroxyl terminated Si surfaces result in more uniform films<sup>44,46</sup> and a linear fractional coverage growth per cycle by HfCl<sub>4</sub> and water ALD deposition,<sup>55</sup> whereas HfO<sub>2</sub> grown on H-terminated Si exhibits nucleation, three-dimensional and nonlinear growth.<sup>56</sup> The disadvantage of starting with a hydroxyl surface is that the interfacial oxide increases the EOT; it is difficult to control the interfacial hydroxyl layer thickness; and it contains a large density of electron-trapping sites due to the existence of surface hydroxyl groups present in the form of silanols.<sup>57</sup>

Substrate temperature also plays a role during the interfacial layer formation. Low temperature (226 °C) deposited HfO<sub>2</sub> is reported to have faster growth rate compared to that grown at high temperatures, but nucleation results in conically grains at low deposition

temperatures. There is an abrupt interface without SiO<sub>2</sub> at temperatures at 300 °C while higher or lower deposition temperature would result in SiO<sub>2</sub> at the interface.<sup>58</sup> Different oxidant sources result in different film properties, for example HfO<sub>2</sub> processed by O<sub>3</sub> has the highest molecular density.<sup>56</sup>

The initial reaction of the Hf precursor with the Si substrate has been studied.<sup>59,60</sup> For example, in ALD processes using Hf[N(CH<sub>3</sub>)(C<sub>2</sub>H<sub>5</sub>)<sub>2</sub>]<sub>4</sub> [tetrakis(ethylmethyamido) hafnium, TEMAH] and Hf[N(C<sub>2</sub>H<sub>5</sub>)<sub>2</sub>]<sub>4</sub> [tetrakis(diethylamido) hafnium, TDEAH] on hydrogen terminated Si surfaces with H<sub>2</sub>O as the oxidant source, it was found that the adsorption was initiated by the metal precursor rather than water, and only ~50% of the H atoms on the hydrogen terminated Si surface reacted after many cycles. For another precursor Hf[N(CH<sub>3</sub>)<sub>2</sub>]<sub>4</sub> [tetrakis(dimethylamido) hafnium, TDMAH], an incubation period during ALD deposition onto the H-Si(100) surface has been observed,<sup>46</sup> suggesting the presence of a kinetic barrier for the initial ALD adsorption step. The dosing amounts for the three precursors are slightly different, which may account for the different observations in the adsorption initialization.

## 2.4 Precursor Decomposition Chemistry

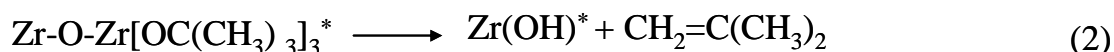
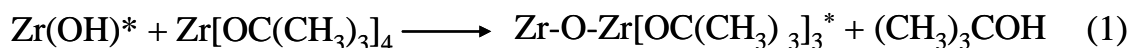
Hf MOCVD precursor types on the market include halides, alkoxides, β-diketonates, alkylamides, amidinates, alkyls, and cyclopentadienyls (Strem Chemicals, Inc. catalogue book). The selection of a precursor is made on the basis of vapor pressure, reactivity to effectively remove ligands, and storage or delivery stability. The three precursors used in the research described in this dissertation include hafnium tert-butoxide (HTB), tetrakis(dimethylamido) hafnium (TDMAH), and tetrakis(methylethylamido) hafnium (TEMAH). Their molecular weight, vapor pressure, decomposition temperature, and market prices are listed in Table 2-1.

**Table 2-1.** Precursor Properties

		TEMAH	TDMAH	Hf(OBu <sup>t</sup> ) <sub>4</sub>
Vapor pressure (Torr)	70 °C	0.3	1.9	2
	100 °C	1	3.4	13.2
Molecular Weight		410.90	354.79	470.94
Melting point (°C)		< -50	38-41	13
Boiling point (°C)		78 °C/0.01 Torr	85°C/0.1 Torr	90°C/5 Torr
Decomposition temperature (°C)		120	150	225
Price (\$/gram, Sigma-Aldrich 2010, approximate price)		40	35	45

CVD with HTB has been performed by Chabal's group.<sup>61</sup> Hydroxyl groups and carbon contained species were observed using Fourier transform infrared spectroscopy to exist in the film grown at 400 °C. The film is reported to be composed of monoclinic crystallines in an amorphous matrix, with the crystalline fraction increasing with thickness.

A similar precursor, zirconium tert-butoxide (ZTB) deposition has been performed by George's group and the following decomposition mechanism (1) and (2) has been proposed.<sup>62</sup>  $\beta$ -hydride elimination occurs on the tertbutoxide group producing one hydroxyl group and one isobutylene. The growth rate vs. substrate temperature (Figure 2-4) suggests the rate limiting step is the  $\beta$ -hydride elimination.



where \* denotes species on the surface.

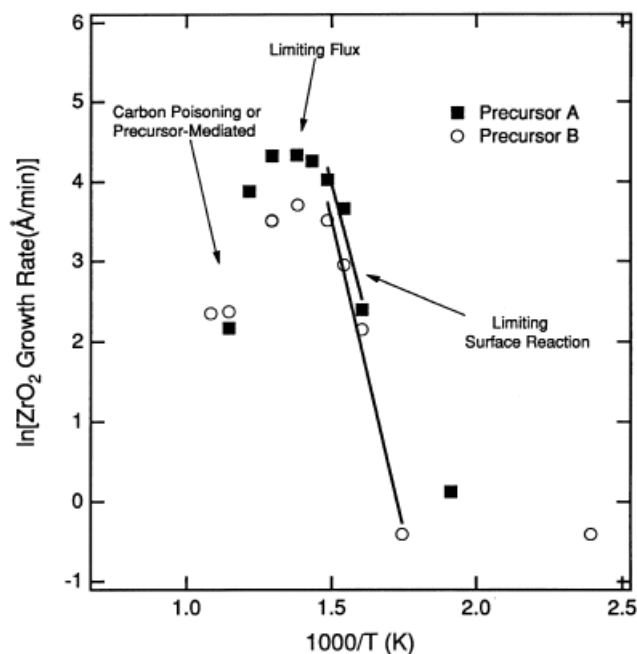
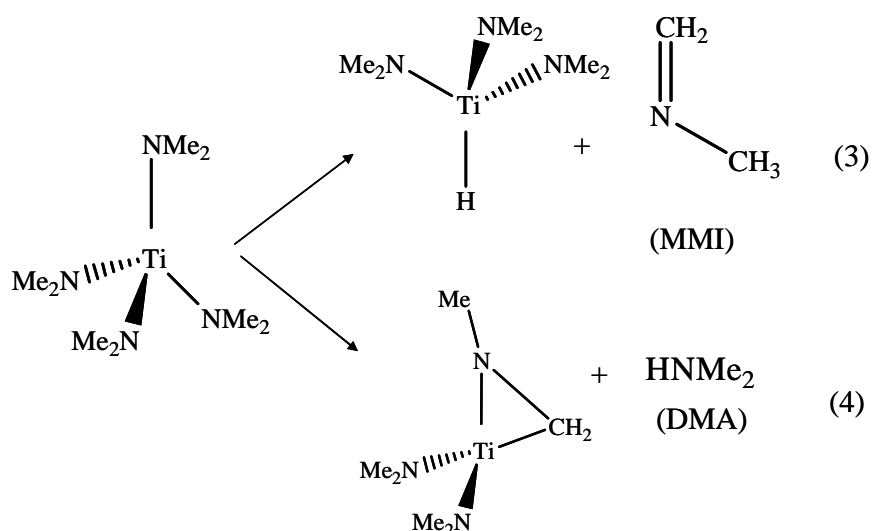
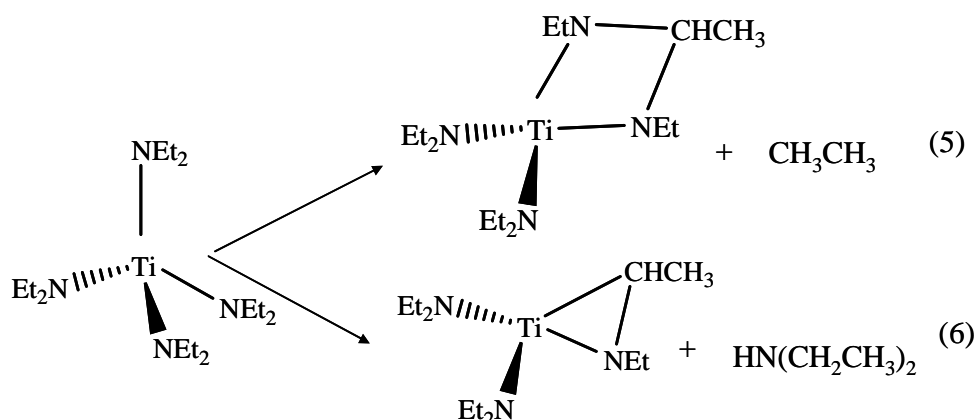


**Figure 2-4.** Arrhenius plot for  $ZrO_2$  growth rate vs.  $1/T$  for ZTB from First Reaction (A) and Aldrich (B). Ref. [62]

The most popular Hf precursors for ALD at present are hafnium alkylamides,<sup>34,39,41,43,63</sup> due to the relatively weak Hf–N bond and their high volatility, which enables efficient deposition at relatively low temperatures. Hafnium alkylamides can be used as the gaseous precursor for both the gate and the oxide. For example, TDMAH has been widely studied for the ALD of  $HfN_x$  and  $HfO_2$  on Si surfaces.<sup>43,46,64,65</sup> The thermal chemistry of tetrakis(dimethylamido) titanium ( $Ti[N(CH_3)_2]_4$ , TDMAT) has been extensively studied.<sup>66,67,68</sup> Different decomposition mechanisms have been proposed, including (3)  $\beta$ -hydride elimination which produces a hydride species and methylmetheneimine ( $CH_3N=CH_2$ , MMI),<sup>69</sup> and (4) an intramolecular insertion metallacycle generation reaction<sup>69</sup> followed by the formation of a MMI dative bond to Ti to produce a three-member metallacycle species.<sup>66</sup>



The product MMI also is formed in the decomposition of other dimethylamido compounds such as  $\text{As}[\text{NMe}_2]_4$  [*tris(dimethylamido)arsenide*, TDMAA].<sup>70</sup> Methane was observed during the gas phase decomposition of TDMAT by FTIR at high decomposition temperatures ( $>350^\circ\text{C}$ ), and was suggested to be formed by a gaseous radical disproportionation reaction.<sup>67</sup> In the crystal phase, a dimeric structure of TDMAH was observed by x-ray diffraction.<sup>71</sup> The decomposition mechanism of tetrakis(diethylamido) M (M = Ta, Nb, Ti) has been proposed as an insertion reaction which forms an intermediate four-member metallacycle (5) or three-member metallacycle (6) species.<sup>72,73</sup>



Two FTIR experiments were found in literature for TEMAH gas phase decomposition: Figure 2-5 is the gas phase IR spectra of TEMAH degradation during isothermal thermal gravimetric analysis (TGA). It shows TEMAH starts decomposing at  $120^\circ\text{C}$  and the

decomposition is said to likely occur after evaporation and during the transfer to the FTIR rather than during the evaporation process. While gaseous TEMAH IR spectra at room temperature by another group show very differently from intact TEMAH as shown in Figure 2-6. The decomposition is dependent on the different systems and is likely affected by time spent in the heated zone.

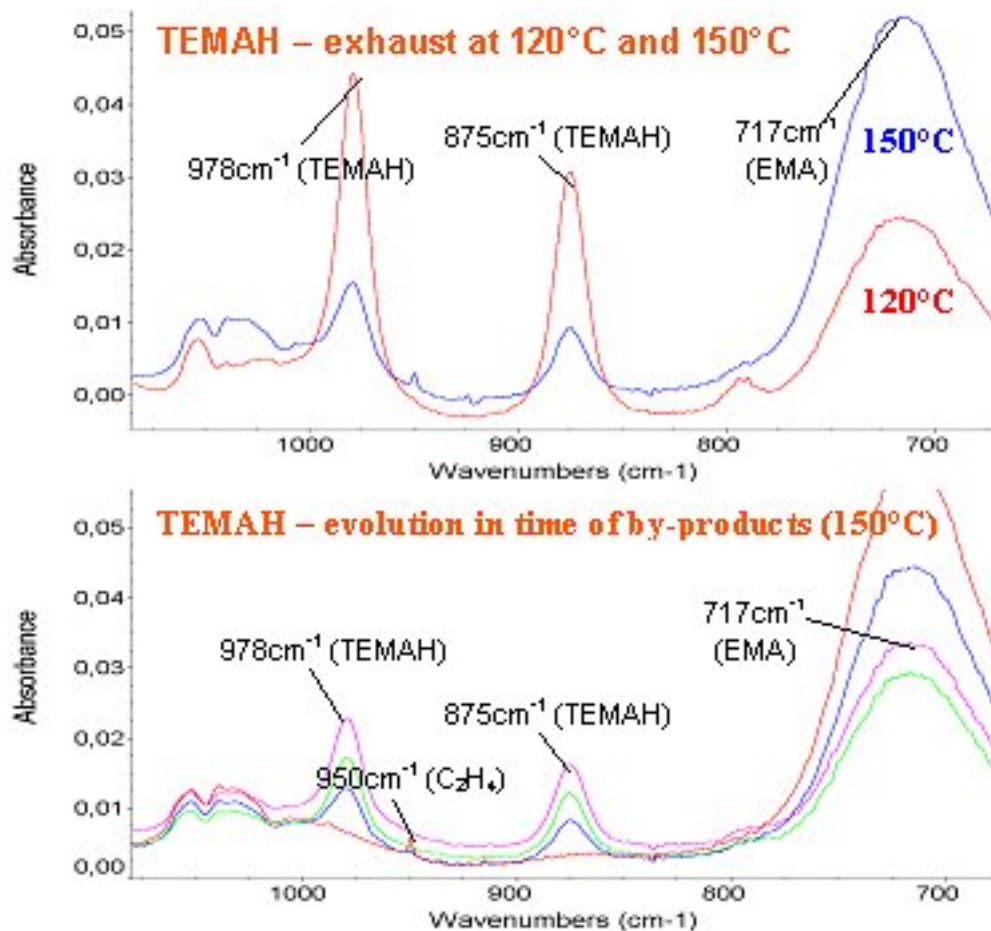


**Figure 2-5.** Degradation of TEMAH during isothermal TGA (120 °C and 150 °C) (Source: image supplied by Air Liquide ALOHA, and reproduced with permission from Semiconductor Fabtech, Edition 27, August 2005).

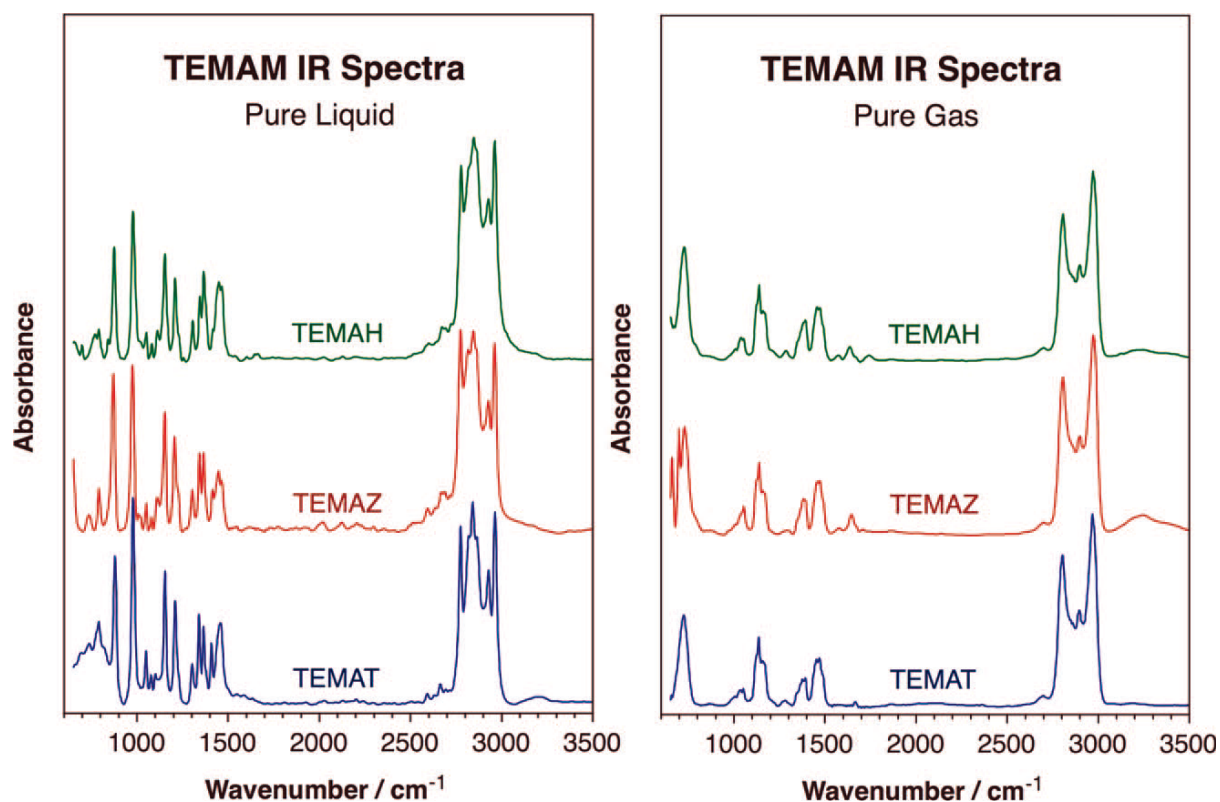


**Figure 2-6.** Infrared absorption spectra of TEMAT, TEMAZ, and TEMAH in both liquid (left panel) and gas (right panel) phases. (Source: reprinted from Ref. [74] by permission.)

## 2.5 Electronic Studies of alkylamide precursor surface reaction in ALD

Electronic structure calculations, for example, at the density functional theory (DFT) level, provide a means to predict the energetics of individual steps for proposed reaction mechanisms, as it is usually impossible to observe all the elementary steps in a hypothesized mechanism experimentally. The calculations also provide IR spectra to help the interpretation of the experimental spectra. Relatively few theoretical studies have been carried out on the reaction mechanisms of CVD or ALD using these relatively large precursors. Recently, Chen et al. studied the reaction of TEMAH on a model of the  $2 \times 1$  H-Si (100) surface with DFT study at the B3LYP/LanL2DZ level, and predicted that chemisorption of TEMAH on the H-Si surface has a high total reaction barrier of greater than 55 kcal/mol.<sup>75</sup> Furthermore, they predicted that the above reaction forms a Hf-Si bond with ethylmethylamine [EMA,  $(\text{CH}_3\text{CH}_2)\text{CH}_3\text{NH}$ ] as a by-product. The potential formation of a bond between Hf and Si may be problematic because if each Hf atom forms bonds with two Si atoms, a strained

interface has the potential to form dangling bonds which can cause more strain in the interface, trap charges and introduce states in the band gap.<sup>6</sup> In the ALD process, it has been proposed that the initially formed Hf-Si bonds may be oxidized to form the Hf-O-Si bonds after the water cycle to relieve the bond strain at the interface.<sup>6</sup> Unlike the reaction with the OH terminated Si surface, all reactions with the hydrogen terminated Si surfaces to form Hf-Si were predicted to be endothermic.<sup>75</sup> As the reaction involves one gaseous molecule (TEMAH) chemisorbing onto the Si surface with the release of another gaseous molecule (EMA),  $\Delta S$  will be small and  $\Delta G$  will be predominantly determined by  $\Delta H$ . Rodriguez-Reyes and Teplyakov<sup>76</sup> have studied the adsorption and dissociation of TDMAT on the bare Si(100) surface. They predicted that the N-C bond cleavage is a more thermodynamically favorable pathway than the Hf-N bond cleavage.

## **Chapter 3 Experimental Characterization Methods**

### **3.1 Summary of Characterization Techniques**

This chapter is an introduction to the basic principles and instrumentation of the six main experimental characterization techniques used in this dissertation: infrared spectroscopy, atomic force microscopy, x-ray photoelectron spectroscopy, quadrupole mass spectrometry, and interferometer.

### **3.2 Infrared Spectroscopy**

#### **3.2.1 Background**

Infrared radiation is electromagnetic radiation with a wavelength between 0.7 and 300  $\mu\text{m}$ . Fourier transform infrared (FT-IR) is a spectroscopic technique that is well established and useful for the examination of molecular structure and composition, with identification of the frequencies of bond vibrations between atoms in the material. The strength of the IR technique is the ability to obtain spectra from a very wide range of solids, liquid and gases. There are a number of types depending on how the infrared beam interacts with the sample. Namely, there are transmission IR, diffuse reflectance infrared Fourier transformer (DRIFT), infrared reflection absorption spectroscopy (IRRAS) and attenuated total reflectance Fourier transforms IR (ATR-FTIR).

#### **3.2.2 History of ATR**

The history of internal reflectance spectroscopy was traced back to four centuries ago with the observation by Newton of an evanescent field in a lower index of refraction medium in contact with a higher index of refraction medium. Harrick<sup>77</sup> and Fahrenfort<sup>78</sup> pioneered the exploration of this phenomenon for the production of absorption spectra for polyethylene.

With improvements in sample preparation such as contact between sample and the internal reflection element (IRE), data-handling ability, and sampling reproducibility, good quality infrared spectra can now be obtained for a wide range of samples. It has since been used to quantify Langmuir-Blodgett monolayers, to identify reaction intermediates and pathways in catalysis,<sup>11-13</sup> and to analyze biomaterials such as protein,<sup>14</sup> phospholipids,<sup>15</sup> and lipid-protein complexes.<sup>16</sup> *In situ* ATR-FTIR spectroscopy is an effective and non-invasive tool for observing reactions on semiconductors.<sup>2,7,8</sup>

### 3.2.3 ATR-FTIR Instrumentation and Basic Theory

The FTIR instrument used in the experiments is a Nicolet 4700 from Thermo Fisher Scientific with a NEXUS<sup>®</sup> source and a deuterated triglycine sulphate (DTGS) detector. The ATR accessory is a Horizon<sup>™</sup> from Harrick Scientific Inc. The instrument is controlled by a Thermo Scientific Omnic program which can record in-situ IR spectra and process data off-line. A Macro sample program written for data processing such as deconvolution of peak, measuring peak area, etc. is in Figure B-1, Appendix A. A vacuum compatible transmission IR gas cell is also from the same company. The main components of the commercially made FTIR include a high temperature wire alloy IR source, a two-beam Michelson interferometer, the sample, and an IR detector. The interferometer consists of a fixed mirror, a moving mirror and a beam splitter. The interferogram is the collection of intensities as a function of the moving mirror retardation at many discrete positions. The spectrum can be reconstructed from the interferogram using a Fourier transform of the temporal coherence of the light to obtain the absorption information for a range of wavelengths at the same time.

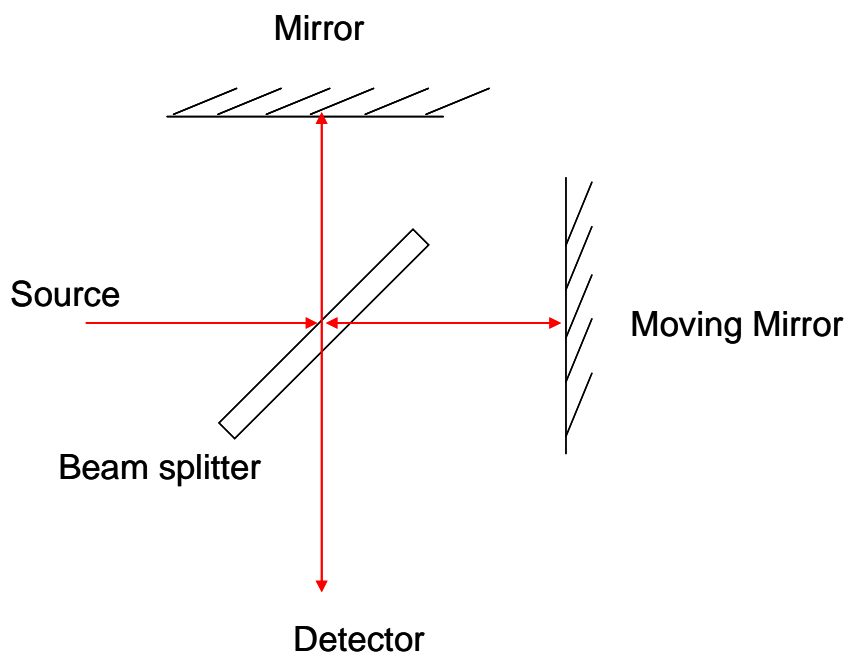


**Figure 3-1.** Schematic apparatus of infrared spectrometry Michelson interferometer.

The ATR component or transmission IR gas cell can be placed in the beam path of the FTIR and comprises the ATR-FTIR. The sample is placed on one side of the ATR crystal also called internal reflectance element (IRE). The IRE has a refractive index higher than the sample and the angle of incidence is higher than the critical angle that makes the incident IR beam totally reflected on the interface between the sample and the IRE. The number of beam reflections,  $N$ , is related to the element's thickness,  $t$ , and its length,  $L$ , as well as the incident angle,  $\theta$ .

$$N = \left( \frac{L}{t} \right) \cot \theta$$

In comparison to transmission IR whose beam is transmitted through the sample, the ATR signal is based on the evanescent field (EF) outside the IRE as a consequence of the interaction between incoming and reflected beams at each reflection. The EF has parallel and perpendicular components similar to an electromagnetic wave, but decays exponentially in the direction  $z$  which is normal to the interface:

$$E(\lambda) = E_0(\lambda)e^{-\gamma z}$$

where  $E_0(\lambda)$  is the field amplitude at the boundary. The field constant  $\gamma$  is given by:

$$\gamma = \frac{2\pi(\sin^2 \theta - n_{21}^2)^{1/2}}{\lambda'}$$

where  $\lambda$  is the wavelength,  $\theta$  is the angle of incidence with respect to the normal of the surface,  $\lambda'$  is the wavelength of infrared within the crystal,  $n_{21}$  is the ratio of the refractive index between the rarer medium and the IRE.

The depth of penetration  $d_p$  is the distance for the electric field amplitude to fall to  $e^{-1}$  of its original value:

$$d_p = \frac{\lambda}{2\pi(n_1^2 \sin^2 \theta - n_2^2)^{1/2}}$$

where  $n_1$  is the refractive index of the crystal and  $n_2$  is the refractive index of the sample with lower refractive index. It is usually about 1 to 4  $\mu\text{m}$  into the sample.

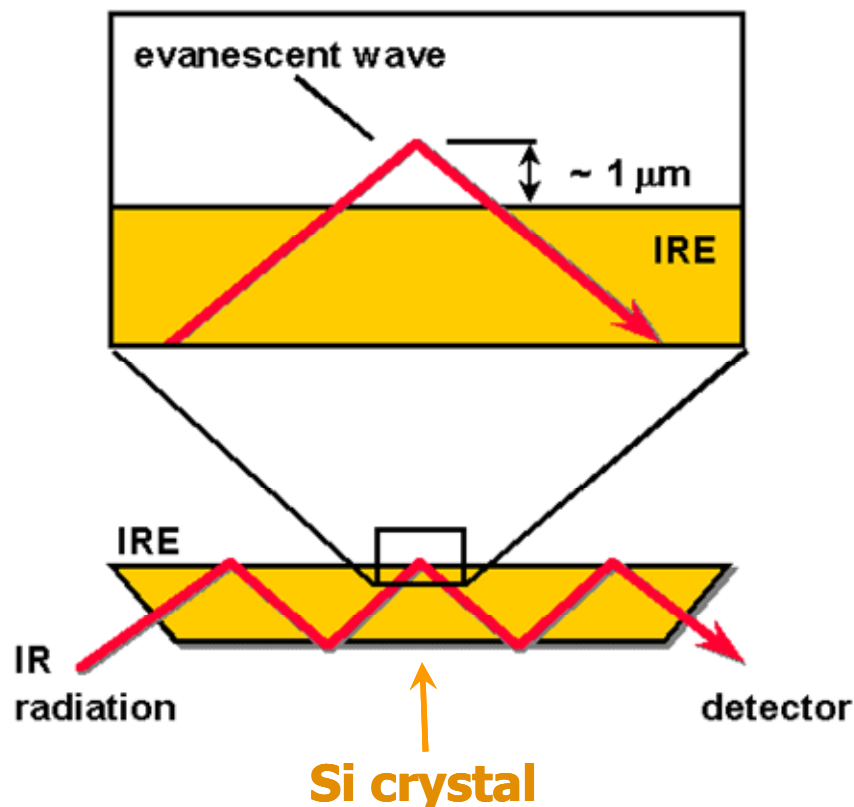


**Figure 3-2.** Internal reflectance element and evanescent wave.

In comparison of the sample absorbance of an ATR measurement to a transmission

measurement, the effective depth of penetration is defined for parallel polarization  $d_{e\parallel}$  and perpendicular polarization  $d_{e\perp}$  respectively:

$$d_{e\parallel} = \frac{n_1^2 n_2 \cos \theta}{(n_1^2 - n_2^2)} \cdot \frac{2n_1^2 \sin^2 \theta - n_2^2}{(n_1^2 - n_2^2) \sin^2 \theta - n_2^2} \cdot \frac{\lambda}{\pi \sqrt{n_1^2 \sin^2 \theta - n_2^2}}$$

$$d_{e\perp} = \frac{n_1^2 n_2 \cos \theta}{(n_1^2 - n_2^2)} \cdot \frac{\lambda}{\pi \sqrt{n_1^2 \sin^2 \theta - n_2^2}}$$

The effective penetration for an unpolarized IR beam is the average of the polarization penetration:

$$d_e = \frac{d_{e\perp} + d_{e\parallel}}{2}$$

The effective path length (EPL) for ATR is determined by the number of reflections:

$$EPL = N \times d_e$$

The absorbance is given as a function of the absorption coefficient,  $\varepsilon(\lambda)$ , and the concentration,  $C$ .

$$A(\lambda) = \varepsilon(\lambda) \cdot C \cdot EPL$$

A quantitative analysis of ATR spectra cannot be obtained straightforwardly by applying Beer's law as in transmission IR. Due to the wavelength dependence of  $d_e$ , peaks at lower wavenumbers for thick films are more pronounced in intensity and need correction for quantitative analysis. The choice of IRE element has to satisfy the following rules: compatibility with the sample unless it is intended to react; a high enough refractive index, because a too low refractive index may produce a derivative shaped absorbance band; and the crystal should be hard enough to withstand the pressure necessary for good contact to the sample.

### 3.3 Scanning Force Microscopy

#### 3.3.1 History of AFM<sup>81</sup>

An atomic force microscopy (AFM) is a high resolution scanning probe surface imaging technique, with a resolution 1000 times better than the optical diffraction limit. It was developed after the scanning tunneling microscope (STM, 1986 Nobel Prize in Physics) by the same working group of Gerd, Binnig, and Gerber in 1986. It compensates for STM's major disadvantage that it can only investigate conductive or conductively coated samples. It is a common and popular tool for morphology imaging, topography measuring, and manipulating nanoscale matter.

### 3.3.2 AFM Instrumentation and Basic Principles

The AFM usually consists of a laser source, a cantilever and tip, a piezoelectric scanner, and a photodiode detector and feedback electronic system. The AFM used in the experiments is a Digital Instruments Dimension 3100 Scans Probe Microscope with a NanoScope VI controller. The ultrasharp silicon cantilever NSC14/AIBS is from Mikro Masch, Narva with a force constant of  $\sim 5.7$  N/m and a resonant frequency of about 160 kHz.

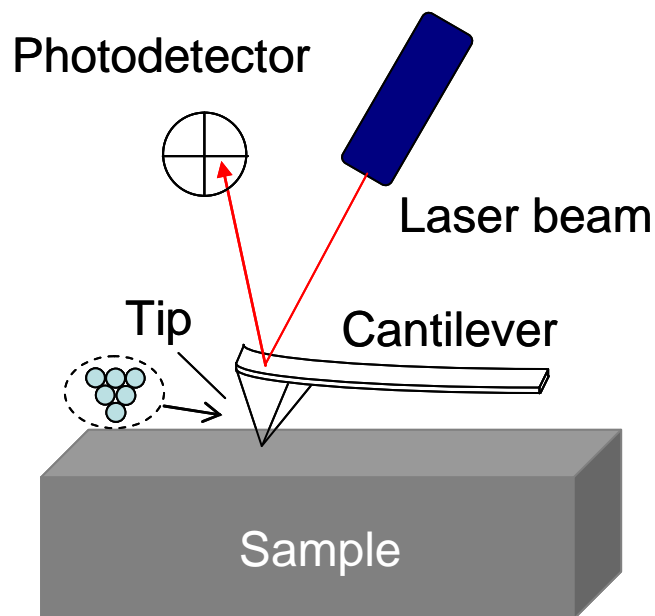


**Figure 3-3.** Atomic force microscopy apparatus schematic drawing.

During noncontact scanning such as in tapping mode, the cantilever is held on the order of tens to hundreds of angstroms from the surface, and the interatomic force between the cantilever and sample is long range attractive Van der Waals interactions or capillary

forces. In tapping mode AFM, the amplitude of cantilever oscillation at its resonance frequency is kept constant by adjusting the vertical position of the piezoscanner, using feedback from the photodiode detector, which varies due to the interatomic forces between the sample and the tip. The piezoscanner adjustment is recorded as the height image. The resonant frequency change of the cantilever due to phase or hardness changes on the surface is presented as a phase image (topography).

### **3.4 Photoelectron Spectroscopy**

#### **3.4.1 Introduction**

X-ray photoelectron spectroscopy (XPS), also known as electron spectroscopy for chemical analysis (ESCA), is one of the most versatile quantitative techniques in surface chemical analysis. It measures the elemental composition, chemical state, and elements' electronic states. Energy gap and band offset can also be measured using photoemission, ultraviolet photon emission spectroscopy.<sup>79</sup> It has a surface sensitivity of  $10^{-2}$  to  $10^{-3}$  monolayer (ML) and is thus can ascertain the level of surface cleanliness and the elemental composition of the surface down to a depth of about 50 Å.<sup>80</sup>

#### **3.4.2 History of XPS**<sup>81</sup>

In 1887, Heinrich Rudolf Hertz discovered the photoelectric effect. Albert Einstein explained the phenomena as the photoelectric effect in 1905 and was awarded the Nobel Prize in Physics 1921. Two years later, in 1907, P.D. Innes experimented with a Röntgen tube, Helmholtz coils, a magnetic field hemisphere (electron energy analyzer) and photographic plates to record broad bands of emitted electrons as a function of velocity, in effect recording the first XPS spectrum. Other researchers, Moseley, Rawlinson and Robinson, independently performed various experiments trying to sort out the details in the broad bands. After WWII, Kai Siegbahn and his group in Uppsala (Sweden) developed several significant improvements in the equipment and in 1954 recorded the first high energy resolution XPS

spectrum of cleaved sodium chloride (NaCl) revealing the potential of XPS. A few years later in 1967, Siegbahn published a comprehensive study on XPS bringing instant recognition of the utility of XPS. In cooperation with Siegbahn, Hewlett-Packard in the USA produced the first commercial monochromatic XPS instrument in 1969. Siegbahn received the Nobel Prize in 1981 to acknowledge his extensive efforts to develop XPS into a useful analytical tool.

### 3.4.3 XPS Instrumentation

The main components of a commercially made XPS system include: a source of X-rays, an ultra high vacuum (UHV) stainless steel chamber with UHV pumps, electron collection lens, an electron energy analyzer, Mu-metal magnetic field shielding, an electron detector system, a moderate vacuum sample introduction chamber, sample mounts and a sample stage.

The XPS system used for the experiments is an APEX system manufactured by Physical Electronics and Omicron. The X-ray source is a PHI model 04-548 with an operation voltage of 4-15 kV for exchangeable non-monochromatic Mg and Al anodes and a beam size of 1 mm. The X-ray source generally requires cooling to remove thermal heat generated. The Al K $\alpha$  source has photon energy of 1486.7 eV (wavelength 0.83386 nm) and a full width at half maximum (FWHM) resolution of 0.85 eV; the Mg K $\alpha$  corresponds to photon energy of 1253.6 eV (wavelength 0.989 nm) and an energy FWHM width of 0.7 eV. The X-ray is emitted when a shell initially vacant of an electron is filled by an electron from an adjacent shell or next adjacent shells. The energy difference between the two shells determines the emitted photon energy. The vacancy filled by an electron from an adjacent shell creates an x-ray termed  $\alpha$ , and  $\beta$  for difference of two shells. The x-ray photon is then absorbed by the sample which emitted a photoelectron that is collected in the analyzer.

The analyzer used is an Omicron EA125 energy hemispherical analyzer (HSA) with two concentric hemispheres with 125 mm diameter gap. The analyzer can be operated in

constant analyzer energy mode (CAE) and constant retard ratio mode (CRR). For CAE mode, the resolution can be increased by decreasing the pass energy  $E_p$ . For CRR mode, the magnification in the zoom lens can be increased by increasing the retard ratio. Most XPS spectra are acquired using CAE mode, while Auger spectra have to use CRR mode to recover weak peaks at high kinetic energies while restricting the intense low energy background that could do damage to the detection system.

### 3.4.4 XPS Physics

The XPS spectrum is usually plotted as the count rate of electrons detected versus the binding energy of the electrons. The electron binding energy ( $E_{BE}$ ) can be determined by Ernest Rutherford equation:

$$E_{BE} = h\nu - (E_{KIN} + \varphi)$$

where  $E_{KIN}$  is the kinetic energy of the emitted photoelectron, and  $h\nu$  is the known photon energy, and  $\varphi$  is the work function of the spectrometer (not the material). The process can be described by the diagram below. Lower quantum orbitals have higher binding energies.

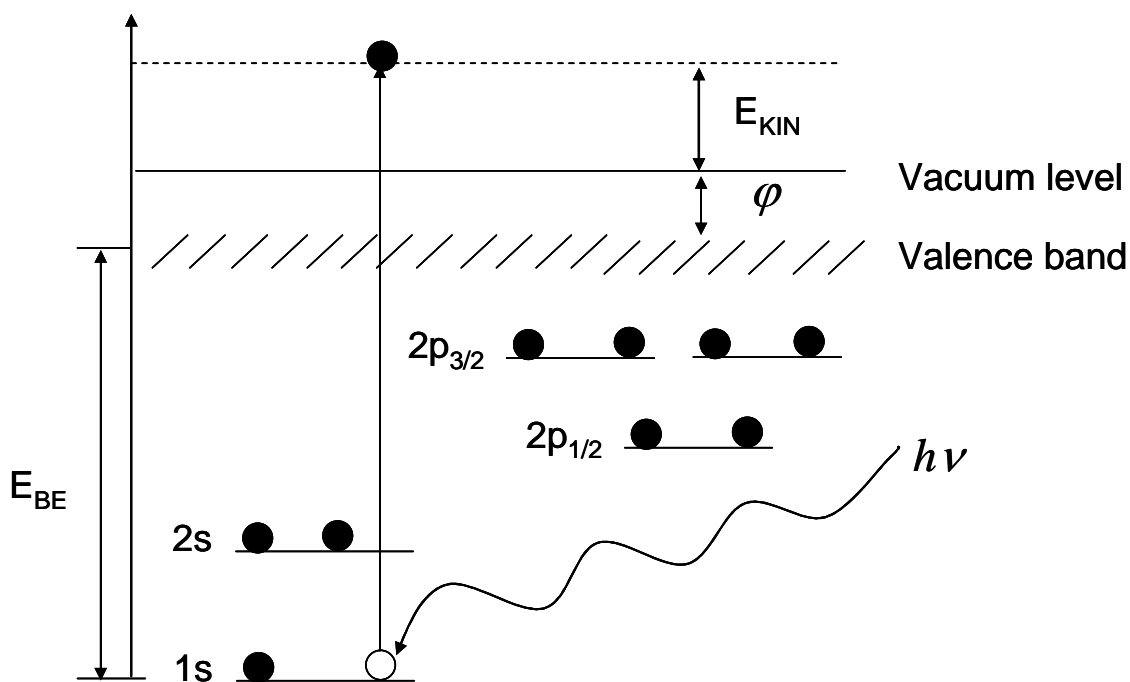


**Figure 3-4.** X-ray photoelectron spectroscopy excitation of electrons.

There are significant differences in the natural widths of the various photoemission peaks and the peak intensities are not simply related to the electron occupancy of the orbitals. Some levels such as p, d and f do not give rise to a single photoemission peak. This arises from spin-orbit coupling effects in the final state. For example, the removal of an electron from an originally full 4f Hf sub-shell leads to a coupling between the unpaired spin and non-zero orbital angular momentum. Using the Russell-Saunders coupling approximation, the  $(4f)^{11}$  configuration gives rise to two states (ignoring any coupling with valence levels) which differ slightly in energy and in their degeneracy:

$${}^2F_{5/2} \text{ g J} = 2 \times 5/2 + 1 = 6$$

$${}^2F_{3/2} \text{ g J} = 2 \times 7/2 + 1 = 8$$

These states arise from the coupling of the  $L = 3$  (F) and  $S = 1/2$  ( $2S + 1 = 2$ ) vectors to give permitted J values of 5/2 and 7/2, and the latter is lower in BE. The relative intensities of the two peaks is the ratio of degeneracies in the final state g J of them ( $g J = 2J + 1$ ), which in turn determines the probability of transition to such a state during photoionization to be  $4f_{5/2} : 4f_{7/2} = 3 : 4$ .

The exact binding energy of an electron also depends on the formal oxidation state of the element, and the local chemical and physical environment. Changes in these conditions give rise to chemical shifts in the peak positions in the spectrum from less than 1 eV to several eVs. Atoms of higher positive oxidation state exhibit a higher BE due to extra coulombic attraction between the electron and the nuclei (less screening). Analogously, an element with a more negative oxidation state has a peak shifted to a lower BE position.

The surface sensitive nature of XPS is due to the limited mean free path of escaped electrons, so variation of the angle between the surface of the sample and the detector, the take off angle can be used to perform nondestructive analysis of the variation of surface composition with depth. Angle resolved XPS (ARXPS) can also be applied for high  $\kappa$

dielectric thin film thickness measurement (1-8 nm) on Si using an overlayer model:<sup>82</sup>

$$\ln\left(\frac{I_o / SF_o}{I_s / SF_s}\right) - \left(\left(\frac{KE_o}{KE_s}\right) - \frac{1}{2}\right)^{0.75} \frac{t}{\lambda_o \cos \theta} - \ln 2 = \ln\left(\sinh\left(\frac{t}{2\lambda_o \cos \theta}\right)\right)$$

where I, SF, KE, and  $\lambda$  are the integrated intensities, atomic sensitivity factor, kinetic energy, and attenuation lengths of the substrate (*s*) and the overlayer (*o*), respectively. Note that  $\lambda_o$  is 1.7 nm using a semiempirical relation developed by Cumpson and Seah,<sup>83</sup> while *t* is the film thickness and  $\theta$  is the electron emission angle with respect to the surface normal. Statistically 95% of the emitted electrons come from about  $3\lambda$  within the surface for a normal takeoff angle where  $\cos(\theta) = 1$ .

### 3.5 Quadrupole Mass Spectrometer

#### 3.5.1 Background and History<sup>81</sup>

Mass spectrometry (MS) is an analytical technique that measures the mass-to-charge ratio of ions from the sample to determine the elemental composition and molecular structure of the material. It was traced back to 1886, when Eugen Goldstein observed the anode rays in low pressure gas discharge into a perforated cathode. Francis William Aston (1922 Nobel Prize in Chemistry) and Arthur Jeffrey Dempster devised the modern techniques of mass spectrometry. An ion trap technique was developed by Hans Dehmelt and Wolfgang Paul in the middle 1950s. Development of ionization techniques continue as electrospray ionization (ESI) and soft laser desorption (SLD) were honored by a Nobel Prize recently.

#### 3.5.2 Quadrupole MS Instrumentation and Basic Theory

The mass spectrometer used in this research is an Inficon 200 Quadrex residual gas analyzer with an electron ionization source, a quadrupole mass analyzer and an electron multiplier detector. The process is shown below:

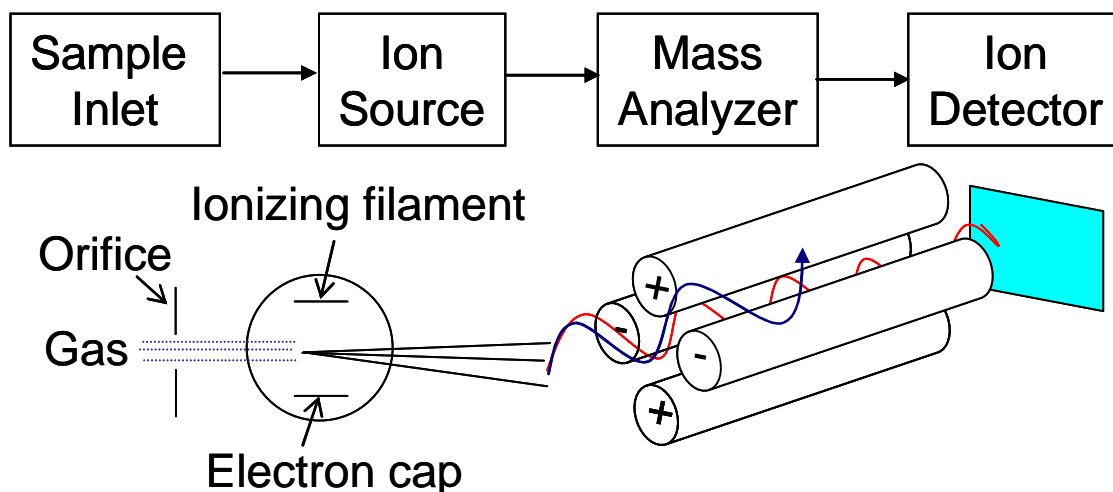
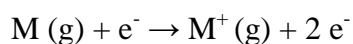


**Figure 3-5.** Mass spectrometer with electron ionization source and quadrupole analyzer.

In electron impact ionization sources, a beam of electrons impact the sampler gas with sufficient energy to ionize or fragmentize the molecule. The process can be summarized by the equation:



The ion source is designed so that when the ions are formed they are accelerated from the source and into the mass analyzer. The quadrupole mass analyzer is composed of four hyperbolic or cylindrical rods with adjacent rods having opposite polarities that serve as a mass filter. Alternating fields subject a force (given by the Lorentz force law) to the charged particles:

$$\vec{F} = -e\nabla\Phi$$

The electrical field  $\Phi$  is a combination of DC (U) and RF (V):

$$\Phi = \pm \frac{[U - V \cos(\omega t)]}{2}$$

Only a single mass/charge ( $m/z$ ) value is stable at certain conditions. The quadrupole uses oscillating electrical fields to select a  $m/z$  ratio by destabilizing the paths of the other ions.

$$\frac{U}{V} \propto m/z$$

Ions are detected by changing V with a fixed U for a constant frequency, or by

changing frequency with a constant U and V. Stable states only exist for a certain combination of U and V. For stable selection, an increase of the U/V ratio results in better resolution and less sensitivity based on the operating line in the following U/V diagram as shown in Figure 3-6.

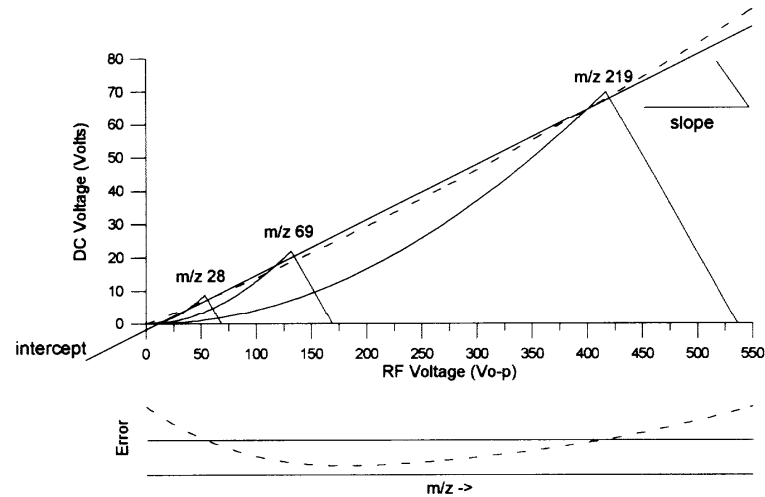


**Figure 3-6.** U-V diagram for quadrupole control line of operation.

### 3.6 Thickness and Pressure Measurement

#### 3.6.1 Thickness Measurement

Thickness is an important parameter for thin film characterization, which can typically range from a few atoms ( $<10\text{\AA}$ ) to  $100\ \mu\text{m}$ . Two main classes of thin film measurement are optical and stylus based techniques. The latter is advantageous in measuring opaque films such as metals, but is limited in speed and accuracy, and needs a “step” in the film to measure the thickness. In comparison, optical techniques can measure thin film characteristics such as thickness, roughness, and optical constants in a more accurate, non-destructive way, with less sample preparation requirements. Interferometry is one of the optical methods and a Filmetrics F20 with an FILMeasure software was applied in this research. It has advantages in speed, simplicity, and cost compared to other techniques such as ellipsometry or profilometry. It is suitable for measuring  $100\ \text{nm}$  to  $50\ \mu\text{m}$  films.

The working principle is reflecting light off the film and then analyzing the reflected light over a range of wavelengths. Light traveling through a material at a fixed time is given by:

$$A \cdot \cos\left(n \frac{2\pi}{\lambda} x\right) \cdot \exp\left(-k \frac{2\pi}{\lambda} x\right)$$

where  $n$  is the refractive index, and  $k$  is the extinction coefficient.

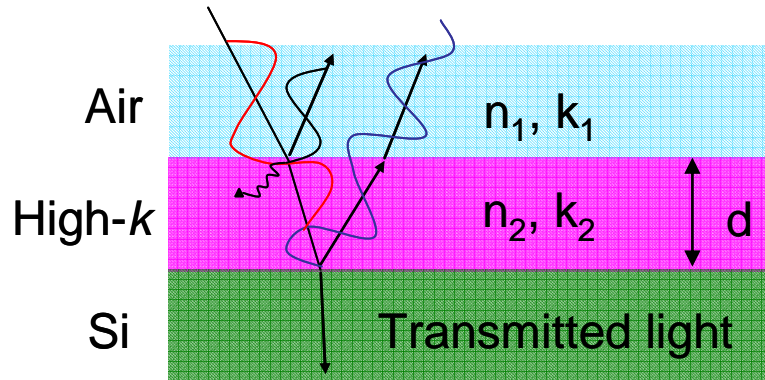


**Figure 3-7.** Light interference in a three-layer model.

Assuming the  $k = 0$  for dielectric films, and light reflected on multiple interfaces, the reflectance can be expressed as a function of film thickness  $d$ :

$$R = A + B \cos\left(\frac{4\pi}{\lambda} Nd\right)$$

where  $A$  and  $B$  are constants and  $N$  is an integer. The reflectance of a thin film varies periodically with  $1/\lambda$ . Thicker films exhibit a greater number of oscillations over a given wavelength.

Optical parameters such as  $n$  and  $k$  are determined by calculating reflectance spectra based on trial values of thickness and the  $n, k$  model parameters. The values are adjusted by the software until the calculated reflectance matches the measured reflectance. A common Cauchy model for dielectrics generally has three parameters:

$$\text{Cauchy: } n(\lambda) = A + \frac{B}{\lambda^2} + \frac{C}{\lambda^4}$$

$$k(\lambda) = 0$$

### 3.6.2 Pressure Measurement

The Pirani gauge was invented in 1906 by Marcello Pirani. The one used in this work is from MKS, a Series 945 with a digital controller. It consists of a metal filament suspended in a tube which connects to a vacuum system. The working principle for the gauge is based on measuring the resistivity of the filament whose temperature changes as a function of the number of gas molecules that absorb energy from it. The output signal is a dc voltage with constant current. Due to different thermal conductivities, the measurement of gases other than N<sub>2</sub> has to be calibrated. The gauge may be used for accurate pressure measurements between 0.5 Torr to 10<sup>-4</sup> Torr. The mean free path of gas molecules is given by  $l = \frac{1}{\sqrt{2}\pi a^2} / \frac{pN_A}{RT}$ . It has to be greater than the diameter of the heated filament for effectively measuring a true pressure, and is inversely proportional to the number of molecules that can carry away the heat. A LabView program which records voltages and converts into pressure vs. time is given in Figures B2 - B4, Appendix A.

## Chapter 4

### Density Functional Theory & Infrared Spectroscopy Calculation

#### 4.1 Chapter Summary

For reaction mechanism studies, a combination between theory and experiment is best. The former has to be tested by experiments and the latter has to be accepted by theory. Many pioneering works of Hartree, Fock, Slater, Thomas, Fermi, Bloch, Dirac, Wigner, Mulliken, Pauling, and Schrödinger in the nineteen twenties and nineteen thirties have laid the groundwork for modern computational quantum chemistry. In this chapter, a brief introduction of these accumulated theories is summarized, especially in correlation with molecular electronic structure, energetic, and spectra calculations that forms the theoretical predictions for the experimental observations. More detailed knowledge and solution procedures can be found in quantum mechanic books such as Levin's Quantum Chemistry<sup>84</sup> and the guide book for Gaussian - Exploring Chemistry with Electronic Structure Methods. The nomenclature and notations are borrowed from them here.

#### 4.2 Quantum Mechanics Theoretical Background

##### 4.2.1 The Schrödinger Equation

The time-independent Schrödinger equation describes the wavefunction of a stationary state of a many-electron system such as an atom or molecule and can be generally expressed as

$$\hat{H}\psi = E\psi$$

where the Hamiltonian operator  $\hat{H}$  is made up of kinetic and potential energy terms and can

be given by the following equation:

$$\hat{H} = -\frac{\hbar^2}{2m} \nabla^2 + V$$

The first term is the kinetic part and the second term is the potential energy component. The Hamiltonian is a Hermitian operator that has to satisfy the following theorems:

Theorem 1: The expected value of a Hermitian operator is a real number

Theorem 2: Eigenvalues of a Hermitian operator are real numbers.

Theorem 3: Eigenfunctions of a Hermitian operator with different associated eigenvalues are orthogonal functions.

Corollary: Eigenfunctions of a Hermitian operator with the same eigenvalues maybe transformed into orthogonal functions while remaining eigenfunctions of the operator.

#### 4.2.2 The Molecular Hamiltonian

For the molecular Hamiltonian, the kinetic energy T is a summation of  $\nabla^2$  over all the particles in the molecule for both electrons  $T_e$  and nuclei  $T_n$ . The potential energy component is the Coulomb repulsion or attraction between each pair of charged entities. Each atomic nucleus is treated as a single charged mass.

$$V = \frac{1}{4\pi\epsilon_0} \left( \sum_i^{e's} \sum_I^{nuclei} \left( \frac{Z_I e^2}{\Delta r_{iI}} \right) + \sum_i^{e's} \sum_{j<i} \left( \frac{e^2}{\Delta r_{ij}} \right) + \sum_I^{nuclei} \sum_{J<I} \left( \frac{Z_I Z_J e^2}{\Delta R_{IJ}} \right) \right)$$

The Born-Oppenheimer approximation<sup>85</sup> leads to a separation of the molecular Schrödinger equation into a part for the electronic wavefunction and a part for the nuclear motions, which is for the vibration and rotation.

The electronic wavefunction is given by

$$\hat{H}_e \psi_e(r) = E_e \psi_e(r)$$

where

$$\hat{H}_e = -\frac{\hbar^2}{2m} \nabla^2 - \sum_I \frac{e^2}{4\pi\epsilon_0 |R_I - r|}$$

and the total energy is

$$E = E_e + E^{(R)}$$

$E^{(R)}$  is the nuclei repulsion potential components.

$$[T_n + V_{nn} + E^{(R)} - E] \Phi_n = 0$$

$\Phi_n$  is one factorial function for the product of separable wavefunction (approximately) of nuclei coordinates only.

Since the electrons are fermions, an electronic wavefunction  $\psi$  must satisfy the antisymmetrization requirement that it is antisymmetric (changes sign) with respect to interchange of any pair of electron position coordinates.

#### 4.2.3 Hartree-Fock Theory

The Hartree-Fock (HF) theory<sup>86,87</sup> is an approximate method to solve the Schrödinger equation for the determination of the ground state wavefunction and energy of a quantum many-body system. The first approximation is making  $\psi$  as a combination of normalized, independent and orthonormal molecular orbitals  $\phi_i$  by forming the Hartree product. To build a wavefunction for fermions, the n-body wavefunction can be approximated by a single Slater determinant of n spin orbitals. For a closed shell wavefunction with n electrons for example, n/2 molecular orbitals in pairs of opposite spin can be built.

$$\psi(\mathbf{r}) = \frac{1}{\sqrt{n!}} \begin{vmatrix} \phi_1(\mathbf{r}_1)\alpha(1) & \phi_1(\mathbf{r}_1)\beta(1) & \phi_2(\mathbf{r}_1)\alpha(1) & \phi_2(\mathbf{r}_1)\beta(1) & \Lambda & \phi_{n/2}(\mathbf{r}_1)\alpha(1) & \phi_{n/2}(\mathbf{r}_1)\beta(1) \\ \phi_1(\mathbf{r}_2)\alpha(2) & \phi_1(\mathbf{r}_2)\beta(2) & \phi_2(\mathbf{r}_2)\alpha(2) & \phi_2(\mathbf{r}_2)\beta(2) & \Lambda & \phi_{n/2}(\mathbf{r}_2)\alpha(2) & \phi_{n/2}(\mathbf{r}_2)\beta(2) \\ \text{M} & & & & & & \text{M} \\ \phi_1(\mathbf{r}_i)\alpha(i) & \phi_1(\mathbf{r}_i)\beta(i) & \phi_2(\mathbf{r}_i)\alpha(i) & \phi_2(\mathbf{r}_i)\beta(i) & \Lambda & \phi_{n/2}(\mathbf{r}_i)\alpha(i) & \phi_{n/2}(\mathbf{r}_i)\beta(i) \\ \phi_1(\mathbf{r}_j)\alpha(j) & \phi_1(\mathbf{r}_j)\beta(j) & \phi_2(\mathbf{r}_j)\alpha(j) & \phi_2(\mathbf{r}_j)\beta(j) & \Lambda & \phi_{n/2}(\mathbf{r}_j)\alpha(j) & \phi_{n/2}(\mathbf{r}_j)\beta(j) \\ \text{M} & & & & & & \text{M} \\ \phi_1(\mathbf{r}_n)\alpha(n) & \phi_1(\mathbf{r}_n)\beta(n) & \phi_2(\mathbf{r}_n)\alpha(n) & \phi_2(\mathbf{r}_n)\beta(n) & \Lambda & \phi_{n/2}(\mathbf{r}_n)\alpha(n) & \phi_{n/2}(\mathbf{r}_n)\beta(n) \end{vmatrix}$$

The notation  $\alpha(i)$  and  $\beta(i)$  are abstract spin functions that  $\alpha$  for a spin up electron equals to 1 and  $\beta$  equals to 0, while for a spin down electron the former is 0 and the latter is 1. This notation realizes the antisymmetric requirement of the expression of the electronic wavefunction.

The second approximation is expressing individual molecular orbital as a linear combination of pre-defined basis functions. For example, Slater-type orbitals (STO) are expressed with an exponential factor  $\exp(-\zeta r)$ . To express the radial part of the STO, the *ab initio* electronic structure program Gaussian employed in this dissertation project uses primitive Gaussian-type atomic functions<sup>88</sup>  $g_p$  (GTO) to form the actual basis functions (contracted Gaussian  $\chi_\mu$ ) by linear combination. The Gaussian functions are written as:

$$g(\alpha, \mathbf{r}) = c x^n y^m z^l e^{-\alpha r^2}$$

where  $\alpha$  is a constant determining the radial size of the function and  $c$  is a coefficient.

The individual molecular orbital then can be expressed using simple linear combination of atomic orbitals (LCAO) where the atomic orbital is expressed in terms of the contracted Gaussian  $\chi_\mu$ <sup>89</sup>

$$\phi_i = \sum_{\mu=1}^N c_{\mu i} \chi_\mu = \sum_{\mu=1}^N c_{\mu i} \sum_p d_{\mu p} g_p$$

where  $c_{\mu i}$  is a molecular orbital expansion coefficient and  $d_{\mu p}$ 's are fixed constants (contraction coefficients) within a given basis set.  $d_{\mu p}$  and  $\alpha$  are given as the input parameters for pre-defined basis sets.<sup>90</sup>

Derivation of N-coupled normalized antisymmetric function can yield Hartree–Fock wavefunctions and energy of the system. For example, by integrating the Schrödinger equation, the energy in principle can be calculated:

$$E = \frac{\int \psi^* \hat{H} \psi d\tau}{\int |\psi|^2 d\tau}$$

The variational principle is the basis for the variational determination of a wavefunction. It says that for a given operator the eigenvalue of an eigenfunction is at a minimum value with respect to small adjustments that might be made to the function. As a consequence, the problem of finding a wavefunction becomes a numerical analysis of finding the set of coefficients  $c_{\mu}$  that minimize the energy of the resultant wavefunction.

The third approximation is to the electron-electron repulsion which treats the electron repulsion in the way that each electron moves in an average field due to nuclei and remaining electrons, which is the so called self-consistent fields (SCF) method, and forms the Hartree-Fock SCF operator. The n-electron problem is thus allowed to be separable to n one-electron problems, which leads to an effective one-electron Hamiltonian operator  $\hat{F}$  :

$$\hat{F} = \hat{h} + \hat{g}$$

The first term  $\hat{h}$  is the operator corresponding to an electron's kinetic energy and its attraction for the nuclei, namely for one electron integrals.  $\hat{g}$  is the associated with the effective field of all the electrons, namely for two electron integrals. The Roothaan-Hall equation<sup>91</sup>  $\hat{F}C_{\mu} = E_{\mu}^{\text{H}} SC_{\mu}$  can then be iteratively solved by solving usual eigenvalue problem for the energy, the wavefunction, and the associated  $C_{\mu}$ 's simultaneously for the N molecular orbital's. The convergence criteria are met when the energy is a minimum and the orbital's generate a field that produces the same orbitals. In this equation, the molecular expansion coefficient is collected into a column vector denoted as  $C$ , and  $S$  is a matrix of overlap integrals.

Gaussian orbitals are widely used in molecular structure calculations, but the shape of a GTO fail to exhibit radial nodal behavior present in atomic orbitals. The modified basis

can reproduce this behavior by manipulating the sign of contraction coefficients. A minimal basis set is featured by one basis function per atomic orbital. But this is usually insufficient and one usually uses more functions to represent the valence atom orbitals such as the following: split-valence multiple  $\zeta$  basis set – one basis set comprises  $\zeta$  times the number of functions in a minimal set; polarized function – one atomic orbital with angular momentum quantum number higher than what is required for the description of each ground state atom, which changes the orbital shape; and diffuse functions – large size versions of functions. For example, in 6-31++G(d,p) basis set, each core atomic orbital has six GTO, and each valence orbital composes of two sets of GTO – one contracted from three primitives and the other from one. The diffuse functions are added to both the heavy and H atoms, while the d functions are added to heavy atoms and p functions are added to hydrogen atoms.

#### 4.2.4 Density Functional Theory

Density functional theory (DFT) has a computational cost similar to HF theory, with possibly more accuracy. DFT is different from a wavefunctional based *ab initio* method in that it is based on the electronic density  $\rho$  which depends only on three spatial coordinates, independent of the number of electrons.

$$\rho(r) = \sum_{\mu} |\chi_{\mu}(r)|^2$$

The Hohenberg-Kohn theorem<sup>92</sup> says that the ground-state electronic energy is determined only by  $\rho$ , and there is the existence of a unique functional connecting these two quantities. This theory lays the basis of DFT to possibly connect the electron density with the energy by designing certain functionals.

The energy of the system can be expressed by three parts analogous to the wavefunction approach as a function of  $\rho$ :

$$E[\rho(r)] = T[\rho] + E_{ne}[\rho] + E_{ee}[\rho]$$

where the terms on the right hand side of the equation stand sequentially for the kinetic energy, nuclei-electron attraction energy, and the electron-electron repulsion energy.

$$E_{ne}[\rho] = \sum_{i=1}^N \int \frac{Z_i \rho(r)}{|R_i - r|} dr$$

where  $R$  and  $r$  are the positions of nuclei and electrons respectively.

The  $E_{ee}[\rho]$  term can be divided into Coulomb repulsion and exchange-correlated parts,  $J[\rho]$  and  $E[\rho]$ .

$$J[\rho] = \frac{1}{2} \iint \frac{\rho(r)\rho(r')}{|r - r'|} dr dr'$$

The exchange-correlation energy  $E_{xc}[\rho]$  corresponds to same-spin and mixed-spin interactions and is usually divided into separate parts as exchange  $E_x[\rho]$  and correlation  $E_c[\rho]$ .  $E_{xc}[\rho]$  is dominated by the exchange energy over correlation energy and it can be expressed as the kinetic correlation energy plus the exchange and potential correlation energy:

$$E_{xc}[\rho] = (T[\rho] - T_s[\rho]) + (E_{ee}[\rho] - J[\rho])$$

Where  $T_s[\rho]$  is the exact kinetic energy calculated from the Slater determinant.

$$T_s = \sum_{i=1}^N \left\langle \phi_i \left| -\frac{1}{2} \nabla^2 \right| \phi_i \right\rangle$$

The major problem in DFT is deriving exact functionals for the exchange and correlation part. There are two types of functionals: a) local density approximations (LDA): the local density is treated as a uniform electron gas; and b) generalized gradient approximation (GGA):<sup>93</sup> the non-uniformity of electron gas is taken into account by including both the electron density as well as its gradient to determine  $E_{xc}$ . For open-shell systems, one uses the local spin density approximation (LSDA) which is given as the sum of individual  $\alpha$  and  $\beta$  densities raised to the 4/3 power. Some of the most popular GGA

functionals are those derived by Lee, Yang, and Parr (LYP)<sup>94</sup> and Perdew (P86).<sup>95,96</sup> The LYP has the form:

$$E_c^{LYP} = -a \frac{\gamma}{(1+d\rho^{-1/3})} - ab \frac{\gamma e^{-c\rho^{-1/3}}}{9(1+d\rho^{-1/3})\rho^{8/3}}$$

$$\times \left[ 18(2^{2/3})C_F(\rho_\epsilon^{8/3} + \rho_\beta^{8/3}) - 18\rho t_W + \rho_\epsilon (2t_W^\alpha + \nabla^2 \rho_\alpha) + \rho_\beta (2t_W^\delta + \nabla^2 \rho_\beta) \right]$$

$$\gamma = 2 \left[ 1 - \frac{\rho_\alpha^2 + \rho_\beta^2}{\rho^2} \right]$$

$$t_W^o = \frac{1}{8} \left( \frac{|\nabla \rho_o|^2}{\rho_o} - \nabla^2 \rho_o \right)$$

Where the  $a$ ,  $b$ ,  $c$  and  $d$  are parameters determined by fitting to data for the helium atom. The  $t_W$  functional is known as the local Weizsacker kinetic energy density.<sup>97</sup>

One of the most popular exchange functionals is Becke's three parameter functional (B3) which includes balanced contributions from the exact exchange functional and the GGA exchange functional.<sup>98</sup> It has the form:

$$E_{xc} = c_0 E_{xc}^{Slater} + (1 - c_0) E_x^{HF} + c_x \Delta E_x^{B88} + E_c(VWN) + c_c \Delta E_c^{non-local}$$

where the non-local correlation is provided by the LYP expression. In the original paper, he used LDA densities and the Perdew/Wang 1991 correlation functional rather than Vosko-Wilk-Nusair (VWN) functional<sup>99</sup> and LYP. VWN is used to provide the excess local correlation.

Recent functionals are formulated including a mixture of Hartree-Fock and DFT exchange along with DFT correlation, namely hybrid functionals such as the B3LYP exchange coupling functional. Adjusting the values of  $c_0$ ,  $c_x$ , and  $c_c$  work well can build hybrid exchange term with different functionals, for example, substituting the Perdew-Wang 1991 GGA correlation functional for LYP.<sup>100</sup>

### 4.3 *Ab initio* Applications in Vibrational Spectroscopy

HF-SCF and DFT can solve the Schrödinger equation to give the ground state energy that is the minimum on its potential energy surface (PES) survey. Energy gradients can be used to optimize the geometry including transition states. The first derivative of energy gives the minima on the PES where the gradients are zero. A global minimum corresponds to the equilibrium structure of the molecular systems. A saddle point corresponds to the transition state structure. The vibrational force constants are the second derivative of potential energies, which can be used to calculate the vibrational spectra, which is to be introduced in detail below. The recommended book on molecular spectroscopy is reference [101].

#### 4.3.1 Harmonic Oscillator

In a three dimensional system, the translational motion, vibration motion and rotation motion are separable according to classical quantum mechanics. So there are  $3N$  degrees of freedom for a system with  $N$  particles. With  $N > 2$ , there are three translational degrees of freedom for the system as a whole. Also, there are two rotational degrees of freedom two-point particle systems, and three independent rotations for nonlinear systems. The number of degrees of freedom remaining for vibrational motion or normal modes is thus  $3N-5$  for linear system and  $3N-6$  for nonlinear system.

The one dimensional normal modes in Cartesian coordinates is based on the quantum mechanical harmonic oscillator:

$$\hat{H} = -\frac{\hbar^2}{2m} \frac{d^2}{dx^2} + \frac{1}{2}kx^2$$

The Schrödinger equation for the harmonic oscillator is expressed with distinct wavefunctions with subscript  $n$  (quantum number):

$$\hat{H}\psi_n(x) = E_n\psi_n(x)$$

It can be solved to get the wavefunctions which are the eigenfunctions of the equation:

$$\psi_n(x) = \psi_n\left(\frac{z}{\beta}\right) = \frac{N}{\sqrt{2^n n!}} h_n(z) e^{-z^2/2}$$

where

$$\beta^2 = \sqrt{km} / \eta$$

$$\text{and } N = \left(\frac{\beta^2}{\pi}\right)^{1/4}$$

The Hermite polynomials is a polynomial:  $h_n(z) = (-1)^n e^{z^2} \frac{d^n}{dz^n} e^{-z^2}$  and correspondingly

the energy is:  $E_n = (n + \frac{1}{2})\eta\omega$ . When  $n = 0$ , the energy is at the lowest state and called the zero-point vibrational energy.

With the right amount of energy from light, which is the difference between different vibrational energy levels,  $E_{n_2} - E_{n_1} = (n_2 - n_1)\eta\omega$ , the light can be absorbed by the molecule and at a certain frequency (wavenumber) which is a characteristic quantum of the oscillator.

There are many corrections to a harmonic oscillator when the molecule response to light in a range of continuum wavelength, for example: rotational energies related to angular momentum change, centrifugal distortion, vibrational and rotational coupling, and vibrational anharmonicity. To include the first three terms, the complete energy level expression is:

$$E_n = (n + \frac{1}{2})\eta\omega + \frac{\eta^2 J(J+1)}{2\mu r_e^2} - \frac{\eta^4 J^2(J+1)^2}{2k\mu^2 r_e^6} + \frac{3\eta^2}{\omega\mu^2 r_e^4} (n + \frac{1}{2})J(J+1)$$

where  $J$  is the rotational quantum number and  $\mu$  is the reduced mass. Thus a more general selection rule for interaction between molecule Hamiltonian  $H'$  and electromagnetic radiation can be written as:

$$\langle \psi_{nJM} | H' | \psi_{n'J'M'} \rangle \neq 0$$

In low-resolution infrared spectroscopy often encountered, the rotational fine structure is usually lost and the frequency in a spectrum assigned as a fundamental transition is just a single peak. To this extent of application, only pure vibration needs to be considered for qualitatively analyzing the data.

#### 4.3.2 Vibrational Calculation

Molecular vibrations in real molecular system are anharmonic. For a multi-atom system, the complicated vibrational motions can be represented as a superposition of different normal mode motions that are separable.

The Hamiltonian has the general form:

$$H = \sum_i \left( \frac{1}{2} \alpha_i q_i^2 + \frac{p_i^2}{2\beta_i} \right)$$

where  $q_i$  represent the mass weighted displacement coordinates,  $p_i$  is the momentum elements of the particles in the oscillator.  $\alpha_i$  and  $\beta_i$  diagonal elements in force matrix  $K_{ij}$  and mass matrix  $M_{ij}$  after linear coordinates transformation, respectively. From classical mechanics, the vibrational frequency can be expressed:

$$\omega_i = \sqrt{\frac{\alpha_i}{\beta_i}}$$

The force matrix elements are force constants, which are evaluated as the second derivatives (Hessian) of the potential energy at equilibrium position.

$$K_{ij} = \left. \frac{\partial^2 V}{\partial q_i \partial q_j} \right|_{eq}$$

The potential energy of a molecule at a chosen set of internal coordinates is the force field, which is zero at an optimized structure. Thus the gradient of energy should be zero for a molecule at equilibrium and the Hessian can be used to determine the nature of a stationary point.

### 4.3.3 Vibrational Anharmonicity

The anharmonicity effects are realistic that in vibrational potentials of molecules are not strictly harmonic. Scaling factors usually have to be used to account for the anharmonicity, which correct the frequency difference between anharmonic and harmonic oscillators. However, the calculation can be improved by using correct qualitative form.

For a diatomic particle, a different potential can be chosen such as the Morse potential. For a polyatomic molecule, different approaches are developed mainly including the following:<sup>101</sup> a) variational (brute-force); b) vibrational second-order perturbation theory (VPT2): anharmonicity is included as a perturbation in the Hamiltonian in which the force constants are cubic and quartic; c) vibrational self – consistent field (VSCF): the vibrational Hamiltonian is built in mass - weighted normal coordinates; d) local modes: from overtone with Morse local mode including coupling as the perturbation.

In the harmonic approximation for the vibrations in the C-H stretch region, hafnium tert-butoxide (HTB) for example, has 36 normal modes which are infrared (IR) active. In the calculated spectrum, the modes show up as two distinct peaks in the C-H stretch region. However, the experimental spectrum contains about four identified smaller peaks which come mostly from anharmonicity. There are two types of anharmonicity which can give rise to these features in the IR spectrum. The first is the called mechanical anharmonicity, which reflects anharmonic dynamics of the vibrational normal modes (and comes from the anharmonicity of the interatomic forces). Two normal modes, for example, can combine together and the result is a quasi mode (with the frequency equal to the sum of the frequencies of the original modes) which can be IR active; the so called "combination" peak. Similarly, two modes can create a "difference" peak, if the resultant quasi mode has the frequency equal to the difference of the original frequencies. The second type of anharmonicity – electrical – has its origin in the nonlinear expansion of the dipole moment in

the normal modes coordinates (light couples to two or more normal modes directly). We showed that only electrical anharmonicity can explain the observed IR spectrum of HTB. Mechanical anharmonicity through the phenomenon known as the Fermi resonance contributes negligibly especially at large frequencies. Electrical anharmonicity, on the other hand, results in appreciable IR activity throughout the whole spectrum; this is observed experimentally.

Density functional theory only calculates harmonic vibrations and a scaling factor can be applied to improve the predictive power. Dipole derivatives of the modes were to determine the infrared intensities.

#### **4.4 Computational Methods**

Electronic structure calculations were performed to help interpret the experimental observations. The calculations were performed with the Gaussian 03 software package.<sup>102</sup> Energetics of possible gas phase and surface reactions of TDMAH, TEMAH, and HTB on a model cluster of hydrogen terminated Si(100) surface were calculated. The 2×1 reconstructed H-Si(100) surface was represented by a Si<sub>9</sub>H<sub>14</sub> cluster.<sup>75</sup> The boundary Si atoms were terminated with H atoms along the cleaved Si-Si directions to avoid unrealistic charge transfer. In previous work, this structure has been shown to provide a good representation for the monohydrogen terminated Si(100) surface<sup>75,103</sup> For comparison, the OH terminated Si(100) surface was modeled by substituting one H atom with one OH group.<sup>59</sup> Although cluster size was studied to have an influence on virtual energies,<sup>104</sup> the energy barriers are actually similar tested by different size clusters, and the neighboring dimers may influence the available reaction sites in real experiment but should not influence the expected chemistry in simulation, so as our previous representation model<sup>105</sup> and also in many related reports.<sup>106</sup> All reactants and products were fully optimized. The calculations were performed at the DFT

level with the B3LYP exchange-correlation functional.<sup>107,108</sup> Transition states were optimized using the STQN method.<sup>109, 110, 111</sup> The DFT geometry optimizations and frequency calculations were carried out with the 6-31+G(d,p) basis set for the non-metal atoms and the LanL2DZ relativistic effective core potential (RECP) based basis set<sup>112</sup> for the Hf atom; this combination of basis sets will be collectively denoted as BS1. Single point DFT energies were also calculated with the aug-cc-pVDZ basis set<sup>113</sup> for the non-metal atoms and the RECP based aug-cc-pVDZ-PP basis set<sup>114</sup> for Hf, denoted as BS2. All energies were corrected with the zero point energies (ZPE).

## Chapter 5 TDMAH Adsorption and Reaction on H-Si(100) Surface

### 5.1 Introduction

The adsorption and reaction of tetrakis(dimethylamido) hafnium (TDMAH) on hydrogen terminated Si(100) were studied by using *in situ* attenuated total reflectance Fourier transform infrared spectroscopy (ATR-FTIR), transmission IR and quadruple mass spectrometry (Q-MS). Surface and gas phase reactions were investigated at temperatures between 25 °C and 300 °C. Density functional theory (DFT) calculations on small models were performed for proposed gas phase reactions of intramolecular insertion and  $\beta$ -hydride elimination as well as the adsorption and reaction of TDMAH and its gas phase reaction products onto a hydrogen terminated Si(100) surface. The interface is predicted to involve Hf-Si, Hf-N-Si or HfNC-Si bonds. TDMAH decomposition products, such as N-methylmethyleimine (MMI) can form a C-Si or N-Si bond with the silicon surface. N-Si and CH<sub>2</sub>-Si bonds due to reactions on the Si windows were observed in transmission IR and N-Ge and CH<sub>2</sub>-Ge bonds on Ge internal reflectance element (IRE) were observed by ATR-FTIR at 100 °C. Also observed were the formation of Hf-H bonds and three-member cyclo species on the surface; the former was confirmed by a control D<sub>2</sub>O exchange reaction experiment. Both transmission IR and Q-MS indicated the presence of decomposition products dimethylamine and MMI. The combined experimental and theoretical results suggest that insertion and  $\beta$ -hydride elimination reactions can occur during bidentate chemisorption on the H-Si(100) surface by forming N-Si bonds.

### 5.2 Experimental and Computational Methods

### 5.2.1 Experimental Methods

The IR experimental setup is shown in Figure 5-1. The base absolute pressure was  $10^{-3}$  Torr. TDMAH (99.99% purity from Strem Chemical Inc.) with a melting point of  $\sim 23$  °C was transferred to a transparent quartz bubbler under  $N_2$  and remained a light yellow liquid during experiments. It was heated for about an hour at 65 °C in a Precision 810 digital oil bath to reach vapor-liquid equilibrium. Deionized  $D_2O$  or  $H_2O$  was kept in a 150  $cm^3$  stainless steel vessel half-filled at room temperature. No carrier gas was used for the precursors.

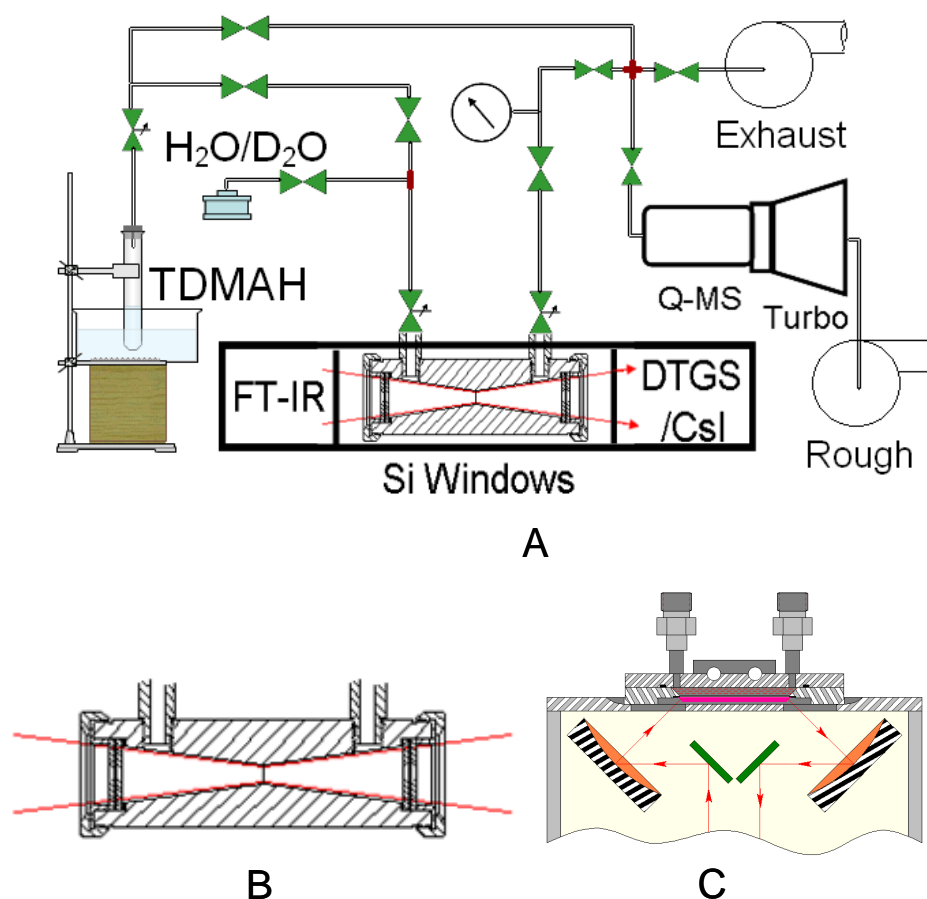


**Figure 5-1.** (A) FTIR schematic. (B) Transmission gas cell cross-section. (C) Attenuated total reflectance compartment. (B) and (C) are interchangeable in the middle component space of FTIR. (B) and (C) are permitted to reprint from HarrickScientific.

In the substrate temperature range of 25-250 °C, the experimental pressure was about 0.7 Torr during the TDMAH cycle and 3.6 Torr for the  $D_2O/H_2O$  cycle. Longer preheating of

the bubbler resulted in higher maximum pressure upon opening, but did not affect the steady state pressure obtained after 1 minute as shown in Figure 5-2.

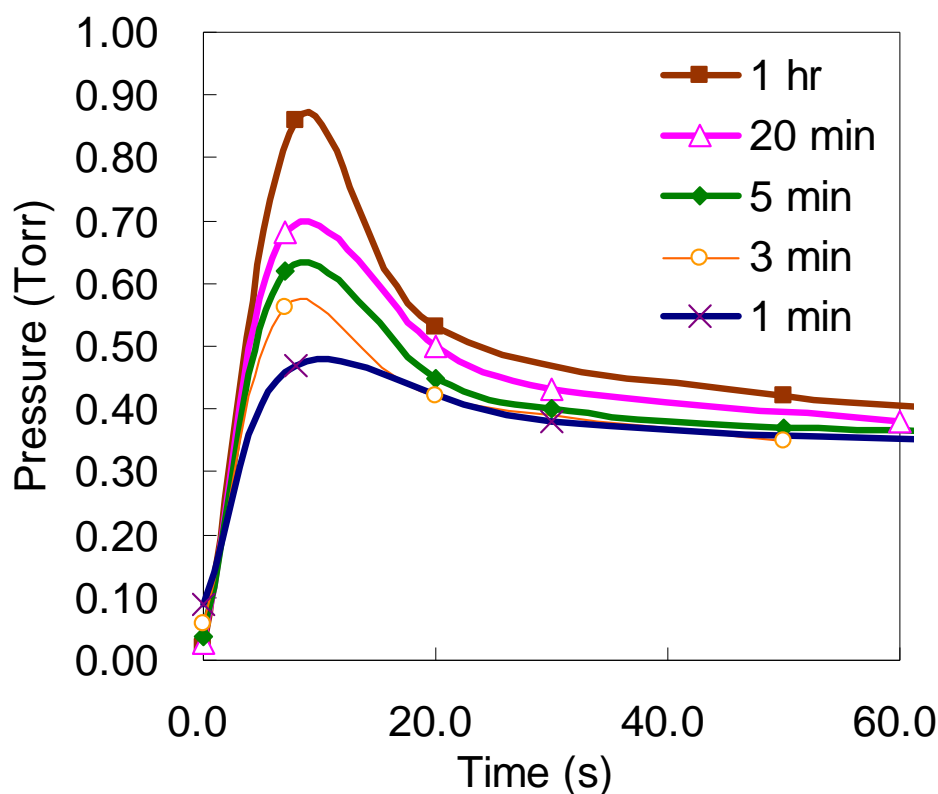


**Figure 5-2.** Pressure change as a function of bubbler equilibrium time at a bubbler temperature of 65 °C. The pressure behaved similarly for the same bubbler temperature and different gas cell temperatures below 150 °C.

A Thermo Nicolet 4700 FT-IR spectrometer with a deuterated triglycine sulphate (DTGS) detector was used with either one of two exchangeable components from Harrick Scientific Inc. designed to fit inside the sample compartment and modified with vacuum compatible fittings (Fig 1 B and C). Spectra using this arrangement have a better signal-to-noise than those taken using IR light diverted out of the spectrometer, through windows on a reactor and back to the detector, likely because the minimal path length results in a larger light intensity at the detector. Transmission infrared spectroscopy of the gas phase was performed in a 17 mL cone cross-section temperature controlled stainless steel gas cell with two 25×2 mm Si windows. The Horizon™ multiple reflection ATR flow-through cell

was used to observe adsorption and reactions on a HF lath trapezoidal cut  $50 \times 10 \times 2$  mm internal reflectance element (IRE) with  $45^\circ$  beveled ends and a  $280 \text{ mm}^2$  surface area on the vacuum side. Before introducing the precursor, the inlet lines were heated to  $100^\circ \text{C}$  for 12 hours to remove residual moisture. Intrinsic Si, Ge and ZnSe IRE crystals were used in the ATR experiments. The spectral collection window was in the middle IR range from  $4000 \text{ cm}^{-1}$  down to  $1150 \text{ cm}^{-1}$  for Si and down to  $700 \text{ cm}^{-1}$  for Ge and ZnSe. Si and ZnSe have limited transparency at low wavenumbers around and above  $300^\circ \text{C}$  while Ge is only useful below  $150^\circ \text{C}$  because of increasingly accessible phonon modes at high temperatures. There were 12 reflections of the IR beam on the adsorption side. ZnSe was simply wiped clean with lens paper, while the Si surface was sequentially treated with acetone, a 1:1:5  $\text{NH}_4\text{OH}:\text{H}_2\text{O}_2:\text{H}_2\text{O}$  solution at  $80^\circ \text{C}$ , a 1:1:100  $\text{HF}:\text{NH}_4\text{F}:\text{H}_2\text{O}$  buffered oxide etch (BOE) solution with a  $\text{pH} \approx 9$  for 3 min., a deionized water rinse, and  $\text{N}_2$  blow drying. Ideally this results in an atomically rough  $3 \times 1$  or  $2 \times 1$  hydrogen terminated Si(100) surface,<sup>115,116</sup> or monohydrogen terminated Si(111) surface, with a mono hydrogen Si-H vibration frequency at about  $2084 \text{ cm}^{-1}$ .<sup>117</sup> The Ge IRE was treated only with the BOE solution and a DI water rinse to remove any native oxide. Spectra of the treated surfaces reprocessed (ratioed) with a background spectrum of thermally oxidized Si(100) surface at  $700^\circ \text{C}$  in air, showed that Si-H peaks were stable in the experimental time range in air. No residual fluorine from the BOE treatment was observed in x-ray photoelectron spectroscopy (XPS) measurements, but a small amount of oxygen ( $532.7 \text{ eV}$ ) probably from surface hydroxyl groups was detected. The  $\nu_{\text{O-H}}$  peak at  $3735 \text{ cm}^{-1}$  from ambient moisture or surface Si-OH groups was observed in the single beam FTIR spectra, consistent with the presence of O in the form of surface hydroxyl group. The surface morphology of the Si(100) crystal was measured by atomic force microscopy (AFM) using an ultrasharp silicon cantilever NSC14/AIBS (Mikro Masch, Narva) with a force constant of  $\sim 5.7 \text{ N/m}$  and a resonant frequency of about  $\sim 160 \text{ kHz}$  on a

Digital Instruments (Dimension 3100 Scans Probe Microscope with NanoScope VI controller). It showed root mean square (RMS) roughnesses of about 5.0 nm at the 200 nm scale and 4.0 nm at the 1  $\mu\text{m}$  scale, suggestive of defects and kinks over the large adsorption area of these IRE crystals.<sup>2</sup>

Two sets of experiments were performed using ATR-FTIR: (1) TDMAH liquid drop and (2) adsorption followed by desorption. For experiment (1) a liquid drop of TDMAH was applied at room temperature on both the Si and Ge ATR crystals under  $\text{N}_2$ . After placement in the FTIR instrument, the crystal was heated at a rate of 100  $^\circ\text{C}/\text{min}$ . to a preset temperature between 60-250  $^\circ\text{C}$ . All of the IR spectra were reprocessed using a background spectrum taken before the precursor introduction at each corresponding temperature. For the adsorption/desorption experiments, immediately upon TDMAH vapor dosing, multi-internal reflection IR spectra were collected in the range of 4000-400  $\text{cm}^{-1}$  with 32 scans at 4  $\text{cm}^{-1}$  resolution, which took approximately 37 seconds for each spectrum. After completing 15 spectra, the flow of the precursor was stopped and the adsorbed species were left in vacuum for 10 min. to desorb while IR spectra were continually recorded. The dosing amounts are given in Langmuirs ( $1\text{L} = 10^{-6}$  Torr-s).

For the transmission IR experiments, the gas cell temperature was set to a value between 100 and 300  $^\circ\text{C}$  by a heating band outside of the cell. The source TDMAH was kept at 65  $^\circ\text{C}$  except for the room temperature IR experiment. The Si windows were also treated by the procedures used for Si IRE crystals before each experiment. The total beam path length for the IR experiments was 10 cm, and the path length to volume ratio was maximized by the conical shaped interior design in order to maximize the signal. For each temperature, the gas cell was evacuated and a background spectrum was taken before introducing the precursor. Upon opening the precursor valve, IR spectra were collected similar to that of the ATR experiments in flow mode. After a desired dose the valves to the pump and the precursor

were closed for the closed system mode and pressure was recorded as a function of time.

An Inficon 200 Quadrex residual gas analyzer (RGA) was connected to the exit side of the flow-through cell for mass spectrometry analysis and the electron ionization energy was set to 102 eV. The flow rate was reduced by a 0.3 mm diameter orifice with an estimated flow rate of 0.5 sccm into the bypass line to reduce the sampling pressure. The pressure in the mass spectrometer was further reduced to  $10^{-10}$  Torr by a turbo pump backed by a mechanical pump. All molecular ions and other fragments up to 50 atomic mass units were monitored in real time for crystal temperatures from 60 °C to 250 °C.

### 5.2.2 Computational Methods

Electronic structure calculations were performed to help interpret the experimental observations. The density functional theory (DFT) calculations were performed with the Gaussian 03 software package.<sup>102</sup> The energetics of possible gas phase and surface reactions of TDMAH on a model cluster of hydrogen terminated Si(100) surface were calculated. The  $2\times 1$  reconstructed H-Si(100) surface was represented by a  $\text{Si}_9\text{H}_{14}$  cluster<sup>75</sup> as shown in Figure 5-3(a).

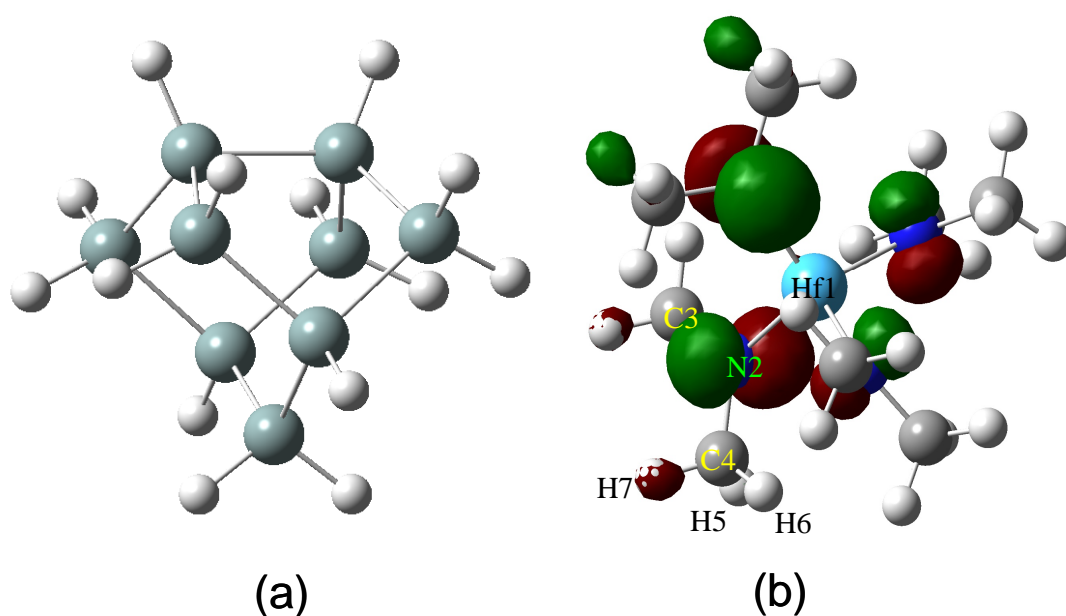


**Figure 5-3.** (A) Structure of model of THE surface.  $\text{H}_{14}\text{Si}_9$  cluster representing H-Si(100). (B) Structure and highest occupied molecular orbital (HOMO) of TDMAH.

The boundary Si atoms were terminated with H atoms along the cleaved Si-Si directions to avoid unrealistic charge transfer. In previous work, this structure has been shown to provide a good representation for the monohydrogen terminated Si(100) surface.<sup>75, 118</sup> For comparison, the OH terminated Si(100) surface was modeled by substituting one H atom with one OH group.<sup>59</sup> All reactants and products were fully optimized. The DFT calculations were performed with the B3LYP exchange-correlation functional.<sup>119,120</sup> Transition states were optimized using the STQN method.<sup>121,122,123</sup> The DFT geometry optimizations and frequency calculations were carried out with the 6-31+G(d,p) basis set for the non-metal atoms and the LanL2DZ large core relativistic effective core potential (RECP) and associated basis set<sup>124</sup> for the Hf atom; this combination of basis sets will be collectively denoted as BS1. Single point DFT energies were also calculated with the aug-cc-pVDZ basis set<sup>125</sup> for the non-metal atoms and the small core RECP plus associated aug-cc-pVDZ-PP basis set<sup>126</sup> for Hf, denoted as BS2. All energies were corrected with the zero point energies (ZPE).

### 5.3 Results and Discussion

The optimized structure for TDMAH shown in Figure 5-3(b) has the expected tetrahedral structure. The average bond lengths of Hf-N, N-C, and C-H are 2.06, 1.46, and 1.10Å, respectively. The highest occupied molecular orbitals are the lone pair electrons on N. Electron density from the lone pair delocalizes into the  $\sigma^*$  orbital of the C-H bond, which weakens the C-H bond and lowers its frequency.<sup>38,127,128,129</sup> The geometry at the N atoms in TDMAH is nearly planar trigonal, suggesting the possibility of  $\pi$ -bonding between vacant 5d orbitals on Hf and the lone pair “p” orbital on N perpendicular to the Hf-N-C-C plane. As discussed later, the Hf-N bond is quite strong, a further indication of the contribution to its bond strength from the additional  $\pi$  back-bonding.

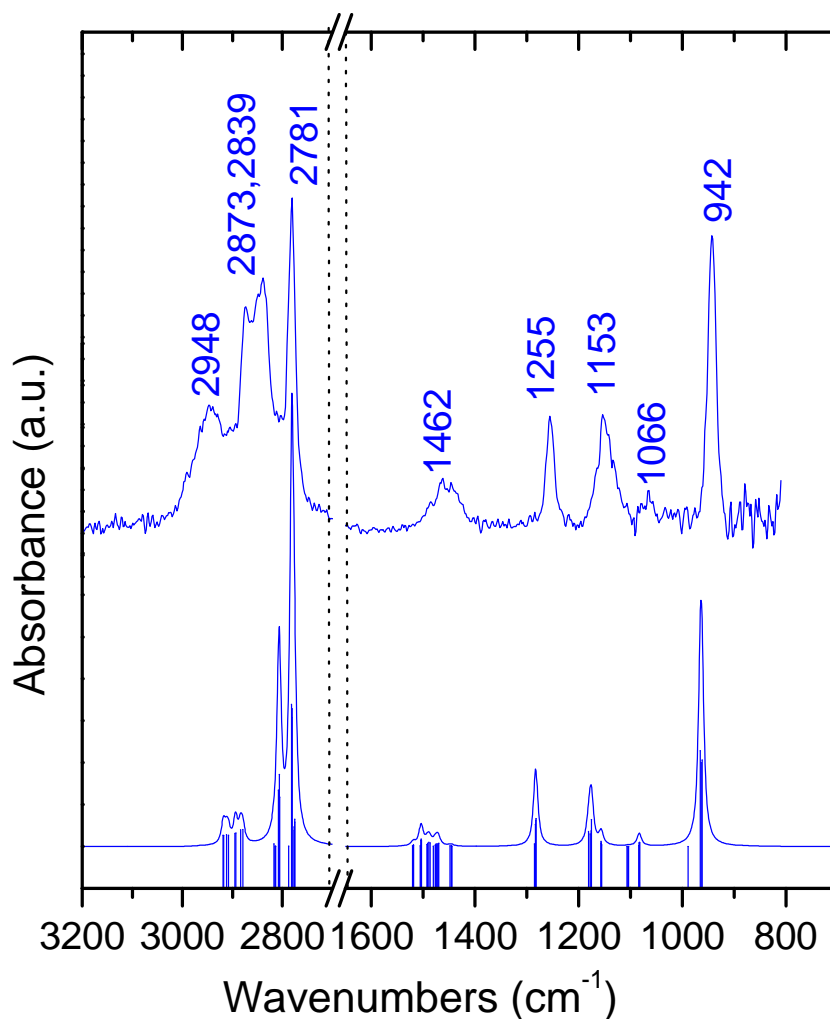


**Figure 5-4.** Top: infrared spectrum of TDAMH in gas phase in flow mode at room temperature. Bottom: Calculated IR spectrum at the DFT/BS1 level with scaling factor 0.9408 applied to the region of C-H stretches for TDAMH.

Figure 5-4 shows the IR spectrum of TDMAH in the gas phase at room temperature together with the calculated harmonic spectrum. Due to the effects of anharmonicity in the C-H stretches, a scaling factor of 0.9408 was applied for comparison to experiment. The scaling factor was calculated as the ratio of the frequency of the most intense C-H band in the liquid drop spectrum and its corresponding calculated frequency. The low frequency C-H peak at  $2781\text{ cm}^{-1}$  could be a Bohlmann-type band,<sup>130</sup> which corresponds to the C-H stretch anti-parallel to the lone pair on N. In the calculated spectrum of TDMAH, this corresponds to the C-H symmetric stretches parallel and anti-parallel to the N lone pair (for example, C4-H5 and C4-H6 in Figure 5-3 (b)). The peak at  $2873\text{ cm}^{-1}$ , which is  $\sim 90\text{ cm}^{-1}$  higher in frequency

than the above low frequency C-H band, corresponds to the asymmetric C-H stretches of the above C-H bonds. The peak at  $2948\text{ cm}^{-1}$  is due to the C-H stretches from the third C-H bond (for example, C4-H7 in Figure 5-3 (b)). Although low in intensity, these peaks exist in all experimental spectra. The unscaled calculated spectrum for frequencies  $<1600\text{ cm}^{-1}$  matches well with the experimental spectrum within  $\sim 20\text{ cm}^{-1}$ . The peak at  $942\text{ cm}^{-1}$  assigned to the Hf-N-C bend could be due to either TDMAH or a similar molecule with not less than two dimethylamido ligands on Hf. The peak assignments are summarized in Table 5-1.

**Table 5-1.** Band Positions (cm<sup>-1</sup>) and Assignments for the Experimental IR Spectra of TDMAH and DMA from the Unscaled Calculated B3LYP/BS1 Values

TDMAH (gas) Expt. at 25 °C <sup>a</sup>	TDMAH (gas) B3LYP/BS1	DMA (gas) Expt. at 25 °C <sup>a</sup>	DMA (gas) B3LYP/BS1	Assignments <sup>b</sup>
2948 (m)	3104, 3074	2966 (s)	3110, 3064	$\nu_{C-H}$
2873, 2893 (s)	2982			$\nu_{C-H}$ (as)
2781 (vs)	2953	2810 (s)	2939	$\nu_{C-H}$
1462 (m)	1505, 1492, 1470	1469 (m)	1516	$\delta_{CH_3}$
1255 (m)	1283			$\nu_{HF-N}$ , $\gamma_{N-C}$ , $\omega_{C-H}$
1153 (m)	1176	1160 (m)	1185, 1176	$\nu_{N-C}$ (as), $\omega/\rho_{C-H}$
	1156			$\gamma_{N-C}$ , $\delta_{HF-N}$ , $\rho_{C-H}$
1066 (w)	1085			$\omega$ , $\rho_{C-H}$ , $\nu_{N-C}$ (as)
		1025 (w)	1035	$\rho_{C-H}$ , $\delta_{N-H}$ (ip)
942 (vs)	963			$\nu_{HF-N}$ , $\nu_{N-C}$ (s)
		930 (w)	942	$\delta_{C-H}$ , $\delta_{N-H}$ (op)
		735 (s)	765	$\delta_{N-H}$ (op)
	527			$\nu_{HF-N}$ (s), $\gamma_{N-C}$

<sup>a</sup> vs – very strong, s – strong, m – medium, w – weak. <sup>b</sup> $\nu$  – stretching,  $\delta$  – bending,  $\gamma$  – scissoring,  $\omega$  – wagging,  $\rho$  – rocking, as – asymmetric, s – symmetric, ip – in plane, op – out of plane.

### 5.3.1 Bulk FTIR Thermal Analysis

A liquid drop of TDMAH was heated during measurement using ATR-FTIR to study its decomposition on Si as shown in Figure 5-5.

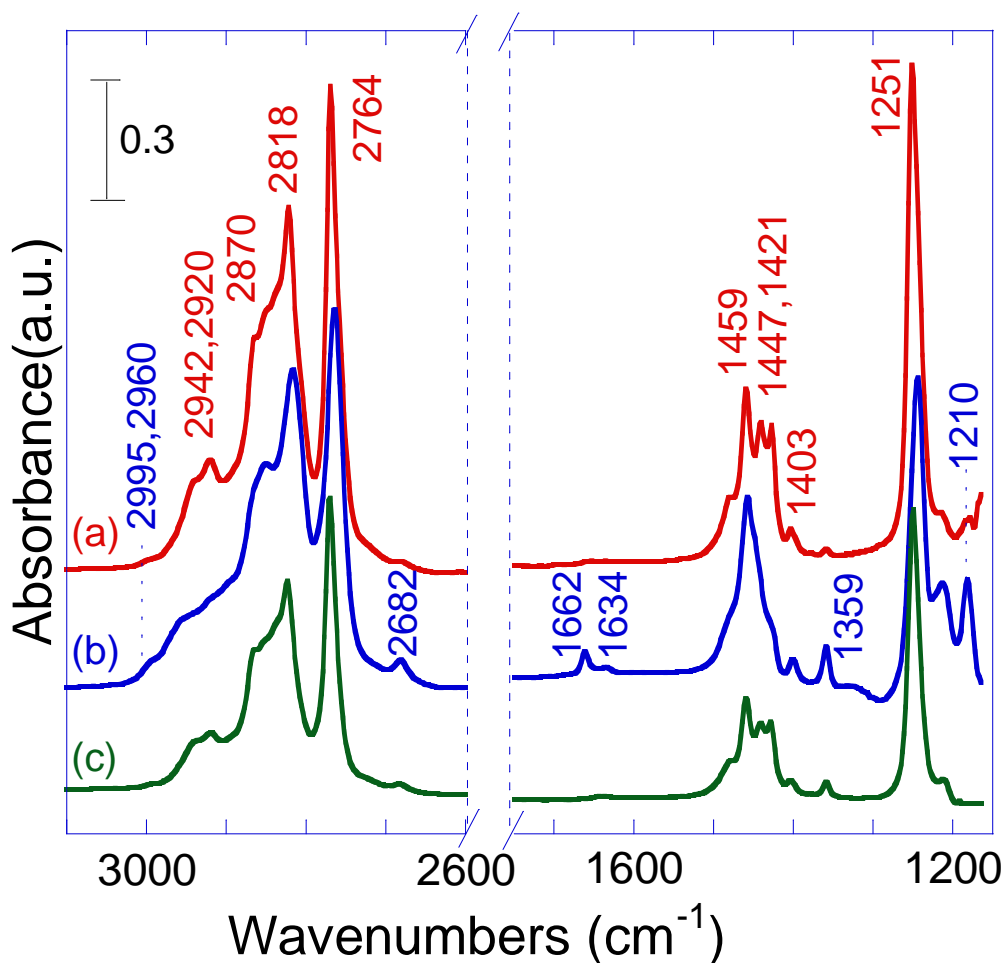


**Figure 5-5.** IR spectra for a liquid drop of TDMAH on Si and raised to (a) 30 °C, (b) 150 °C, (c) 150 °C under vacuum. The temperature ramping rate was 50 °C/min. Spectra were reprocessed with bare Si backgrounds at their corresponding temperature.

The vibrational modes such as the low frequency C-H band were red shifted by a few wavenumbers from the gas phase values (Figure 5-4). Upon heating to 150 °C, new peaks appear at 2995, 2960, 2682, 1662, 1634, 1359, and 1210  $\text{cm}^{-1}$ , consistent with the previous report that minor decomposition of TDMAH starts at around 90 °C<sup>68</sup> in a closed system and TDMAH partially decomposes at 150 °C in a flow mode.<sup>131</sup>

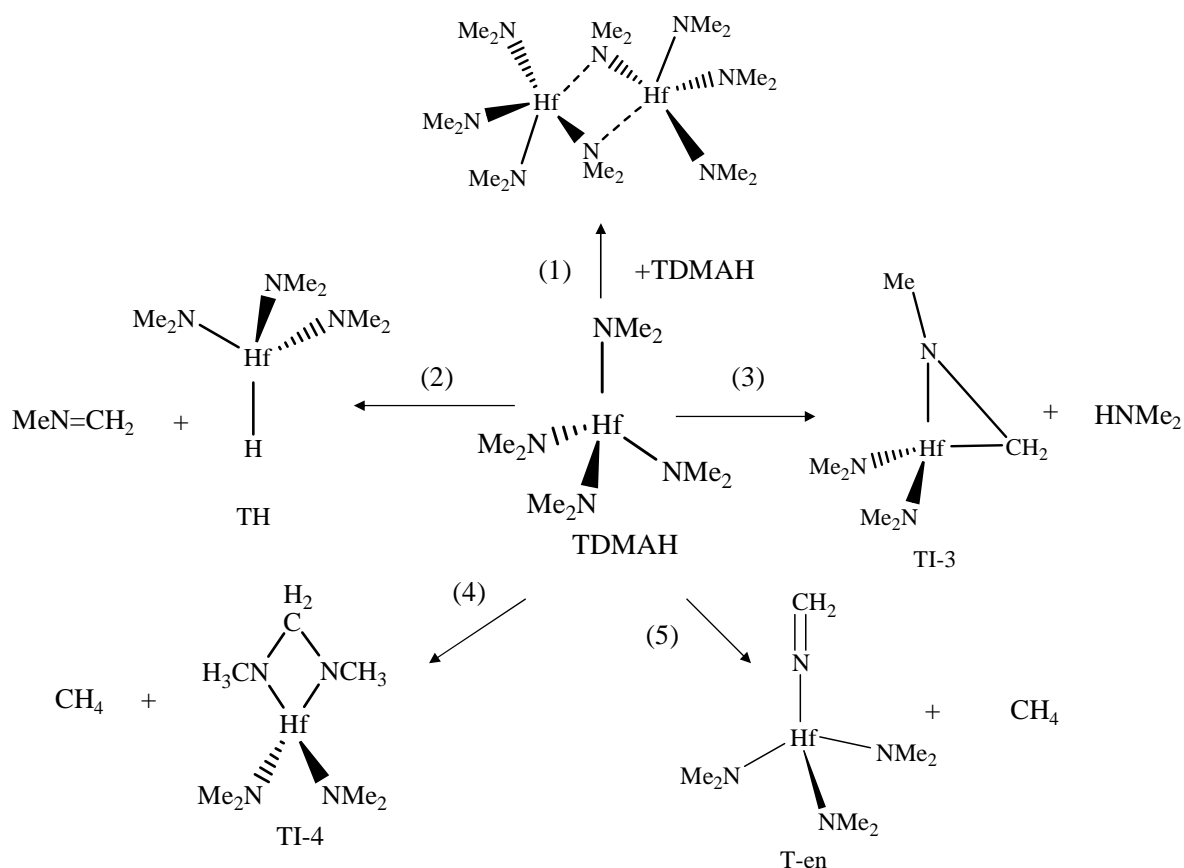


**Figure 5-6.** Gas phase TDMAH reactions 1 to 5: (1) dimerization; (2)  $\beta$ -hydride elimination reaction; (3) intramolecular insertion reaction leading to TI-3; (4) intramolecular insertion reaction leading to TI-4; and (5) 1,2- $\beta$ -hydride elimination reaction.

Although dimerization of TDMAH is detected in the condensed phase,<sup>71</sup> it is calculated to be an endothermic reaction by 13 kcal/mol in the gas phase as discussed below (reaction (1), Figure 5-6). The  $\nu_{\text{C-H}}$  on the bridged N in the TDMAH dimer may account for the peak at  $2682 \text{ cm}^{-1}$ . When TDMAH was heated to  $150 \text{ }^\circ\text{C}$  under vacuum, the peak at  $1662 \text{ cm}^{-1}$  as discussed above disappeared, which indicates that this peak is due to a volatile gas phase molecule and could be assigned to the  $\nu_{\text{C=N}}$  in MMI.<sup>132</sup> However, no apparent peak was observed at  $\sim 3012 \text{ cm}^{-1}$  as observed by other experiments,<sup>132</sup> so the amount of MMI may be small. The peak at  $1634 \text{ cm}^{-1}$  is assigned to the  $\nu_{\text{Hf-H}}$  mode, which will be discussed in detail later. The two assigned species, MMI and Hf-H, are likely products of  $\beta$ -hydride elimination (reaction (2), Figure 5-6). The peaks at  $2995 \text{ cm}^{-1}$  and  $2960 \text{ cm}^{-1}$  are likely to be due to  $\nu_{\text{C-H}}$  in DMA or MMI. A dative bond between adsorbed MMI and the Hf-H containing molecule may

cause red shifts for the  $\nu_{\text{C}=\text{N}}$  and  $\nu_{\text{Hf-H}}$ . The peak at  $1359\text{ cm}^{-1}$  differs from the  $\delta_{\text{H-C-H}}$  in methane by  $40\text{ cm}^{-1}$ , and cannot be due to  $\text{CH}_4$  because of the absence of a sharp  $\nu_{\text{C-H}}$  peak at  $3016\text{ cm}^{-1}$ .<sup>67</sup> The peak at  $1210\text{ cm}^{-1}$  may be due to the  $\nu_{(\text{Hf})\text{N-C}}$  in a three-member ring of  $[-\text{Hf-N-C-}]$  in TI-3 (reaction (3), Figure 5-6) in comparison to a previously assigned mode for the corresponding Ti compound at  $1235\text{ cm}^{-1}$ .<sup>66,133</sup> A slight red shift from Ti to Hf is expected as Hf is a heavier atom than Ti. On the other hand, the formation of this species and dimethylamine  $[(\text{CH}_3)_2\text{NH}$ , DMA] is not thermodynamically favorable for TDMAH as discussed in the later section. Instead, the two peaks at  $1359\text{ cm}^{-1}$  and  $1210\text{ cm}^{-1}$  are tentatively assigned to the  $\delta_{\text{H-C-H}}$  and  $\nu_{(\text{Hf})\text{N-C}}$  modes of a thermodynamically favorable species with a four-member ring  $[-\text{Hf-N-CH}_2\text{-N-}]$  (reaction (4), Figure 5-6) by comparing the experimental and calculated spectra.

### 5.3.2 Gas Phase FTIR Analysis

Gas phase spectra of TDMAH at temperatures between  $25\text{ }^\circ\text{C}$  and  $300\text{ }^\circ\text{C}$  were measured both in an open cell and a closed cell arrangement where the valves to and from the cell were either left open or closed respectively. The total integrated absorbance of the  $\nu_{\text{C-H}}$  bands from  $3030\text{-}2730\text{ cm}^{-1}$  for the spectra measured in a flow mode was linearly dependent on the pressure, so the infrared signal in this region is a good indicator for the gas phase information. The gas phase IR spectra in the closed gas cell as a function of time is shown in Figure 5- 7.

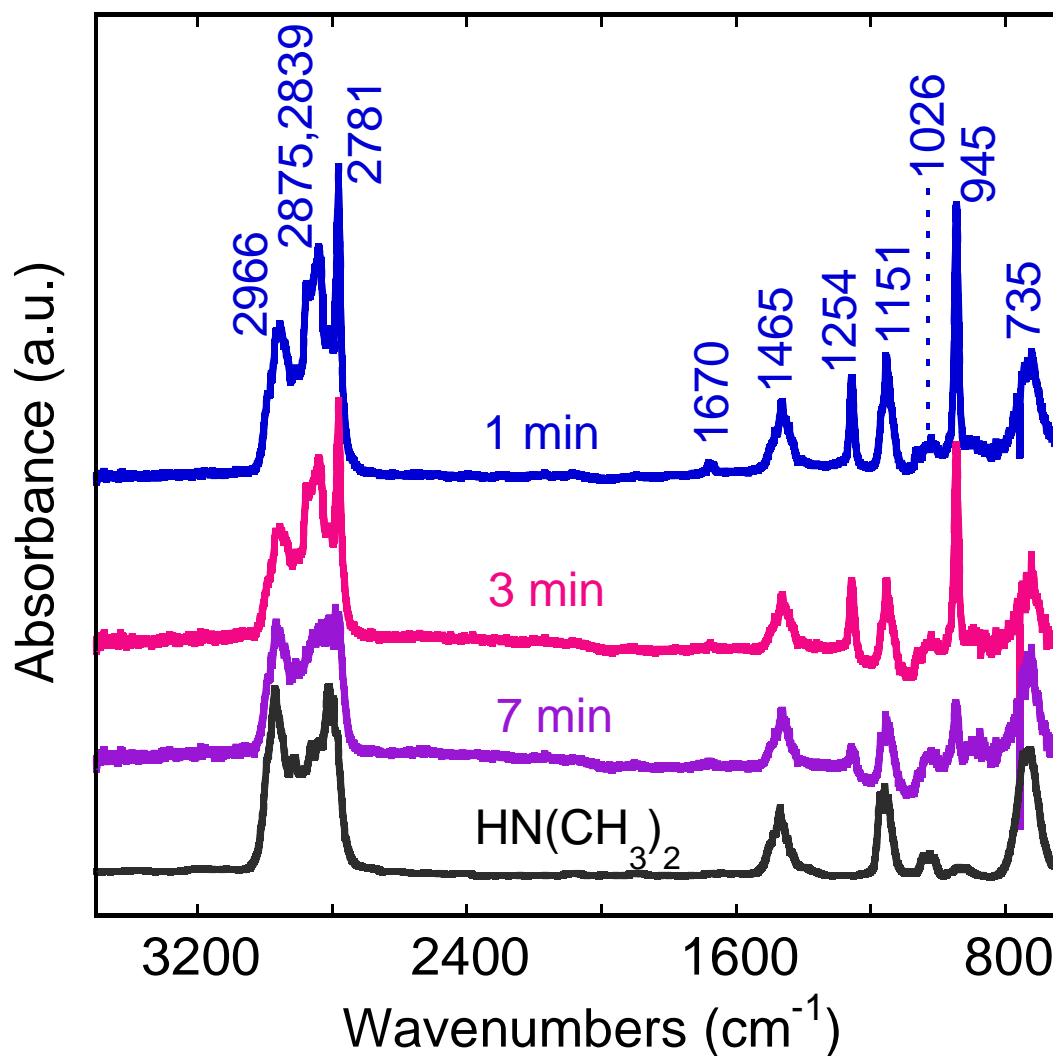


**Figure 5-7.** IR spectra at 100 °C of gas phase TDMAH in a closed gas cell with Si windows using a resolution of 2  $\text{cm}^{-1}$  as a function of time.

The temperature of the gas cell was  $100 \pm 5$  °C, slightly above the decomposition temperature of TDMAH. In comparison to the liquid drop, the  $\nu_{\text{C-H}}$  region of the liquid drop was broadened. Comparing with the gas phase spectrum for pure TDMAH at room temperature in Figure 5-4, the spectrum at  $t = 1$  min. shows several new peaks at 2966, 1670, and  $735 \text{ cm}^{-1}$ . The strong peaks at  $2966 \text{ cm}^{-1}$  and  $735 \text{ cm}^{-1}$  are characteristic peaks of the  $\nu_{\text{C-H}}$  (as) and  $\delta_{\text{N-H}_2}$  modes with respect to the C-N-C plane in DMA respectively as compared to a reference IR spectrum of gaseous DMA (bottom spectrum in Figure 5-7). We conclude that the gas phase in the closed cell at 100 °C is a mixture of TDMAH and DMA. Most TDMAH decomposed into DMA over time as shown by the diminishing peak intensity at  $2781 \text{ cm}^{-1}$ .

and  $945\text{ cm}^{-1}$ . The low frequency C-H stretching band at  $2781\text{ cm}^{-1}$  for TDMAH is replaced by that in DMA at  $2810\text{ cm}^{-1}$  at  $t = 7\text{ min}$ . The calculated peak for  $\nu_{\text{N-H}}$  in DMA at  $\sim 3200\text{ cm}^{-1}$  is too weak to be detected.

A small peak at  $1670\text{ cm}^{-1}$  at  $t = 1\text{ min}$ , characteristic of MMI together with a broad peak around  $1026\text{ cm}^{-1}$  ( $\delta_{\text{H-C-H}}$ ) were observed.<sup>132</sup> The peak at  $1670\text{ cm}^{-1}$  is  $8\text{ cm}^{-1}$  higher than that observed for liquid TDMAH heated to  $150\text{ }^\circ\text{C}$  as shown in Figure 5-5. As TDMAH decomposed into DMA in the closed cell, this peak disappeared, indicating that either MMI adsorbed onto the wall or underwent further reaction. We note that MMI was not observed in the later surface adsorption experiments except for room temperature, indicating that it easily desorbs into the gas phase.

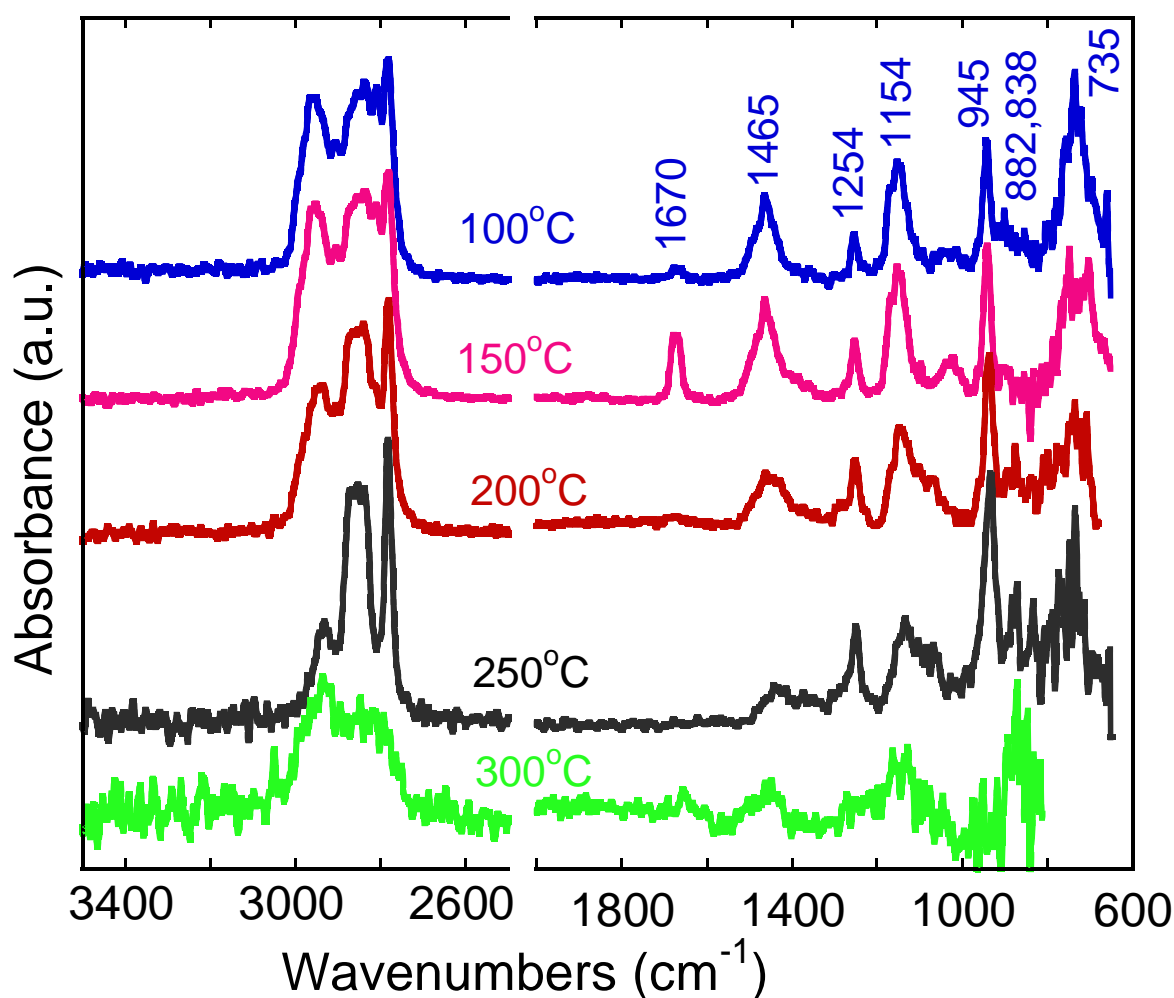


**Figure 5-8.** Gas phase TDMAH IR spectra at different temperatures in flow mode at 5 min. and 0.6 Torr.

The gas phase IR spectra of TDMAH in the flow mode at elevated temperatures is shown in Figure 5-8. The spectra were taken 5 min. after introducing TDMAH into the cell when the flow was steady. Previous workers<sup>131</sup> have shown that TDMAH under their ALD conditions does not decompose below 350 °C, while in our flow system, we observe it to decompose at the lower temperature 300 °C, suggesting that different flow conditions can lead to considerably different behavior. Without a carrier gas, a longer residence time of molecules in the heated zone where the signal can be collected may account for our observed decomposition temperature. The peak due to MMI at 1670 cm<sup>-1</sup> was largest at 150 °C, and diminishes at higher temperatures. With the same preheating time and temperature for the bubbler, the possible formation of MMI during this period cannot explain the difference in its behavior at different gas cell temperatures. One possibility for the disappearance of the band at 1670 cm<sup>-1</sup> at >200 °C may be due to faster MMI convection. Another possibility is that at higher temperatures, MMI undergoes further reactions. Interestingly, the C-H stretch began to resemble the intact molecule spectrum with higher temperatures perhaps due to desorbed TDMAH or partially decomposed TDMAH coated on hot reactor walls. The signal-to-noise ratio is smaller at higher temperatures especially at the lower wavenumbers. However, some characteristic peaks are still discernible. The peaks at 882 and 838 cm<sup>-1</sup> grow with increasing temperature as the peak at 1670 cm<sup>-1</sup> diminishes, and they remain even after evacuating the gas cell at 300 °C. Peaks of similar frequency were previously assigned to  $\nu_{\text{as Si-N}}$  in ammonia treated H-Si(111) (840, 870 and 1040 cm<sup>-1</sup>),<sup>36,60,134</sup> in Si<sub>x</sub>N<sub>y</sub> films (840 cm<sup>-1</sup>),<sup>135</sup> and  $\delta_{\text{CH}_3}$  in (CH<sub>3</sub>)<sub>2</sub>GeO (857 cm<sup>-1</sup>).<sup>136</sup> Monolayer adsorption of DMA and trimethylamine on Ge also showed strong peaks at 887 and 870 cm<sup>-1</sup>, which have been assigned to the N-C stretch.<sup>137</sup> However, N-C stretches usually appear at frequencies higher than 1000 cm<sup>-1</sup>.<sup>138</sup> Upon further evaluation, it is likely that these peaks should be assigned to the Ge-N stretch due to decomposition on the Ge IRE. By comparison to our calculated DFT spectra, the two peaks at

882 and 838  $\text{cm}^{-1}$  can be tentatively assigned to monodentate  $\nu_{\text{Si-N}}$  and  $\delta_{(\text{Si})\text{C-H}_2}$  in species formed by reactions of TDMAH with hydrogen terminated Si surfaces (reactions (7) and (8), Figure 5-9) or symmetric and asymmetric  $\nu_{\text{Si-N}}$  in the bidentate form which will be discussed later.

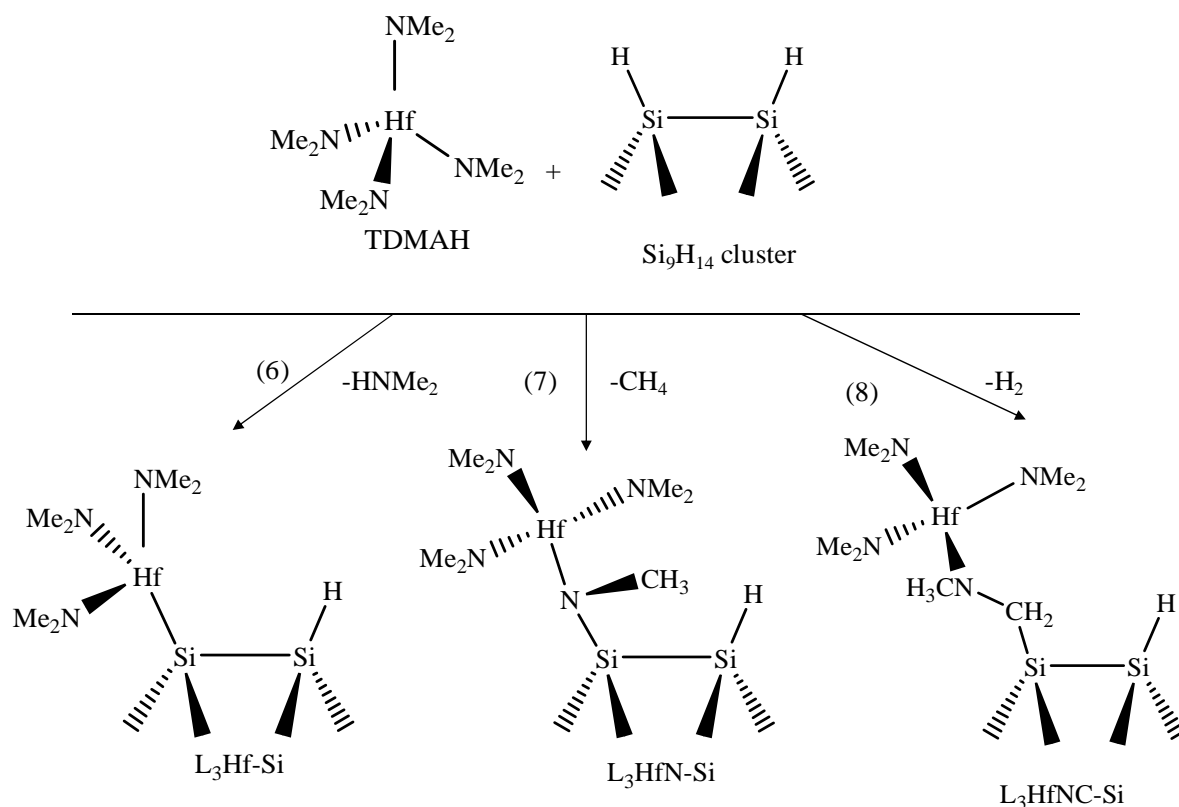


**Figure 5-9.** Reactions (6) to (8): first step surface reaction from TDMAH forming different interfacial bonds: (6)  $\text{L}_3\text{Hf-Si}$ , (7)  $\text{L}_3\text{HfN-Si}$ , and (8)  $\text{L}_3\text{HfNC-Si}$ .

### 5.3.3 Surface FTIR Analysis of TDMAH and $\text{D}_2\text{O}$ or $\text{H}_2\text{O}$ ALD on H-Si(100)

Initial growth of thin films occurred immediately upon opening the precursor inlet valve for TDMAH within the time scale of the measurement as monitored by the  $\nu_{\text{C-H}}$  region. Figures 10 through 12 show IR data for experiments conducted at the low temperatures of 25  $^\circ\text{C}$  and 100  $^\circ\text{C}$  using the following sequence: (a) 1<sup>st</sup> cycle, multilayer adsorption of  $3.5 \times 10^8$  L of TDMAH; (b) desorption by pumping for 10 min.; (c) 2<sup>nd</sup> cycle, dose of  $5.0 \times 10^7$  L of TDMAH; (d) 1<sup>st</sup> cycle of  $1.0 \times 10^8$  L of  $\text{D}_2\text{O}$  or  $\text{H}_2\text{O}$ ; (e) 3<sup>rd</sup> cycle a dose of another  $5.0 \times 10^7$  L of TDMAH; (f) 2<sup>nd</sup> cycle of  $5.0 \times 10^7$  L of  $\text{D}_2\text{O}$  or  $\text{H}_2\text{O}$ .

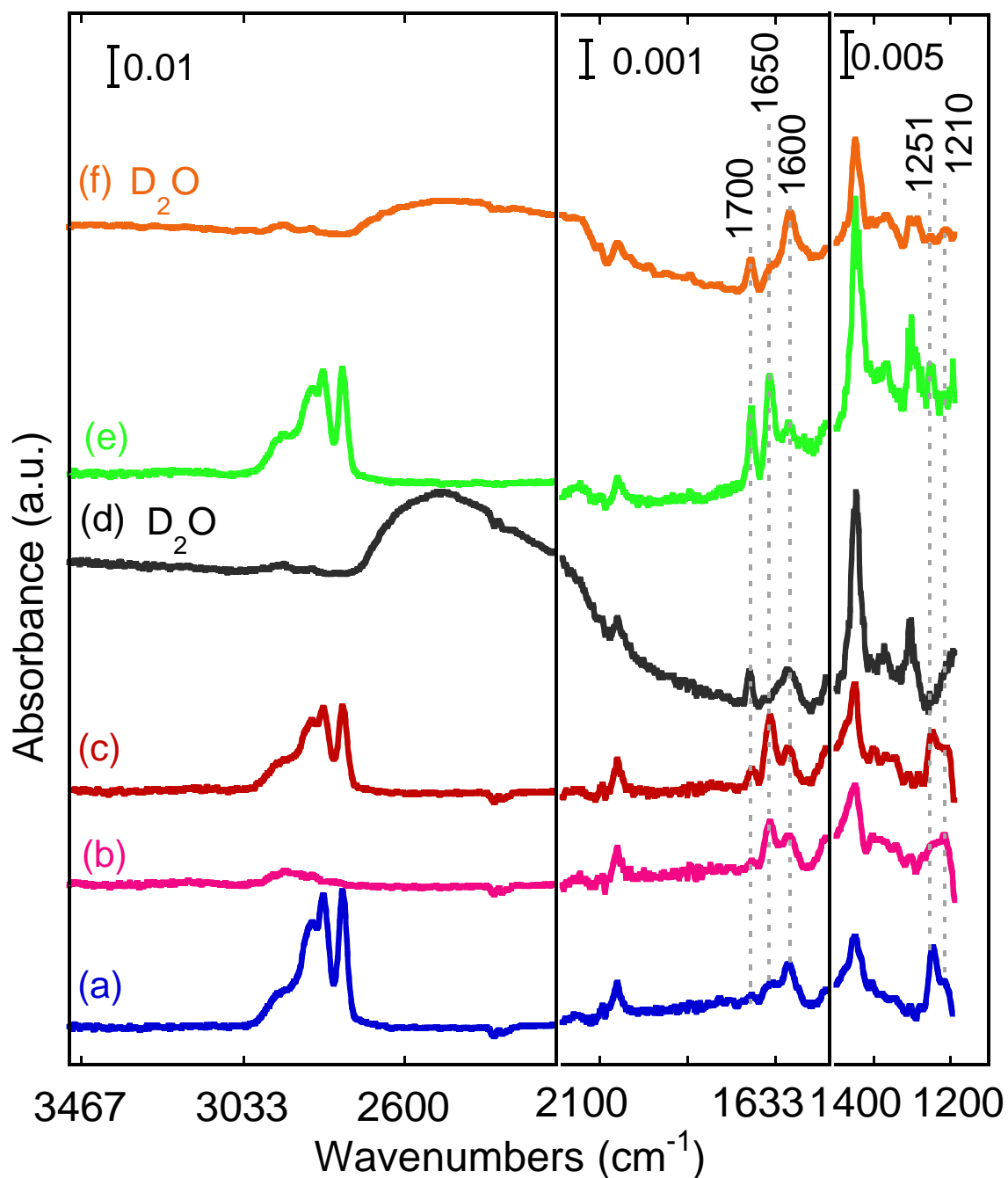


**Figure 5-10.** IR spectra for TDMAH/D<sub>2</sub>O adsorption on H-Si(100) at room temperature. In sequence: (a)  $3.5 \times 10^8$  L TDMAH; (b) desorption under vacuum for 10 min. (c)  $5.0 \times 10^7$  L dose of TDMAH; (d)  $1.0 \times 10^8$  L of D<sub>2</sub>O cycle; (e)  $5.0 \times 10^7$  L dose of TDMAH; (f)  $5.0 \times 10^7$  L dose of D<sub>2</sub>O.

Adsorption experiments were also performed for longer times than the usual ALD pulse to determine whether the adsorption saturates. After an initial rapid increase, the intensity of the  $\nu_{C-H}$  region monotonically increases with time even after 30 min of exposure, showing evidence of multilayer adsorption and consistent with the observation that the ALD

process window is dependent on the purge time between TDMAH and oxidant exposure.<sup>149</sup> This is in contrast to hafnium tert-butoxide adsorption,<sup>139</sup> where the  $\nu_{\text{C-H}}$  region was observed to saturate. The intensity of the C-H stretches decreased during desorption and was almost completely absent after the D<sub>2</sub>O or H<sub>2</sub>O cycle, consistent with observations by other groups.<sup>59,60</sup> We note that our dosing amount is one or two magnitudes larger than the traditional ALD dose, and the higher dosing level is critical for the observation of these adsorbed surface products. The assignments for the characteristic peaks for the adsorption experiment are given in Table 5-2.

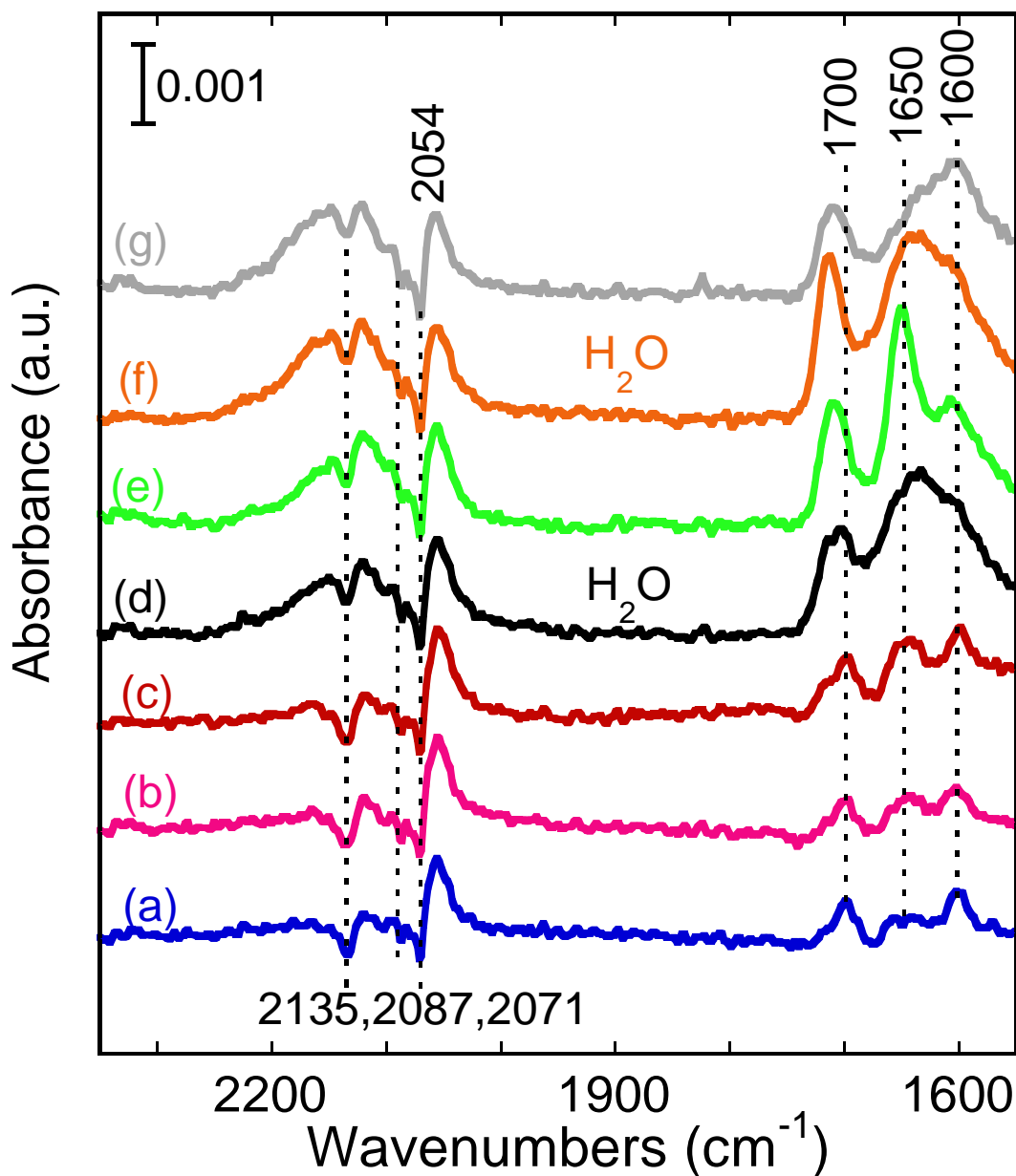
**Table 5-2.** Peak positions ( $\text{cm}^{-1}$ ), IR Intensities ( $\text{km/mol}$ ), and Assignments for the Characteristic Experimental IR Peaks from the Calculated B3LYP/BS1 Values.

Expt.	Assignments	Calc. Freq.	Calc. Intensity
1700 (m) (Figure 5-10)	$\nu_{\text{N}=\text{CH}_2}$ in T-en	1783	297
1662 (m) (Figure 5-5) 1670 (Figure 5-8)	$\nu_{\text{N}=\text{CH}_2}$ in MMI	1743	18
1634 (m) (Figure 5-5) 1650 (Figure 5-10)	$\nu_{\text{Hf-H}}$ in $\text{Si}_2\text{N}_2(\text{Hf-H})\text{L}$ $\nu_{\text{Hf-H}}$ in TH <sup>a</sup>	1648 1612	288 325
1600 (m) (Figure 5-10, 14)	$\delta_{\text{NH}_2}$ in methylamine	1665	19
1359 (w) (Figure 5-5)	$\delta_{\text{CH}_2}$ in TI-4 <sup>a</sup>	1362	48
1210 (w) (Figure 5-5, 10) 1220 (w) (Figure 5-14)	$\nu_{(\text{Hf})\text{N-C}}$ in TI-4 $\nu_{(\text{Hf})\text{N-C}}$ in TI-3 <sup>a</sup>	1222 1255	212 200
945 (s) (Figure 5-7, 14)	$\nu_{\text{Hf-N}}, \nu_{\text{N-C}}$ (s) in TDMAH	963	200
882 (m) (Figure 5-8)	$\nu_{\text{Si-N}}$ in $\text{Si-N}(\text{CH}_3)_2$ $\nu_{\text{Si-N}}$ in $\text{Si}_2\text{-N}_2\text{HfHL}$ $\nu_{\text{Si-N}}$ in $\text{Si-NHfL}_3$	991 782 (s), 753 (as) 816	188 265, 99 316
839 (m) (Figure 5-14)	$\nu_{\text{Ge-N}}$ in $\text{Ge-N}(\text{CH}_3)_2$ $\nu_{\text{Ge-N}}$ in $\text{Ge-NHfL}_3$	960, 554 717	127, 41 371
838 (m) (Figure 5-8)	$\delta_{\text{CH}_2}$ in $\text{SiCNHfL}_3$ $\delta_{\text{CH}_2} / \delta_{\text{N-H}}$ in MMI-Si	804 801	51 108
798 (w) (Figure 5-14)	$\delta_{\text{CH}_2} / \nu_{\text{C-N}}$ in TI-3 $\delta_{\text{NH}_2}$ in $\text{SiCH}_2\text{NH}_2$	793 826	19 367
735 (s) (Figure 5-7, 8, 14)	$\delta_{\text{NH}}$ in DMA	765	131

<sup>a</sup> See labeling for TI, TH, TI-3, and TI-4 in Figure 5-6.

Figure 5-10 shows the spectra for the adsorption of  $3.5 \times 10^8$  L TDMAH followed by the introduction of  $\text{D}_2\text{O}$  on H-Si(100) at 25 °C. These results demonstrate that TDMAH can initiate adsorption onto H-Si(100) as shown by the increase in the intensity for the  $\nu_{\text{C-H}}$  peaks and the loss of the peaks for  $\nu_{\text{Si-H}}$  (amplified region shown in Figure 5-11). A peak for  $\nu_{\text{O-H}}$  on Hf-OH at  $3680 \text{ cm}^{-1}$ ,<sup>139</sup> was not observed. After desorption under vacuum for 10 min., there

was only a small amount of residual C-H stretches and the intensity of the peak at  $2839\text{ cm}^{-1}$  and the low frequency C-H band at  $2781\text{ cm}^{-1}$  became very weak. In comparison to prior work,<sup>137</sup> the adsorption of DMA on a Ge(100) surface showed a peak at  $2834\text{ cm}^{-1}$  during multilayer adsorption, whereas for monolayer adsorption this peak was not observed. The fact that the low frequency C-H band intensity becomes weaker than the higher frequency C-H stretches suggests that N in the residue remaining after desorption may be chemically or datively bonded to the surface, which would affect the availability of the lone pair on N for delocalization to the C-H  $\sigma^*$  orbital.<sup>137</sup> The continuous increase of the integrated C-H stretch IR absorption during TDMAH adsorption and the remaining C-H stretch as well as the Si-H abstraction after desorption indicate that after the first cycle of TDMAH, both physisorbed and chemisorbed TDMAH could be present. A broad set of peaks in the region of  $2200\text{-}2000\text{ cm}^{-1}$  centered at  $2086\text{ cm}^{-1}$  is readily assigned to  $\nu_{\text{Si-H}}$ . After a  $3.5 \times 10^8$  L dose of TDMAH, a maximum of one third of the surface H atoms were abstracted and there was no change after 10 min. of pumping. The full width at half maximum (FWHM) is about  $90\text{ cm}^{-1}$ , due to thermal and inhomogeneous broadening,<sup>140</sup> and/or the existence of kink or steps with the presence of both mono and di-hydrogen bonds on the Si surface. The peak at  $2054\text{ cm}^{-1}$  is consistent with other IR reports of the first ALD cycle of TEMAH or TDEAH onto H-Si surfaces.<sup>59,60</sup> The red shift of  $\nu_{\text{H-Si}}$  to  $2054\text{ cm}^{-1}$  is likely due to the adsorption effect or interaction of Si-H with neighboring Si sites bonded to Hf. The insertion reaction product TI-3 (reaction (3), Figure 5-6) can also induce this shift when it adsorbs onto the H-Si surfaces with negative charges on H. Spectra at higher temperatures have fringes that are not readily analyzed in this region.



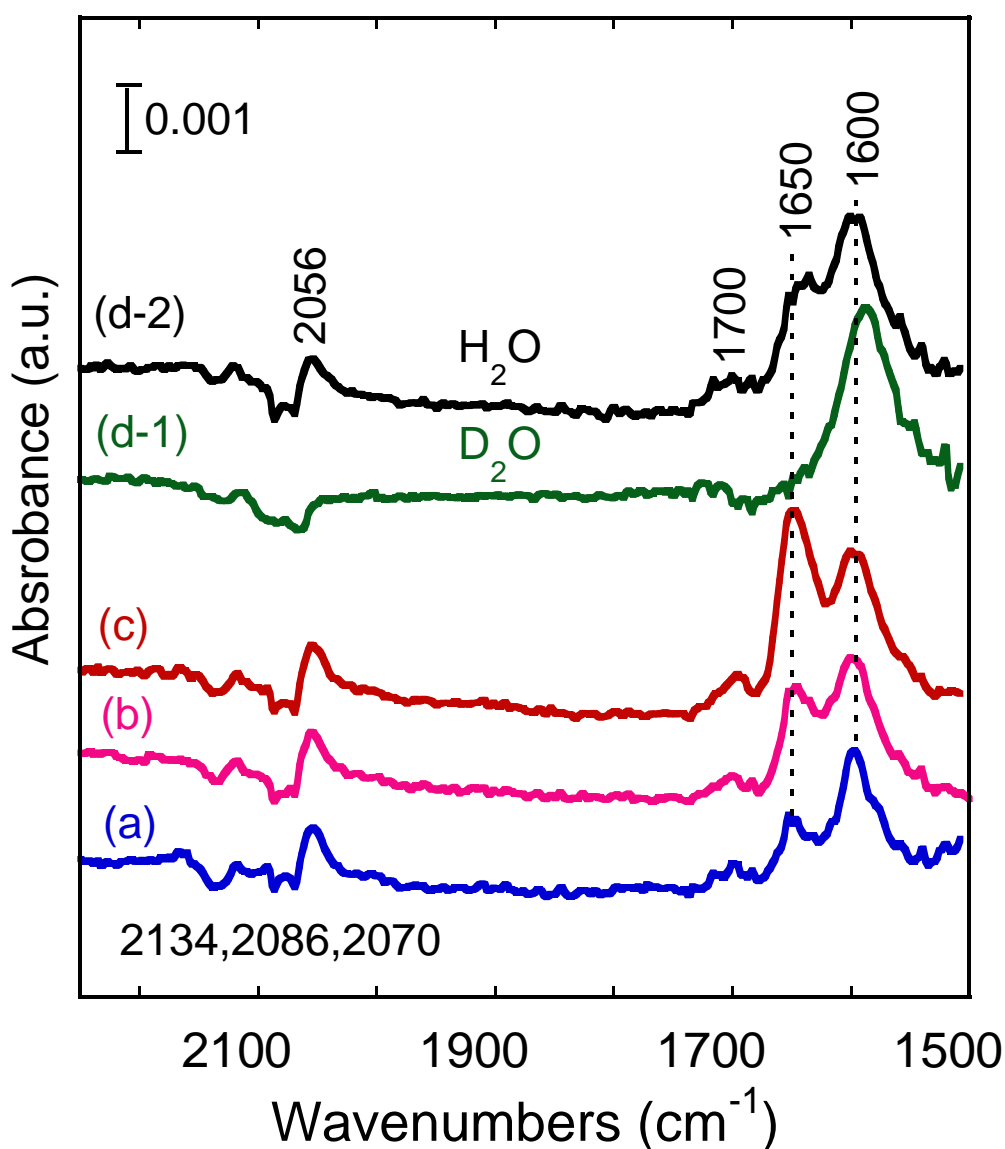
**Figure 5-11.** IR spectra for the H-Si and H-Hf stretching regions for TDMAH followed by H<sub>2</sub>O adsorption at room temperature, sequentially: (a)  $3.5 \times 10^8$  L TDMAH; (b) desorption under vacuum for 10 min.; (c)  $5.0 \times 10^7$  L dose of TDMAH; (d)  $1.0 \times 10^8$  L of H<sub>2</sub>O cycle; (e)  $5.0 \times 10^7$  L dose of TDMAH; (f)  $5.0 \times 10^7$  L dose of H<sub>2</sub>O; (g) desorption under vacuum for 10 min.

Figure 5-11 is an amplified region for Si-H and 1700-1600 cm<sup>-1</sup>. The control experiments were done with H<sub>2</sub>O following the same procedure as Figure 5-10. The last added procedure was 10 min. desorption under vacuum after the H<sub>2</sub>O pulse to observe the hydroxyl exchange reaction. Three new peaks at 1700, 1650, and 1600 cm<sup>-1</sup> appear after the 1<sup>st</sup> cycle TDMAH adsorption. The unknown peak at 1700 cm<sup>-1</sup> was observed after the

adsorption of TDMAH followed by the D<sub>2</sub>O or H<sub>2</sub>O cycle as shown both in Figures 5-10 and 5-11. The peak at 1700 cm<sup>-1</sup> is not readily observed at T > 100 °C. It is not associated with the peak at 1600 cm<sup>-1</sup> as they do not have the same change in intensity.  $\nu_{C-O}$  was measured to be 1705 cm<sup>-1</sup> for TDMAT after CO<sub>2</sub> insertion.<sup>141</sup> The peak at 1700 cm<sup>-1</sup> increased after the 3<sup>rd</sup> TDMAH cycle (spectrum c in Figure 5-10 and Figure 5-11), which indicates that there may be a carbamato-type (ca. MO<sub>2</sub>CN) compound forming between TDMAH and the surface after the H<sub>2</sub>O cycle.<sup>141</sup> The second possibility is that the  $\nu_{C=N}$  mode is being blue shifted from MMI. The MMI was calculated to have a high desorption energy from Hf-H (discussed below), which indicates that energy needs to be added to desorb it and can explain why it was not observed in the gas phase spectra of TDMAH at room temperature but was observed in those at 100 °C and 150 °C. Another possibility is that the  $\nu_{C=N}$  mode is from the product of the 1,2- $\beta$ -hydride elimination reaction which releases methane (reaction (5), Figure 5-6).

The peak at 1634 cm<sup>-1</sup> in heated liquid TDMAH (Figure 5-5) appears on the surface adsorption located at 1650 cm<sup>-1</sup>. With the assistance of the calculations, we tentatively assign this peak to the  $\nu_{Hf-H}$  of a surface Hf-H species possibly generated by  $\beta$ -hydride elimination. The presence of a transition metal hydride has been reported by several groups. For example, a silica supported transition metal hydride complexes, [Zr]<sub>s</sub>-H, was synthesized from hydrogenolysis of a tris(neopentyl)zirconium surface complex and its IR peak was centered at 1635 cm<sup>-1</sup>;<sup>142</sup> a similar result is observed for [Ta]<sub>s</sub>-H.<sup>143</sup> The asymmetric Hf-H stretch in HfH<sub>4</sub> was measured to be 1678 cm<sup>-1</sup>,<sup>144</sup> and calculated to be 1687 cm<sup>-1</sup> at the B3LYP/6-31+G(d,p) level; the Hf-H stretch in HHfO was observed at 1626 cm<sup>-1</sup>.<sup>145</sup> This peak was not observed in the gas phase spectra, indicating that it results from a surface species. To provide insight into the identity of this Hf-H species, Figures 5-10 to 5-12 show the exchange reaction of Hf-H with D<sub>2</sub>O or H<sub>2</sub>O at 25 °C and 100 °C. The peak at 1650 cm<sup>-1</sup> disappeared after a pulse of D<sub>2</sub>O (Figure 5-10 (d) and (f), Figure 5-12 (d-1)) but it remained

for some time after a pulse of H<sub>2</sub>O (Figure 5-11 (d) and (f), Figure 5-12 (d-2)) in both the 25 °C and 100 °C spectra.



**Figure 5-12.** IR spectra for the H-Si and H-Hf stretching regions for TDMAH followed by D<sub>2</sub>O or H<sub>2</sub>O adsorption on H-Si(100) at 100 °C, sequentially: (a)  $3.5 \times 10^8$  L TDMAH; (b) desorption under vacuum for 10 min. (c)  $5.0 \times 10^7$  L dose of TDMAH; (d-1)  $1.0 \times 10^8$  L of D<sub>2</sub>O cycle; (d-2)  $1.0 \times 10^8$  L of H<sub>2</sub>O cycle. (d-1) is after baseline correction.

The reaction of a surface Zr-H with KOH-water has been reported.<sup>142</sup> It is expected that a reaction of Hf-H with water can release H<sub>2</sub>, which would explain the diminished peak at 1650 cm<sup>-1</sup> after pumping for 10 min. (Figure 5-11 (g)) after the water pulse. It is likely that the proton exchange reaction generating Hf-D and the OH substitution reaction releasing H<sub>2</sub> can occur competitively, and that the exchange reaction is faster than the substitution reaction

(reactions (9) and (10), Figure 5-13). The Hf-D stretch is reported<sup>145</sup> to be around  $1230\text{ cm}^{-1}$  and is calculated to be at  $1154\text{ cm}^{-1}$  for the compound TH in reaction (2); these peaks overlap the  $\text{D}_2\text{O}$  bending mode. After a  $\text{D}_2\text{O}$  or  $\text{H}_2\text{O}$  cycle, another TDMAH cycle would generate new Hf-H species as shown in Figure 5-10 (e) and Figure 5-11 (e).

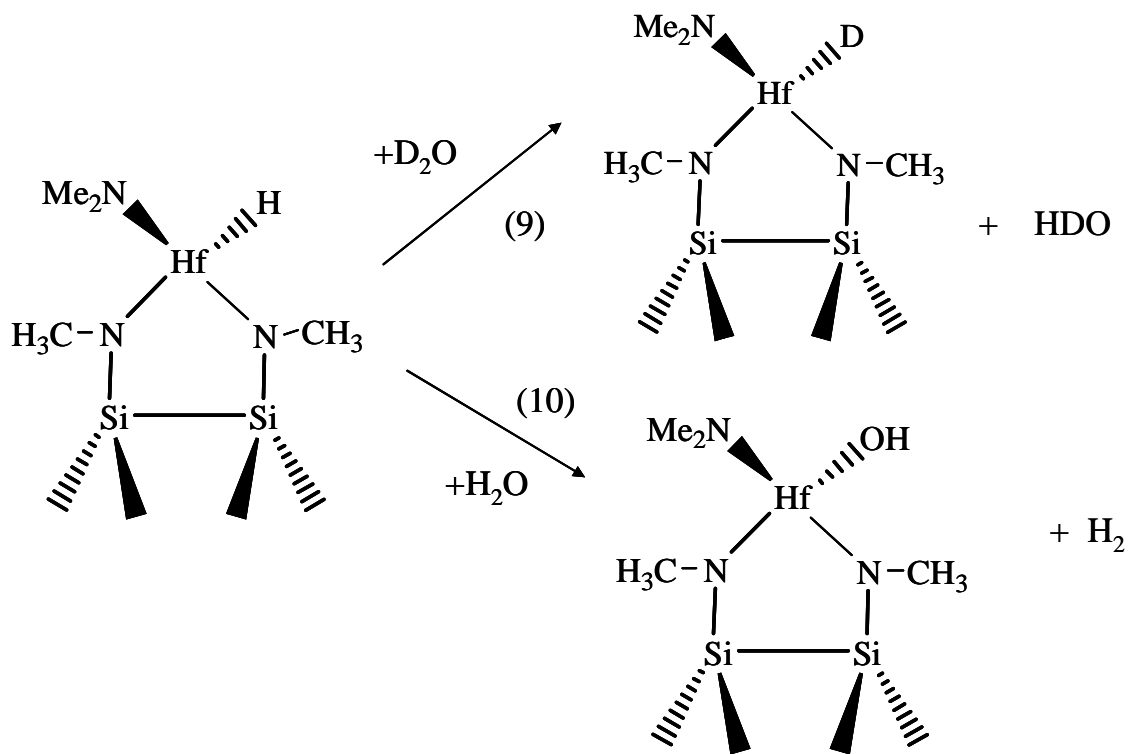


**Figure 5-13.** Reactions (9) and (10): Proton exchange reaction and hydroxyl substitution reaction for Hf-H with  $\text{D}_2\text{O}$  (9) or  $\text{H}_2\text{O}$  (10).

The new peak at  $1600\text{ cm}^{-1}$  exists during the adsorption cycles at both 25 and  $100\text{ }^\circ\text{C}$ . It is an unknown peak prevalent in the decomposition residual of  $\text{TDMAT}^{66,67,133}$  and of  $\text{TDEAH}^{59}$  left on the IR windows. It is not likely to be due to the  $\text{N}=\text{C}$  stretch whose frequency is usually higher than  $1600\text{ cm}^{-1}$  for pure gas compounds containing this functional group. There are many possibilities for this band:  $\text{NH}_2$  scissoring in methylamine,<sup>146</sup>  $\text{OH}_2$  scissoring in water for Hf silicates prepared in solution<sup>147</sup> and from the water cycle control experiment, and the  $\text{C}=\text{C}$  stretch in methoxyethylene containing  $\text{O}-\text{C}=\text{C}$ .<sup>146</sup> Although  $\text{H}_2\text{O}$  has an intense bending peak around  $1600\text{ cm}^{-1}$  on the surface, the presence of this peak with no change in intensity after the TDMAH cycle indicates that it should not be assigned to  $\text{H}_2\text{O}$ .

The remaining possible assignment is  $\delta_{\text{N-H}_2}$ . To identify this species, adsorption of TDMAH on Ge and ZnSe was performed, as these species have a broader observable window for IR as shown in Figure 5-14. Due to the weak intensity at  $1600\text{ cm}^{-1}$  on Ge, the otherwise intense peak for  $\omega_{\text{N-H}_2}$  around  $780\text{ cm}^{-1}$ <sup>136</sup> was hidden by the broad peak at  $735\text{ cm}^{-1}$ . We tentatively assign this peak to  $\delta_{\text{N-H}_2}$  but further work is needed for a definitive assignment.

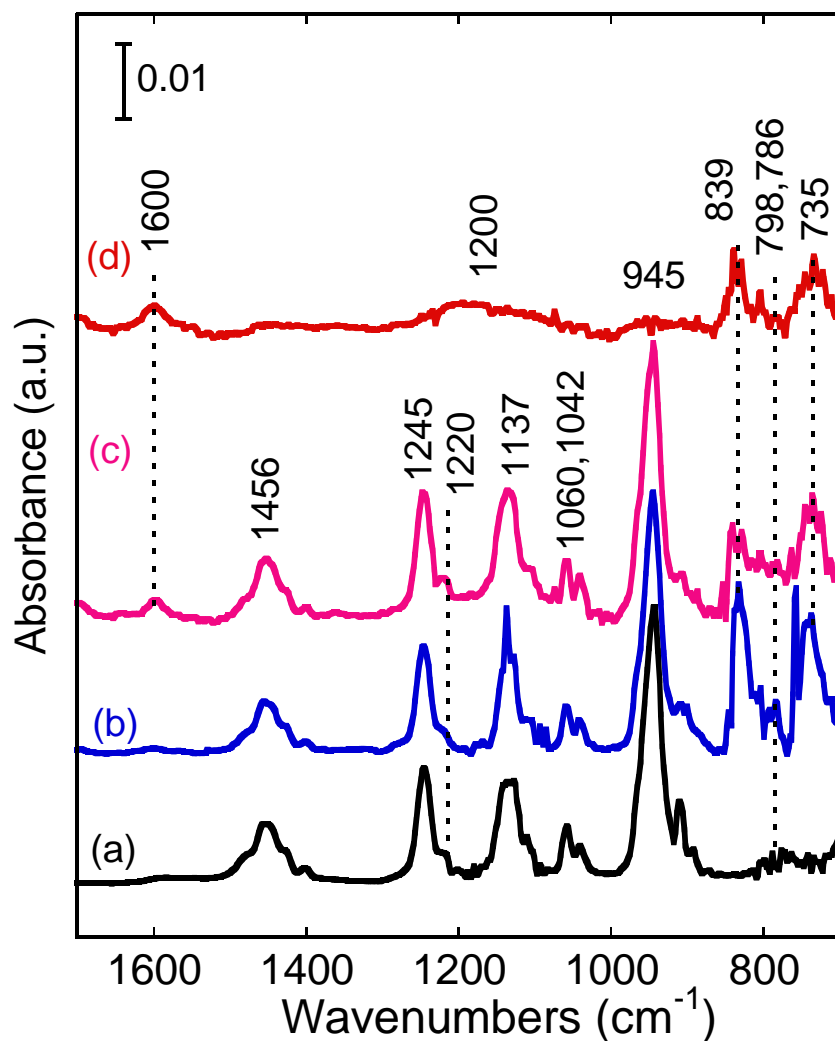


**Figure 5-14.** IR spectra for TDMAH followed by D<sub>2</sub>O adsorption on Ge and ZnSe IRE for the lower wavenumber region. (a)  $3.5 \times 10^8$  L dose of TDMAH on ZnSe at  $100\text{ }^\circ\text{C}$ ; (b)  $3.5 \times 10^8$  L dose of TDMAH on Ge at room temperature; (c)  $3.5 \times 10^8$  L dose of TDMAH on Ge at  $100\text{ }^\circ\text{C}$ ; (d) D<sub>2</sub>O cycle after TDMAH cycle on Ge at  $100\text{ }^\circ\text{C}$ .

The C-H bending peak at  $1251\text{ cm}^{-1}$  was broadened and a deconvoluted peak at  $1210\text{ cm}^{-1}$  may contribute to the broadening shown in Figure 5-10. Since there was no apparent peak associated with the peak at  $1359\text{ cm}^{-1}$  for the four member ring in TI-4 as in the bulk

spectrum in Figure 5-5 (b), this peak at  $1210\text{ cm}^{-1}$  is tentatively assigned to a three-member ring TI-3, resulting from the insertion reaction (3) with DMA as the by-product. After the  $\text{D}_2\text{O}$  cycle, this peak disappears.

#### 5.3.4 Surface Adsorption/Desorption FTIR Analysis on Ge and ZnSe

In order to obtain more information at lower frequency, adsorption of TDMAH on hydrogen terminated Ge and ZnSe surfaces was performed. The C-H stretch region is consistent with the adsorption on H-Si(100). Characteristic peaks at 1456, 1245, 1137, 1060, and  $945\text{ cm}^{-1}$  in Figure 14 (a)-(c) for TDMAH are similar to the gas phase spectra. However, the peaks at  $1650\text{ cm}^{-1}$  for Hf-H species and  $1600\text{ cm}^{-1}$  for  $\text{NH}_2$  species on Ge and ZnSe surfaces are not as strong as those on the H-Si(100) surface. With a dose of  $\text{D}_2\text{O}$ , most peaks due to TDMAH disappeared showing an abstraction of the dimethylamido ligands. The broad peak centered at  $1200\text{ cm}^{-1}$  is due to  $\delta_{\text{D-O-D}}$ , which may overlap the  $\nu_{\text{Hf-D}}$  around  $1154\text{ cm}^{-1}$  after the exchange reaction.

Compared with the IR spectrum for pure TDMAH, there are several new peaks located at 1220, 839, 758, and  $735\text{ cm}^{-1}$ . The shoulder peak at  $1220\text{ cm}^{-1}$  observed in both the Ge and ZnSe experiments is assigned as  $\nu_{(\text{Hf})\text{N-C}}$  in TI-3. The peak at  $839\text{ cm}^{-1}$  in Figure 5-14 on the Ge (Figure 5-14 b) surface which is absent on the ZnSe surface (Figure 5-14 a) can be assigned to  $\nu_{\text{N-Ge}}$  in comparison to the peak position for  $\nu_{\text{N-Si}}$  as discussed above in the gas phase FTIR analysis, which remained after the  $\text{D}_2\text{O}$  pulse. The reported Ge-N and Si-N bond strengths are 55 kcal/mol and 78 kcal/mol respectively,<sup>148</sup> so these bonds are reasonably strong. DMA has a strong intensity for  $\delta_{\text{N-H}}$  at  $735\text{ cm}^{-1}$  as shown in Figure 5-5. The small peak at  $798\text{ cm}^{-1}$  is likely to be due to  $\delta_{\text{CH}_2}$  in the chemisorbed TDMAH or MMI.

#### 5.3.5 Residual Gas Analysis

Figure 5-15 shows the mass spectra from 2 to 50 amu for the gaseous effluents from the Si ATR flow through cell. The background at room temperature was taken before opening

the TDMAH valve. The ATR crystal was heated from room temperature to 250 °C, and mass spectra were obtained at different temperatures. Results are shown for 25 °C, 150 °C, and 250 °C. The background shows a significant amount of moisture in the cell or tubing between the cell and the MS. After introducing TDMAH, the H<sub>2</sub>O peak intensity drops by ~15%.

With an electron ionization energy of 102 eV, most of the detected ions should be fragments of the effluent molecules, while only a small portion of the spectrum is expected to be due to parent molecular ions. The strong peak at  $m/e = 44$  can be assigned to the ion  $N(CH_3)_2^+$  from a fragment of TDMAH or DMA. The known peaks for DMA are  $m/e = 45, 44, 30$  ( $HNCH_3^+$ ), and  $15$  ( $CH_3^+$ ). The existence of peaks at  $m/e = 28$  ( $N=CH_2^+$ ),  $27$ , and  $26$  is consistent with the presence of MMI. MMI can also be identified by the peak at  $m/e = 42$ , which otherwise should follow a Gaussian distribution for DMA and be less intense than the peak at  $m/e = 43$ . A portion of the peak at  $m/e = 15$  ( $CH_3^+$ ) may also come from the fragmentation of MMI. It is a common product from the decomposition of the dimethylamido-metal precursors.<sup>67,133</sup> Thus, for low temperature ALD using TDMAH, possible reactions in the gas phase or on the surface leading to MMI cannot be neglected. The ratios of the peak at  $m/e = 18$  to the peak at  $m/e = 16$  are 24.8, 23.6, 24.9, 26.3 in Figure 5-15 (a)-(d) respectively.

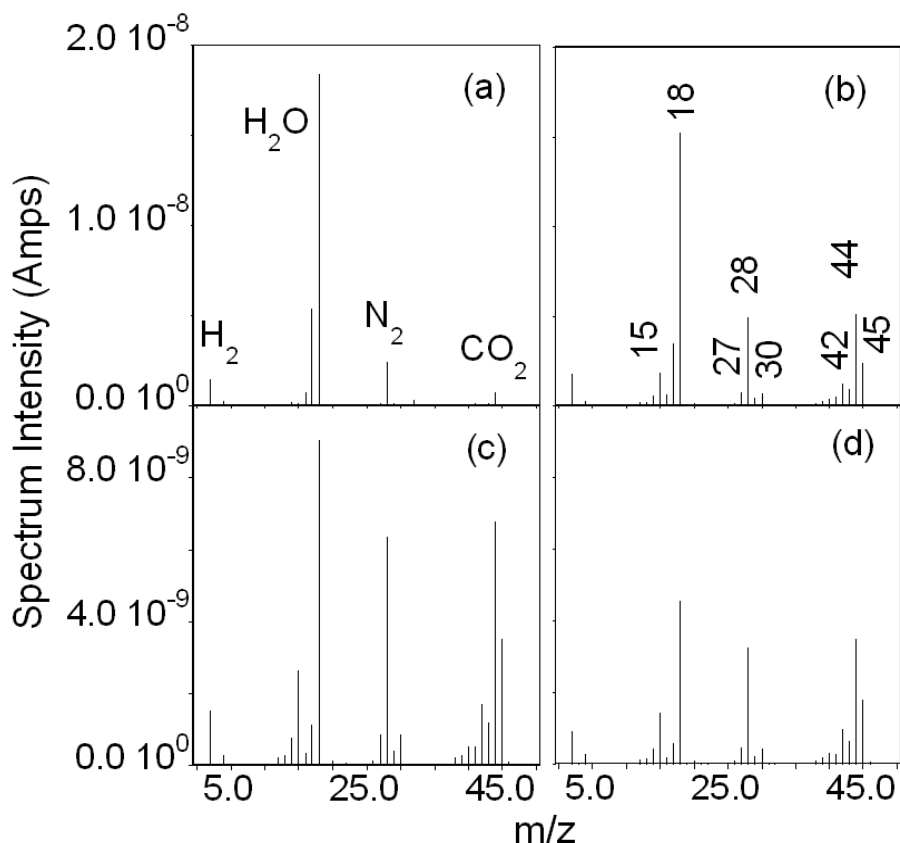


**Figure 5-15.** Q-MS spectra. Background (a) at room temperature; (b) TDMAH effluent from the flow through cell at (b) room temperature, (c) 150 °C and (d) 250 °C.

This variation indicates that some methane may have formed, accounting for a portion of the peak at  $m/e = 16$  as  $\text{CH}_4^+$ . However, it is not as big as the peaks for MMI or DMA, which may indicate that methane formation is not as favorable among the decomposition processes at these temperatures. The intensity ratio for the  $\text{CH}_3^+$  peak to  $\text{H}_2\text{O}^+$  peak grows above 150 °C, because the precursor starts to fully decompose above this temperature. The spectra at 150 °C and 250 °C are similar. The MS data shows that DMA is a major product, although it is impossible to distinguish between the gas phase decomposition reaction and the surface reaction. Other by-products such as MMI and methane could also form through competitive reactions. We note that this precursor is likely to coat the quadrupole sensor, so a long exposure time is not recommended.

#### 5.4 DFT Calculations of Gas Phase Reactions

The exposure time during the TDMAH pulse is important for ALD. Ideally,

monolayer surface coverage should be fully reached to prepare for the oxidation cycle which follows as well as to prevent unsaturated bonds from being oxidized in this step. An over-exposure of TDMAH may result in multilayer adsorption rather than the desired atomic layer control. As a consequence, the ALD process window has been found to depend strongly on an adequate purge time between precursor pulses.<sup>149</sup> To study possible oligomerization effects that may occur during the first cycle, the dimer of TDMAH  $[\text{Hf}(\text{NMe}_2)_4]_2$  (Figure 5-6) was calculated. The dimerization is endothermic by 12.9 kcal/mol at the B3LYP/BS1 level. The dimer of TDMAH has been reported to exist in the solid phase by crystallization from toluene, with two bridging N atoms between two Hf atoms forming a nonplanar structure of  $C_{2v}$  symmetry.<sup>71</sup> The optimized Hf–N bridging bond lengths at the B3LYP/BS1 level are 2.326 Å and 2.360 Å, in reasonable agreement with the crystal structure values of 2.262 Å and 2.324 Å.<sup>71</sup>

Reactions (2) to (5) (Figure 5-6) show possible decomposition mechanisms for TDMAH in the gas phase: reaction (2) is a  $\beta$ -hydride elimination reaction, reaction (3) is an intramolecular insertion reaction leading to a three-member ring structure, reaction (4) is another intramolecular insertion reaction leading to a four-member ring structure, and reaction (5) is a 1,2- $\beta$ -hydride elimination reaction. The reaction energies and barriers for these gas phase reactions calculated at the B3LYP level are given in Table 5-3.

**Table 5-3.** Relative Energies from the Reactants at 0 K in kcal/mol for the Gas Phase Reactions Calculated with the B3LYP Functional and the BS1 and BS2 Basis Sets.

Reaction	TS		Product Complex		Products	
	BS1	BS2	BS1	BS2	BS1	BS2
(2)	45.0	43.4	33.5	33.4	39.2	39.4
(3)	39.9	38.6	30.1	30.8	53.2	54.6
(4)	84.0	83.8	10.9	11.8	10.8	11.7
(5)	69.9	68.6	2.6	3.6	2.0	3.4

The reaction energies were calculated at the B3LYP/BS1 level and are within  $\pm 1.5$  kcal/mol difference from those calculated at the B3LYP/BS2 level. Both the  $\beta$ -hydride

elimination reaction (2) and the three-member ring formation reaction (3) are endothermic with high reaction barriers. As a comparison, similar calculations were also done for reaction (3) for TDMAT, which has a reaction barrier of 37.4 kcal/mol and reaction energy of 24.1 kcal/mol at the B3LYP/BS1 level. This reaction was reported to be observed in similar experiments on TDAMT, and it has been proposed to be followed by the formation of a dative bond from MMI.<sup>66</sup> Although the energy of reaction (3) for TDMAT is 6 kcal/mol lower than that for TDMAH, all the above gas phase reactions are predicted to be quite endothermic and would not readily occur in the gas phase under our experimental conditions below 300 °C. In addition, we calculated that the decomposition of TI-3 to MMI and Hf(NMe)<sub>2</sub> is thermodynamically unfavorable, which rules out the generation of MMI from TI-3. The thermodynamically feasible decomposition reactions (4) and (5) have high reaction barriers of 84.0 and 69.9 kcal/mol respectively, which is consistent with the observation of methane only at very high temperatures,<sup>67</sup> or a long preheating which may assist such slow reactions. The high endothermicity and/or high energy barriers of the thermal decomposition reactions (2) to (5) indicate that these reactions are not likely to occur in gas phase under low temperature conditions. However, since there are unavoidable surfaces in the system such as quartz bubbler, tubing walls, hydrogen terminated Si windows or IRE substrate surfaces, these reactions may be exothermic on surfaces and could occur as discussed below.

In addition, TDMAH is very reactive towards water and the reported TDMAH hydrolysis reaction:<sup>59</sup>  $\text{Hf}(\text{NMe}_2)_4 + \text{H}_2\text{O} \rightarrow (\text{HO})\text{HfN}(\text{Me}_2)_3 + \text{HNMe}_2$ , was predicted to be exothermic by -20.3 kcal/mol with a calculated barrier height of only 2.2 kcal/mol at the B3LYP/BS1 level. This reaction is likely to occur during ALD due to the usual residual moisture left inside the chamber and gas lines. However, as the hydrolysis reaction is very fast due to the very lower reaction barrier, it is likely to readily deposit HfO<sub>2</sub>(s) on the gas line wall, which is less likely to be transported by the flowing gas. Any surface OH groups on

defect sites should be consumed quickly upon exposure to TDMAH.

The calculated vibrational frequencies of gas phase reaction products have characteristic peaks which match the experimental IR spectra as described above. The unscaled frequencies of TDMAH, TH, TI-3, and TI-4 are listed in Table 5-2.

#### 5.4.1 Calculations of Surface Reactions

Figure 5-1(a) shows the structure of  $\text{Si}_9\text{H}_{14}$  used as a model for the Si(100) surface. A Mulliken charge analysis<sup>150</sup> shows that the surface H has a charge of about -0.06 e and the BDE of surface Si-H was calculated to be 80.6 kcal/mol for this cluster at the B3LYP/BS1 level. In comparison, the BDE of Si-H is calculated to be 84.1 kcal/mol for the  $\text{Si}_7\text{H}_{14}$  cluster representing the H-Si(111) surface and 89.1 kcal/mol in  $\text{SiH}_4$ , in good agreement with experimental value. It is well established that  $\text{H}_2$  desorption from H-Si(100) is at about 540 °C.<sup>151,152</sup> Thus, silicon radicals due to breaking an Si-H terminal bond are not likely to be present under low temperature ALD conditions.

Interfacial bonding states would be of interest as the stability of different bonding arrangements determine interface quality and band offset. Incorporation of C contaminants can influence the resistivity and density of the desired high dielectric materials. The ideal interface should have no Si dangling bonds, but have either Si-Hf direct bonding or Si-O-Hf bonding to avoid charge trapping and band offset shifts.<sup>153</sup> Potential surface reactions starting from TDMAH on a model 2×1 H-Si(100) surface result in different interfacial bonding such as reactions (6) to (8) (Figure 5-9). The reaction energetics are listed in Table 5-4.

**Table 5-4.** Relative Energies from the Reactants at 0 K in kcal/mol for the Surface Reactions Calculated with the B3LYP Functional and the BS1 and BS2 Basis Sets

Reaction	Product Complex		Products	
	BS1	BS2	BS1	BS2
(6)	7.7	6.9	9.7	10.2
(7)	-23.4	-21.4	-23.6	-21.3
(8)	8.6	9.1	8.2	8.7
(11)	-34.4	-33.0	–	–
(12)	-25.6	-24.7	–	–
(13)	22.1	22.0	39.8	36.9
(14)	-15.0	-12.1	-15.1	-12.1
(15)	15.9	17.3	15.9	17.3
(16)	31.2	31.9	58.3	59.0
(17)	32.3	31.8	47.0	47.1
(18)			18.1	19.4
(19)			-24.9	-21.7

No physisorption energy was predicted at the B3LYP level with either basis set. This is not surprising as most current DFT functionals including B3LYP are known to have difficulty in predicting weak intermolecular interactions such as would be present here. This is also consistent with the weak adsorption observed in the experiment;<sup>60</sup> such an adsorption is likely due to weak dispersion interactions. The interfacial bonding species have BDEs in the following decreasing sequence: Si-N > Si-C > Si-Hf, which is consistent with the reaction energy sequence of the reactions (6) to (8) (Figure 5-9). The only exothermic reaction is (7) for these three reactions. Thus the most likely reaction between TDMAH and the Si surface is cleavage of the N-C bond and the formation of the L<sub>3</sub>Hf-N-Si moiety with release of methane. It can be used to explain the observations of  $\nu_{\text{Si-N}}$  or  $\nu_{\text{Ge-N}}$  in the IR spectra. However, the formation of Hf-Si as shown in reaction (6) is also possible. The Hf-Si bond length is predicted to be 2.901 Å for the product, comparable to the literature value of 2.743 Å in TDMAH-silyl complex.<sup>71</sup> The rate of reaction (6) with a reaction barrier of 19.2 kcal/mol

calculated at the DFT/BS1 level was predicted to be  $\sim 0.05 \text{ s}^{-1}$  at 298 K using transition state theory.<sup>154</sup> The imaginary frequency of the transition state was  $500i \text{ cm}^{-1}$ , so we estimated the effect of tunneling using the Wigner expression.<sup>154</sup> The tunneling correction will increase the rate by about 25% at room temperature. The estimated average residence time of TDMAH in the flow cell is about 0.3 seconds assuming a pumping speed of 30 l/min for the total transport volume. Thus from a kinetic point of view, reaction (6) could play a role at room temperature. Reaction (8) has a reaction energy similar to that of reaction (6), which leads to possible C incorporation and this type of interfacial bonding is not desired. It can be used to explain the observation of  $\delta_{\text{C-H}_2}$  in the experimental IR spectra. The possible formations of different interfacial bonds suggest that carbon contamination may remain with the alkylamido metal precursors during low temperature ALD using TDMAH.

Whether by-products can be easily removed is an important factor with respect to decreasing the contaminant level. We predict the desorption energy for DMA in reaction (6) to be  $\sim 2 \text{ kcal/mol}$  (the difference in energy between the product complex and the dissociated products). Thus under vacuum, the by-product DMA with a low desorption energy could be pumped away quickly for this first step.

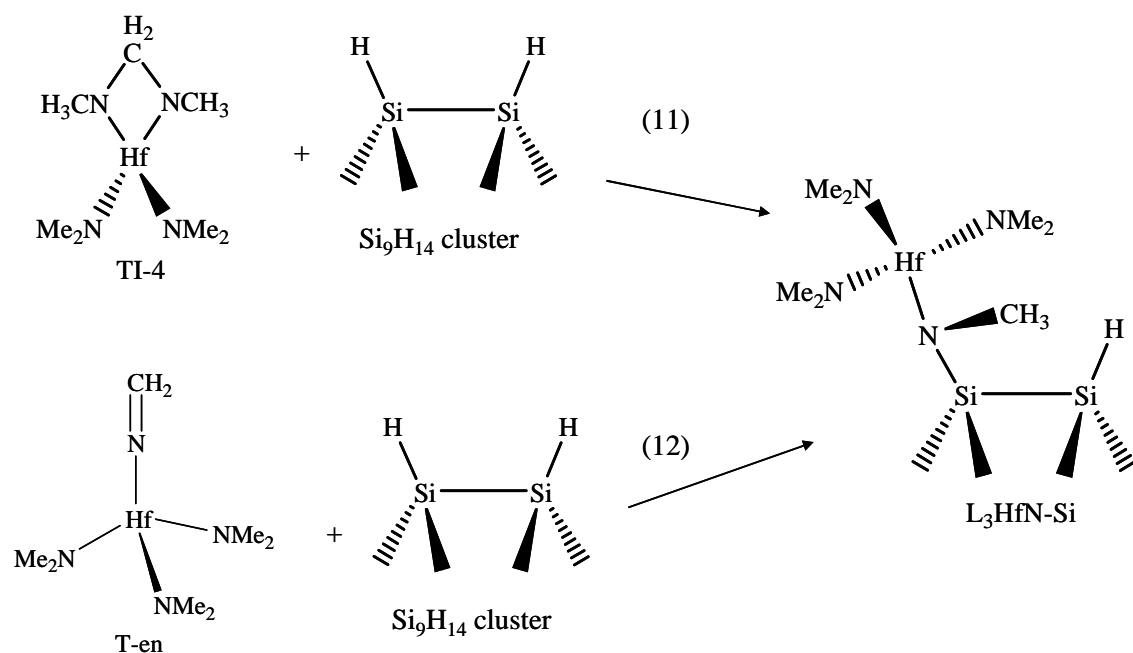


**Figure 5-16.** Reactions (11) and (12): first step surface reaction from possible gas phase intermediates. Reaction (11) from TI-4, and reaction (12) from T-en.

Although the previous calculated gas phase reactions are not likely to occur and products such as TI and TH were not observed in gas phase IR spectra, the decomposition is time dependent and some surface catalytic reactions may produce similar species that can be reactive intermediates affecting the adsorption process. In the gas phase reactions (2) to (5) (Figure 5-9), the most thermodynamically feasible products are TI-4 and T-en. With any possible intermediate reactants in the gas phase, the chemisorption reactions can be initiated with no barriers such as reactions (11) and (12) (Figure 5-16). Both reactions are exothermic producing the same product with the Hf-Si bond as that in reaction (7) (Figure 5-9).

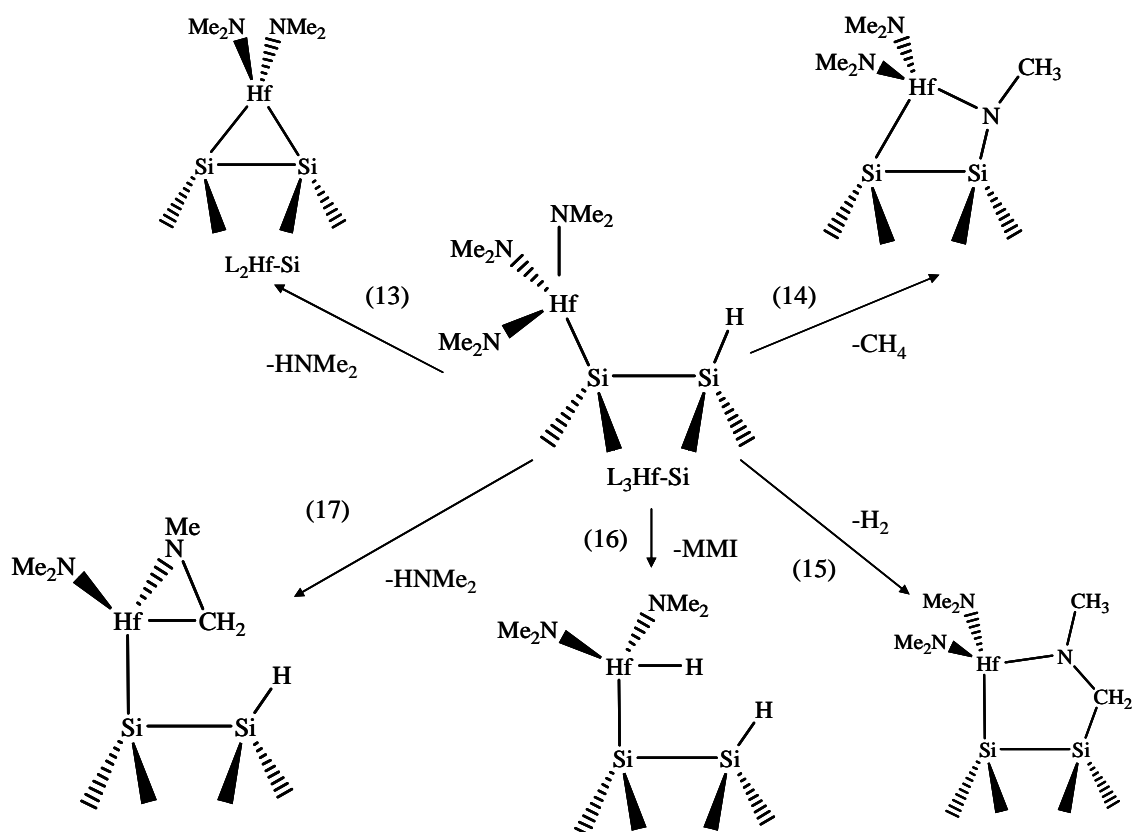


**Figure 5-17.** Reactions (13) to (17): second step surface reactions from  $L_3Hf-Si$ .

The ratio of Hf to Si is of importance with respect to dangling bond formation and surface hydrogen removal. As an example, reactions (13) to (17) (Figure 5-17) show possible second steps for the reaction of  $L_3Hf-Si$  on the H-Si(100) surface where one TDMAH molecule consumes two Si-H bonds. Reaction (14) yields a Si- $L_2Hf-N-Si$  moiety and is exothermic. All of the other reactions are endothermic. The desorption energy of DMA in reaction (13) is 17 kcal/mol, which is 15 kcal/mol larger than its desorption energy in the first reaction step (6) where there is less steric hindrance in the  $L_3Hf-Si$  structure. The  $\beta$ -hydride elimination and insertion reactions from  $L_3Hf-Si$  are even less likely to occur thermodynamically than gas phase. In addition, DMA and MMI are predicted to have high adsorption energies and will thus be difficult to desorb.

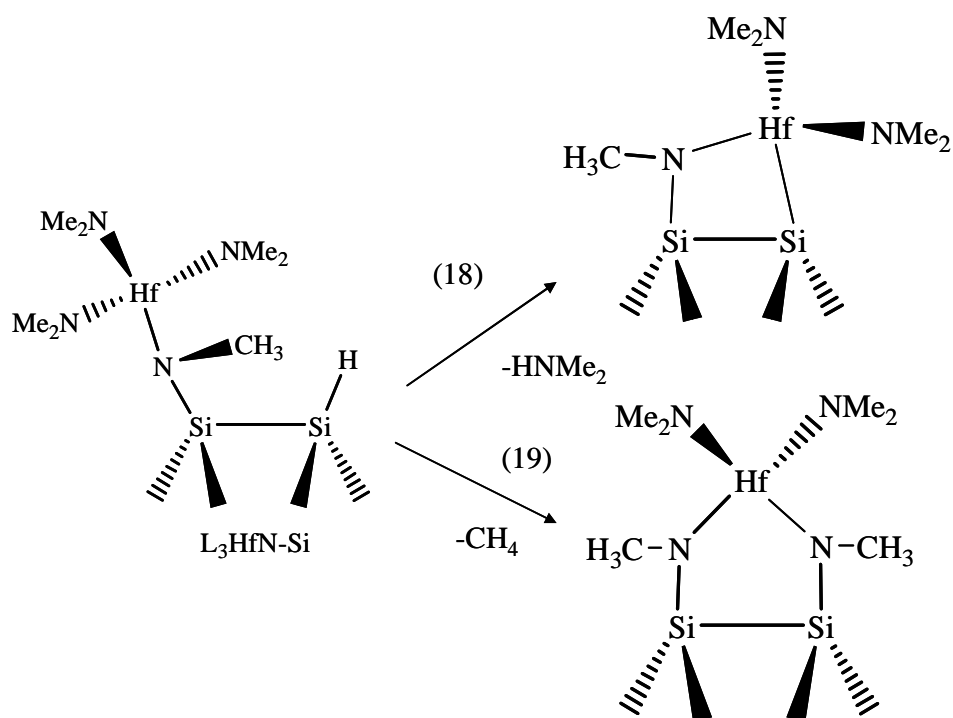


**Figure 5-18.** Reactions (18) and (19): second step surface reactions bridged on Si dimer from  $\text{L}_3\text{HfN-Si}$ .

Similarly, reactions of  $\text{L}_3\text{HfN-Si}$  with surface Si-H can lead to further linkages to the surface. For example reactions (18) and (19) (Figure 5-18), with respective energies of 18.1 and -24.9 kcal/mol (B3LYP/BS1), and 19.4 and -21.7 kcal/mol (B3LYP/BS2) demonstrate that starting from surface products of the chemisorption reactions,  $\beta$ -hydride elimination and insertion reactions are highly endothermic similar to reactions (16) and (17).

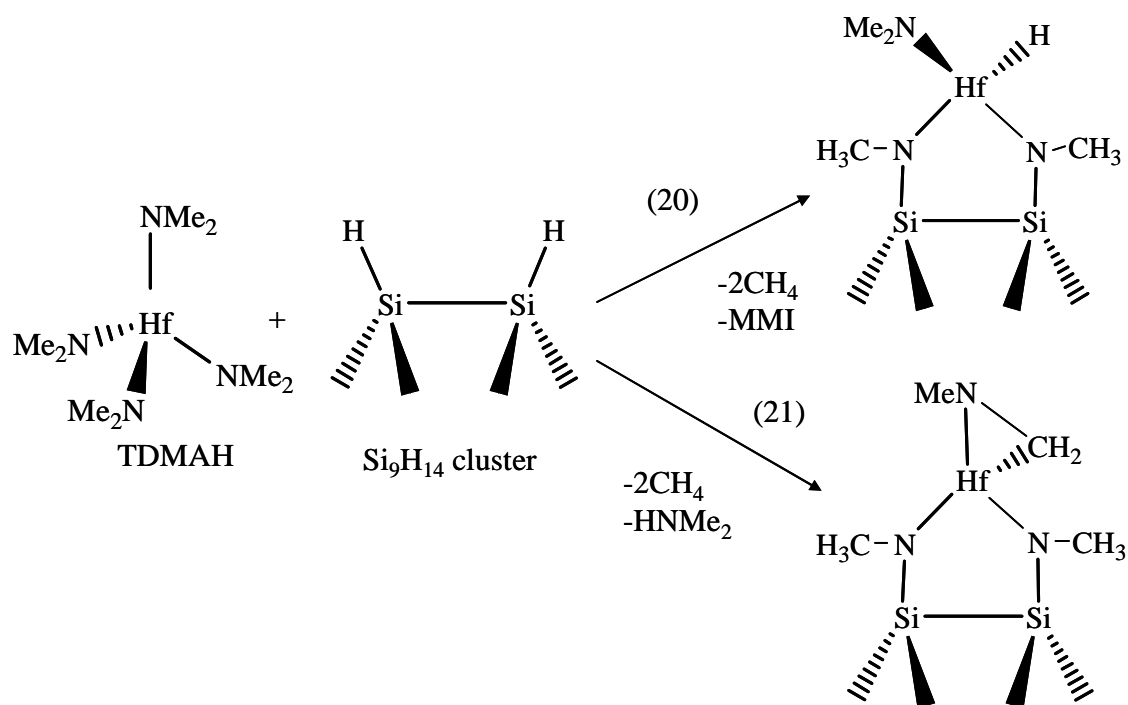


**Figure 5-19.** Reactions (20) and (21): proposed mechanisms to form Hf-H and TI-3 on Si surface.

In order to explain the formation of the Hf-H and TI-3 species observed in the adsorption IR experiments, reactions (20) and (21) (Figure 5-19) show two thermodynamically possible reactions for the generation of Hf-H and TI-3. TDMAH can be chemisorbed onto H-Si(100) through N-Si bonds in a bidentate fashion together with the two self elimination reactions. Reaction (20) is exothermic by -8.2 kcal/mol whereas reaction (21) is endothermic by 4.5 kcal/mol. However, these are complex global reactions and further studies will be needed to map out their details.

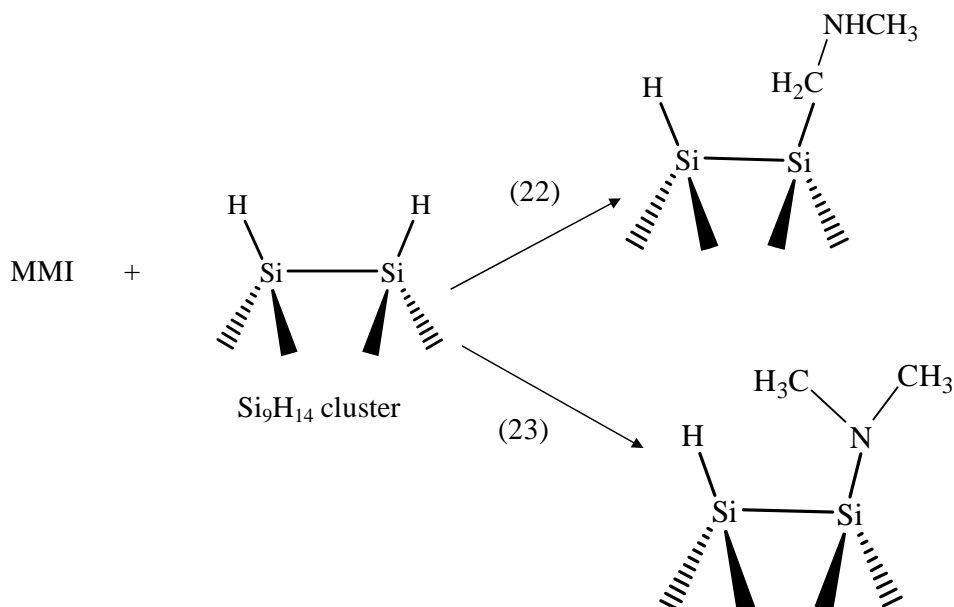


**Figure 5-20.** Reactions (22) and (23): silylation reactions from MMI to H-Si surface.

When species containing Hf-H are generated, as observed experimentally, the resulting Hf-H bond can undergo proton exchange reaction with  $\text{D}_2\text{O}$  as shown in reaction (9) (Figure 5-13) or by the H/OH exchange reaction leading to  $\text{H}_2$  formation with water shown as reaction (21). Reaction (10) was calculated to have a reaction barrier of 3.3 kcal/mol and is essentially thermoneutral as expected. This is consistent with the reaction observed after the  $\text{D}_2\text{O}$  or  $\text{H}_2\text{O}$  dose. The by-product MMI can also react with the surface. Reactions (22) and (23) (Figure 5-20) are two possible exothermic silylation reactions with the H-Si surface. Reaction (22) has a reaction barrier of 38.5 kcal/mol and is exothermic by -11.3 kcal/mol. Reaction (23) has a reaction barrier of 34.2 kcal/mol and is exothermic by -21.8 kcal/mol. These reactions can also account for C residue at the interface.

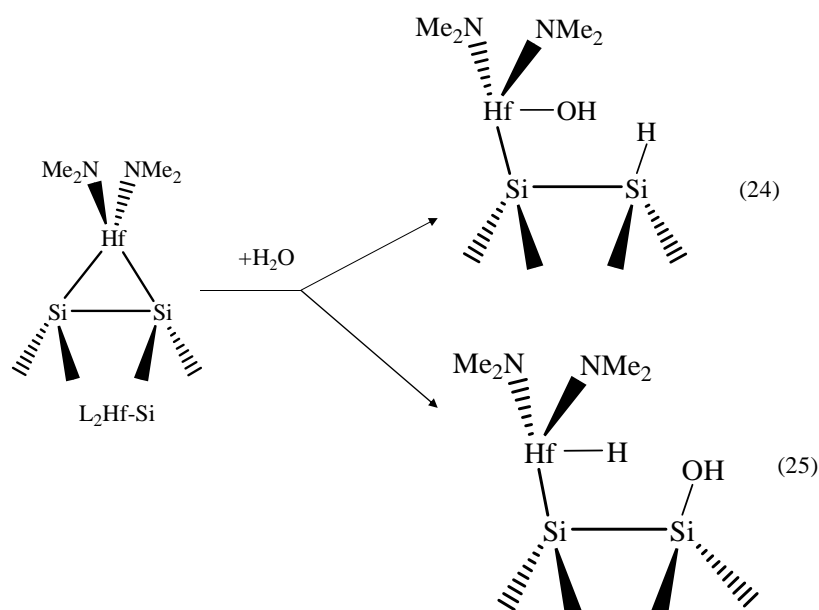


**Figure 5-21.** Reactions (24) and (25): hydroxylation of  $\text{L}_2\text{Hf-Si}$ .

After the first TDMAH cycle, the chemisorbed species are likely to be in the form of the products in reactions (13) to (15). With the second water cycle, the interfacial Hf-Si bonds could readily break in addition to the hydrolysis on the ligands. The reaction of the product  $\text{L}_2\text{Hf-Si}$  from reaction (13) with  $\text{H}_2\text{O}$  (reaction (24), Figure 5-21) was calculated to have a small barrier of 1.6 kcal/mol with respect to the adsorption state and to be highly exothermic by -57.0 kcal/mol to form Hf-O(H) and Si-H bonds, which may be one of the reasons that Si-H remains after many ALD cycles.<sup>59,60</sup>

Further reaction with another water molecule leads to a similar reaction. Thus, if water is the oxidant source, the Hf-Si bond will not remain during the water cycle. Reaction (25) shows another possibility for  $\text{L}_2\text{Hf-Si}$  to react with water, which generates a Hf-H bond and a OH group on Si. The reaction energy for (25) is exothermic by -31.0 kcal/mol. However, the chemisorbed species with C-Si or N-Si may occur instead due to stronger interfacial bonds.

## 5.5 Chapter Summary

As discussed above, a conceptually simple ALD process can involve quite complex

reactions, and different interfacial bonding formations should be taken into consideration. During the first cycle of ALD of TDMAH on to a H-Si surface at a temperature range of 25 °C to 250 °C, we observed that multilayer physisorption occurred with a large precursor dose. The proposed insertion reaction and  $\beta$ -hydride elimination were calculated to be thermodynamically not favorable in the gas phase. Instead TDMAH can form a bidentate chemisorbed species on the hydrogen terminated Si surface by forming two N-Si bonds through cleavage of N-CH<sub>3</sub> on the complex and H-Si on the surface. The TH and TI-3 species were identified by the  $\nu_{\text{Hf-H}}$  at 1650 cm<sup>-1</sup> and  $\nu_{(\text{Hf})\text{N-C}}$  at 1210 cm<sup>-1</sup> only on the hydrogen terminated Si surface as probed by ATR-IR. A growth of TDMAH after one water cycle generated more Hf-H species. A variety of by-products such as MMI and DMA can be produced as shown by the detection of  $\nu_{\text{C=N}}$  at 1670 cm<sup>-1</sup> in MMI and  $\delta_{\text{N-H}}$  at 735 cm<sup>-1</sup> in DMA in the gas phase by transmission IR with further support by Q-MS experiments. The MMI either undergo a silylation reaction leading to the incorporation of contaminants or desorb into the gas phase.

## Chapter 6 TEMAH Adsorption and Reaction on H-Si(100) Surface

### 6.1 Chapter Introduction

As discussed in the previous chapter, multilayer physisorption of TDMAH occurs with a large precursor dose. The proposed gas phase insertion and  $\beta$ -hydride elimination reactions were calculated to be thermodynamically not favorable in the gas phase. The TH and TI-3 species were detected on the surface and the by-products MMI and DMA were detected in the gas phase. In this chapter, a set of control experiments for tetrakis(diethylmethylamido) hafnium (TEMAH), another alkylamido hafnium precursor was studied. Its  $\beta$ -hydride elimination decomposition was confirmed. Hf-H species was observed on both the Ge and Si surfaces by ATR-FTIR. Methyl ethyleneimine (MEI) was detected in the transmission IR. DFT calculations were performed and the gas phase decomposition reactions are all exothermic but have lower energy barriers than TDMAH. The MEI by-product can lead to silylation on the Si surface. The similar experimental and computational results give support to the conclusions in the previous chapter.

### 6.2 Results and Discussion

#### 6.2.1 Experimental and Computational Spectra Comparison

A Liquid drop of both of TEMAH was placed on a Ge IRE to measure the intact molecule IR spectrum. The calculated TEMAH molecule vibrational and the liquid IR spectra are shown in Figure 6-1. Due to the anharmonicity effect, a scaling factor of 0.9398 was applied in the C-H stretch region for comparison to experiment. The scaling factor was calculated as the ratio of  $2777\text{ cm}^{-1}$  and the most intense C-H band in the calculated spectrum.

The assignment of the liquid drop peaks are given in Table 6-1 in comparison to the calculated vibrational modes. The lowered frequency C-H stretch peak at  $2777\text{ cm}^{-1}$  corresponds to the C-H symmetric stretches parallel and anti-parallel to the N lone pair on the methyl groups, and C-H symmetric and asymmetric stretches on the methylene groups. The characteristic peaks for intact TEMAH is  $1208$ ,  $977$  and  $874\text{ cm}^{-1}$ .

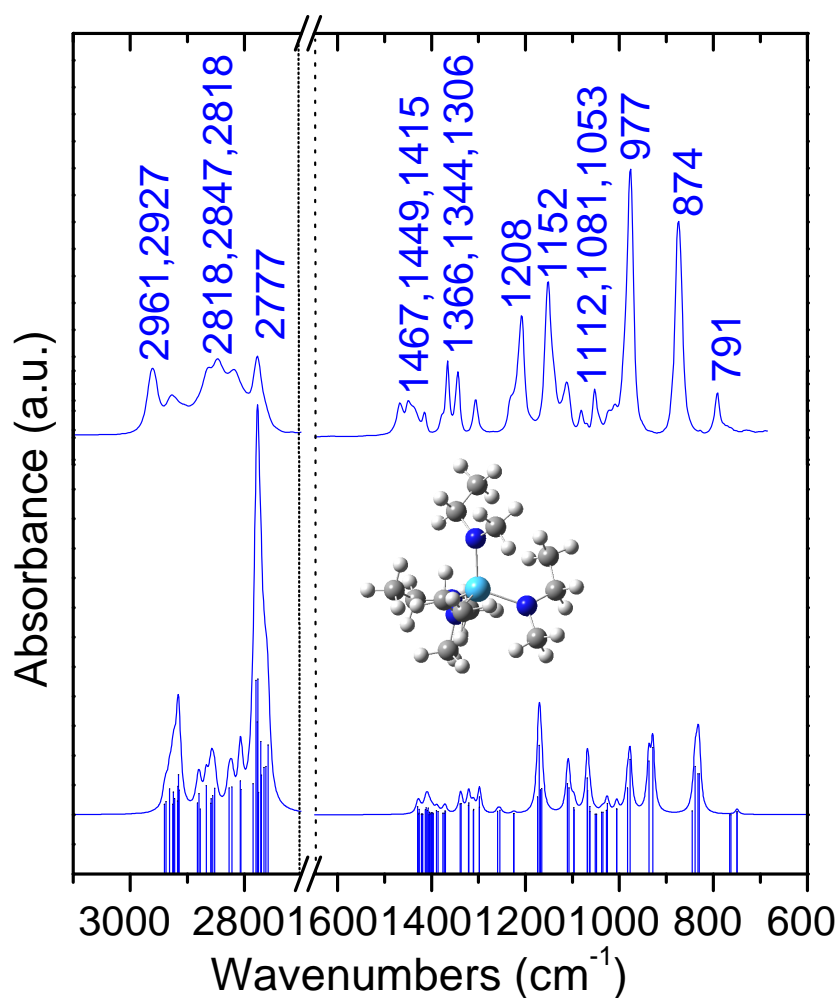


**Figure 6-1.** Top: Liquid drop of TEMAH on Ge IRE; Bottom: Calculated TEMAH gas vibrational spectrum at B3LYP/6-31+G(d,p), applied with a scaling factor of 0.9398 for the  $3100\text{-}2700\text{ cm}^{-1}$  region.

**Table 6-1.** TEMAH Liquid Drop IR Spectrum and B3LYP/BS1 Calculated Vibrational Assignments at 25 °C, 1 atm. without Scaling Factor (wavenumbers in  $\text{cm}^{-1}$ )

Liquid TEMAH, 25 °C ( $\text{cm}^{-1}$ )	Calculated TEMAH ( $\text{cm}^{-1}$ )	Assignments
2961	3101	$\nu_{\text{as}}(\text{CH}_3)\text{Et}$ , $\nu_{(\text{C-H})\text{Me}}$
2927	3066	$\nu_{\text{as}}(\text{CH}_2)\text{Et}$
2847	3040	$\nu_{\text{s}}(\text{CH}_3)\text{Et}$
2818	3007, 2967	$\nu_{\text{as}}(\text{CH}_3)\text{Me}$
2777	2963	$\nu_{\text{s}}(\text{CH}_3)\text{Me}$
	2946, 2935	$\nu_{\text{as}}(\text{CH}_2)\text{Et}$ , $\nu_{\text{s}}(\text{CH}_2)\text{Et}$
1467, 1449	1519, 1502	$\delta_{\text{as}}(\text{CH}_2)$
1415	1458	$\gamma(\text{CH}_2)$
1366	1425	$\delta_{\text{s}}(\text{CH}_3)\text{Et}$
1344	1396, 1381	$\tau(\text{CH}_2)$
1306	1336	$\omega(\text{CH}_2)$
1208	1224	$\rho(\text{CH}_3)\text{Me}$
1152	1176, 1137	$\nu_{\text{as}}(\text{C-N-C})\text{gauche}$
1112, 1081, 1053	1167, 1073, 1045	$\nu_{\text{s}}(\text{C-N-C})$
977	1000	$\rho(\text{CH}_3)\text{Et}$ , $\nu_{(\text{C-C})}$
874	885	$\nu_{\text{HF-N}}$ , $\nu_{\text{N-C}}$
790	799	$\rho(\text{CH}_2)\text{Et}$

### 6.2.2 Gas Phase FTIR Analysis

The gas phase infrared spectra of TEMAH during flow mode at room temperature and 1 min. after being introduced into the transmission cell are shown in Figure 6-2. As a comparison, spectra of TDMAH at the same 65 °C bubbler temperature were plotted together.

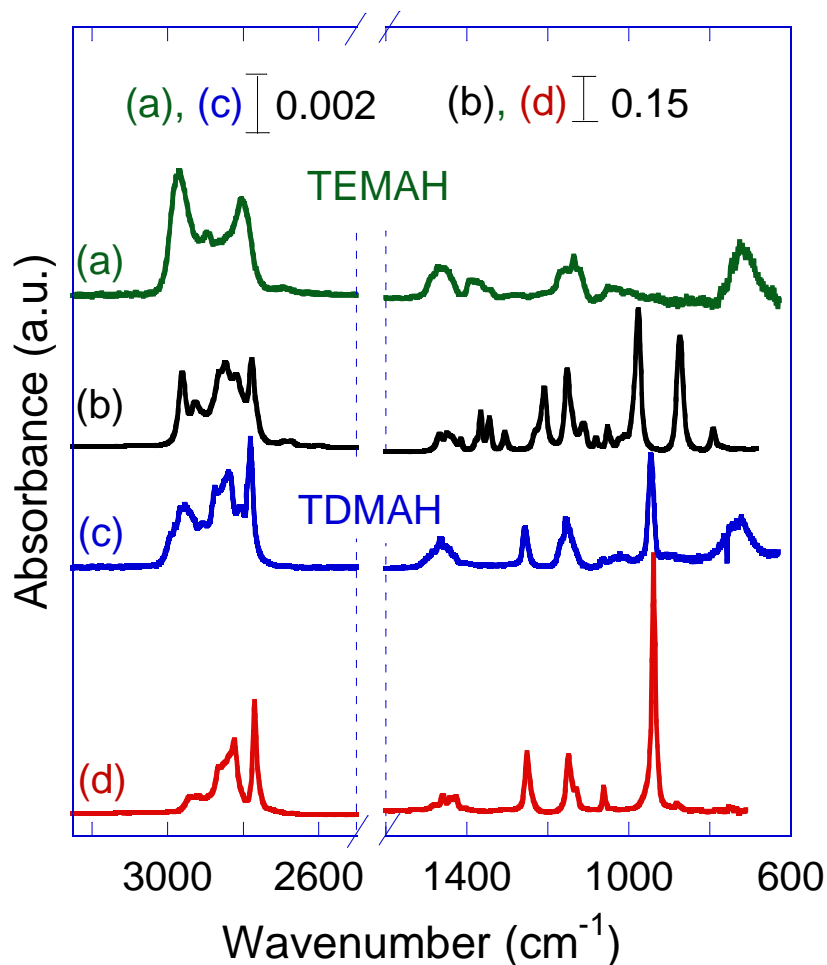


**Figure 6-2.** Spectra of (a) gas phase TEMAH, (b) liquid drop of TEMAH on Ge IRE, (c) gas phase TDMAH, (d) liquid drop of TDMAH on Ge IRE. All spectra were taken at room temperature. Gas phase spectra (a) and (c) were recorded at 1 min. after introducing sample into the gas cell.

It shows that most of the TEMAH introduced into the gas cell within 1 min. was already decomposed, and was likely to be ethylmethylamine ( $\text{CH}_3\text{C}_2\text{H}_5\text{NH}$ , EMA) in comparison to the calculated spectra. The  $\nu_{\text{N-H}}$  around  $3200\text{ cm}^{-1}$  is intrinsically too weak ( $0.3544\text{ km/mol}$  in the calculated EMA spectrum) to be detected. The readily observed decomposition behavior is consistent with what was seen at around  $70\text{ }^\circ\text{C}$  by Zaera's group.<sup>63</sup> In comparison, TDMAH indicates a more intact molecule by comparing the gas phase and liquid IR. Soulet et. al. studied the decomposition temperatures using thermal gravimetric analysis (TGA) and found that TEMAH has a decomposition temperature of  $120\text{ }^\circ\text{C}$  at 760 Torr and TDMAH partially decomposes at  $150\text{ }^\circ\text{C}$ .<sup>68</sup> The transport of TEMAH was reported

to be slow. It is possible that the light decomposed molecules such as EMA reached the cell faster than TEMAH. However, a longer flow time did not improve the detection of intact TEMAH as shown in Figure 6-3, indicating most of the molecules transported were not intact TEMAH. In addition, TEMAH has a much smaller vapor pressure than TDMAH at the same 65 °C bubbler temperature (0.3 Torr for TEMAH and 1.9 Torr for TDMAH). The lower pressure drives the TEMAH decomposition reaction forward to a greater degree than TDMAH.

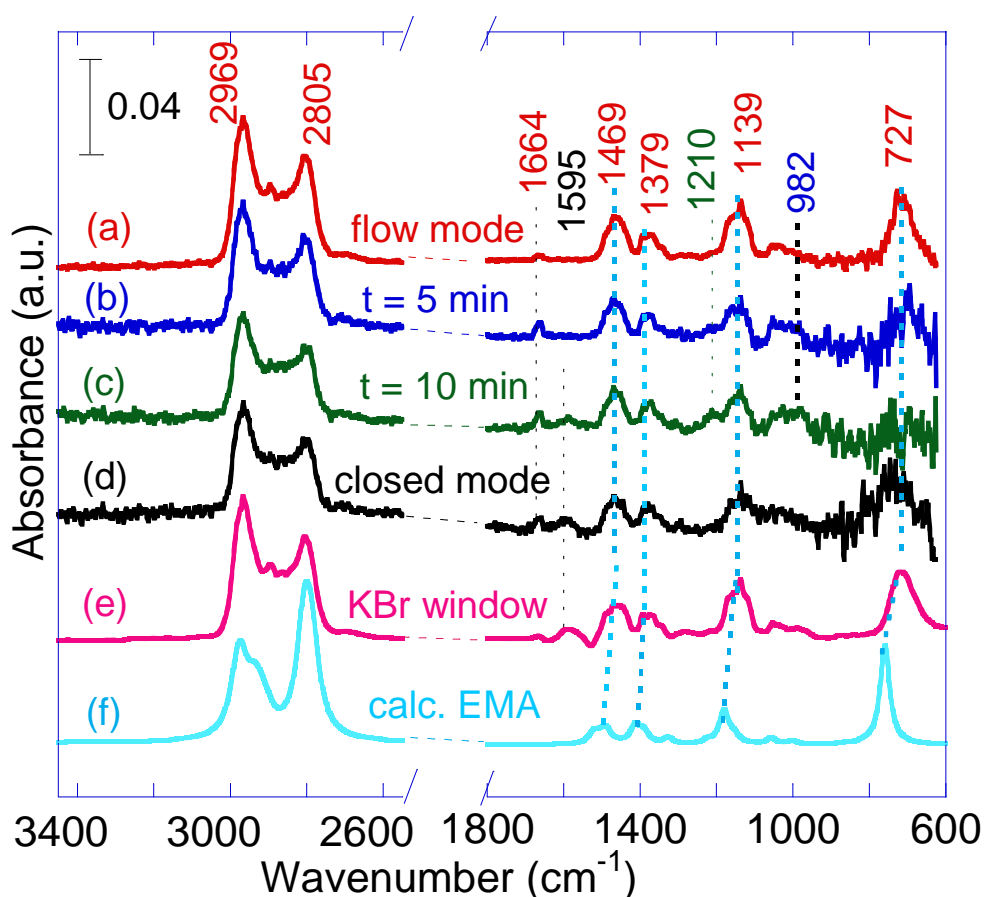


**Figure 6-3.** 100 °C gas phase infrared monitoring for introducing TDMAH into the gas cell. (a) - (d) were using Si windows, and (e) was using KBr windows. (a) - (c) were in the flow mode for 1, 5, and 10 min. (d) was under closed system mode for 5 min. (e) was in the flow mode for 1 min using KBr windows. (f) was the calculated vibrational spectrum for ethylmethylamine with scaling factor of 0.9557 and FWHM of 10 applied to the C-H stretching region between 3400 and 2600  $\text{cm}^{-1}$ .

A longer flow time introduced more TEMAH as shown in Figure 6-3 (a) - (c) and represented by the characteristic TEMAH peaks at 1210  $\text{cm}^{-1}$  and 982  $\text{cm}^{-1}$ . However the

majority species detected in the gas phase was still the decomposed product EMA. At 100 °C, another small peak located at 1664 cm<sup>-1</sup> with a full-width at half maximum of 20 cm<sup>-1</sup> appeared in the spectra. It is likely to be the  $\nu_{C=N}$  in methylethyleneimine<sup>155</sup> (CH<sub>3</sub>CH=NCH<sub>3</sub>, MEI) which can be produced from  $\beta$ -hydride elimination and is more stable than N-methylvinylamine.<sup>70,155</sup> A new peak at 1595 cm<sup>-1</sup> appeared after 10 min. It has been observed by other groups at the same time, ca. in the decomposition of tetrakis(dimethylamido) titanium<sup>67,156</sup> and transformation of N-methylvinylamine.<sup>155</sup> It has been assigned as the stretching of a N=C dative bond to Ti from an insertion reaction,<sup>67</sup> However, our calculation didn't show a thermodynamically plausible dissociation of MEI from the three-member metallacycle Ti species. An overtone<sup>155</sup> is not likely because of the prevalence and intensity of this peak and the absence of peak around 800 cm<sup>-1</sup>. Instead, we tentatively assign this peak as the  $\gamma_{N-H2}$ . The mechanism to generate this species needs further study.

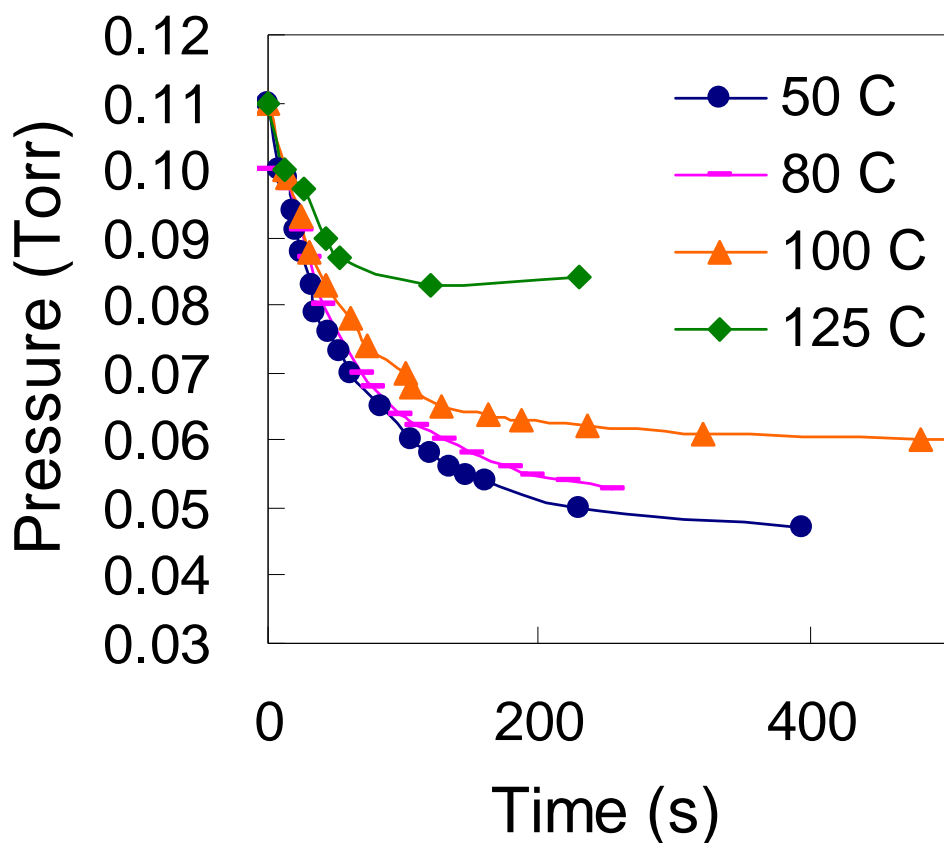


**Figure 6-4.** Pressure drop vs. time for TEMAH gas in a closed gas cell mode at different temperatures.

The integrated absorbance of  $\nu_{C-H}$  from  $3030-2730\text{ cm}^{-1}$  is linearly proportional to the pressure indicating a measurement of the gas phase rather than accumulation on windows. At  $100\text{ }^{\circ}\text{C}$  and after 10 min. of continual introduction of TEMAH into the gas cell, the valve after the gas cell was closed to fill the gas cell without pumping. When the pressure read 0.1 Torr, the valve before the gas cell was closed and the cell was kept in a closed system mode. Pressure change was recorded for different temperatures as shown in Figure 6-4. As a function of time, the pressure went down instead of going up indicating most of the molecules filling the gas cell already decomposed below  $125\text{ }^{\circ}\text{C}$ , and these decomposed by-products were able to adsorb onto the stainless steel walls or Si windows. Lower temperatures had bigger pressure drops because of a smaller desorption rate than at higher temperature. It is worthwhile to mention here that opposite pressure change trend due to decomposition was observed for TDMAH as shown in B-5, Appendix A.

### 6.2.3 Surface Adsorption/D<sub>2</sub>O/H<sub>2</sub>O FTIR Analysis

Low temperature adsorption of TEMAH was performed on H-Si(100) and Ge IRE's at 100 °C. On H-Si(100), no C-H stretch was observed until about 20 min. flow of the precursor, indicating either slow transportation of TEMAH to the surface or a growth barrier on the H-Si(100) surface. On Ge, the incubation time was about 10 min. Correlating the adsorption starting time with the slow gas phase transport of TEMAH, we may speculate that the incubation for adsorption resulted from slow TEMAH transport speed on both Ge and Si, while there was a higher adsorption barrier on H-Si(100), but not on Ge.

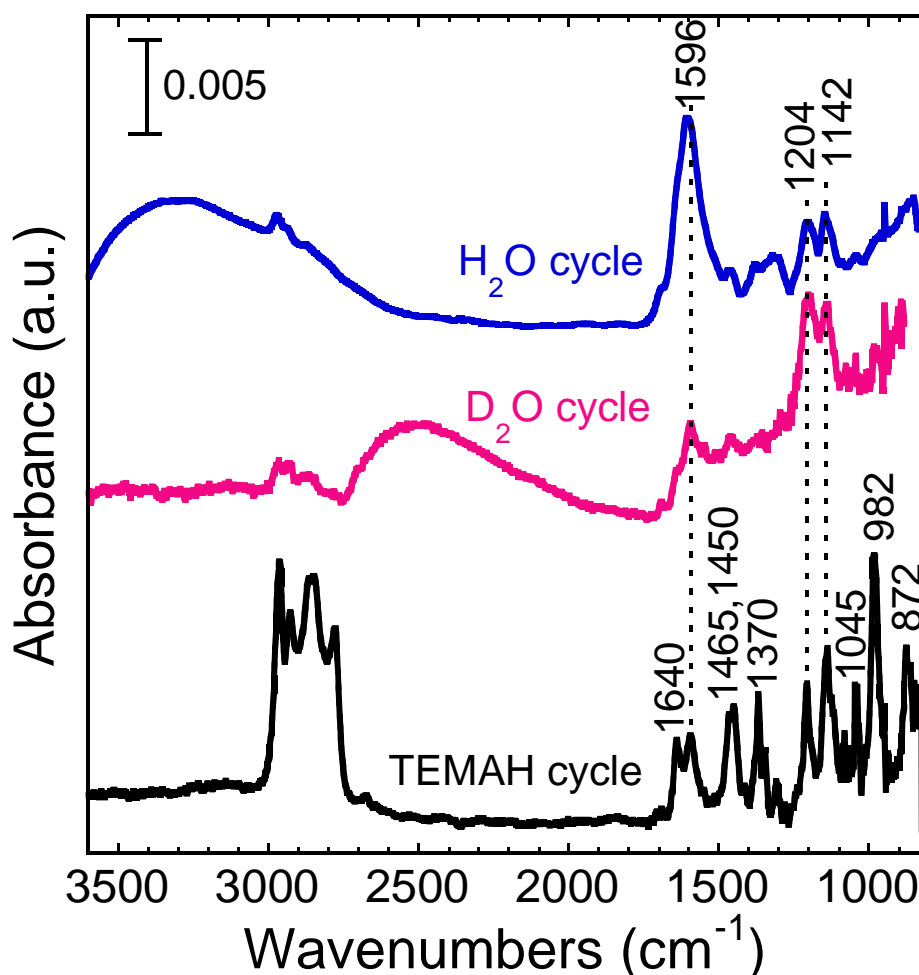


**Figure 6-5.** Infrared spectra of TEMAH/D<sub>2</sub>O or H<sub>2</sub>O on Ge. The bottom was a  $4.0 \times 10^8$  L dose of TEMAH. The top two were  $2.0 \times 10^8$  L H<sub>2</sub>O or D<sub>2</sub>O after the TEMAH cycle.

The adsorption spectra of TEMAH on H-Si(100) and Ge were similar except that the Si IRE has a narrower observable window down to 1200 cm<sup>-1</sup>, while the latter has a broader

window down to  $700\text{ cm}^{-1}$ . The adsorbed spectrum after a  $4\times 10^8$  L dose (20 min., 16<sup>th</sup> spectrum) of TEMAH on Ge is shown in Figure 6-5. The C-H stretch for adsorbed TEMAH was very similar to the liquid drop of TEMAH on Ge at room temperature, indicating a non-self-limiting behavior of TEMAH. This is in the condensation window in ALD where the precursor is can physisorb on itself forming a multilayer as discussed in Chapter 2. Thus, for an ALD process at room temperature using TEMAH, a very short dose length or a long purge time to remove the physisorbed layers would be required.

Two new peaks at  $1640\text{ cm}^{-1}$  and  $1596\text{ cm}^{-1}$  appeared on both surfaces after adsorption. To identify the  $1640\text{ cm}^{-1}$  peak, a  $2.0\times 10^8$  L dose of  $\text{D}_2\text{O}$  or  $\text{H}_2\text{O}$  control experiments after the TEMAH adsorption cycle were performed. After the  $\text{D}_2\text{O}/\text{H}_2\text{O}$  cycle, the peak at  $1640\text{ cm}^{-1}$  was abstracted while the  $1596\text{ cm}^{-1}$  persisted. One possibility is a  $\nu_{\text{N}=\text{C}}$  in the EMI. Another possibility more likely is  $\nu_{\text{Hf}-\text{H}}$  which results from  $\beta$ -hydride elimination as discussed in Chapter 5.

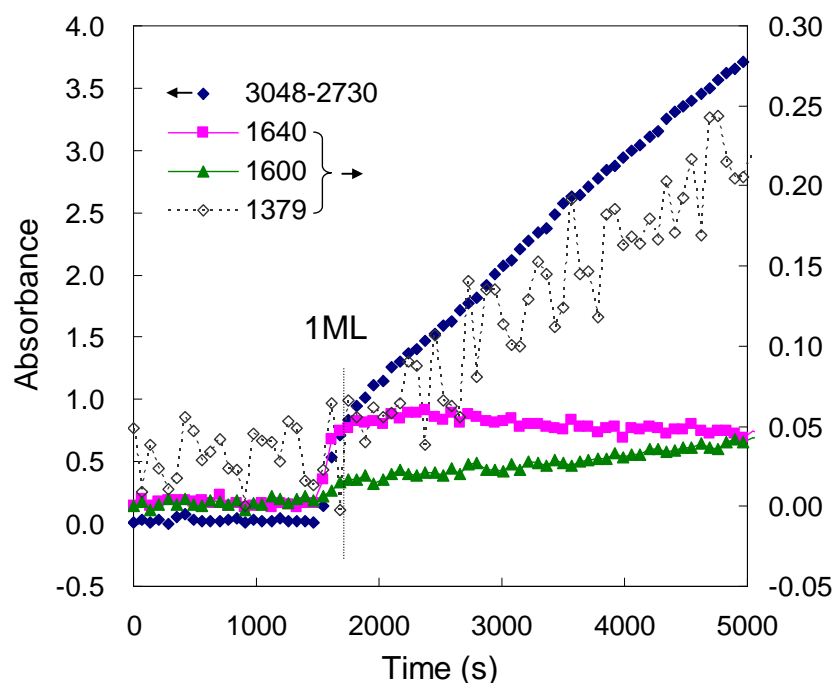


**Figure 6-6.** Integrated peak area as a function of exposure time of TEMAH to H-Si(100) for the C-H stretch,  $1640$ ,  $1600$  and  $1379\text{ cm}^{-1}$  peaks. The C-H stretch region  $3048\text{--}2730\text{ cm}^{-1}$  is to the left axis, and the other three to the right axis.

Figure 6-6 is the integrated peak area vs. time for TEMAH adsorption on H-Si(100) for the  $\nu_{C-H}$  region 3048-2730  $\text{cm}^{-1}$ , the Hf-H stretch 1676-1615  $\text{cm}^{-1}$ , the 1615-1569  $\text{cm}^{-1}$ , and the 1378-1333  $\text{cm}^{-1}$  region. Adsorption on Ge shows a similar trend. From the rate graph of these peaks, the integrated  $\nu_{C-H}$  region showed a continuous growth with time, indicating a non-self-limiting adsorption behavior for either the precursor itself or decomposed by-products which contain alkyl groups. The peaks at 1640  $\text{cm}^{-1}$  and 1600  $\text{cm}^{-1}$  rather than exhibiting continuous growth, almost saturated after 6 min. once the precursor started nucleation, indicating these two peaks are different species from TEMAH. 1 monolayer (ML) is defined on the saturation of the  $\nu_{Hf-H}$  at 1640  $\text{cm}^{-1}$ , which may be a submonolayer with coverage less than one but with all the available adsorption sites consumed. There was a slight decrease of about  $4 \times 10^{-6}$  a.u./sec. in the slope of 1640  $\text{cm}^{-1}$  and a small increase of about  $8 \times 10^{-6}$  a.u./sec. for the 1600  $\text{cm}^{-1}$ . On Ge, the decrease slope was  $9 \times 10^{-6}$  a.u./sec. for 1640  $\text{cm}^{-1}$  and  $1 \times 10^{-5}$  a.u./sec. increase for 1596  $\text{cm}^{-1}$ . There may be some transformation reaction between these two species that correlate the two peaks. Further study on a possible mechanism is needed to explain this phenomenon.

The intramolecular insertion reaction of TEMAH was expected similar to TDMAH. However, due to the presence of  $\rho_{(CH_3)Me}$  at 1208  $\text{cm}^{-1}$ , the cyclo stretch peak may be hidden under this peak and as a result other methods have to be used to probe the insertion reaction of TEMAH on Si or Ge surface. Figure 6-7 shows an *in vacuo* XPS spectrum of 30 min. TEMAH adsorption on H-Si(100) substrate at room temperature with bubbler at 65 °C in an ALD chamber which had a background pressure of  $10^{-7}$  Torr and experimental pressure about 0.03 Torr. All the peaks were shifted with respect to Si 2p at 100.4 eV (with silanol islands at subsurface). C 1s peak located at 281.7 eV indicates the formation of carbide, which was also observed by another group using tetrakis(diethylamido) titanium (TDEAT) at 281.9 eV.<sup>72</sup> This supports the insertion reaction on condition that the x-ray didn't activate the reaction.

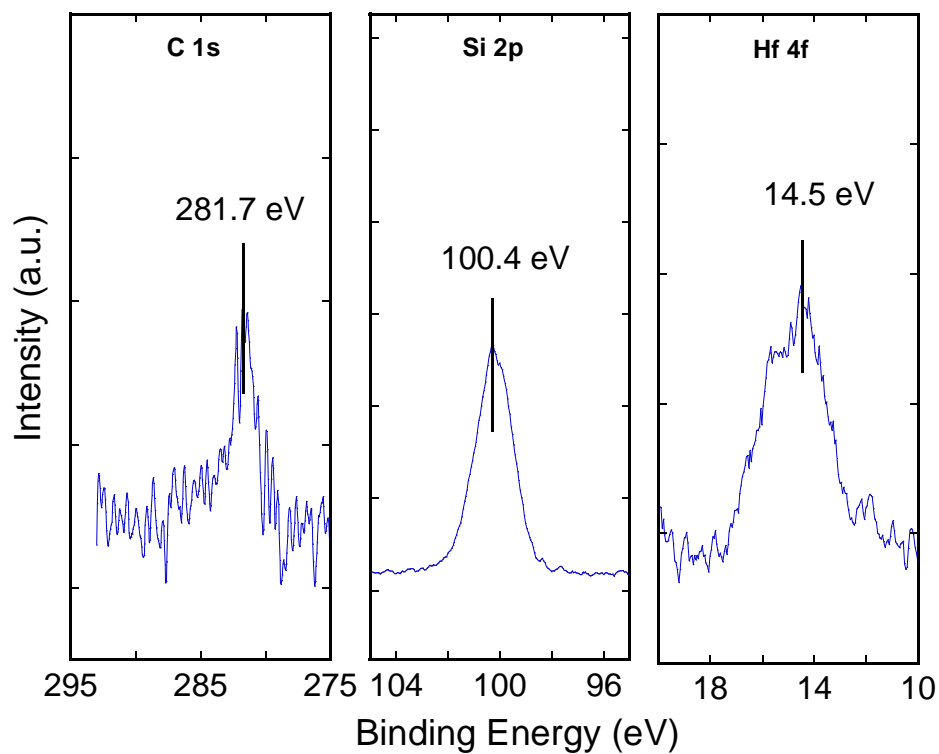


**Figure 6-7.** In vacuo XPS spectrum of TEMAH adsorption at room temperature on H-Si(100) wafer.

### 6.3 Calculations of Reaction Mechanisms

The proposed gas phase intra molecular insertion reaction (1) and  $\beta$ -hydride elimination (2) were calculated at the B3LYP/BS1//BS2 level of theory similar to the ones in Chapter 5. Two other similar reactions (3) and (4) with isomer products to reaction (1) and reaction (2) were also calculated.

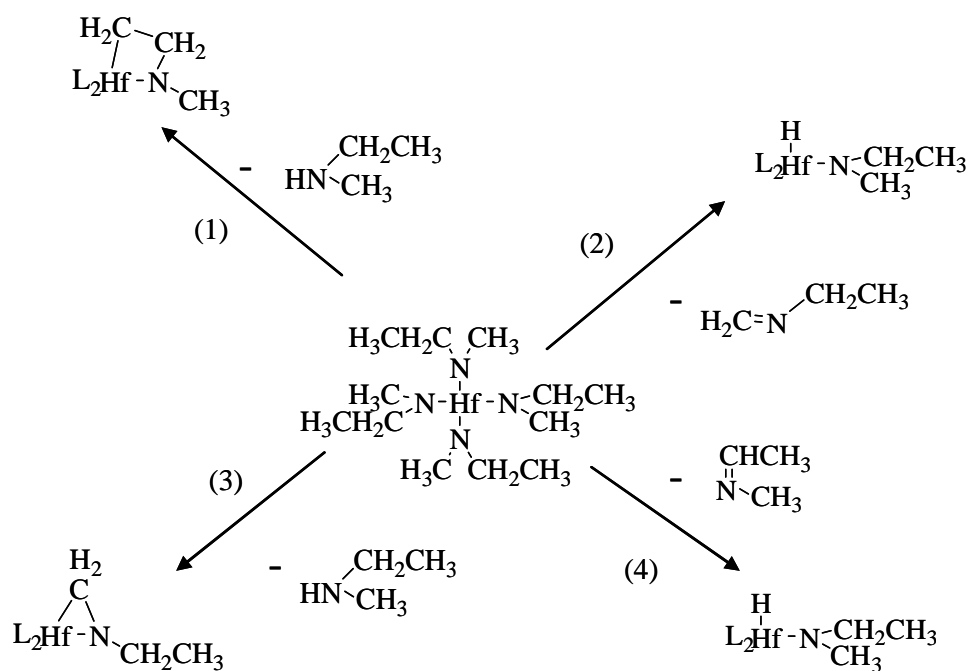


**Figure 6-8.** Decomposition of TEMAH: (1) Insertion reaction with H from 2-ethyl; (2)  $\beta$ -hydride elimination for EMI; (3) Insertion reaction with H from methyl; (4)  $\beta$ -hydride elimination for MEI.

The energies are given in Table 6-2, from which the transition state for the most thermodynamically favorable reaction (1) was calculated, as shown by Figure 6-8. The relatively low barrier of 37.9 kcal/mol and an exothermic reaction energy of 24.7 kcal/mol indicate the feasibility of this reaction to occur at elevated temperatures and low pressure. If there is no hydrolysis reaction on the wall to give rise to EMA as observed in the gas phase IR in Figure 6-2 and Figure 6-3, reaction (1) may account for the detection of EMA as a by-product. Reaction (2) gives an Hf-H species which has a calculated  $\nu_{\text{Hf-H}}$  at 1607  $\text{cm}^{-1}$ , and may explain the observed 1640  $\text{cm}^{-1}$  in Figure 6-5. These are characteristic peaks in the gas phase, which may be a few wavenumbers different on the surface.

**Table 6-2.** Energetic Data for Gas Reactions (kcal/mol) <sup>c</sup>

Reaction	TS		Product Complex		Products	
	BS1	BS2	BS1	BS2	BS1	BS2
(1)	37.9	37.0	24.7	25.3	34.3	35.4
(2)	45.7	44.3	28.2	28.3	35.5	36.3
(3)	—	—	28.0	28.9	50.0	51.4
(4)	—	—	—	—	37.6	36.3

<sup>c</sup> Energies in kcal/mol at B3LYP level for two basis sets: 6-31+G(d,p) (BS1) and aug-cc-pVDZ (BS2). E(Complex) is the reaction energy of adsorbed products complexes compared with separated reactants. E(Separated) is the reaction energy of separated products compared with separated reactant. All the listed reactions are endothermic reactions. “—” means the configuration was not calculated.

From the gas phase down to the surface, TEMAH reaction with H-Si(100) has been predicted by Chen et al. to form a Hf-Si bond to release one EMA molecule, which has a energy barrier of 17.8 kcal/mol for the first step.<sup>75</sup> Another pathway starting from the gas phase reaction (1) product the four-membered metalacycle species (denoted as TEI-4), may react with H-Si(100), as shown in Figure 6-9 for reaction (5), which has a similar reaction barrier to form a Hf-Si bond. It may also have another pathway forming different bonds at the interface as in scheme (6), which is also possible as seen by the energetic data listed in Table 6-3. Although the  $\nu_{\text{N-Si}}$  around 882  $\text{cm}^{-1}$  and  $\delta_{\text{CH}_2}$  around 838  $\text{cm}^{-1}$  as discussed in Chapter 5 should be observable on Ge, the  $\nu_{\text{Hf-N-C}}$  at 874  $\text{cm}^{-1}$  in TEMAH overlaps these two possible peaks, and the interfacial bonding cannot be identified.

**Table 6-3.** Energetic Data for Surface Reaction of Gas Phase Products (kcal/mol) <sup>c</sup>

Schemes	TS		E(Chemisorbed)	
	BS1	BS2	BS1	BS2
(5)	19.1	16.0	-24.4	-25.3
(6)	—	—	-7.8	-9.4
(7)	45.5	45.7	-19.4	-18.4
(8)	—	—	-9.3	-10.0

<sup>c</sup> Energies in kcal/mol at B3LYP level for two basis sets: 6-31+G(d,p) (BS1) and aug-cc-pVDZ (BS2). E(Complex) is the reaction energy of adsorbed products complexes compared with separated reactants. E(Separated) is the reaction energy of separated products compared with separated reactant. All the listed reactions are endothermic reactions.

“—“ means the configuration was not calculated.

On the other hand, the by-product such as EMI from the  $\beta$ -hydride elimination reaction (2) or the gas phase detected species that contains  $N=C^{157}$  may also chemisorb on the H-Si(100) surface such as reactions (7) and (8). The reactions are exothermic, however, they have a high reaction barrier of about 45.5 kcal/mol as shown in Figure 6-8, indicating only a small chance for them to react with the H-passivated surface.

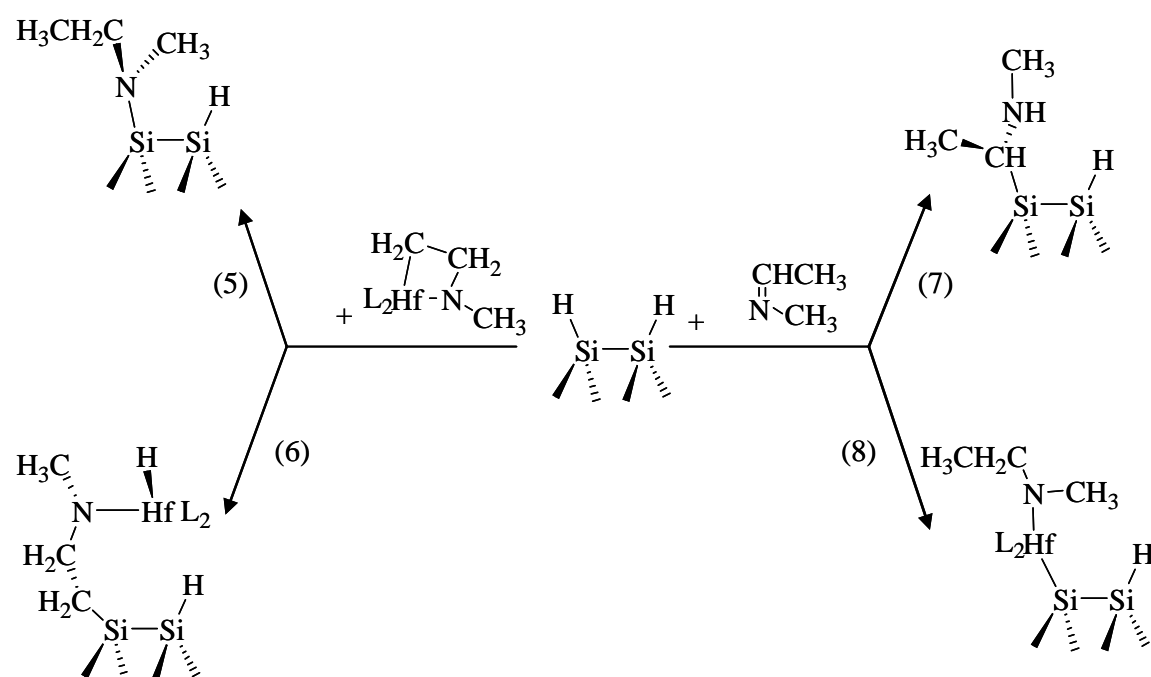


**Figure 6-9.** Reactions (6)-(8): TEMAH intermediates surface reaction on H-Si(100).

#### 6.4 Chapter Conclusions

*In situ* transmission and ATR infrared spectroscopy study of the gas phase chemistry of TEMAH and the surface adsorption at relatively low temperatures were reported. There was a longer incubation time due to slow TEMAH transport. The incubation period was longer on H-Si(100) than Ge due to a higher energy barrier. The proposed  $\beta$ -hydride elimination products MEI and species containing Hf-H were identified in the gas phase at  $1664\text{ cm}^{-1}$  and on the surface at  $1640\text{ cm}^{-1}$ . It is difficult to identify the insertion reaction product with the cyclo functional group and the interfacial bonding through Si-N or Si-C because of the band overlapping with TEMAH molecular vibrations. Energetics of possible

gas phase reactions were calculated at B3LYP/BS1 level of theory and was found to have high barrier but may be feasible at elevated temperatures. The gas phase reaction products lead to chemisorption onto a H-passivated Si surface and provide other paths to transfer gas phase molecules onto the solid phase. Compared with TDMAH, TEMAH has a lower vapor pressure and is easier to decompose in the gas phase. MEI is more stable than MMI, but is less likely to chemisorb onto H-Si(100) surface.

## Chapter 7

### HTB Adsorption and Reaction on Si (100) and Si(111) Surfaces

#### 7.1 Chapter Introduction

In this chapter, adsorption of hafnium (IV) tert-butoxide (HTB) onto a H-Si (100), a H-Si (111) and a Ge ATR crystal was studied for temperatures between 60 °C and 250 °C and under 0.4 Torr. Most of the content is taken from the journal article Ref. [105]. HTB is a liquid at room temperature and has a relatively high vapor pressure of 0.07 Torr at 25 °C and 1 Torr at 65 °C, thus it can be handled at low temperatures minimizing the heating of the precursor and the delivery lines. During adsorption of HTB onto the Si surfaces, another  $\beta$ -hydride elimination generates hydroxyl group and tert-butene. Bonding of HTB adsorbed on Ge at 100 °C was thought Ge-O-Hf. Spectra generated by density functional theory calculations of monodentate and bridging adsorbed precursors as well as a spectrum of an applied liquid drop of HtB precursor were used to identify the chemisorbed species. Two symmetric O-tBu umbrella modes from bridged Si-O-Hf(O-tBu)<sub>2</sub>-O-Si located at 1226 and 1016 cm<sup>-1</sup> present in the chemisorbed spectra show the precursor dissociates and is present as a bridging ligand on both Si(100) and Si(111) surfaces.

#### 7.2 Experiments

The experimental temperatures were between room temperature and 250 °C. The transparency cutoff is 1150 cm<sup>-1</sup> for Si and 700 cm<sup>-1</sup> for Ge. Si and Ge ATR crystal substrates were cleaned immediately before each experiment by sonication in trichloroethylene for 30 minutes to remove any organic residue, followed by a dip in a 50:10:1 H<sub>2</sub>O:ammonium fluoride:fluoric acid (PH=5) buffered oxide etch solution to remove the native oxide and to

terminate the Si or Ge with hydrogen. Finally, residual fluorine as measured by x-ray photoelectron spectroscopy was removed by sonication in deionized H<sub>2</sub>O for 30 minutes. The internally reflected IR beam has 20 reflections onto the surface of the adsorbing precursor which leads to sufficient sensitivity. The deposition area is 280 mm<sup>2</sup>, and the depth of penetration is calculated to be about 700 nm at 2000 cm<sup>-1</sup>, which well exceeds the thickness range of the adsorbing film.

The bubbler temperature was 50 °C. Immediately upon opening the precursor valve, a spectrum was collected from 4000 cm<sup>-1</sup> to 400 cm<sup>-1</sup> with 32 scans, and a 4 cm<sup>-1</sup> resolution which took approximately 75 seconds. Spectra were taken repeatedly at 1 min intervals until saturation was observed as an unchanging absorbance spectrum with time. All spectra were reprocessed using the background spectrum of a clean crystal at the adsorption temperature. After cooling down, the crystal was taken out and transferred into the XPS for composition analysis.

Electronic structure calculations were used to generate spectra for the free HTB molecule, as well as monodentate and bridged HTB molecules on the Si(100) surface. The hydrogen terminated Si(100)-2×1 surface was represented by a single dimer cluster model (Figure 7-1), which was generated by truncating a local structure of the surface and terminating the boundary Si atoms with hydrogens along the cleaved Si-Si directions.

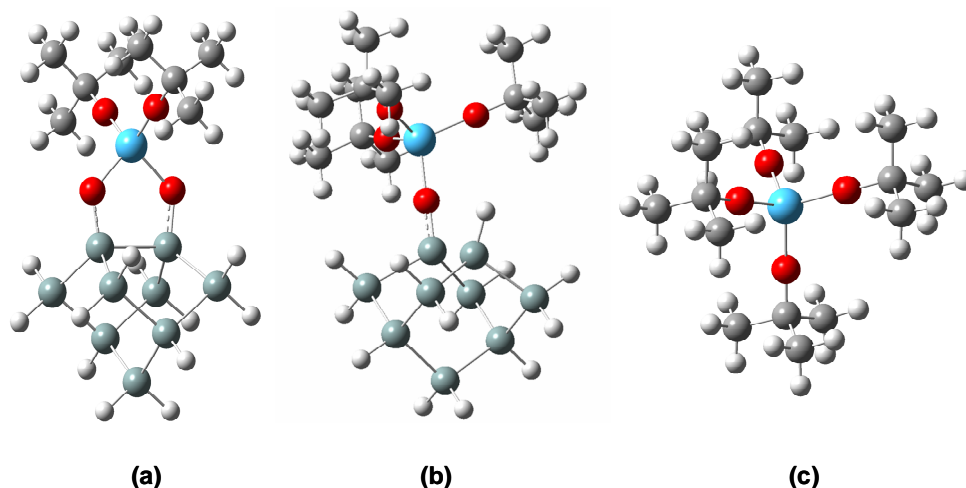


**Figure 7-1.** 3D Atomic groups for calculated spectra (a) bridged HTB on a H terminated Si cluster; (b) monodentate HTB on H terminated Si with one O-H termination; and (c) the HTB molecule.

Boundary constraints were applied to avoid over-relaxation of the cluster model. The Si atoms in the two bottom layers were fixed at their bulk positions, and the H atoms that represent third and lower layer bulk Si atoms were also fixed in tetrahedral directions with the Si-H distance of 1.48 Å. These calculations were performed using gradient-corrected density functional theory (DFT) with the Becke three-parameter exchange functional and the Lee-Yang-Parr correlation functional (B3LYP). The atoms in the top layers of the Si(100) substrate (which were fully relaxed) and the precursor molecules (except Hf) were treated with a polarized 6-31G(d,p) double zeta basis set, whereas the Hf was expanded using a Lanl2DZ relativistic effective core potential (RECP) basis set. The Lanl2DZ basis set consists of a LANL RECP and a double- $\zeta$  valence basis set. The remaining frozen atoms were approximated by the less expensive 6-31G basis set.

## 7.2 Results and Discussion

The liquid drop of HTB and its calculated spectrum is shown as Figure 7-2. Peaks at lower wavenumbers match well with the experimental data. In C-H stretch region, the  $\nu_{as}$ C-H and  $\nu_{sym}$ C-H are broadened in the experimental spectrum due to anharmonic stretch effects. Peak assignments are given in Table 7-1. The gas phase spectrum (refer to B-6, Appendix A)

was collected for 50 °C and 100 °C for HTB in a transmission IR gas cell in flow mode.

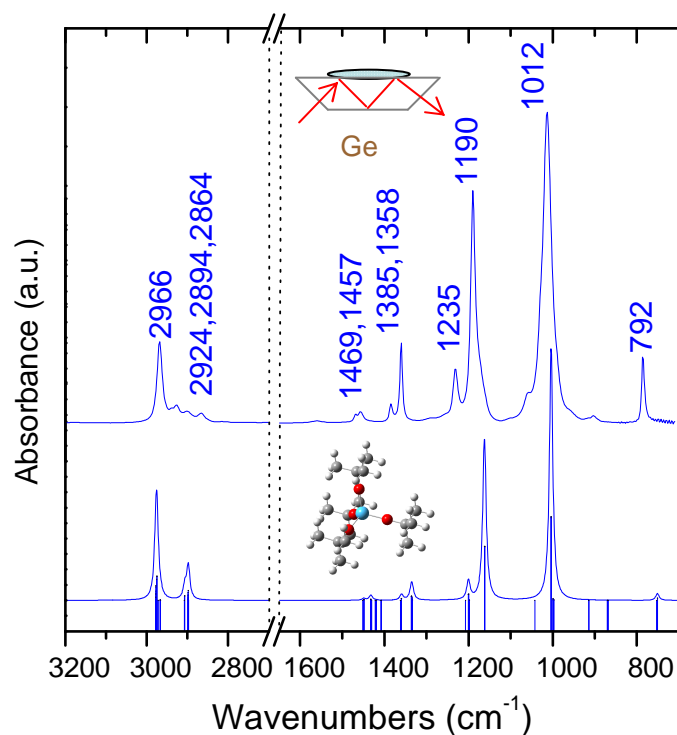


**Figure 7-2.** Top: liquid drop of HTB on Ge IRE. Bottom: calculated HTB vibrational spectrum, using scaling factor of 0.9545.

In an analogous reaction, Cameron and George proposed a two step mechanism for thermally activated deposition of  $\text{ZrO}_2$  from Zirconium (IV) tert-butoxide (ZtB) based on surface reflectance FTIR spectroscopy and mass spectroscopy measurements of the effluent,<sup>158</sup> as introduced in Chapter 2. During the initial step, gaseous ZtB chemically adsorbs onto a hydroxylated Si surface producing tert-butanol as a product. This step is followed by a decomposition of the adsorbed Zr tert-butoxy species through  $\beta$ -hydride elimination producing hydroxylated  $\text{ZrO}_2$  and isobutylene. Additional ZtB would be able to adsorb on the hydroxylated  $\text{ZrO}_2$ . Film growth was not observed for temperatures less than 200 °C, however, tert-butyl and hydroxyl species were observed with FTIR spectroscopy at these lower temperatures and their surface concentration decreased with increasing temperatures.

**Table 7-1.** HTB Related Infrared Spectra (Gas Phase not Shown, and HTB Liquid Drop on Ge) and DFT Calculated Vibrations Assignments (in  $\text{cm}^{-1}$ )

50 °C Gas Phase	Liquid drop of HTB on Ge	Calculated HTB molecule	Calculated isobutylene	Assignments
3640 (w)				$\nu\text{O-H}$
–		–	3227,3148	$\nu\text{C-H}_2$
2973(s,4bands)	2966, 2924, 2984, 2864	3119, 3035	3120 3070, 3025	$\nu\text{C-H}_3$
–		–	1719	$\nu\text{C=C}, \gamma\text{C-H}_2$
1471(m)	1469, 1457	1518, 1500	1510 1491, 1485	$\tau, \gamma\text{C-H}_3$
			1447	$\gamma\text{C-H}_2$
			1414	$\omega\text{C-C}, \delta\text{C-H}$
1387, 1365(s)	1385, 1358	1425, 1400		$\omega\text{C-H}_3$
			1296	$\rho\text{C-H}_2, \omega\text{C-H}, \delta_{i./p.}\text{C=C}$
1233, 1196(s)	1235, 1190	1256, 1218		$\nu\text{O-C}, \omega\text{C-C}, \delta\text{C-H}$
1024 (s)	1012	1054		$\nu_{\text{as}}\text{Hf-O-C}, \delta\text{C-H}$
920 (m)		–	916	$\omega(\text{C=C})\text{-H}_2$
785 (m)	792	786		$\nu_{\text{sym}}\text{Hf-O}$
745 (w)		–		$\delta\text{Hf}(\text{O-H})_3^*$
545, 477 (m)		526, 479		$\nu_{\text{as}}\text{Hf-O}$
			438	$\tau\text{C-H}_3$

$\nu$  – stretches (subscripts: as – asymmetric stretches, sym – symmetric stretches)  
 $\delta$  – bending (o./p.  $\delta$ :  $\omega$  – wagging,  $\tau$  -- twisting; i./p.  $\delta$ :  $\gamma$  – scissoring,  $\rho$  – rocking)  
o./p.-- out of plane, i./p.-- in plane  
Observed band intensity: w – weak, s – strong, m – medium strong

In our experiments, the starting surface is mostly dehydroxylated. Immediately after exposure to HTB, O-H is clearly observed as a relatively narrow peak at  $3678 \text{ cm}^{-1}$  which

decreases in intensity with increasing temperature until 185 °C after which the O-H stretching mode broadens and increases as shown in Figure 7-3.

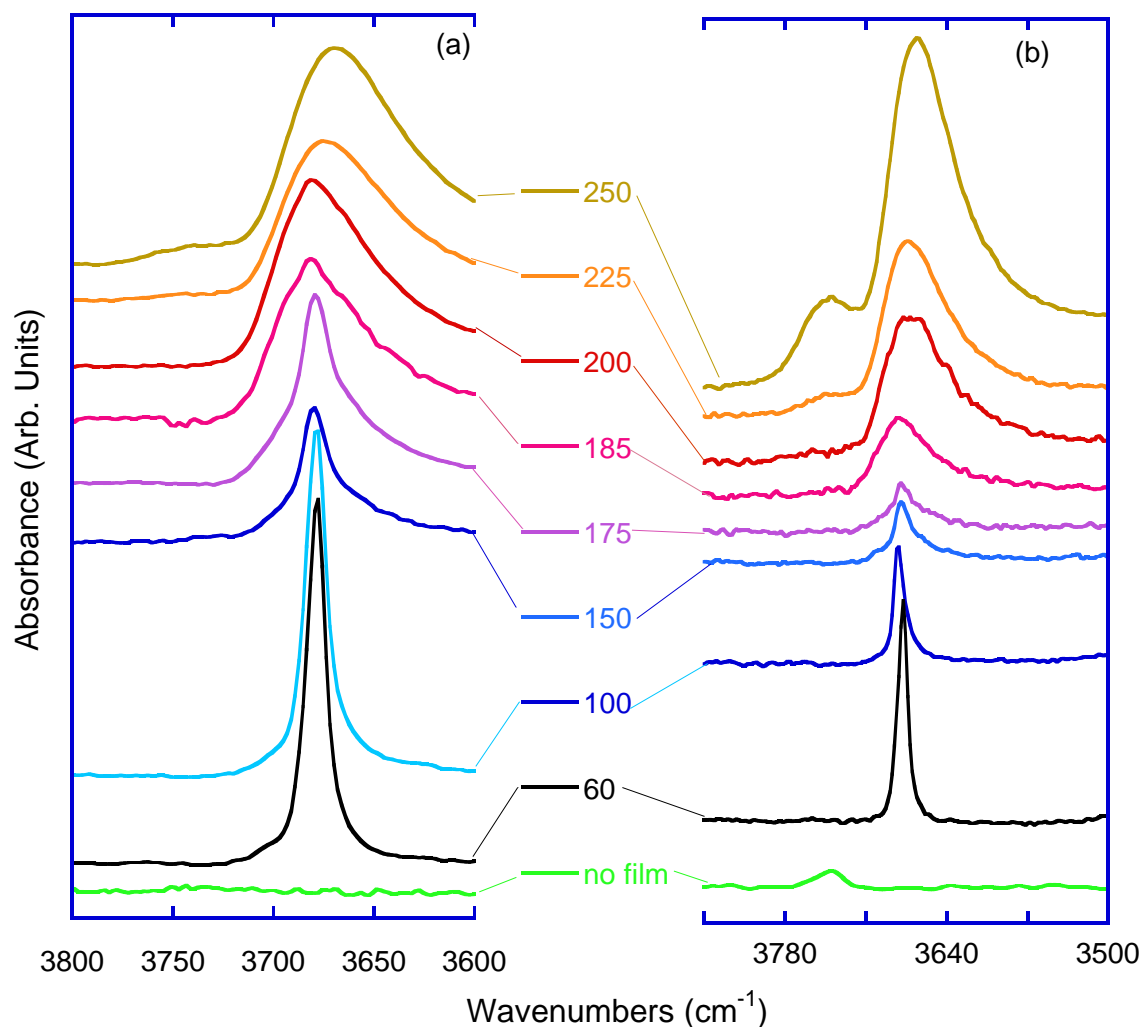


**Figure 7-3.** OH stretch region for different temperatures at saturation on (a) Si (100) and (b) Si (111). No film is spectrum of a clean ATR crystal after 24 hours in atmosphere at room temperature.

Si-O-H formed by atmospheric water dissociation on Si after 24 hours present on a clean Si(111) ATR crystal is apparent at  $3746\text{ cm}^{-1}$  consistent with literature values,<sup>159,160</sup> but is mostly absent on clean Si(100). To determine whether the  $3678\text{ cm}^{-1}$  peak can be assigned to tert-butanol as a possible product from the dissociative chemisorption of HTB, a liquid drop of tert-butanol was measured and the spectrum is shown in Figure 7-4.

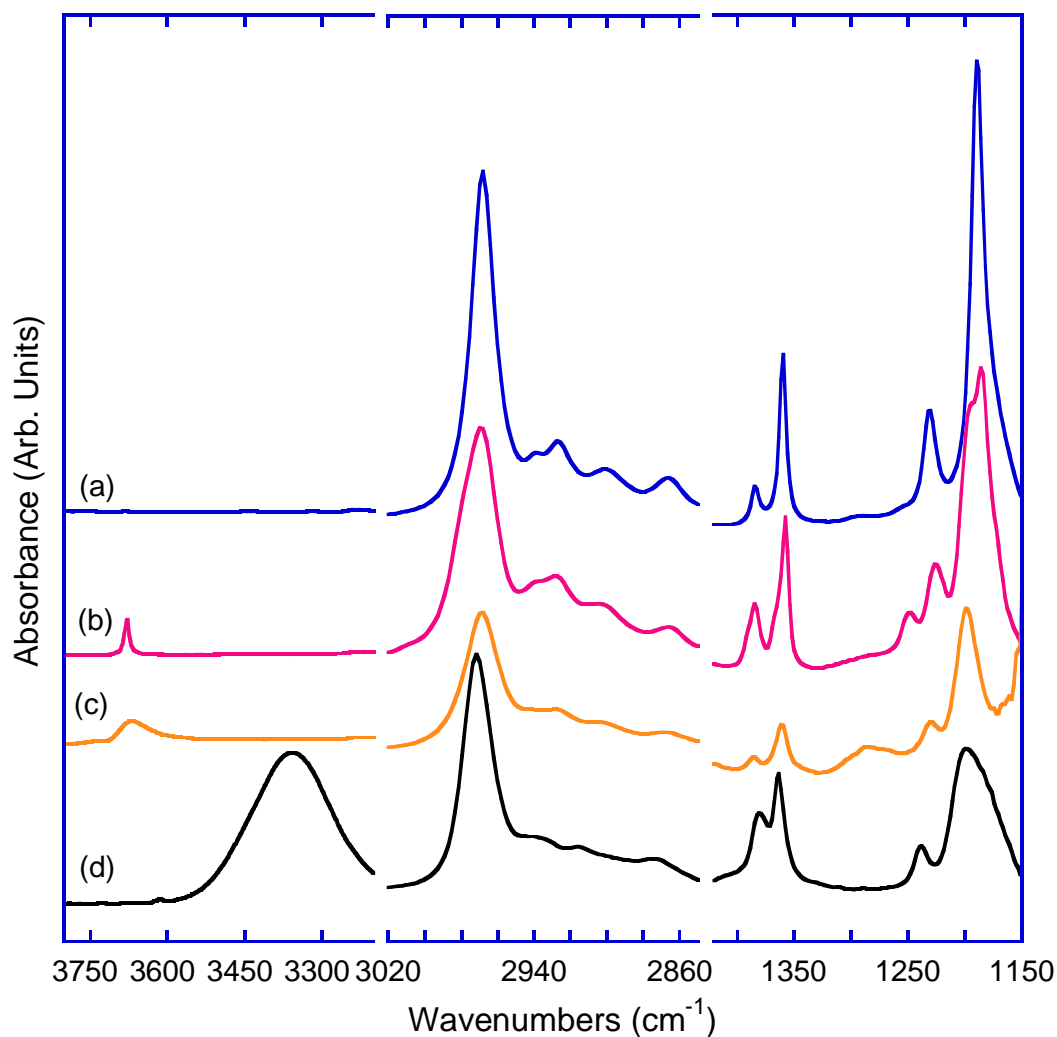


**Figure 7-4.** O-H, C-H and C-O stretching regions for (a) liquid HTB at 25 °C; (b) adsorbed HTB at 60 °C; (c) adsorbed HTB at 250 °C; and (d) liquid tert-butanol at 25 °C on Si (100).

The liquid tert-butanol O-H stretch appears at a lower wavenumber around 3350  $\text{cm}^{-1}$  due to H-bonding and even in the gas phase it locates at 3650  $\text{cm}^{-1}$ , so the O-H stretch appearing at low temperatures is assigned to hydroxyl groups on hafnium in the adsorbed layer and not tert-butanol. At temperatures above 185 °C, film growth is observed by a color change on the crystal and the broad O-H peak becomes characteristic of adsorbed moisture.<sup>159</sup> The increasing absorbance and peak broadening due to H-bonding effect seen in Figure 7-3 is attributed to an increasingly thick film formed as the precursor decomposes at these higher temperatures. For temperatures below 185 °C, the loss of hydroxyl groups with increasing temperatures indicates a shift in the equilibrium concentration of species in the condensed

layer. The hydrolysis of titanium tetra-butoxide in solution with tert-butanol between 20-80 °C for example, was shown to be very fast and reversible followed by a much slower condensation reaction between OH groups or O-H and O-R groups.<sup>161</sup> Any tert-butanol formed should quickly desorb at these temperatures and pressure.

To assist in the identification of reaction intermediates, simulated spectra were generated using density functional theory (DFT). HTB chemisorbed on Si (100) by a bridge between two adjacent Si atoms, a monodentate attached molecule, as well as a free HTB molecule were all considered in the atomic configurations shown in Figure 7-1. These simulated spectra of possible adsorbates on Si (100) are compared to experimentally obtained spectra of adsorbed HTB and liquid HTB on Ge in Figure 7-5.

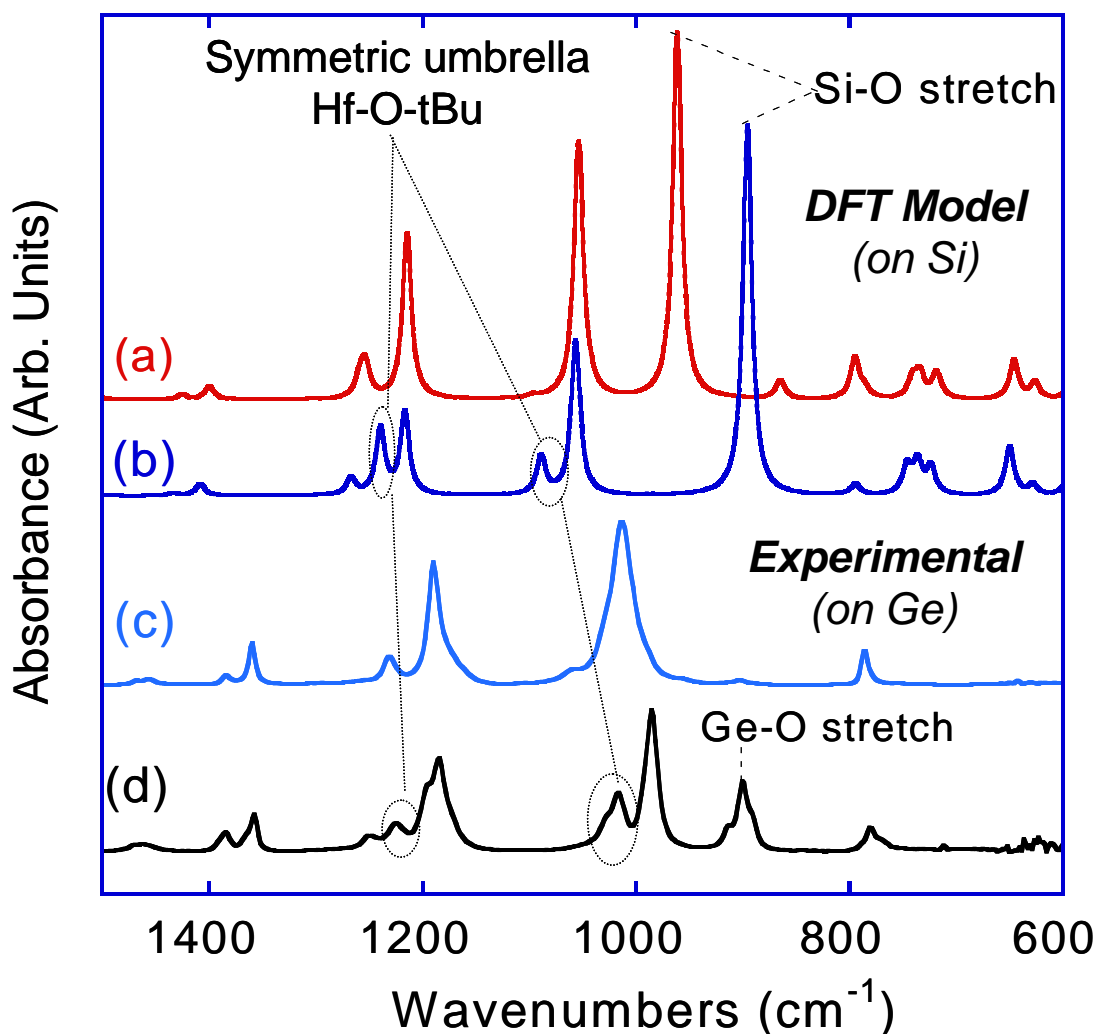


**Figure 7-5.** HTB spectra given by (a) monodentate model; (b) bridged model; (c) liquid HTB

on Ge; (d) adsorbed HTB on Ge. (a), (b) are at 0°C, (c) is at 25°C, and (d) is at 100°C.

Ge data are shown rather than data from Si experiments in order to see peaks below 1050  $\text{cm}^{-1}$ . Also, scaling factors have been excluded from the calculated spectra so that peak positions are considerably shifted from the corresponding experimental values. Two peaks at 1226  $\text{cm}^{-1}$  and at 1016  $\text{cm}^{-1}$  were attributable to bridging Si-O-Hf(O-tBu)<sub>2</sub>-O-Si symmetric umbrella modes as stated in published work. However, further consideration and model development shows a similar “triplet” around 1000  $\text{cm}^{-1}$  can be found in various models including: a) decomposed free HTB molecule with only two ligands (for example, (HO)<sub>2</sub>Hf(O[C(CH<sub>3</sub>)<sub>3</sub>]<sub>2</sub>); b) the bidentate model as in this discussion; c) monodentate HTB through Hf-O-Si with two ligands left and the third one decomposed into a hydroxyl group; and d) monodentate HTB chemisorbed on the surface through Hf-Si bonds; e) bidentate HTB chemisorbed on the surface through Hf-Si. The spectra and their models can be found in Figure B-7, Appendix A. This phenomena is very interesting and seems to be associated with the deconvoluted peaks at 2983  $\text{cm}^{-1}$  and 2967  $\text{cm}^{-1}$ . Further studies would be necessary for explanation. Among all these models, b) and c) make more sense than the others. Model a) is for a gas, while the detection was on the surface; model d) and e) are less likely as the Hf-O bond is strong and Hf-Si would be difficult to form in the presence of O. Besides, the presence of Ge-O peak suggests the interfacial bonding Ge-O-Hf. b) and c) are more likely. In both of the models, the 1226  $\text{cm}^{-1}$  peak results from carbon displacement in the O-tBu moiety, while the 1016  $\text{cm}^{-1}$  corresponds to oxygen displacement relative to Hf-O and the tert-butyl group. Although the 1016  $\text{cm}^{-1}$  peak can not be observed on Si due to the transparency cut-off, the 1226  $\text{cm}^{-1}$  peak is present as seen in Figure 7-4(b). Therefore, the 1226  $\text{cm}^{-1}$  peak is more likely a sum of the bridged arrangement b) and the monodentate with one hydroxyl group c) on Ge, as well as the (100) and (111) surfaces of Si.

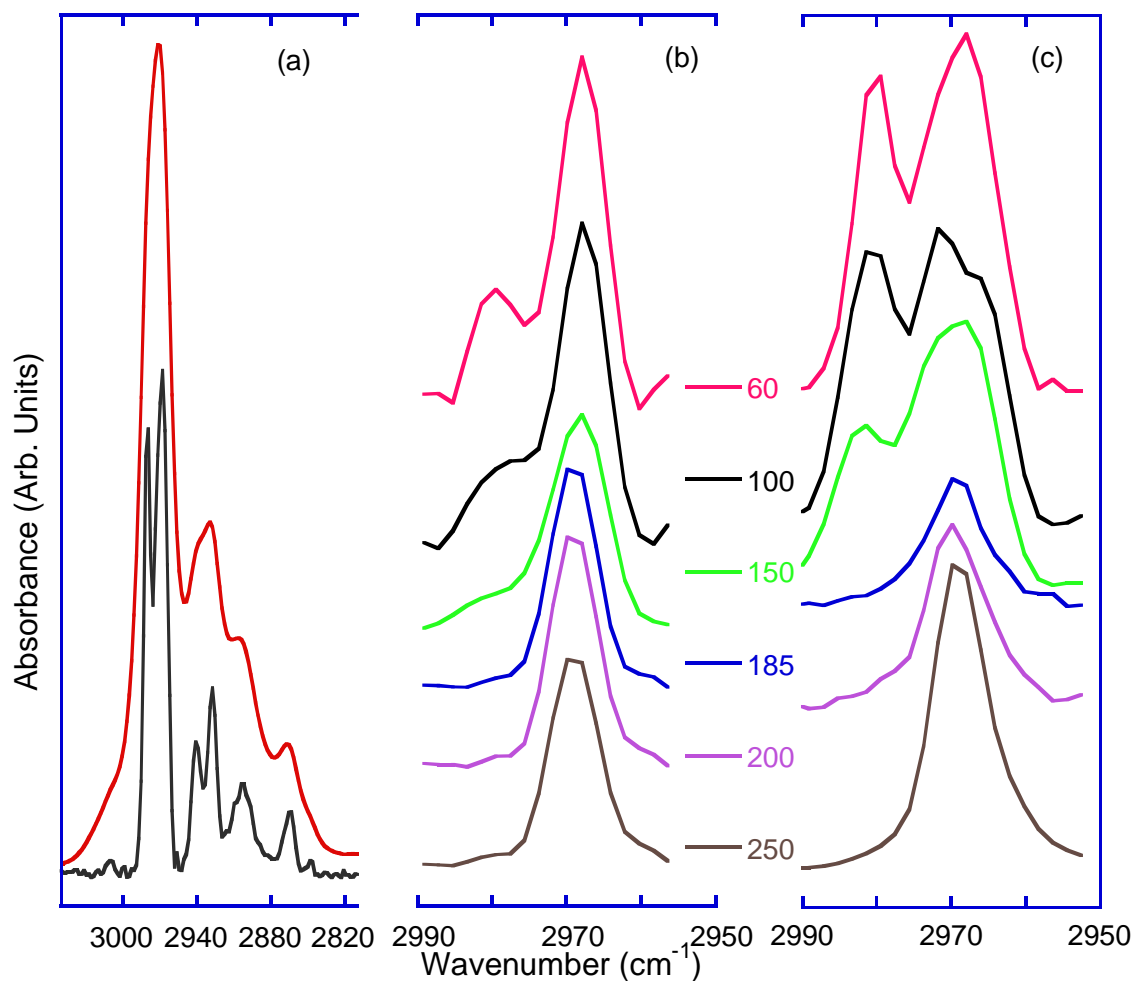


**Figure 7-6.** (a) C-H stretch of adsorbed HTB on Si (111) at 60°C, showing Fourier self-deconvoluted peaks. (b) and (c): Deconvoluted C-H stretching at various temperatures on Si (100) and Si (111) respectively.

Other peak assignments starting with the far IR are  $\nu\text{OH}$  (3720-3620  $\text{cm}^{-1}$ ),  $\nu\text{CH}$  (3120-2760  $\text{cm}^{-1}$ ),  $\delta\text{CH}$  (1490-1440  $\text{cm}^{-1}$ ), umbrella C-(CH<sub>3</sub>)<sub>3</sub> (1400-1340 $\text{cm}^{-1}$ ), O-tBu out of plane deformation about the O-C bond (1250  $\text{cm}^{-1}$ ), asymmetric umbrella mode for O-C(CH<sub>3</sub>)<sub>3</sub> with carbon displacement (1190  $\text{cm}^{-1}$ ), asymmetric umbrella Hf-O-C(CH<sub>3</sub>)<sub>3</sub> with oxygen displacement (1015-980  $\text{cm}^{-1}$ ), and  $\nu\text{Ge-O}$  (900  $\text{cm}^{-1}$ ). Si-H stretching at 2110  $\text{cm}^{-1}$  was observed for a freshly cleaned Si ATR element when reprocessed with a Si ATR element with a native oxide, however, it is completely absent in the first spectrum taken after HTB exposure for all substrate temperatures.

A closer view of the C-H stretching region between 3050 and 2800  $\text{cm}^{-1}$  is shown in

Figure 7-6 (a). Deconvolution of the  $2969\text{ cm}^{-1}$  peak shows there are at least two species ( $2967$  and  $2983\text{ cm}^{-1}$ ) present which have different temperature and substrate orientation dependencies as illustrated in Figure 6 (b) and (c) for Si (100) and Si (111) respectively. DFT calculated spectra predicts a small red shift ( $4\text{ cm}^{-1}$ ) of the tert butyl peaks between the monodentate or free HTB molecule and the bridged ligands and this possibility fits well with the expected higher temperature dependence of the more strongly bonded bridged arrangement. FTIR spectra of the liquid precursor do not exhibit this high frequency shoulder. Yet another possibility may be a shift occurring due to C-H interaction with Hf-OH groups formed by hydrolysis with trace amounts of water, however, the  $2983\text{ cm}^{-1}$  species is about twice as prevalent on the (111) than the (100) orientation while the opposite is true for O-H. If the split is due to a physisorbed versus a chemisorbed species, more insight may be gained by observing the aforementioned symmetric O-tBu modes at  $1226\text{ cm}^{-1}$ .

The temperature dependence of the symmetric umbrella mode of the symmetric O-tBu groups located at  $1226\text{ cm}^{-1}$  for Si(100) and Si(111) is shown in Figure 7-7(a) and (b). Starting from the right in this figure, the largest peak is from coupling between O-C stretching and C-CH<sub>3</sub> bending (umbrella) in an antisymmetric fashion for the tert-butoxide ligands. The next peak ( $1226\text{ cm}^{-1}$ ) is the symmetric umbrella mode for a bridged molecule on silicon and the smallest of this triplet group is the out of plane O-C bending. The monodentate arrangement also has a predicted symmetric umbrella mode, but it is very small and is located nearly at the same wavenumber as the out of plane O-C bend. The  $1226\text{ cm}^{-1}$  peak doesn't disappear with increasing temperature as does the high wavenumber shoulder of the C-H stretch at  $2983\text{ cm}^{-1}$  however, it does shift towards higher energy around  $150\text{ }^{\circ}\text{C}$  for Si(100) and  $175^{\circ}\text{C}$  for Si(111).

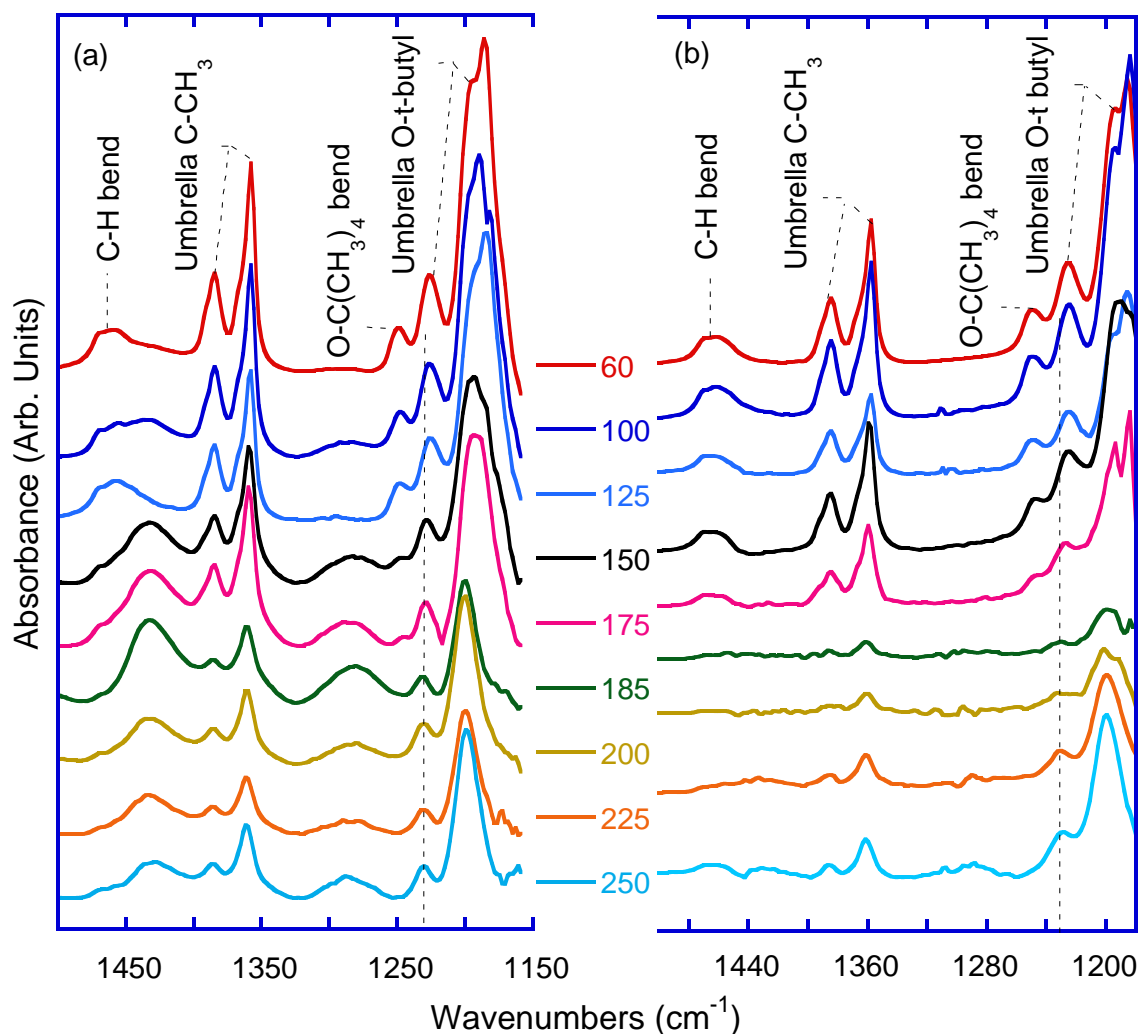
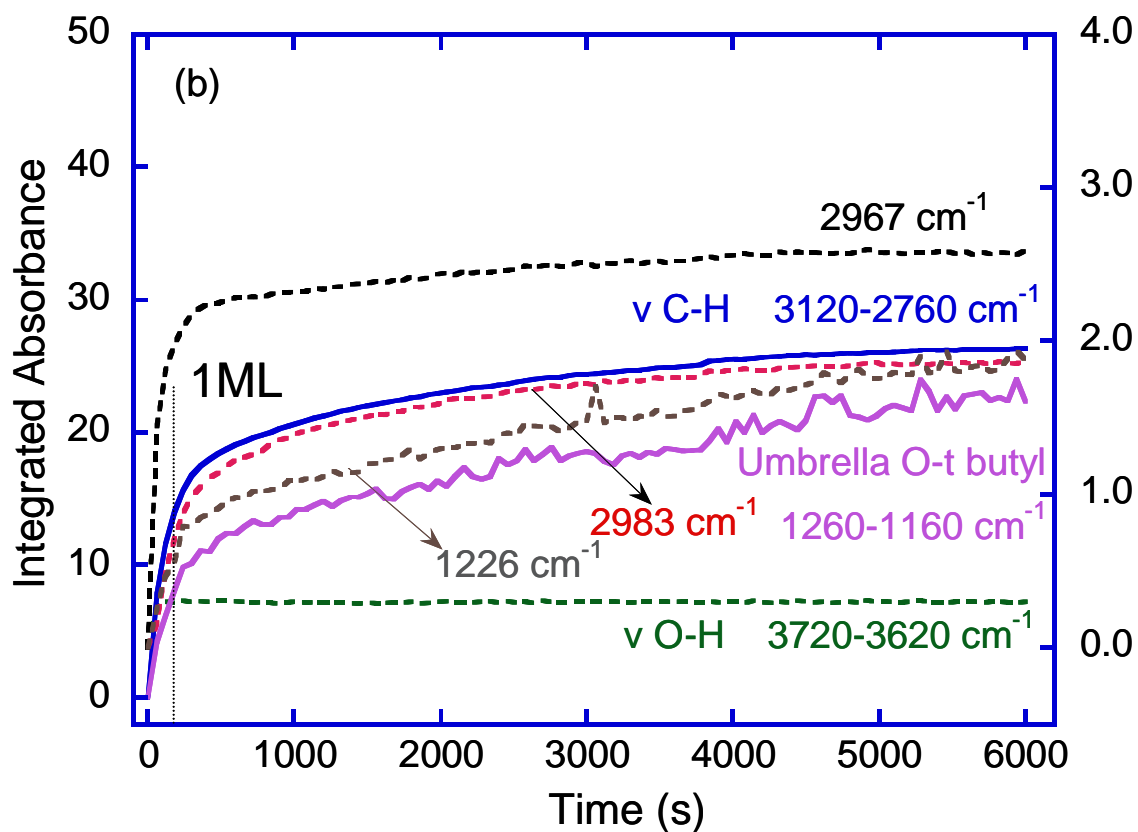
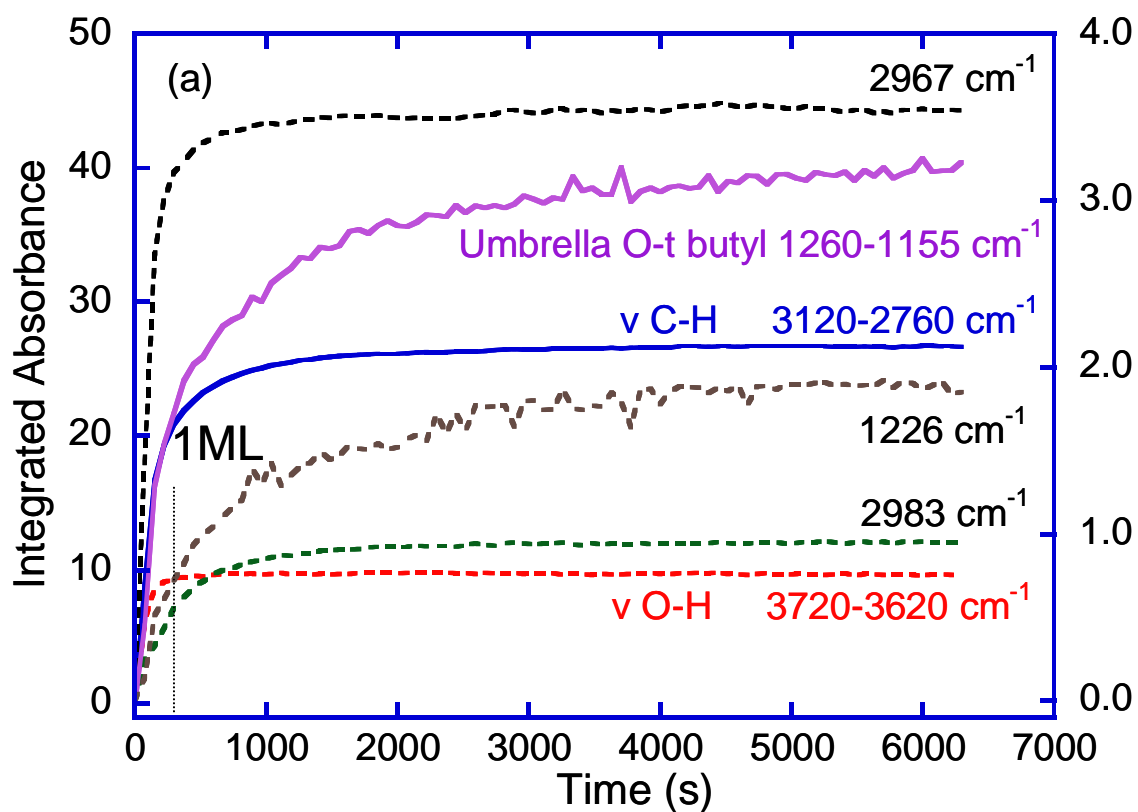


**Figure 7-7.** Spectra of adsorbed HTB at saturation for different substrate temperatures on (a) Si(100) and (b) Si(111).

Interestingly,  $\nu_{\text{O-H}}$  reaches a minimum at 150 °C for Si (100) and 175 °C for Si (111). In addition, the larger asymmetric umbrella mode begins to shift to higher wave numbers at these temperatures. DFT calculations predict a nearly identical monodentate and free molecule peak position for this asymmetric umbrella mode, while the bidentate arrangement is predicted to be red shifted by 6 cm<sup>-1</sup>. Figure 7-7 also illustrates an interesting difference between Si(111) and Si(100) which is the appearance of two relatively broad peaks around 1435 cm<sup>-1</sup> and 1280 cm<sup>-1</sup> at temperatures above 150°C that are not predicted by any of the simulations. This signature is likely from asymmetric and symmetric stretching of O-C-O units from a carbonate (CO<sub>3</sub>) or a carboxylate (COO-R) moiety.<sup>162</sup> The absence of features

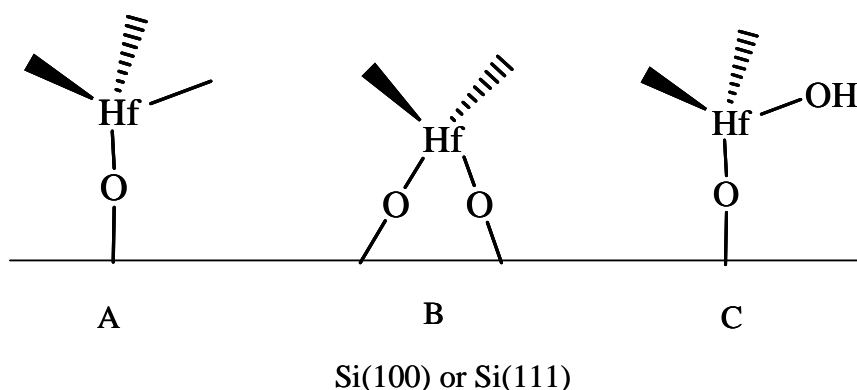
around  $1600\text{ cm}^{-1}$  imply that no C=C bonds are present and the absence of peaks around  $1700\text{ cm}^{-1}$  indicate there are no carbonyl groups (C=O)<sup>163</sup> suggesting carbonate species are present on Si(100) at temperatures greater than  $150\text{ }^{\circ}\text{C}$ . Unfortunately, the dependence of the bridging peak on orientation and temperature doesn't produce a clear explanation for the additional peaks in the C-H stretch region. Additional information may be gained by the time dependence of the peak development.

Figure 7-8 shows the time dependence and integrated absorbance values of the major peaks at  $60\text{ }^{\circ}\text{C}$ . The first peaks to saturate are the  $3678\text{ cm}^{-1}$  ( $\nu_{\text{O-H}}$ ) and the  $2967\text{ cm}^{-1}$  ( $\nu_{\text{C-H}}$ ) peaks from the deconvoluted C-H stretch region followed by the  $2983\text{ cm}^{-1}$  peak of the  $\nu_{\text{C-H}}$  region, the total integrated C-H stretch region between  $3200 - 2760\text{ cm}^{-1}$ , the bridged symmetric O-tBu umbrella mode at  $1226\text{ cm}^{-1}$ , and the total integrated peak area for the C-O stretch and bend between  $1260$  and  $1155\text{ cm}^{-1}$ . Saturation occurs earlier on the Si (100) compared to the Si (111) surfaces as can be seen by the total C-H stretch ( $3200 - 2760\text{ cm}^{-1}$ ), but the integrated absorbance value of the C-H stretch is similar for the two orientations (26.6 and 26.3) as is the saturated value for the symmetric O-tBu umbrella mode at  $1226\text{ cm}^{-1}$ . 1 ML of adsorption is defined here in comparison to that in Chapter 6. It should be noted again that this not a concept of coverage since the equilibrium changes as a function of temperature. Rather, the dose length is more of the idea which took about 6 min. ( $10^8\text{ L}$ ) to reach "1 ML" for all temperatures below  $150\text{ }^{\circ}\text{C}$ . On the other hand, the  $\nu_{\text{O-H}}$  peak and the total peak area of the C-O region ( $1260\text{-}1155\text{ cm}^{-1}$ ) are approximately two times larger on Si(100) than on Si(111) while the  $2983\text{ cm}^{-1}$  peak from the deconvoluted  $\nu_{\text{C-H}}$  is two times smaller on Si(100) than on Si(111) due to less available sites (ideally saturated dangling bonds density is  $6.78 \times 10^{14}\text{ cm}^{-2}$  for H-Si(100) and  $7.84 \times 10^{14}\text{ cm}^{-2}$  for H-Si(111)).



**Figure 7-8.** Growth of OH group, CH stretching, CH bending, and characteristic bridged bond grows with time at 60°C on (a) Si(100) and (b) Si(111). The solid lines are primary axis, the dashed are secondary axis.

The sequence indicates that adsorption ( $2967\text{cm}^{-1}$ ) is immediately followed by rapid hydrolysis. A slow decrease in the  $\nu_{\text{O-H}}$  suggests a condensation reaction may occur. Linkages to the substrate, indicated by the  $1226\text{cm}^{-1}$  peak are the last to form and its trend is closely matched by the  $2983\text{cm}^{-1}$  peak suggesting the C-H shoulder is associated with the bridged model. A tentative mechanism is thus deduced that both the bidentate and monodentate form of the HTB chemisorbed species may be prevalent on the surface. The hydroxyl is from the monodentate chemisorbed HTB and encountered  $\beta$ -hydride elimination quickly which formed the submonolayer. The molecules can diffuse on the surface and find their sites to form bridged chemisorbed species which is related to the slow increase of the peak at  $1226\text{cm}^{-1}$ . On Si(100), more molecules are monodentate with further  $\beta$ -hydride elimination on the surface and thus have a lower hydroxyl density, while  $1226\text{cm}^{-1}$  is almost identical for the two surfaces. Using L to denote a tert-butoxy ligand, then A to denote the monodentate form:  $\text{L}_3\text{Hf-O-Si}$ , B for bridged form:  $\text{Si-O-L}_2\text{Hf-O-Si}$ , and C for monodentate form with one hydroxyl:  $\text{L}_2\text{Hf(OH)-O-Si}$ . The density of these species on the two surfaces is in the following sequence:  $\text{A-Si(100)} > \text{A-Si(111)}$ ,  $\text{B-Si(100)} < \text{B-Si(111)}$ ,  $\text{C-Si(100)} > \text{C-Si(111)}$ . The formation may be in the sequence  $\text{A} \rightarrow \text{C} \rightarrow \text{B}$ . However, detailed microscopic reactions and product arrangements are not available from this technique.



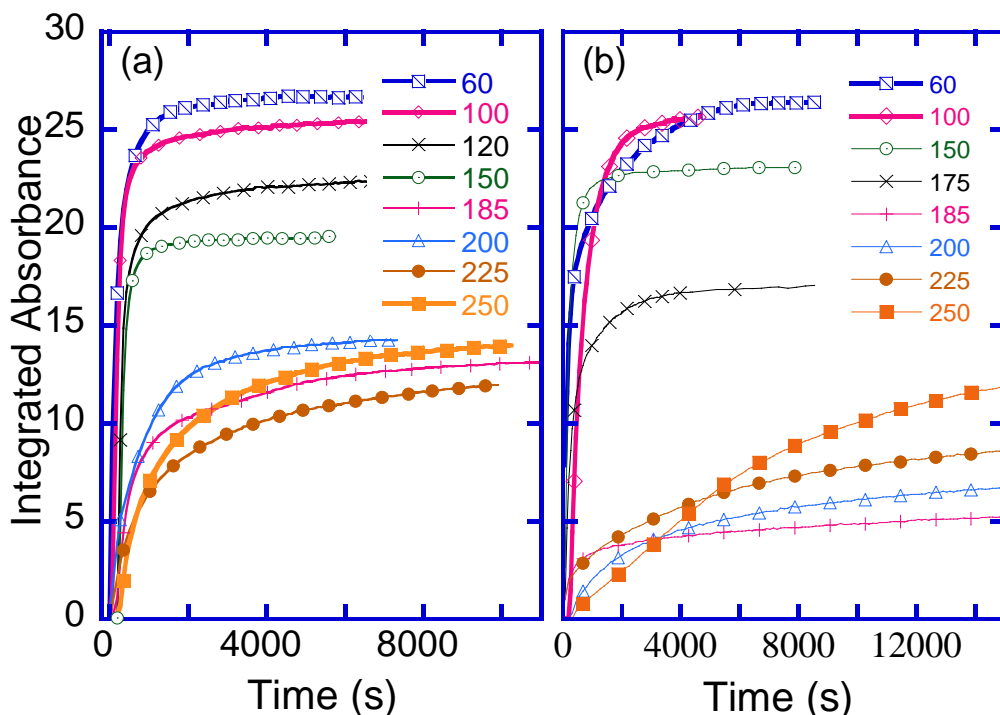


**Figure 7-9.** Peak area of the peak between  $3118\text{-}2763\text{ cm}^{-1}$  (CH stretch absorbance peak area) plotted with time for varying crystal temperatures. (a) Si(100) and (b) Si(111).

Figure 7-9 shows the integrated absorbance of the  $\nu\text{C-H}$  region vs. time for all temperatures studied. Generally, the saturated absorbance decreases with increasing temperature until  $185\text{ }^{\circ}\text{C}$  when the saturation value begins to increase due to the onset of film growth. For temperatures at and below  $185\text{ }^{\circ}\text{C}$  the saturated absorbance was used to generate an Arrhenius plot shown in Figure 7-10 which illustrates the dependence of the equilibrium concentration of the precursor on the surface with temperature. This plot shows two adsorption/reaction regimes above and below  $110\text{ }^{\circ}\text{C}$ . Below  $110\text{ }^{\circ}\text{C}$ , the slope corresponds to an energy of  $1 (\pm 0.1)\text{ kJ/mole}$  which is too small for a simple heat of adsorption measurement assuming reversible adsorption of HTB. Dissociative chemisorption would lower this apparent value by the bond energy.<sup>164</sup> For temperatures above  $110\text{ }^{\circ}\text{C}$  up to  $185\text{ }^{\circ}\text{C}$ , the slope corresponds to an energy of  $11 (\pm 2)\text{ kJ/mol}$ , also lower than expected even for physisorption at high surface coverage. For simple reversible multilayer adsorption, a measurement close to the latent heat of vaporization would be expected as assumed in the Brunauer, Emmett, and

Teller model.<sup>165</sup>

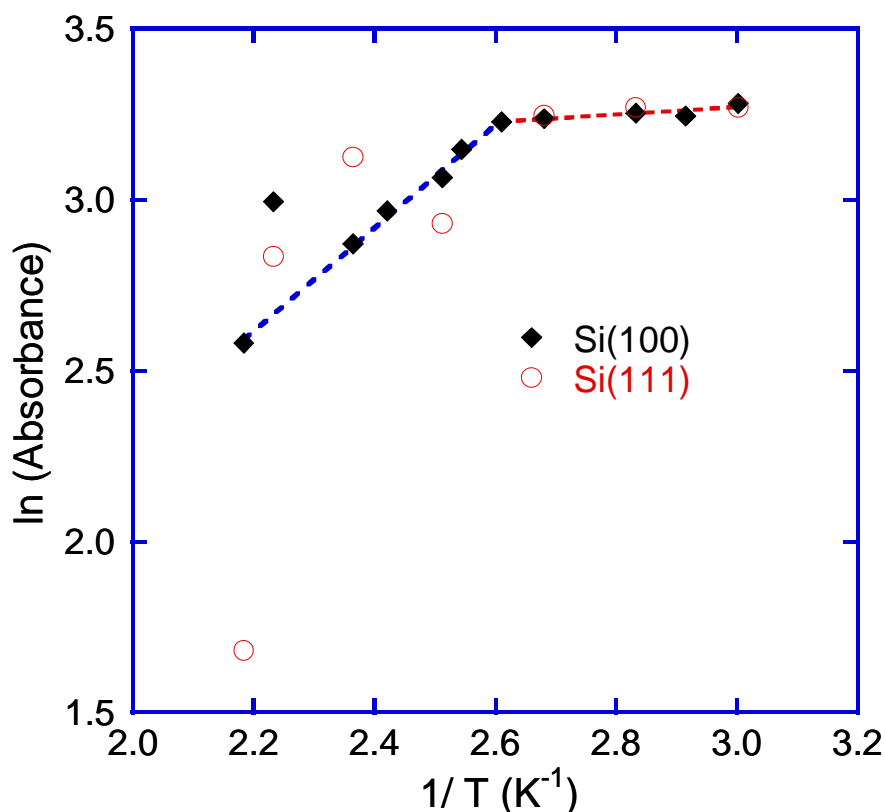


**Figure 7-10.** Arrhenius plot from 60°C to 185°C CH stretching peak area vs. temperature on Si(100) and Si(111).

$\Delta H_{\text{vap}}$  HTB is 54 kJ/mol at 100°C, but varies somewhat with temperature due to slight molecular association in the liquid state.<sup>161</sup> Clearly, a more complicated scenario than simple reversible adsorption is occurring, and two regimes are apparent. From the time resolved ATR data, it is apparent that precursor adsorption is followed by rapid hydrolysis with trace amounts of water yielding Hf-OH which is likely involved in oxidation of hydrogen terminated Si and the formation of bridging bonds to the substrate. At higher temperatures  $\beta$  hydride elimination results in the loss of t-butyl groups from the chemisorbed layer.

### 7.3 Kinetic Calculations

#### 7.3.1 Adsorption Energy

The vapor pressure of HTB purchased from Strem Chemical ® is 2.0 Torr at 70 °C, 1.0 Torr at 65 °C, 0.1 Torr at 25 °C. It is within 1.2% error consistent with the vapor pressure

reported for 54 kJ/mol at 100 °C.<sup>158</sup> The vapor pressure of HTB is estimated to be about 0.4 Torr at 50 °C by Clapeyron equation. When the system reaches steady state flow after about 15 minutes, the pressures are less than 0.4 Torr, corresponding to a residence time of 0.3 seconds. Assuming the base pressure from outgassing is not considered, the average pumping speed is 34 L/min, 50% the full pumping speed, consistent with the Edwards' pumping performance characteristic.

Since the pressure was measured for the same temperature, the concentration or flux reaching the H-Si surface was also an exponential function of time and is estimated to be  $[HTB] = 0.057 \exp(-t/187.8)$  [mol/m<sup>3</sup>], where t is in seconds

The rapid growth of the integrated OH peak at 60°C is within 500 seconds. Thus it is critical to include the pressure influence into consideration.

$$\frac{d[HTB^*]}{dt} = k_a[HTB](1 - [HTB^*]) - k_d[HTB^*]$$

$$\Rightarrow [HTB^*] = \frac{k_a[HTB]}{k_d + k_a[HTB]} \{1 - \exp[-t \cdot (k_d + k_a[HTB])]\}$$

where  $[HTB^*]$  is normalized coverage,  $k_a$  is in unit of m<sup>3</sup>·(L·sec)<sup>-1</sup>.

After integration, the relationship between  $[HTB^*]$  and time is as follows:

$$\ln(1 - [HTB^*]) = 10.7k_a \exp(-t/187.8) + C$$

From the linear relationship between the logarithmic and exponential term for OH region at 60 – 110 °C region, every temperature follow this linear trend with a R squared value bigger than 0.99. From the calculated coefficient data, the [OH] adsorption energy can be calculated to be -9.0 kJ/mol.

Similarly for the CH region, only the peak at 2967 cm<sup>-1</sup> by deconvolution shows linear behavior, which is assigned as the β hydride decomposed precursor. The peak at 2983cm<sup>-1</sup> does not follow a linear trend. Linear analysis for the  $\nu_{CH}$  at 2967cm<sup>-1</sup> initial adsorption rate, coefficients. From these data, the [CH] adsorption energy can be calculated

to be -24.4 kJ/mol.

### 7.3.2 Decomposition and Hydrolysis Reaction

The transition states for  $\beta$ -hydride elimination and hydrolysis reaction is calculated as shown in Figure 7-11 and Figure 7-12. The gas phase reaction of  $\beta$ -hydride elimination has a big kinetic barrier of 58 kcal/mol, indicating that the reaction is not likely to occur at room temperature and in the gas phase. The hydrolysis reaction is calculated to occur easily and is an exothermic reaction with a small reaction energy. This indicates that if there is any moisture on the surface, HTB may encounter hydrolysis and be stable on the surface.

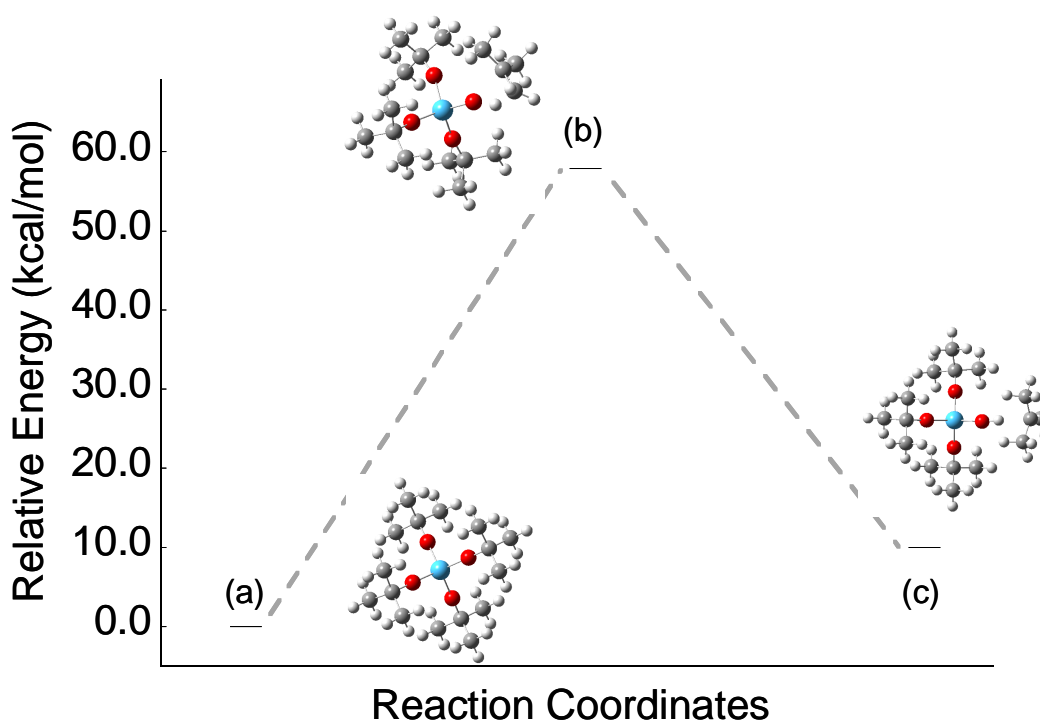


**Figure 7-11.** ZPE-corrected PES for the HTB  $\beta$ -hydride elimination: a) HTB molecule; (b) beta-hydride elimination transition state; (c) products: 2-butene and OH-terminated HTB. Electron Energies in kcal/mol: (a) 0 (b) 57.9 (c) 9.98

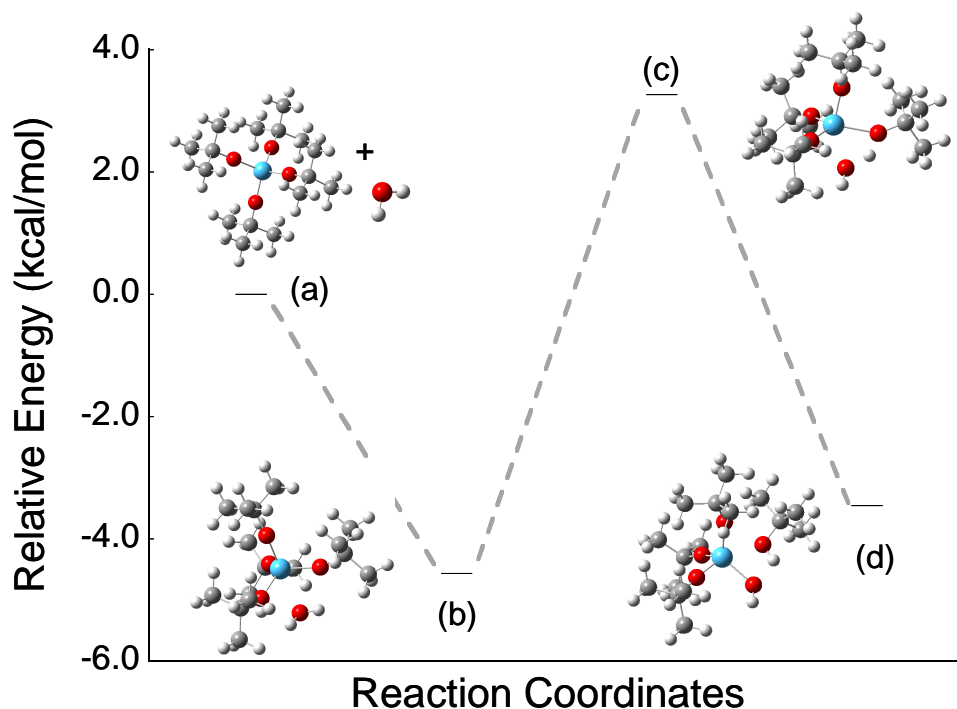


**Figure 7-12.** ZPE-corrected PES for the hydrolysis of HTB: (a) separate HTB and water molecule; (b) H-bonded HTB and water adsorption; (c) transition state; (d) products: Hydroxyl terminated HTB and tert butyl alcohol. ZPE Energies in kcal/mol: (a) 0 (b) -4.56 (c) 3.27 (d) -3.45.

#### 7.4 XPS Study

Figure 7-13 shows the O 1s, C 1s, and Hf 4f XPS peaks for HTB adsorbed at elevated temperatures on a H-Si(100) substrate. The peaks were shifted with respect to the Si 2p substrate at 98.8 eV. The binding energy peaks for O 1s and Hf 4f were at 530.2 eV and 16.9 eV respectively. The higher BE peak at 290.5 eV in C 1s is attributed to the carbonate. With increasing temperature, the O 1s peak broadens and was deconvoluted into three states as shown in Figure 7-14. The higher BE peak may be attributed to the O 1s in water molecules from hydrolysis moisture embedded in the film as shown in Figure 7-3.

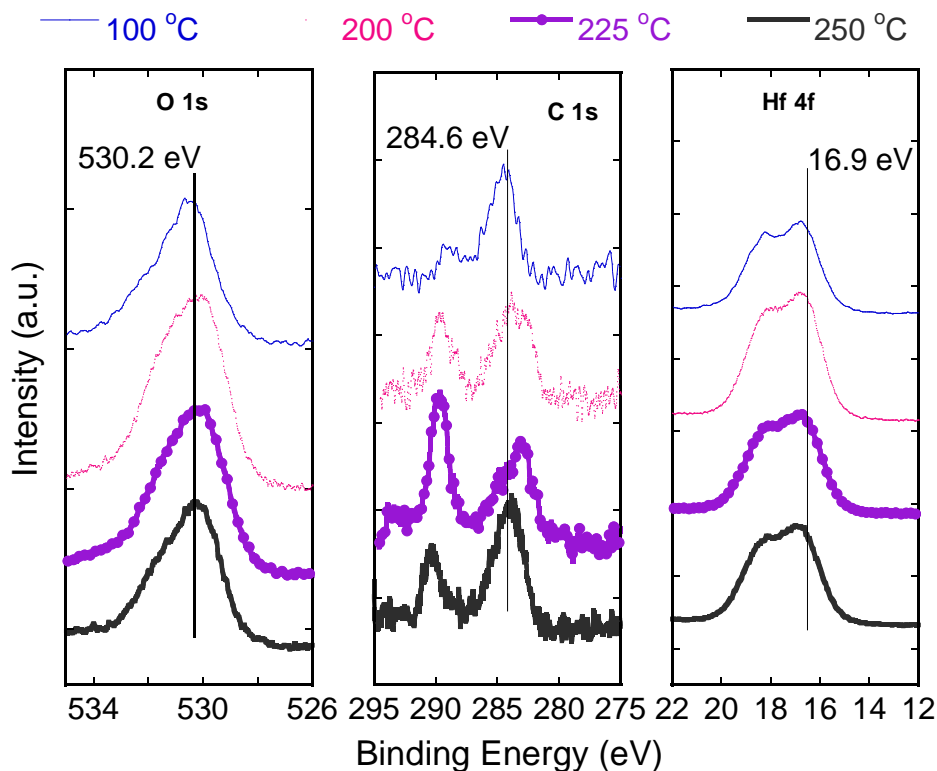


**Figure 7-13.** *ex-situ* XPS spectra for HTB adsorption on H-Si(100) at different temperatures.

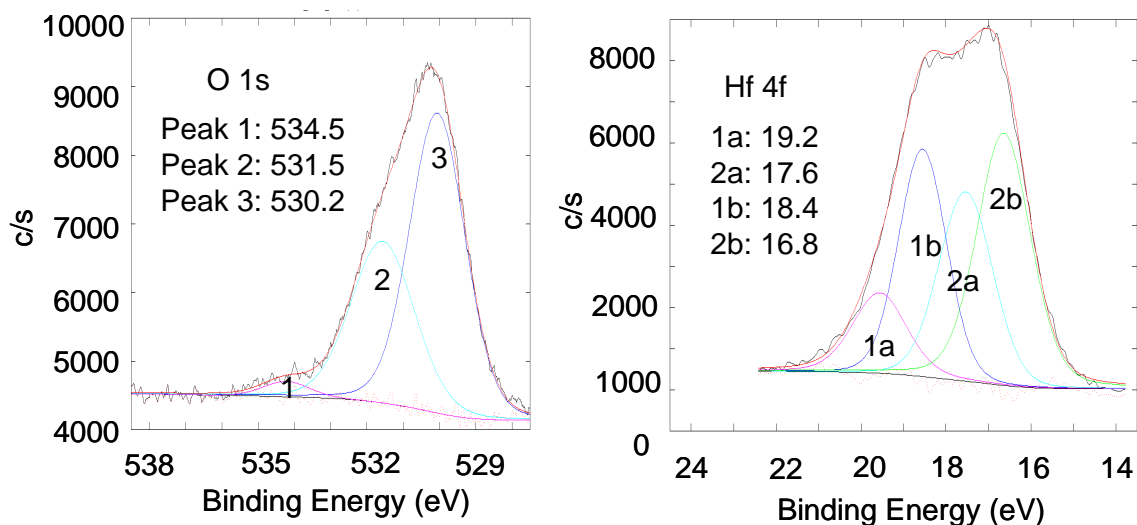


**Figure 7-14.** Deconvoluted O 1s and Hf 4f peak for 1 hr. HTB adsorption on H-Si(100) at 250 °C.

The ratios of O:Hf and C:Hf at different temperatures is shown in Figure 7-15. The sensitivity factors for C, O, Hf are 0.314, 0.733, and 2.901, respectively. The film was nearly stoichiometric, with C contaminates in the form of residual ligands or carbonates as discussed earlier. However, due to *ex vacuo* exposure to air, it is difficult to determine the number of

residual ligands after the adsorption.

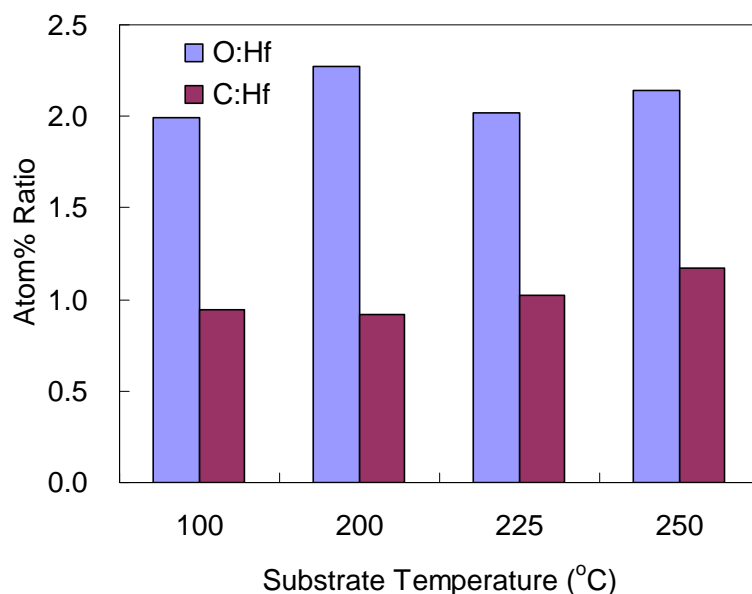


**Figure 7-15.** Ratio of O:Hf and C:Hf at different temperatures.

As a comparison, XPS for HTB adsorbed on H-Si(111) at 250 °C is shown in Figure 7-16. The O has a less concentration in the lower O 1s BE associated with the carbonate form. While for C 1s, there is a sharper mono peak compared to that on Si(100).

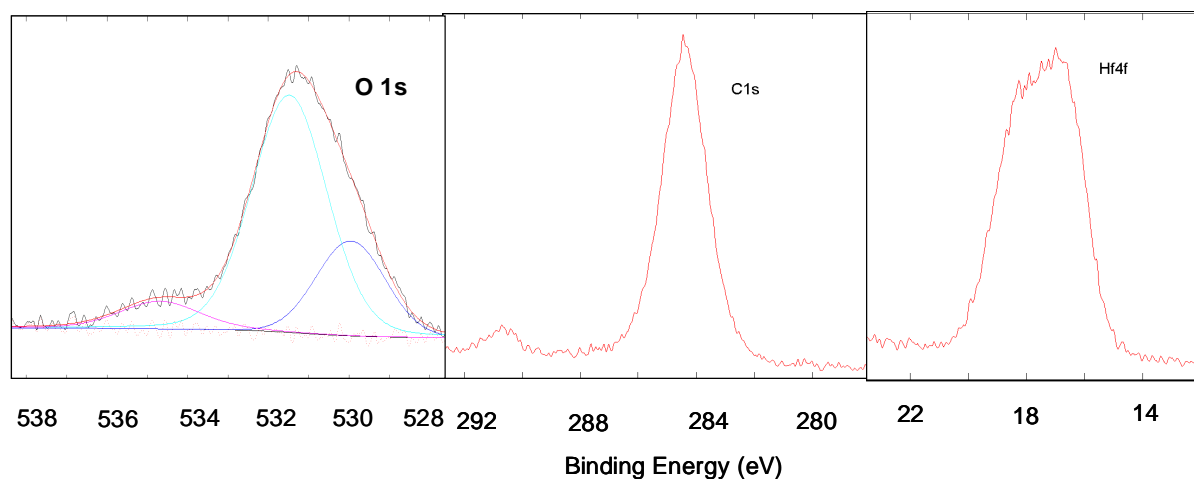


**Figure 7-16.** *ex-situ* XPS spectra for HTB adsorption on H-Si(111) at 250 °C.

## 7.5 Chapter Summary

Spectra generated by density functional theory (DFT) calculations of monodentate and bridging adsorbed precursors as well as a spectrum of an applied liquid drop of HTB

precursor were used to identify the chemisorbed species. Two symmetric O-tBu umbrella modes from bridged Si-O-Hf(O-tBu)<sub>2</sub>-O-Si located at 1226 cm<sup>-1</sup> and 1016 cm<sup>-1</sup> present in the chemisorbed spectra show the precursor dissociates and is present as a symmetric ligand on both Si(100) and Si(111). Surface concentration of the chemisorbed species was dependant on the substrate temperature allowing for determination of adsorption activation energies of 11 (± 2) kJ/mol for HTB on Si (100) for the temperature range of 110-185 °C and 1 (± 0.1) kJ/mol on Si(100) and Si(111) at temperatures between 60-110 °C. Precursor decomposition on the surface is observed at temperatures above 185°C and forms carbonate. Equilibrium concentrations on the surface is achieved for times greater than 1 hour consistent with a reaction limited by steric effects and the adsorption follows an Arrhenius trend with temperature.

## Chapter 8 ATR-FTIR Flow Through Meso-Reactor

### 8.1 Chapter Introduction

Chemical vapor deposition (CVD) is an important technique in thin film deposition. It is widely applied in coatings for micro-electro-mechanical systems (MEMS), hard drive read/write heads, anti-corrosion layers and other related fields.<sup>166</sup> It has been realized that temperature uniformity,<sup>167</sup> flow dynamics, and reaction kinetics<sup>168</sup> are important for achieving better film uniformity and contamination control. However, due to the complex phenomena involved with a CVD process, how the precursor vapor transport influences the kinetic behavior is discussed in some modeling work<sup>169</sup> but relatively few supporting experiments directly addresses this issue.

Geometry influences the flow pattern by a big degree. With the trend of increasing Si wafer diameters used in ultra-large-scale-integration (ULSI) circuits every four to five technology generations, the need for reactor optimization and prediction of the flow behavior becomes necessary. The pilot line production for the next generation wafer size is expected in 2012 for 450 mm.<sup>170</sup> A full understanding of the fluid behavior in these reactors would help the optimization of the reactor design.

There are three common types of reactors used by industry: stagnation flow type reactors, horizontal reactors and low pressure multi-wafer barrel-type reactors. As introduced in Chapter 2, horizontal multiple-wafer-in-tube type reactors are the main production tool for growing polycrystalline Si, dielectric materials, and passivating films used in Si integrated-circuit manufacturing. The precursor flows to the substrate from the source driven by the pressure gradient by a vacuum pump at the back end. The precursor's flux is

perpendicular to the imposed temperature gradient. It is a classical configuration and has the advantage of high throughput.

Chemical reaction engineering can also have a significant impact on CVD or organometallic vapor phase epitaxy (OMVPE).<sup>171, 172</sup> The depletion of reactants downstream,<sup>19</sup> and non-uniformity caused by free conduction due to a temperature difference between the substrate and the wall<sup>169</sup> was realized to be issues that have to be considered. However, for coexisting homogeneous and heterogeneous gas phase and surface reactions, the modeling is often hampered by the absence of details of the reaction chemistry and microscopic behavior during the film growth.

HfO<sub>2</sub> growth from hafnium tert-butoxide (HTB) has been reported.<sup>61</sup> In the previous chapter, the mechanism and kinetics for HTB adsorption and reactions on semiconductor surfaces were studied. In this chapter, we utilized HTB to deposit HfO<sub>2</sub> in a flow type cell and investigated the film growth kinetics, composition and morphology in order to reflect the reactor geometry influenced gas fluid behavior.

## 8.2 Experimental Setup and Meso-Reactor

The system setup was shown as below. The meso-reactor reactor was designed to be compatible to precursor inflow and vacuum outflow with an Edwards rotary vane pump downstream. HTB (99.99% purity from Strem Chemical Inc.) was transferred to a quartz bubbler under N<sub>2</sub> and the bubbler was kept in an oil bath with controllable temperatures. The bubbler was preheated for 45 min. before introducing to the flow cell. The base absolute pressure was 10<sup>-3</sup> Torr, and the experimental pressure was around 0.3 Torr depending on the bubbler temperature. Two MKS pioni gauges were equipped before and after the flow cell to measure the pressure difference. No carrier gas was used due to the high vapor pressure of HTB. A bypass line of Ar was used to calibrate the flow rate and purge the gas line before and after experiments.

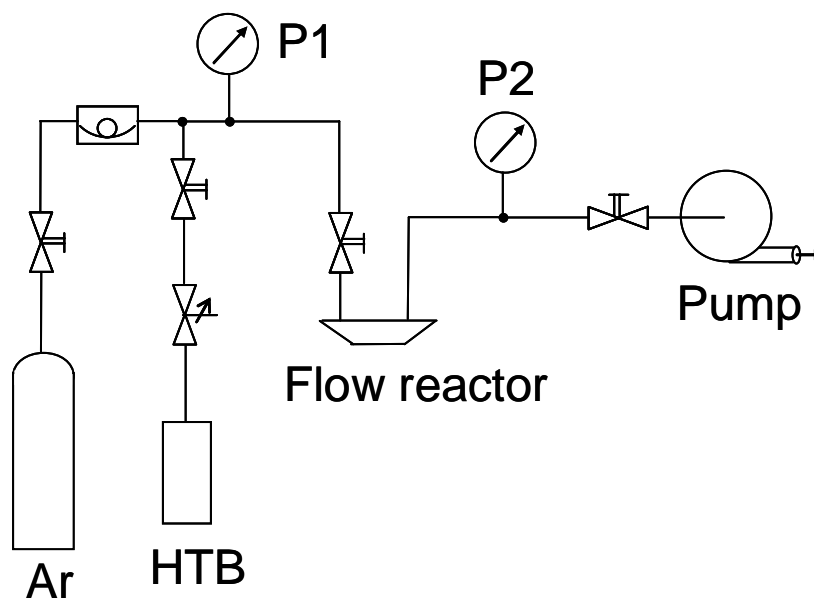


**Figure 8-1.** Fluid Dynamics Study Experimental Setup

The flow through cell interior has the design dimensions shown in the following diagram in Figure 8-2. It is bigger than micro reactors,<sup>173</sup> but smaller than industrial CVD flow reactors. The  $100 \times 50 \times 8$  mm meso flow reactor body is made of stainless steel (ss), with inlet and outlet tubes and a top smaller rectangular plate including two copper heating rods. The roundness of corners is neglected. In the flow through cell, the thickness is 0.889 mm for tubing wall, 0.2 mm for the ss sheet, 1.5 mm for the Al sheet, and 1.2 mm for the Kalarez gasket. The main rectangular body is made of ss, with one top part and one bottom part. The two parts are sealed together by two screws and a Kalarez® o-ring. The substrate is  $45^\circ$  trapezoidal cut  $50 \times 10 \times 2$  mm ATR Si crystal or an n-type, 0.01 parts per million (PPM) boron doped Si (100) wafers, which were pressed to the upper stainless steel body by one sheet of the ss cover and two aluminum covers. The Si crystal and the ss body was sealed by a Kalarez gasket.

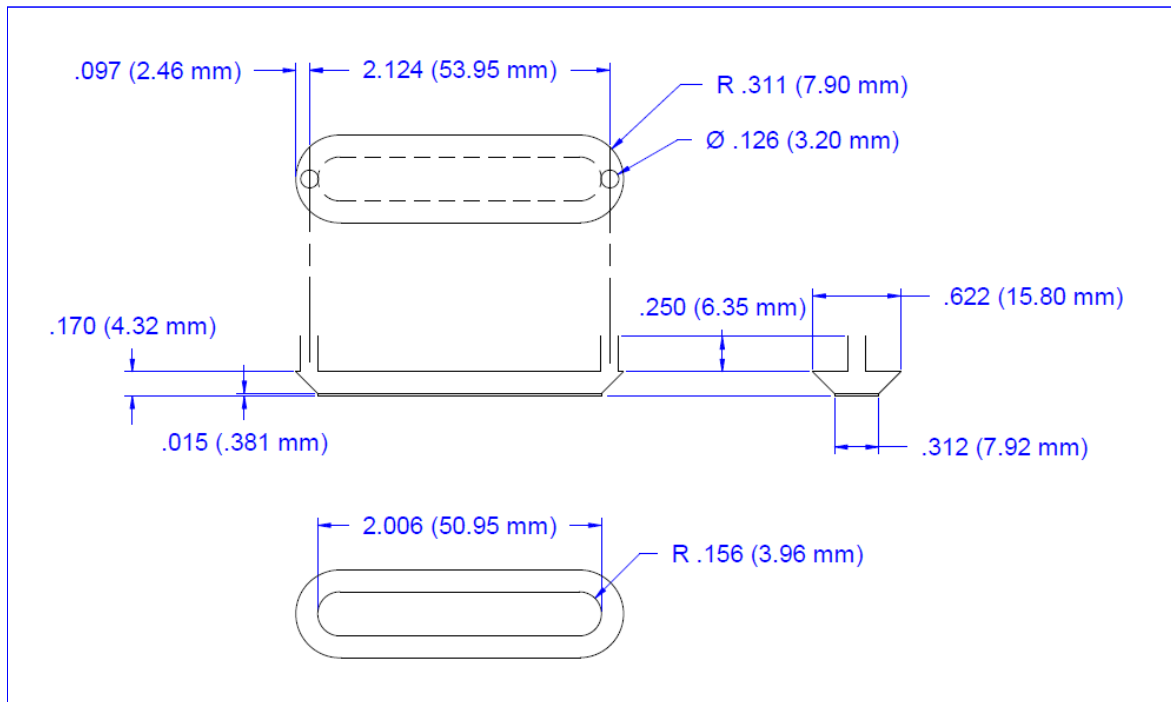


**Figure 8-2.** AutoCAD schematic drawing of the flow through cell with dimensions.

### 8.3 Temperature Profile of the Meso-Reactor

#### 8.3.1 Temperature Modeling

A thermal profile is an important issue in the deposition process. A minimization of the temperature gradient would help the uniformity of the film deposited as the diffusion and reaction rate are exponentially dependent on the substrate temperature. In normal operation conditions, it is usually difficult to get a full profile of the substrate temperature because of two reasons: the substrate is usually in a closed vessel which makes it difficult to attach thermocouples inside; and the thermal couple only measures one spot at a time on the surface. With the aid of a supercomputer, finite element analysis (FEA) enables a prediction of the temperature distribution on the substrate surface without having to take apart the compartment during the experiment.

Thin films deposited at thermal CVD conditions are normally less than 100 nm and the heat released from the reaction has a negligible influence on the substrate temperature which has a much bigger volume compared to the thin film. We assume that the reaction heat,

either exothermic or endothermic, is quickly transferred through the thin film. The substrate temperature is measured when depositing thin films and the substrate temperature profile can be assumed to be the adsorption/reaction temperature profile on the substrate.

### 8.3.2 FEA Model and Formulation

Finite element analysis (FEA) simulation using ANSYS multiphysics 11.0 is performed to investigate the heat loss due to convection in air as well as the temperature distribution on the surface of the Si substrate. The geometry was generated using the actual dimensions and all the components were made according to the real system, since gross simplification can cause a significant accuracy drift. The model was generated by 3-D thermal elements and nodes, meshed with Solid87 and a total number of 314851 nodes. The following assumptions are made in order to simplify the model:

- 1) The temperature distribution is calculated during steady state;
- 1) Radiation is negligible at temperatures below 250 °C and thus not considered.
- 2) Thermal coefficients of each component at 1 atm are referred from the CRC handbook<sup>174</sup> and the manufacturers' website as listed in Table B-1, Appendix A.
- 3) The thermal contact resistance is negligible between the top plate and bottom plate as these plates are polished flat and fastened with good contact by two screws.

The heat transport equations for the flow through cell without the gas flow can be described as three parts: the faces open to air, copper heat generation rods, and the main part. On the faces open to air, the general heat transport equation can be described by Fourier's Law and Newton's Law of Cooling, where the convection equals to conduction at steady state:

$$-k \cdot A \cdot \nabla T + h(T_{\infty} - T_{sur}) = 0$$

$$\text{B.C.: } T_{\infty} = 25^{\circ}\text{C}, \nabla^2 T = 0$$

The copper heater has a power range from 0 to 100W, depending on the desired temperature

for the Si substrate, which determines the final component temperature profile.

$-k \cdot \nabla^2 T + \dot{q} = 0$ , where  $\dot{q}$  is the rate of heat generation per unit copper volume. Within other components without heat generation, the heat flux is simply based on a heat diffusion equation:  $-k \cdot \nabla^2 T = 0$  where a corresponding  $k$  is applied with respect to different materials and temperatures.

Figure 8-3 shows the temperature distribution predicted on the reactor. Figure 8-3 (a) is an overview of the temperature at the reactor cross section. With a heat power 80W, the top heating plate is about 100 degrees higher than the bottom plate. Figure 8-3 (b) is the temperature distribution on the Si substrate surface. It shows that there is about 10 degrees' difference along the transverse direction, and the middle area has the highest temperature.

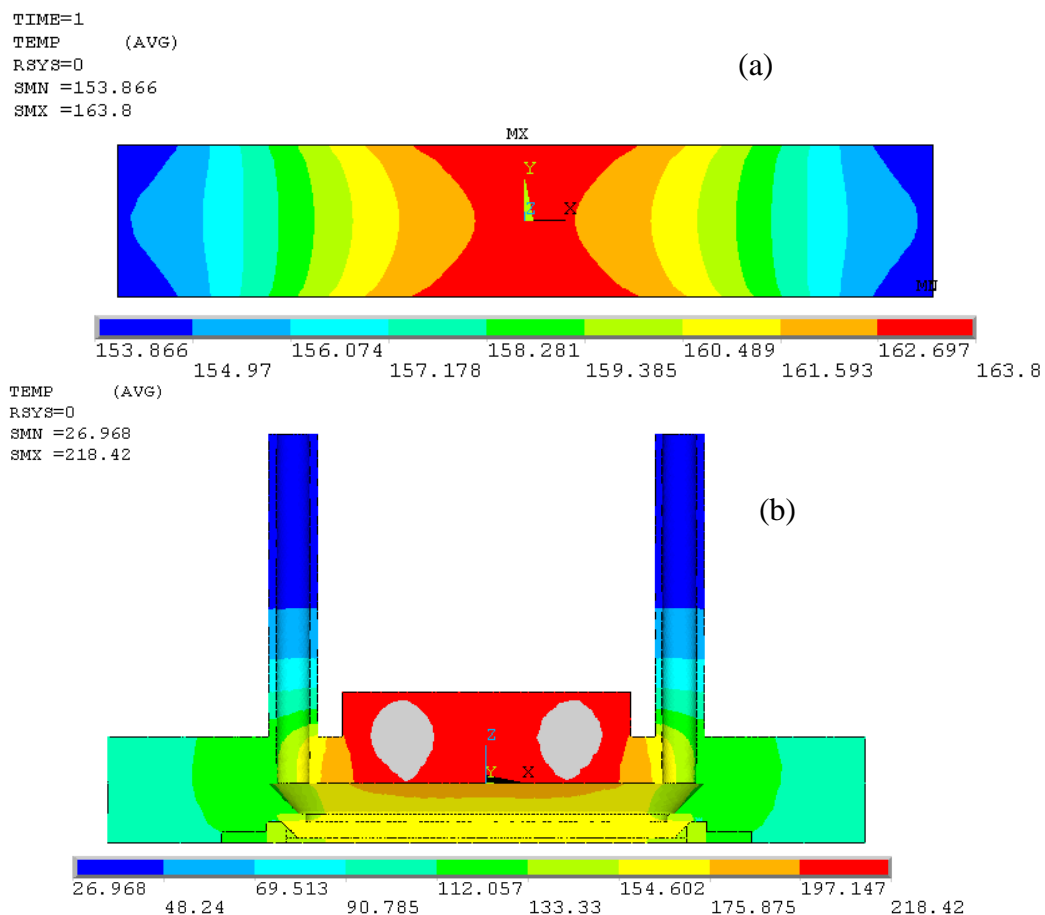


**Figure 8-3.** (a) temperature distribution on the Si surface with power 80W; (b) temperature profile on the flow through cell cross section with a power of 80W.

### 8.3.3 Experiment Temperature Measurement

With an Omron<sup>®</sup> Thermo temperature controller, the temperature profile on the substrate was measured to test the above FEA model by taking the reactor apart and measuring five spots on the substrate back (ss sheet). By changing the two heating rod temperatures from 60 °C to 250 °C, it usually took 10 to 15 min. for the bottom substrate to reach thermal equilibrium. As shown in Figure 8-4, the temperature distribution along the ss plate is wider with higher a heating rod set point. At a set point of 225 °C, the ss plate is about 100 °C lower. Compared to the calculated substrate temperature distribution, there are only a few degrees deviation from the experimental values. This indicates that the calculation is accurate enough to determine the Si surface temperature which is difficult to measure in the closed system. This result also means special attention has to be paid when mentioning temperature in the future but wouldn't influence the previous discussions about experiments at lower temperatures.

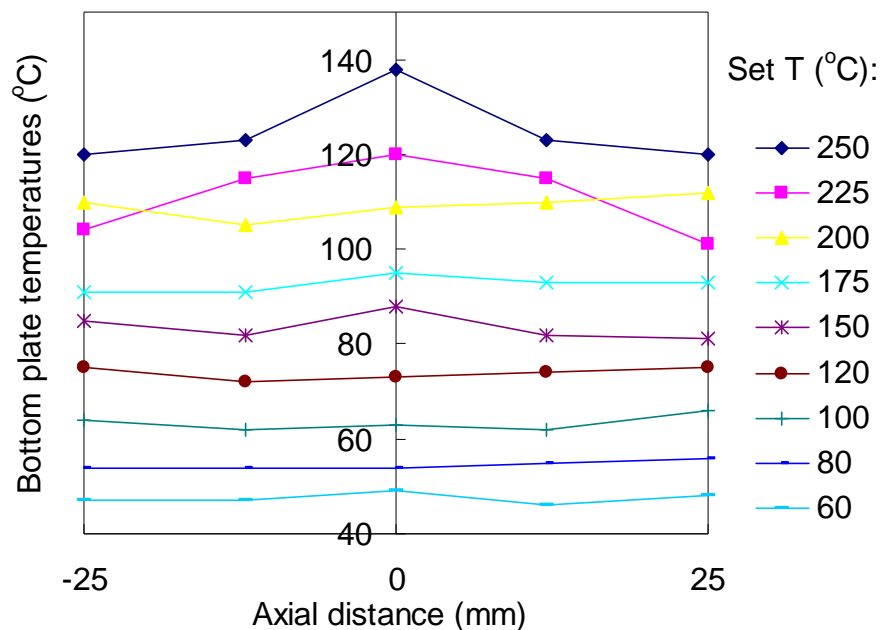


**Figure 8-4.** Measured temperatures on ss sheet at the back of Si substrate.

A few temperature degrees variation usually may be neglected in discussion. However, at higher temperature settings, the difference across a wafer is more significant and should be

accounted for. When applying a different substrate material, it is also suggested that the substrate needs to equilibrate for some time based on the material's thermal conductivity. A lower value requires longer time to reach a steady state temperature distribution and will have a larger temperature distribution. In particular, ZnSe needs a longer time to reach steady state than Si.

#### **8.4 Fluid Behavior Model**

The gas flow in the CVD reactor may influence the extent of non-uniformity in thin film thickness and composition. The fluid behavior is complex, depending on the geometry and operational settings such as temperature, pressure and flow rate. Vortices are undesirable for either film uniformity or interface abruptness.<sup>175</sup> The flow type is usually sensitive to several parametric numbers: Reynolds number  $Re$ , Grashof number  $Gr$ , Raleigh number  $Ra$ , and Knudsen number  $Kn$ . At  $Re$  less than 2000, the flow is laminar. For laminar Poiseuille flow in a rectangular horizontal duct,  $Gr$  or  $Ra$  large enough to exceed a certain critical point can result in mixed convective flow.<sup>169</sup> The relation between  $Re$  and  $Ra$  is considered to influence the occurrence of longitudinal or transverse rolls.

Some pioneers in the early 1980s have performed visual experiments for liquid Poiseuille flow<sup>2</sup> and  $TiO_2$  smoke in horizontal reactors with flow perpendicular to the susceptor.<sup>3</sup> The geometry of these reactors was designed with a hot substrate and cold wall. The flow was Rayleigh Bénard natural convection in addition to a Poiseuille flow. The Rayleigh Bénard problem is a description of the formation of natural convection flow in a system with a big enough temperature difference between the top and bottom plates to overcome the viscosity and thermal diffusivity, when the Rayleigh number  $Ra$  exceeds a certain critical value.

$$Ra = \frac{\alpha \beta g d^4}{k \nu}$$

where  $\beta = \frac{dT}{dz} = \frac{\Delta T}{d}$ ,  $g$  is the acceleration due to gravity,  $\alpha$  is the coefficient of thermal expansion,  $d$  is the depth of the chamber and  $k$ ,  $\nu$  are the thermal diffusivity and kinematic viscosity respectively.

In our horizontal flow reactor with top and bottom plates having a big temperature difference, the mixed convection phenomena can possibly occur. To estimate the above characteristic fluid dynamic parameters, thermal properties of the precursor, HTB, was obtained by using density functional theory (DFT) calculations with the Gaussian 03 software package.<sup>102</sup> The DFT geometry optimizations and thermodynamic quantities were carried out with the 6-31+G(d,p) basis set for the non-metal atoms and the LanL2DZ large core relativistic effective core potential (RECP) and associated basis set<sup>176</sup> for the Hf atom. The molecular diameter of the HTB molecule was calculated to be 9.15 Å, and the constant volume heat capacity  $C_v = 0.4551 \text{ kJ}\cdot\text{mol}^{-1}\cdot\text{K}$ , corresponding to a specific capacity of  $0.9636 \text{ kJ}\cdot\text{kg}^{-1}\cdot\text{K}^{-1}$ . With the molecular weight of  $0.4722 \text{ kg/mol}$ , the thermal conductivity coefficient  $k_T$  is calculated to be  $0.03 \text{ W}\cdot\text{m}^{-1}\cdot\text{K}^{-1}$  and the dynamic viscosity  $\eta$  about  $1.25 \times 10^{-5} \text{ Pa}\cdot\text{s}$  based on the rigid hard sphere theory<sup>177</sup> for gases:

$$k_T = \frac{25C_v}{32N_A} \left(\frac{RT}{\pi M}\right)^{1/2} \frac{1}{d^2}$$

$$\text{and } \eta = \frac{2k_T M}{5C_v}$$

The flow is usually assumed as incompressible. It is verified with the Mach number using a speed of the density perturbation propagation given by equation:<sup>178</sup>

$$c = \sqrt{\gamma RT}$$

where  $\gamma = \frac{C_p}{C_v}$  is the ratio of specific heats. The speed of sound is calculated to be 52.3 m/s.

For HTB preheated at 50 °C for half an hour, the experimental pressure was about 0.3 Torr.

From linear interpolation of the volume flow rate using N<sub>2</sub> at room temperature (Figure B-8, Appendix A), the flow rate of HTB is around 0.15 sccm, which corresponds to an average inlet velocity of 0.34 m/s in the 1/4” 316L stainless steel tube. Thus the Mach number is small enough to assume the steady state flow is incompressible.

With these values and a temperature difference of 100 °C with a set point of 250 °C at the top heating plate, the characteristic parameters are summarized in the table below. The temperature used in the estimation is 60 °C, at 0.3 Torr. For incompressible flow, the coefficient of thermal expansion is assumed using air’s thermal expansion coefficient  $\alpha = 3 \times 10^{-3} \text{ K}^{-1}$ . The characteristic length of the reactor is 4 mm. Since  $Gr/Re^2 \sim 0.1$ , any small fluctuation in the parameters may cause the ratio to be bigger than 1 that the natural convection has to be taken into consideration.

**Table 8-1.** Estimated Fluid Mechanics Parameters for 60 °C HTB at 0.3 Torr

Name	Definition	Value
Knudsen	$Kn = \frac{l}{L}, l = \frac{1}{\sqrt{2\pi a^2 n}}, n = \frac{pN_A}{RT}$	0.0075
Mach	$Ma = \frac{v}{c}$	0.0065
Prandtl	$Pr = \frac{C_p \cdot \eta}{M \cdot k_T}$	0.41
Renolds	$Re = \frac{\rho \cdot v \cdot L}{\eta}$	0.83
Grashof	$Gr = \frac{Ra}{Pr} = \frac{\rho^2 g \Delta T \alpha L^3}{\eta^2}$	0.07
Raleigh	$Ra = Gr \cdot Pr$	0.03

#### 8.4.1 CFD Formulation and Simulation

The flow working volume is composed of two half-cut circular cones with radiuses R

(8cm) and r (4cm) respectively, and an inverse trapezoid with matching sides on the diameter with the two half cones. The height, d, between the inlet and the substrate is 4mm, and the length, L, of the flow path on the substrate is 45 mm, which gives a finite horizontal duct L/d  $\approx$  10. Due to mixing of longitudinal rolls and transverse convection, the calculation has to be performed as a three dimensional model.

The governing equations can be written as a collective of Navier-Stokes (N-S) equations for continuity, momentum and energy balances. The velocities and pressure can be solved iteratively through implicit or explicit ways in the finite volume method, and then will give other transport scalars. For steady state incompressible flow, the non-conservative form of the N-S equations is given as: <sup>20,179</sup>

$$\nabla \cdot \mathbf{u} = 0$$

$$\nabla \cdot \rho \mathbf{u} \mathbf{u} = -\nabla p + \nabla \left\{ \mu \left[ \nabla \mathbf{u} + (\nabla \mathbf{u})^T - \frac{2}{3} (\nabla \mathbf{u}) \cdot \mathbf{I} \right] \right\}$$

$$\rho C_p \mathbf{u} \cdot \nabla T = \nabla_2 \cdot (k \nabla_2 T) + \sum_{i=1}^s \bar{H}_i \left[ \left( \nabla \cdot \mathbf{J}_i - \sum_{j=1}^g \nu_{ji}^g R_j^g \right) \right]$$

where the  $\mathbf{u}$  is the velocity vector,  $\mathbf{I}$  is the unit tensor, and superscript T is the transpose of the tensor,  $H_i$  is the energy for reaction  $i$ ,  $\mathbf{J}_i$  is the molar flux, and  $\nu_{ji}$  is the stoichiometric coefficient. Dufour and Soret diffusion<sup>180</sup> for reactants and by-products are neglected here.

Assuming the rate of deposition is limited by mass transfer, then the deposition rate is proportional to the local density, concentration gradient and diffusivity. The concentration is transported as a scalar, and can be expressed in the mass transport equation:

$$\nabla \cdot \rho \mathbf{u} c_{HTB} = \nabla \cdot (\rho D \nabla c_{HTB})$$

where  $c_{HTB}$  is the concentration of HTB vapor, and  $D$  is the diffusion coefficient that can be calculated from Chapman-Enskog theory:<sup>181</sup>

$$D_{AB} = \frac{1}{4} \bar{c} l \propto \frac{T^{7/4} \left( \frac{1}{M_A} + \frac{1}{M_B} \right)^{1/2}}{p(a_A + a_B)^2}$$

Thus, the impingement flux on the surface is:

$$J_{HTB} \left( \frac{mc}{m^2 \cdot s} \right) = D_{HTB} c_{HTB}$$

The computational fluid dynamics (CFD) modeling used the solver CFD-ACE from ESI-CFD of Huntsville, Alabama. An unstructured grid of 160,826 cells was created using the CFD-GEOM module. A steady-state solution for N<sub>2</sub> or HTB flow velocities and temperature was computed, assuming constant properties (density, viscosity, thermal conductivity, and specific heat). No-slip conditions and constant temperatures were specified on all surfaces. The velocity at the inlet was specified according to the flow rate, with the exit velocity determined from the fixed pressure there. A typical calculation converged in 179 iterations in 8 minutes.

#### 8.4.2 Flow Rates and Pressure Drop

Pressure difference was measured by two piana gauges P1 and P2. The background pressure drop was about 0.08 Torr. The pressure drop between P1 and P2 was measured as a function of time after opening the bubbler valve as shown in Figure 8-5.

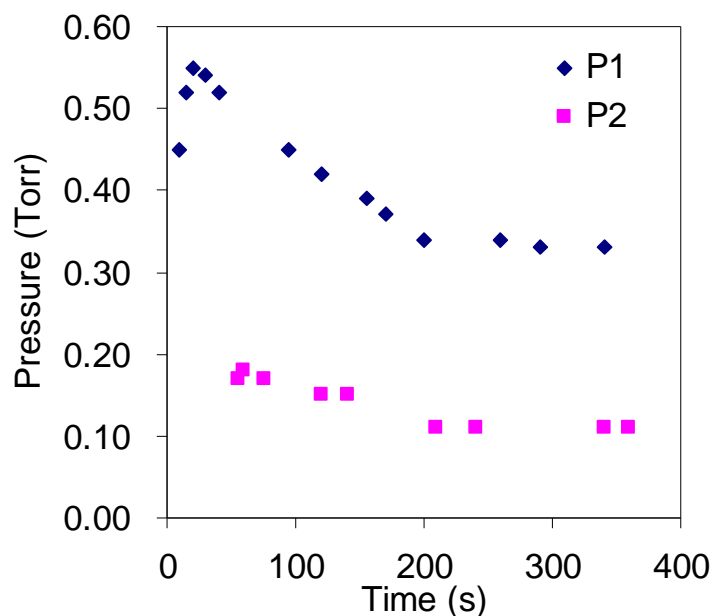


**Figure 8-5.** Pressure difference between P1 and P2 as a function of time.

The pressure difference became smaller and reached a steady state after about 3 min. Based on the Clapeyron-Clausius equation, the vapor pressure should increase exponentially with bubbler temperature. However, in flow mode, the evaporation coefficient is usually smaller than 1 due to a slower evaporation rate than the pumping speed. The vapor pressure as a function of bubbler temperature was measured by two gauges as shown in Figure 8-6.

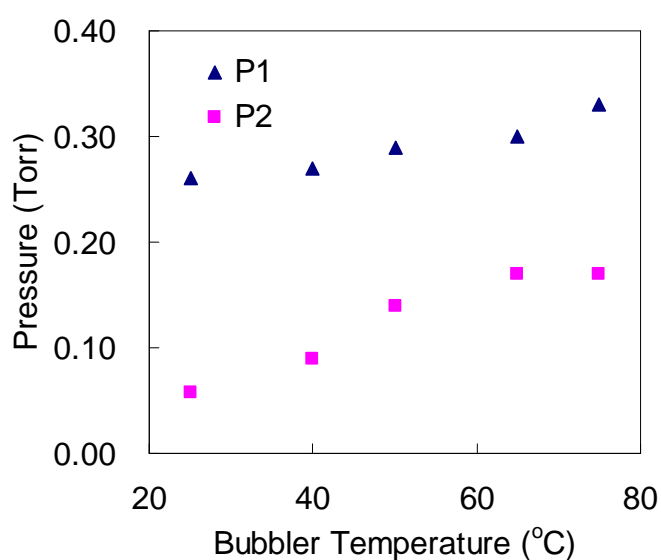


**Figure 8-6.** Pressure at P1 and P2 as a function of different bubbler temperatures.

The pressure drop  $\Delta P$  between P1 and P2 as a function of different bubbler temperatures with a crystal temperature setting temperature at 250 °C can be read from Figure 8-6. Pressure differences at different temperature set points with a bubbler temperature at 50 °C are shown in Figure 8-7.

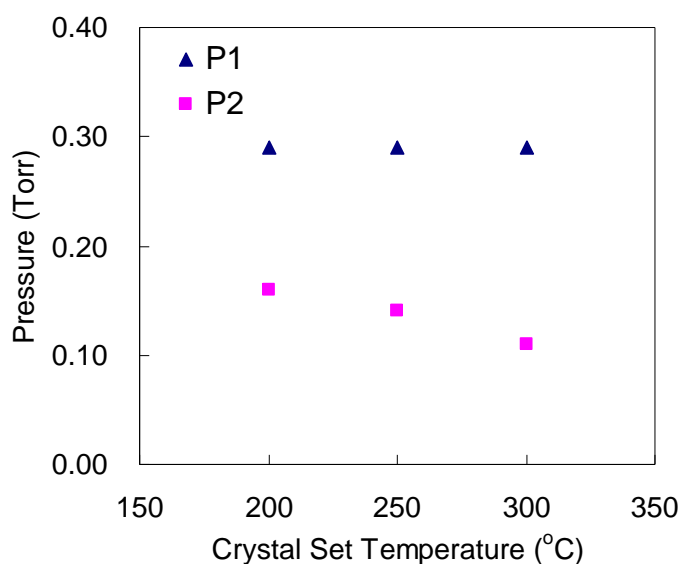


**Figure 8-7.** Pressure difference between P1 and P2 as a function of different crystal temperatures.

It can be seen that  $\Delta P$  decreased with increasing bubbler temperatures or flow rates, and increased with crystal temperature. The reaction rate can be influenced by the pressure drop. As the reaction rate is proportional to the concentration of reactants and the reaction coefficient, with the same crystal temperature (same reaction coefficient), the concentration should be proportional to the flux. However, decomposition, by-products such as tert-butanol from a hydroxylation reaction and tert-butene from the  $\beta$ -hydride elimination can account for pressure effects. As a result, below 65 °C higher bubbler temperatures have higher adsorption or reaction rates and a smaller pressure decrease. At 75 °C however, there is a return of the pressure drop, which indicates the reaction becomes more mass transfer limited due to a lower diffusion coefficient at higher pressure. The crystal temperatures were all above the decomposition temperature of 185 °C. The pressure difference is larger with higher crystal

temperatures, indicating a faster reaction rate. It can also be deduced that more adsorption occurred than decomposition reactions by the fact that pressure decreased after the cell instead of increased, consistent with multilayer adsorption observed by ATR-FTIR experiments in Chapter 7.

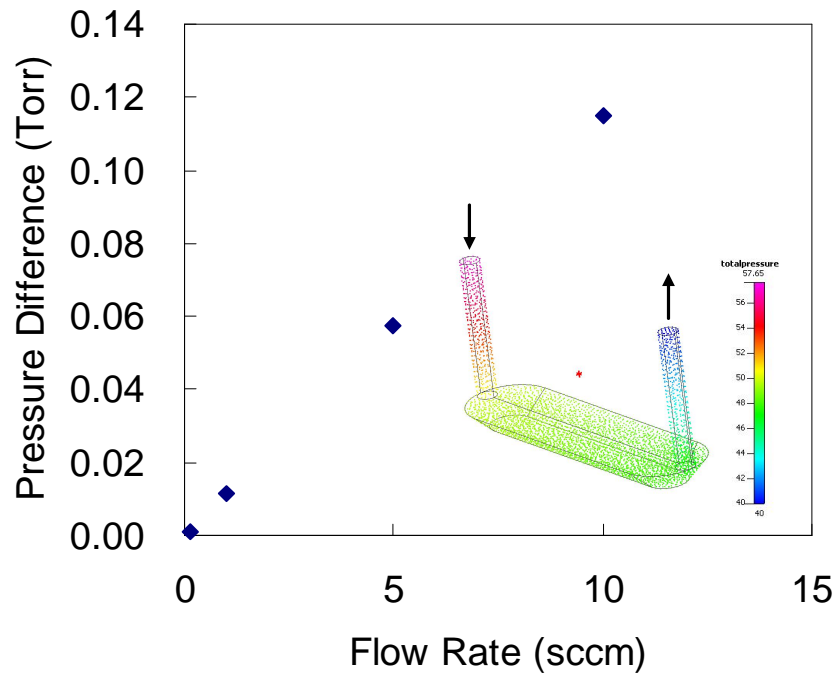


**Figure 8-8.** Pressure difference as a function of flow rate.

Since no reactions were included in the fluid behavior model, the simulated pressure difference was calculated to increase with increasing flow rate as shown in Figure 8-8, which is opposite to what was observed in experiment. Besides, pressure drop at 0.15 sccm was one magnitude less than what was observed in experiments. This indicates that in the real case, there was pressure drop due to friction and precursor consumption in the cell. It is worthwhile to mention that the pumping speed is assumed to stay in a limited range of throughput change.

#### 8.4.3 Film Thickness

Film thickness is a function of residence time and deposition rate. Instead of growing

ultrathin films, this article is focused on the fluid behavior during the deposition in the top plate heated horizontal flow through reactor from a macro point of view. Due to the limitation of the temperature range of the Kalrez gasket, a temperature range between 200 °C and 300 °C was investigated. Assumptions are made that several factors remain constant along the axis such as chemical composition, starting surface, coverage, and residence time. Growth kinetics is a function of temperature and concentration. It can also be assumed that the gas phase transport is much faster than the film growth rate, and that it may be assumed to be in pseudo-steady state.

Figure 8-9 shows the thickness variation along the axis after 1 hour of HTB adsorption with different bubbler temperatures when crystal was set at 250 °C. The average thickness trend is consistent with the pressure drop. It was perceived that in horizontal reactors, depletion occurs along the streamline. However, Figure 8-9 shows that by changing bubbler temperature, the precursor can either accumulate or be depleted at the latter part of the substrate, depending on the supply of precursor. For 65 °C, there are many possible causes for the accumulation. The most likely ones are as follows: since the top plate is hotter than the bottom substrate, it is likely that there are gas phase reactions leading to gaseous intermediates before the molecules reach the substrate. Due to a longer residence time in the horizontal reactor at the back end, the reactive intermediate concentration is higher than at the front end. The trapping coefficient for HTB is low and the precursor has to make several bounces before sticking to a surface site. Variation in the velocity field across the reactor can lead to film thickness dispersion. For other bubbler temperatures, the pressure decrease along the axis is a reflection of the decrease of the number of molecules per unit volume, or namely the concentration, or impingement flux which is linearly proportional to the pressure:

$$J_i \left( \frac{mc}{m^2 \cdot s} \right) = \frac{N_A P}{\sqrt{2\pi MRT}}.$$

Pressure is the force per unit area exerted on a surface and is

proportional to the number of molecules as well as temperature.  $p = \frac{1}{3} n m \overline{c^2} = n k_B T$  where

$n$  [ $\text{mc}/\text{m}^3$ ] = molecular concentration =  $N/V$ . However, the pressure term doesn't influence the flux perpendicular to the substrate due to cancellation of the effect by increased diffusivity.

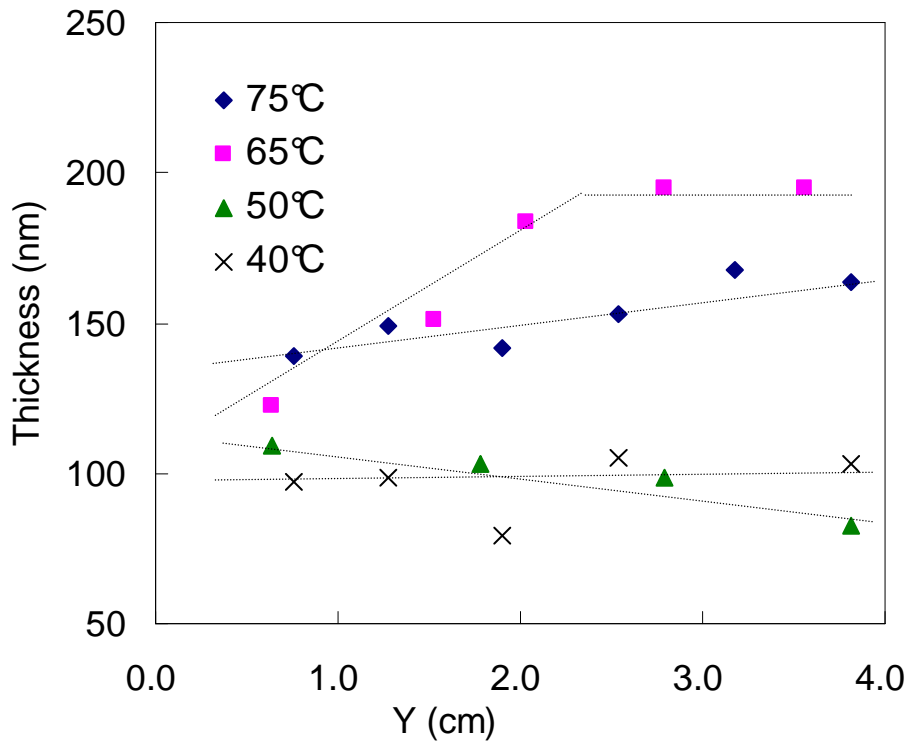


**Figure 8-9.** Thickness along axis with different bubbler temperature while the crystal temperature was 250 °C.

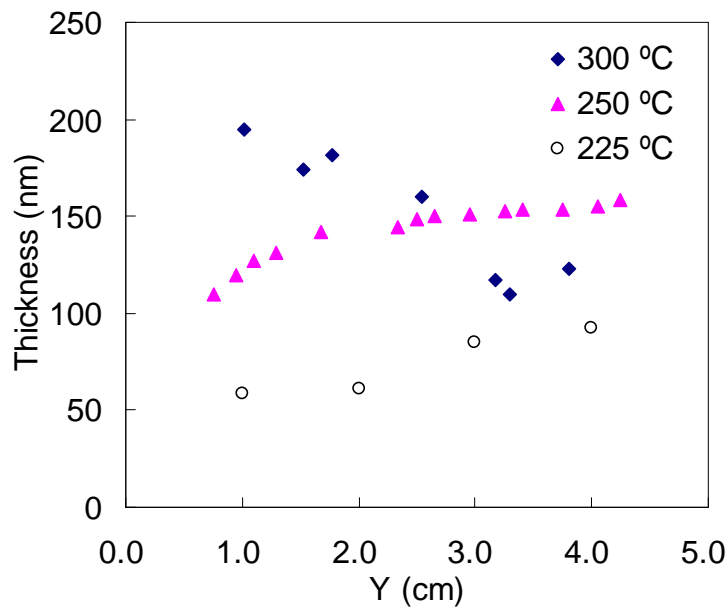


**Figure 8-10.** Thickness along axis with different crystal temperature, 1 hour HTB adsorption

with bubbler temperature of 65 °C.

Figure 8-10 shows the thickness variation along axis for various crystal temperature setting points with a bubbler temperature of 65 °C. The reaction becomes mass transfer limited at 300 °C, and depletion caused a thickness decrease occur along the axis.

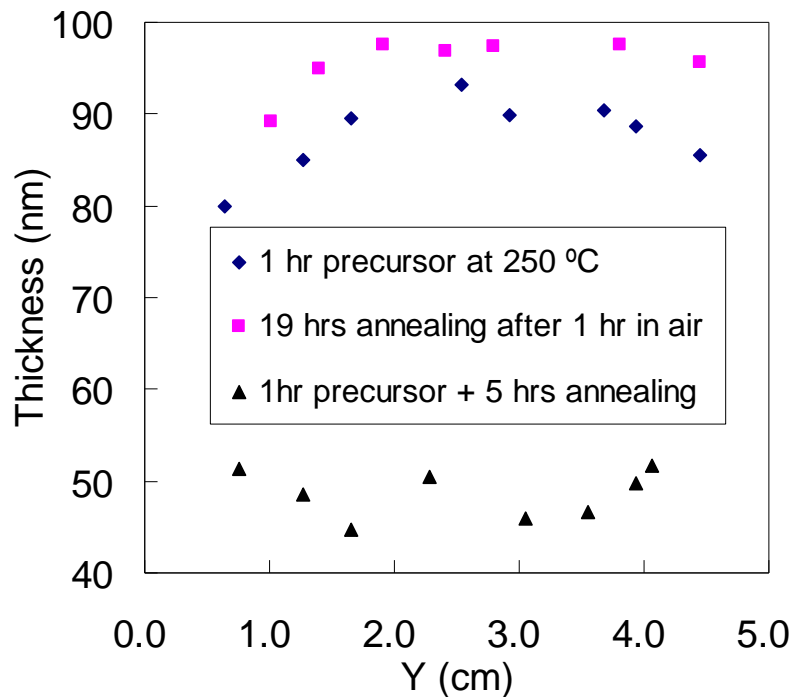


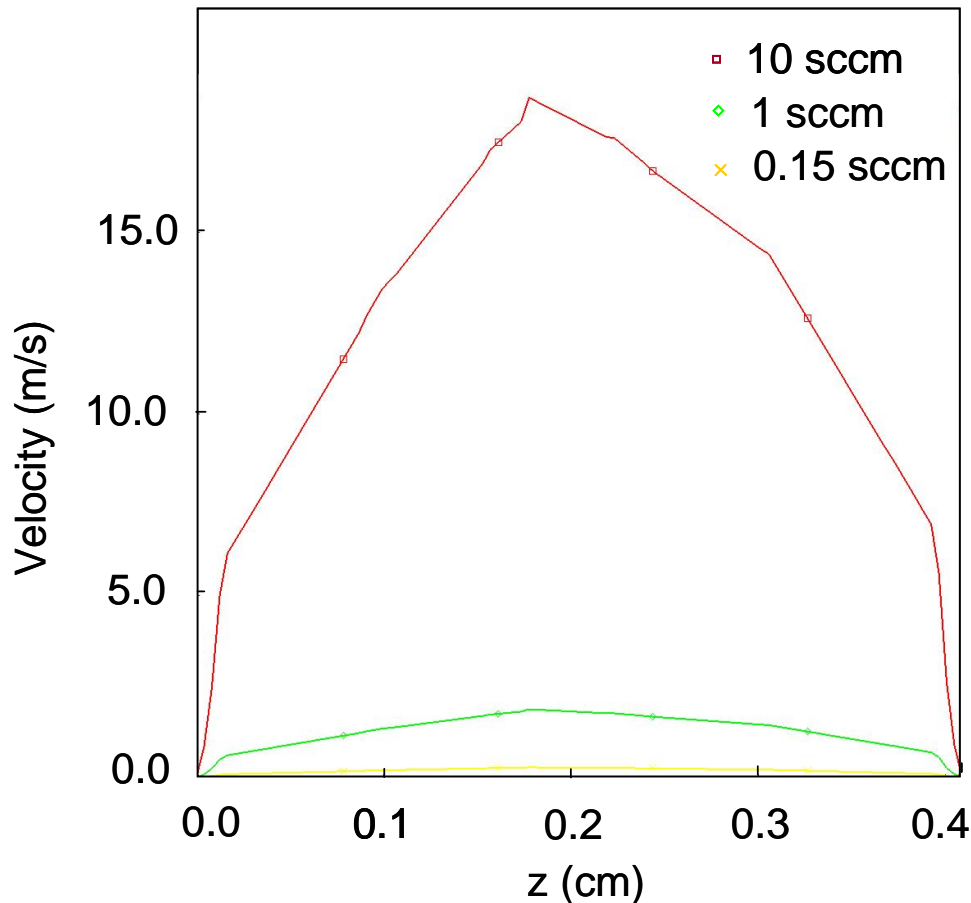
**Figure 8-11.** Thickness along the axis for HTB deposited on H-Si(100) crystal with bubbler at 65 °C and crystal setting temperature at 250 °C.

It is worthwhile to mention here that special attention has to be paid to sample preparation and time between disassembly and removal for the thickness measurement. Figure 8-11 shows a big difference when measuring the thickness with 5.5 hours annealing after stopping the precursor, because of desorption. During pump down, the trapped molecules may diffuse downstream on the surface during substrate cooling and before disassembly and measurement.

#### 8.4.4 Velocity Field and Flow Patten

Even without these complex flow patterns, the analysis of the deposition rate to determine film uniformity and composition with operation parameters is a nontrivial task.

The quantitative analysis of transverse dispersion in a particular flow has to be analyzed with precise calculation which requires setting parameters very accurately and carefully. Mixed convection may affect the thin film growth by the concentration of vapor supply and the density of films. A horizontal reactor with a uniform substrate temperature profile, and an inert gas stream velocity at steady state were modeled.



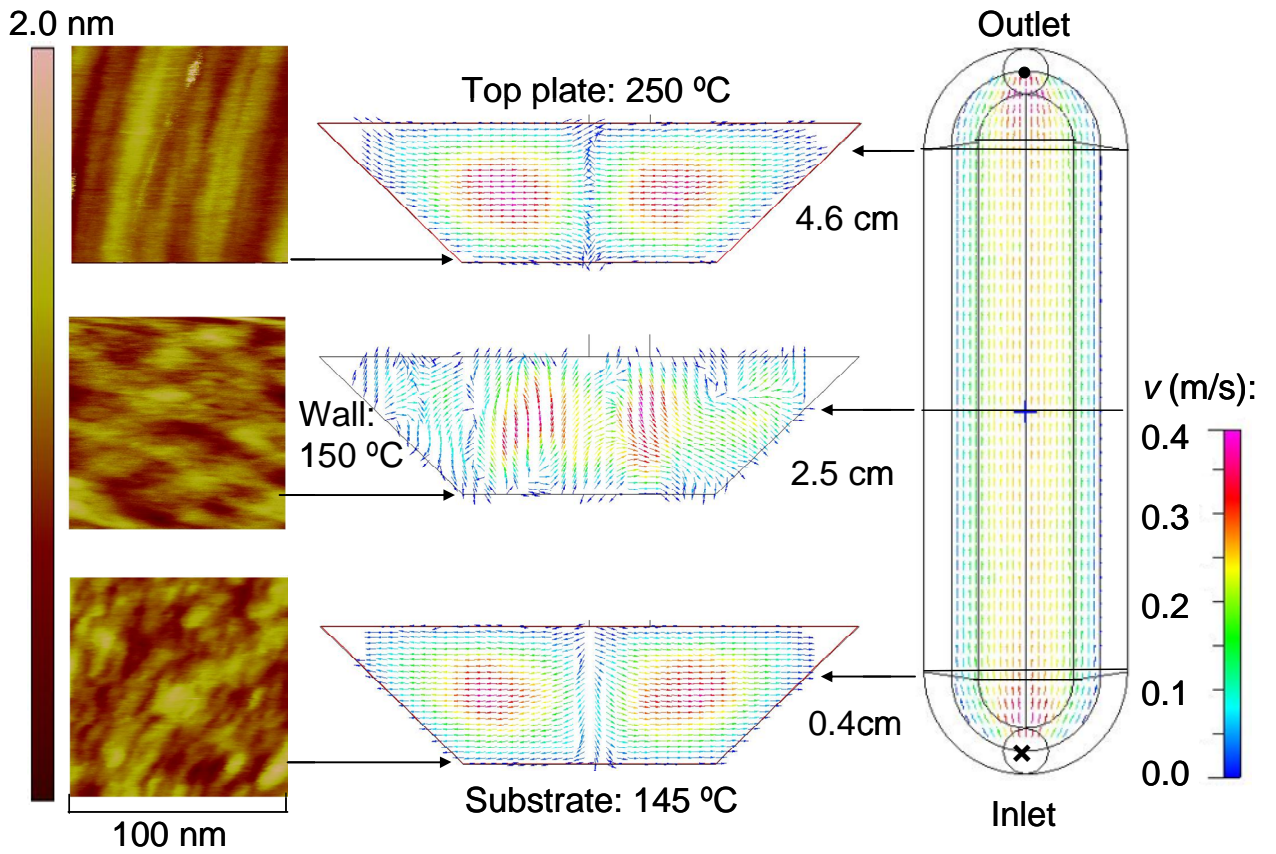
**Figure 8-12.** Velocity profile of the flow.

Figure 8-12 show the characteristic velocity profile with three flow rates using a very fine mesh. The parabolic shape of the velocity is due to viscosity. A non slip assumption was made for the laminar flow.

With a temperature difference of about 100 °C between the top heated plate and the bottom substrate, the Ra number gives the possibility of roll formation in the gas phase flow, which is known as the Bénard thermal instability problem. Instead of incorporating the possible homogeneous and heterogeneous reactions of the film growth, a simplified model

only investigating the pure inert flow pattern was simulated. On the other hand, while the modeler can try to differentiate the leading factors in fluid behavior, the experimentalist can provide intuitional real evidences.

Figure 8-13 shows mixed convection observed by calculation and verified by AFM images. The left column contains AFM images of the thin film surface at three locations along the axis on the H-Si(100) substrate. The crystal set point temperature was 250 °C with a bubbler temperature of 50 °C. The deposition duration was 1 hour. The middle and right columns are the CFD calculated flow behavior for 1 sccm N<sub>2</sub> in the isothermal flow cell with the top plate at 250 °C, the bottom substrate at 145 °C, and the wall at 150 °C. Mixed convection was observed. At the inlet and outlet positions, free convection occurs and forms roll type flow. Velocity vectors point away from the center at the inlet, and toward the center at the outlet. Compared with the AFM image on the left, it can be seen the flow pattern indeed influences the growth of the film by its morphology in addition to the growth rate as discussed above. A wavy type film surface was observed at the later part of the substrate. However, the exact location was difficult to control due to the instability of the flow and the scale of the meso-reactor. Only at the end of the substrate was the wavy surface observed. It is the first time the modeling prediction has been verified using the morphology of the thin film.



**Figure 8-13.** Mixed convection and film morphology with bubbler at  $50\text{ }^{\circ}\text{C}$  and HTB deposition on H-Si(100) for 1 hr.

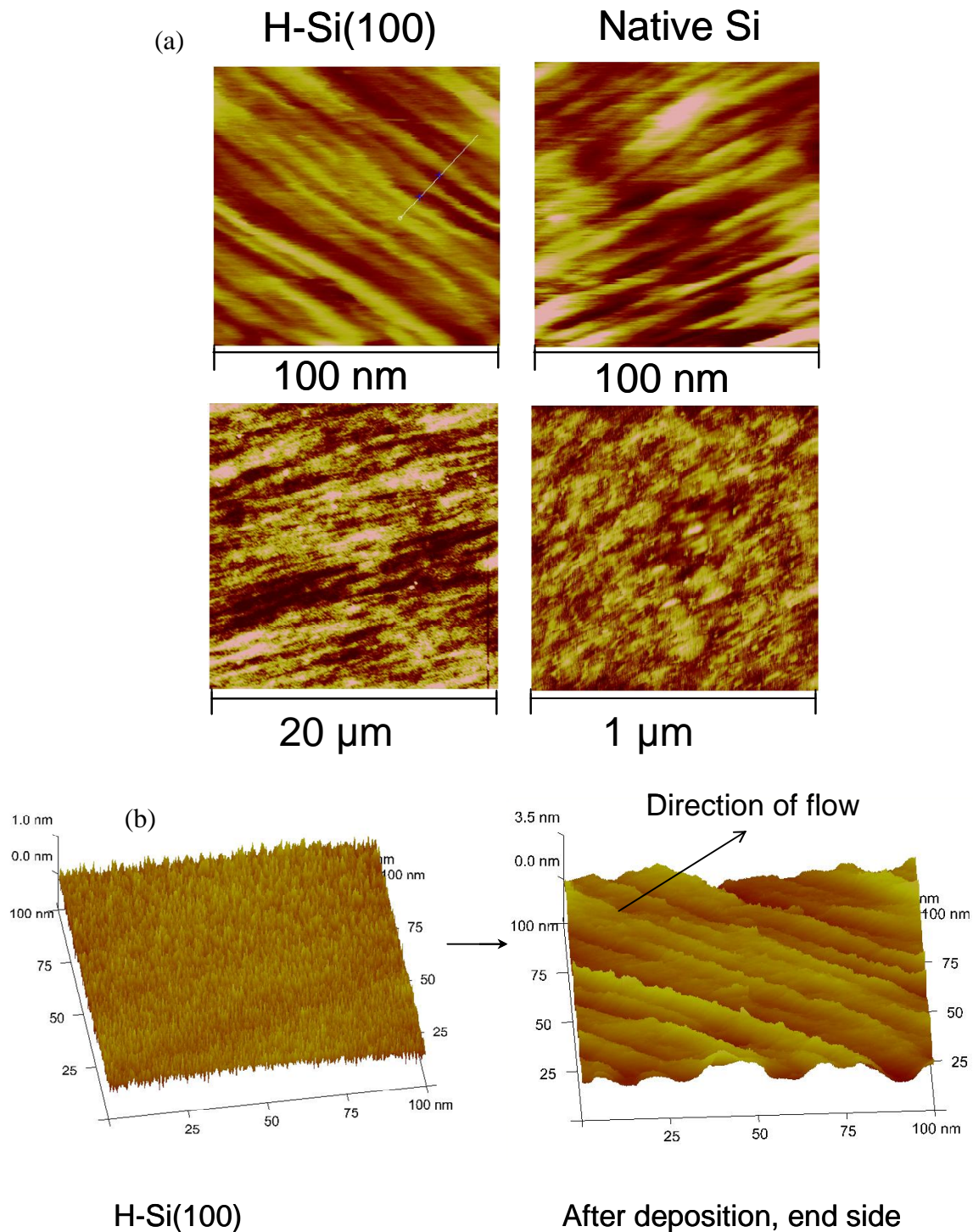


**Figure 8-14.** (a) AFM images at the end of the substrate for 1 hour HTB deposition with 65 °C bubbler temperature on 250 °C hydrogen terminated Si(100) crystal (left column) or with 50 °C bubbler temperature on 250 °C n-Si(100) wafer (right column). (b) 3-D AFM image for comparison between surface morphology before and after HTB adsorption on the H-Si(100) at the end side.

Figure 8-14 is a control experiment starting from different surfaces on both H-Si(100) crystal and n-Si(100) wafer with a 1.07 nm native oxide. Both reactor temperatures were 250

°C. The bubbler temperature was 65 °C for the H-Si(100) and 50 °C for the native Si oxide surfaces. It is likely that higher flow rates produced “condensed” rolls that make the wavy periodicity smaller as observed on the H-Si(100) surface. The wavy surface was observed at 100 nm for both surfaces and at larger scales only for the H-Si(100), which may be due to the isotropic nature of the amorphous native oxide that cause the molecules to diffuse more easily than on a H-Si(100) surface.

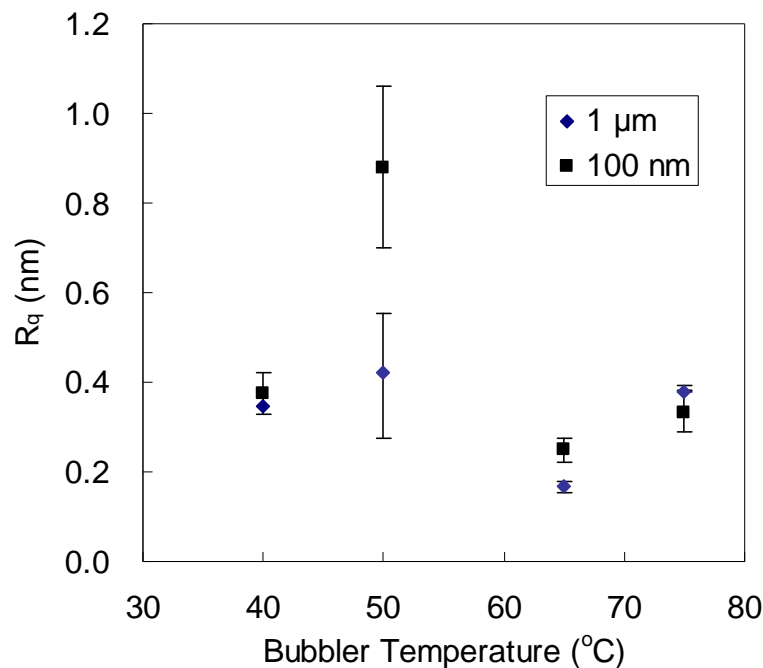


**Figure 8-15.** Roughness with different bubbler temperatures on native Si wafer.

The rolls increased with residence time and may enhance the diffusivity at the microscopic level. When diffusivity is faster than advection, the concentration field downstream can be bigger than that upstream, which may explain the thickness increase downstream as discussed in the previous section.

Starting with a different surface, roughness behaves differently. With a H-Si surface, roughness decreased with thickness, while for a native Si wafer, roughness increased with thickness. The average roughness for 1 hour of HTB on a 250 °C Si wafer is shown in Figure 8-15. During the deposition experiment, the pressure was around 0.3 Torr. Since the Si

substrate temperature was 250 °C, the ratio of the substrate temperature to the HfO<sub>2</sub> melting point 2812 °C is about 0.17, and it is expected to have minimal adatom diffusion, so the film has many defects, is fine-grained, with a columnar structure and with low density boundaries between columns based on the Movchan-Demchishin model.<sup>2</sup> In this case, all the roughnesses are actually very small compared to the film thickness. The largest RMS roughness occurred with a bubbler temperature at 50 °C, which is consistent with the observation of wavy film at this condition.

## **8.5 Chapter Summary**

The temperature profile for a Horizon<sup>TM</sup> flow cell was measured and the reactor heat transfer analysis for temperature set points between 60 °C and 250 °C was done by FEA method. Temperature difference between the top heated plate and the bottom substrate was found to increase with temperature set point with the highest temperature at the middle of the axis. At a set point of 250 °C, the temperature difference was about 100 °C, which caused mixed convection for the flow in the cell with a bubbler temperature between 50 to 65 °C. The roll type flow influenced thin film growth and was confirmed by AFM. The depletion problem common in horizontal reactors and film uniformity was found to be tunable with different precursor supply flow rates. However, the periodicity of the rolls cannot be controlled very well at this time and further study has to be performed on this phenomena.

## Chapter 9 Conclusion and Future Work

### 9.1 Conclusions

The gas phase and surface chemistry of TDMAH, TEMA, and HTB during the initial ALD adsorption processes are complex reactions rather than simple steps as often described in the literature. *In situ* transmission and ATR infrared spectroscopy showed the three precursors' adsorption and reaction onto hydrogen terminated Si surfaces involve some common characters. In the gas phase, only a very small amount of by-products due to slight decomposition or hydrolysis were detected for all of these precursors, which is consistent with the DFT calculation that these decomposition reactions are thermodynamically unfavorable in the gas phase. However, decomposition products were observed prevalently on the surfaces even at room temperatures after certain amount of dose. These decompositions can occur during chemisorptions onto the surface from a thermodynamic point of view.

During the first cycle of ALD of TDMAH on to a H-Si surface at a temperature range of 25 °C to 250 °C, multilayer physisorption occurred with a large precursor dose. TDMAH was calculated to form a bidentate chemisorbed species on the hydrogen terminated Si surface by forming two N-Si bonds through cleavage of N-CH<sub>3</sub> on the complex and H-Si on the surface. The  $\beta$ -hydride elimination and insertion reactions generated the TH and TI-3 species, and were identified by the  $\nu_{\text{Hf-H}}$  at 1650 cm<sup>-1</sup> and  $\nu_{\text{(Hf)N-C}}$  at 1210 cm<sup>-1</sup> on the hydrogen terminated Si surface as probed by ATR-IR. A variety of by-products such as MMI and DMA can be produced as shown by the detection of  $\nu_{\text{C=N}}$  at 1670 cm<sup>-1</sup> in MMI and  $\delta_{\text{N-H}}$  at 735 cm<sup>-1</sup> in DMA in the gas phase by transmission IR with further support by Q-MS

experiments. The MMI either undergo a silylation reaction leading to the incorporation of contaminants or desorb into the gas phase.

For TEMAH, the proposed  $\beta$ -hydride elimination product MEI was detected in the gas phase at  $1664\text{ cm}^{-1}$  and a species containing Hf-H were identified on the surface at  $1640\text{ cm}^{-1}$ . Energetics of possible gas phase reactions was found to have a high energy barrier but may be feasible at elevated temperatures. The MEI can either undergo a silylation reaction leading to the incorporation of contaminants or desorb into the gas phase.

For HTB,  $\beta$ -hydride elimination generated Hf-OH located at  $3678\text{ cm}^{-1}$ . The symmetric t-butyl umbrella modes on two ligands at  $1226\text{ cm}^{-1}$  and  $1016\text{ cm}^{-1}$  indicate bidentate chemisorption of HTB on Si surfaces at temperatures below  $150\text{ }^\circ\text{C}$  and carbonate incorporated in the film at higher temperatures. Spectra generated by density functional theory (DFT) calculations of monodentate and bridging adsorbed precursors as well as a spectrum of an applied liquid drop of HTB were used to identify the chemisorbed species. Surface concentrations of the mono- or bidentate- chemisorbed species were dependant on both the substrate temperature as well as the substrate orientation.

The transport speed or vapor pressures of the three precursors are in the decreasing sequence:  $\text{HTB} > \text{TDMAH} > \text{TEMAH}$ , while their decomposition liability in the gas phase is in the opposite sequence. Multilayer adsorption and continuous condensation were observed for TDMAH and TEMAH at room temperature, while saturation was observed for HTB at  $60\text{ }^\circ\text{C}$ .

Free convection with roll type flow in the flow through cell with a temperature set point at  $250\text{ }^\circ\text{C}$  was predicted by CFD and confirmed by AFM. The temperature was calibrated for the reactor with a wider substrate distribution with increased set points and smaller influence with lower temperature set points. Thin film uniformity can be tuned by varying the supply precursor rates.

## 9.2 On-going and Future Work Proposals

There are several problems remaining to be solved and needs further analysis listed below:

1. IR peak at  $1600\text{ cm}^{-1}$  needs identification for both TDMAH and TEMAH.
2. Although the interfacial bonding was probed for TDMAH and HTB to be N-Si and O-Si respectively, the bidentate model needs further analysis to see if it is a prevalent phenomena for all.
3. It would be interesting to know how the surface catalyzed the decomposition of these precursors or calculate some other Hf-H species.
4. If possible, a control experiment of  $\text{HfH}_4$  + water is suggested to confirm the mild reaction between Hf-H and water.
5. A control experiment of gas phase IR using KBr windows for TDMAH or TEMAH is needed to exclude the Si window causing decomposition reactions on the observation of by-products yet only a very small amount.
6. The middle peak at  $1226\text{ cm}^{-1}$  in the triplet band during low temperature HTB adsorption seems to be a degenerated vibration from one of the neighbor peaks. A fundamental electron transfer effect could be behind this phenomenon like a Bohlmann-type band and would be interesting to investigate.
7. Interface band calculation can be performed with the Vienna *ab-initio* simulation package (VASP) using pseudopotentials and a plane wave basis set. Since interfacial bonding has been observed, the band structure at the interface can be predicted in order to quantify the interfacial bond influence on the important MOSFET FOMs such as band offsets.
8. As a preliminary trial, the thickness along the substrate axis was measured after 100 cycles of ALD using TDMAH and water. The procedure is in Figures B-9 and B-10 Appendix A. The uniformity was not as good as reported as shown in Figure 9-1. Further flow dynamic

influenced thin film growth and precursor selection can be investigated.

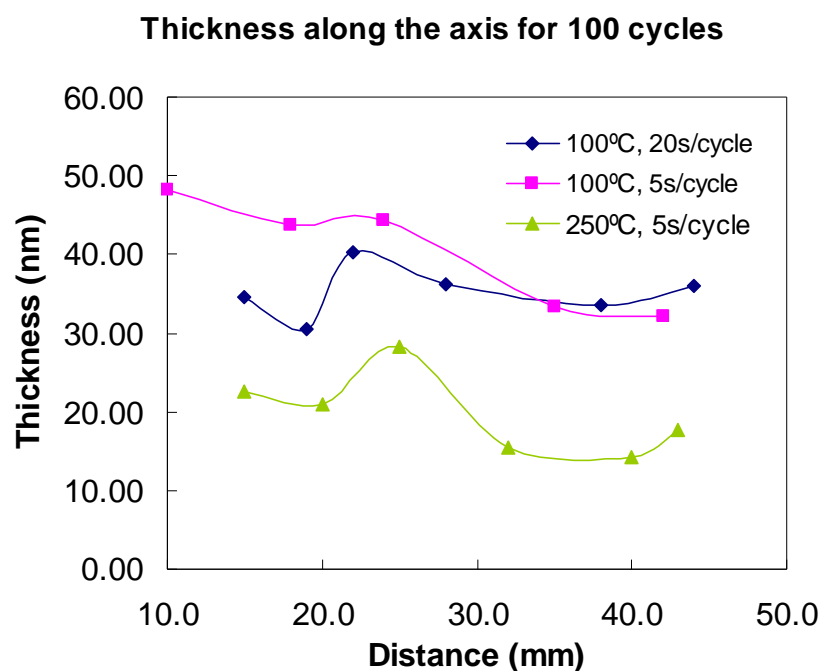


**Figure 9-1.** Thickness variation along axis for TDMAH/H<sub>2</sub>O ALD.

9. Various deposition conditions have to be probed for HTB flow influenced thin film topography pattern. However, there is a limit of temperature range to change for Gr number due to the reactor design. To find how the periodicity of the rolls on the surface changes as a function of flow rate or temperature gradient, the flow reactor has to be modified.

10. TEMAH gas phase induced reaction and liquid creep induced surface adsorption rate can also be investigated. The slow transport and decomposition behavior of TEMAH is very different from that of TDMAH. In order to measure the creep rate, draw kinetic information and elucidate reaction mechanisms for the whole process, the following schematic setup is proposed which can help realize these goals. The conversion can be deduced from the precursors' transmission IR intensities in two gas cells. Combining the *in situ* ATR - FTIR monitoring of 1 ML (defined by the saturation of  $\nu_{\text{Hf-H}}$  as discussed in Chapter 5), the sticking coefficient can be deduced.<sup>19</sup>

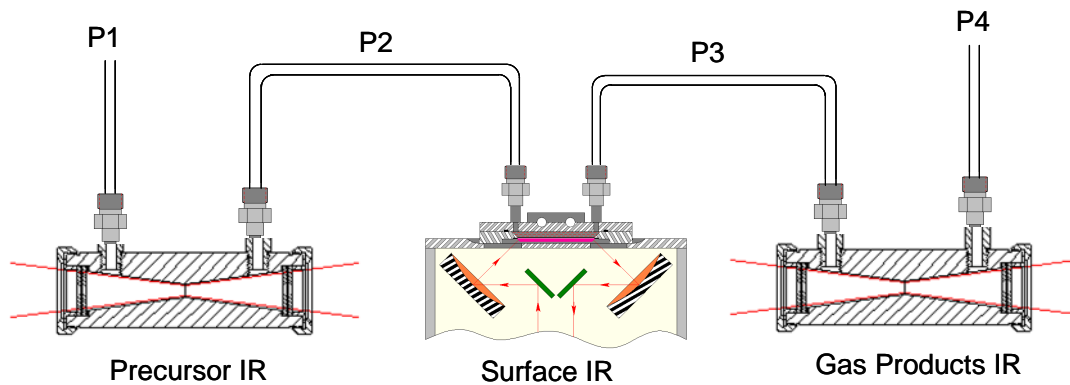


**Figure 9-2.** Experimental setup for IR monitoring of the whole process.

11.  $\text{HfO}_2$  Issues. Recently it is reported that devices that utilize  $\text{HfO}_2$  gate dielectrics suffer from mobility degradation, fixed charge issues, threshold voltage instability, and a  $\kappa$  dependence on the crystal structures, lower carrier mobility and degraded reliability. Additional elements were added to  $\text{HfO}_2$  such as Si, Al,<sup>182</sup> N, and Zr.<sup>183</sup> Different precursors can be investigated that may influence the adsorption and reaction mechanisms.

12. Gate Materials and Higher Mobility Substrates. While  $\text{HfO}_2$  is employed, the conventional gate material, poly-Si, is reported to have serious problems in forming Hafnium silicate ( $\text{HfSi}_x\text{O}_y$ ) during high temperature annealing.<sup>184</sup> Nitrides such as TaN and conductive oxides such as  $\text{RuO}_2$  were considered as gate candidates for sub-0.13  $\mu\text{m}$  CMOS, and poly  $\text{Si}_x\text{Ge}_y$  for sub-0.1  $\mu\text{m}$  CMOS.<sup>185</sup> Hafnium nitride ( $\text{HfN}$ ) is considered to be the most suitable electrode material candidate due to its low resistivity, high melting point, high density, and being an excellent barrier against oxygen diffusion.<sup>186</sup> Some groups have begun to study the underlying chemistry reactions of ALD for certain systems such as titanium nitride films.<sup>187,188</sup> Another trend is using a higher carrier mobility channel and gate such as strained Ge, MBE  $\text{HfO}_2$  grown on Ge, which is reported to have a sharp interface due to Fermi level pinning.<sup>189</sup> A GeON layer passivated by a  $\text{NH}_3$  anneal is an effective barrier layer to form hafnium germanides. The interfacial bonding between the thin film and the Ge substrate can be studied by IR.

## References

- 
- <sup>1</sup> D. Kahng, M. M. Atalla, *IRE Solid-State Device Res. Conf.* Pittsburgh, PA , **1960**.
- <sup>2</sup> J. R. Brews, *Metal-oxide-semiconductor field-effect transistor. In Microelectronics*; J. C. Whitaker; CRC Press: Boca Ranton, FL, **2006**; 4-1.
- <sup>3</sup> [ftp://download.intel.com/museum/Moores\\_Law/Video-Transcripts/Excepts\\_A\\_Conversation\\_with\\_Gordon\\_Moore.pdf](ftp://download.intel.com/museum/Moores_Law/Video-Transcripts/Excepts_A_Conversation_with_Gordon_Moore.pdf)
- <sup>4</sup> Semiconductor Industry Roadmap **2009**.  
[http://www.itrs.net/Links/2009ITRS/2009Chapters\\_2009Tables/2009\\_FEP.pdf](http://www.itrs.net/Links/2009ITRS/2009Chapters_2009Tables/2009_FEP.pdf)
- <sup>5</sup> Y. Taur, D.A. Buchanan, W. Chen, D.J. Frank, K.E. Ismail, S.-H. Lo, G.A. Sai-Halasz, R.G. Viswanathan, H.-J.C. Wann, S.J. Wind, H.-S. Wong, *Proc. IEEE*, **1997**, 85, 486.
- <sup>6</sup> J. Robertson, *Reports on Progress Physics*, **2006**, 69, 317.
- <sup>7</sup> R.P. Vasquez, M.H. Hecht, E.J. Grunthner and M.L. Naiman, *Appl. Phys. Lett.*, **1984**, 44, 969.
- <sup>8</sup> H. Wong, H. Iwai, *Microelec. Eng.* **2006**, 83, 1867.
- <sup>9</sup> J.D. Livingston, *Electronic properties of engineering materials*, John Wiley & Sons, Inc. MA, **1999**.
- <sup>10</sup> P.A. Cox, *Transition metal oxides*, Oxford Sci. Pub.: Oxford, U.K., **1992**.
- <sup>11</sup> M.L. Cohen, *J. Vac. Sci. Technol.* **1979**, 16, 1135.
- <sup>12</sup> J. A. T. Suntola, *B05D 5/00 ed.* Finland, **1977**; page 58.
- <sup>13</sup> M. Leskelä, M. Ritala, *Thin Solid Films*, **2002**, 409, 138.
- <sup>14</sup> R.G. Gordon, D. Hausmann, E. Kim, J. Shepard, *Chemical Vapor Deposition*, **2003**, 9, 73.
- <sup>15</sup> Hausmann, D. M.; Gordon, R. G. *J. Cryst. Growth*, **2003**, 249, 251.
- <sup>16</sup> George, S. *Chem. Rev.*, **2010**, 110, 111.
- <sup>17</sup> Puurunen, R. *J. Appl. Phys.* **2005**, 97, 121301.
- <sup>18</sup> Mitchell, D. R. G.; Aidla, A.; Aarik, *J. Applied Surf. Sci.*, **2006**, 253, 606.
- <sup>19</sup> D.L. Smith, *Thin Film disposition*, McGraw-Hill , Inc. **1995**.

- 
- <sup>20</sup> K.F. Jensen, E.O. Einset, D.I. Fotiadis, *Annu. Rev. Fluid Mech.* **1991**, 23, 197.
- <sup>21</sup> T. C. Cheng, P. H. Chiou, T. F. Lin, *Intl. J. Heat & Mass Transfer*, **2002**, 45, 3357.
- <sup>22</sup> W.G. Breiland, G.H. Evans, *J. Electrochem. Soc.*, **1991**, 138, 1806.
- <sup>23</sup> H. Moffat, K.F. Jensen, *J. Crystal Growth*, **1986**, 77, 108.
- <sup>24</sup> V. Mikhelashvili, B. Meyler, S. Yoffis, J. Salzman, M. Garbrecht, T. Cohen-Hyams, W. D. Kaplan, and G. Eisenstein, *Appl. Phys. Lett.* **2009**, 95, 023104.
- <sup>25</sup> A. Khodakov, B. Olthof, A.T. Bell, E. Iglesia, *J. Catalysis*, **1999**, 181, 205.
- <sup>26</sup> J. Tsaur, K. Onodera, T. Kobayashi, Z.-J. Wang, S. Heisig, R. Maeda, T. Suga, *Sensors and Actuators A*, **2005**, 121, 275.
- <sup>27</sup> G. Tsutsui, T. Hiramoto, *IEEE Transactions on Electron Devices*, **2006**, 53, 2582.
- <sup>28</sup> Y. Zhao, T. Wang, D. Zhang, J. Shao, Z. Fan, *Appl Surf. Sci.* **2005**, 245, 335.
- <sup>29</sup> D.A. Neumayer, E. Cartier, *J. Appl. Phys.* **2001**, 90, 1801.
- <sup>30</sup> P. Yang, D. Zhao, D.I. Margolese, B.F. Chmelka, G.D. Stucky, *Nature*, **1998**, 396, 152.
- <sup>31</sup> T. Moon, J. Lee, M. Ham, *J. Myoung, Microelec. Eng.* **2006**, 83, 2452.
- <sup>32</sup> M. Song, S. Kang, and S. Rhee, *Thin Solid Films*, **2004**, 450, 272.
- <sup>33</sup> X. Liu, S. Ramanathan, A. Longdergan, A. Srivastava, E. Lee, T. E. Seidel, J. T. Barton, D. Pang, R. G. Gordon, *J. Electrochem. Soc.*, **2005**, 152, G213.
- <sup>34</sup> P.A. Williams, A.C. Jones, N.L. Tobin, P.R. Chalker, S. Taylor, P.A. Marshall, J.F. Bickley, L.M. Smith, H.O. Davies, G.W. Critchlow, *Chem. Vap. Deposition* **2003**, 9, 309.
- <sup>35</sup> A.S. Zoofakar, H. Hashim, S. Taylor, *Solid-State and Integrated-Circuit Tech., 9<sup>th</sup> International Conference*, **2008**, 1268.
- <sup>36</sup> Y. Wang, M.T. Ho, L.V. Goncharova, L.S. Wielunski, S. Rivillon-Amy, Y.J. Chabal, T. Gustafsson, N. Moumen, M. Boleslawski, *Chem. Mater.* **2007**, 19, 3127.
- <sup>37</sup> J.J. Ganem, I. Trimaille, I.C. Vickridge, D. Blin, F. Martin, *Nuclear instruments and Methods in Physics Research Section B: Beam Interactions with Materials and Atoms*, **2004**, 219-220, 856.
- <sup>38</sup> A. Milanov, R. Thomas, M. Hellwig, K. Merz, H.-W. Becker, P. Ehrhart, R.A. Fischer, R. Waser, A. Devi, *Surface and Coatings Technology*, **2007**, 201, 9019.
- <sup>39</sup> A. Deshpande, R. Inman, G. Jursich, C. Takoudis, *Microelectr. Eng.* **2006**, 83, 547.
- <sup>40</sup> D. Schmeier, E. Zschech, *Materials Science in Semiconductor Processing*, **2006**, 9, 934.

- 
- <sup>41</sup> K. Kukli, M. Ritala, T. Sajavaara, J. Keinonen, M. Leskelä, *Chem. Vap. Deposition* **2002**, *8*, 199.
- <sup>42</sup> L. Zhong, Z. Zhang, S.A. Campbell, W.L. Gladfelter, *J. Mater. Chem.* **2004**, *14*, 3203.
- <sup>43</sup> D.M. Hausmann, R.G. Gordon, *J. Cryst. Growth* **2003**, *249*, 251.
- <sup>44</sup> X.L. Green, A.J. Allen, X. Li, J. Wang, J. Ilavsky, A. Delabie, R.L. Puurunen, B. Brijs, *Appl. Phys. Lett.* **2006**, *88*, 032907.
- <sup>45</sup> Axel, D. B. *J. Chem. Phys.* **1993**, *98*, 5648.
- <sup>46</sup> J.C. Hackley, J.D. Demaree, T. Gougousi, *J. Vac. Sci. Technol. A* **2008**, *26*, 1235.
- <sup>47</sup> S.C. Chen, J.C. Lou, C.H. Chien, P.T. Liu, T.C. Chang, *Thin Solid Films*, **2005**, *488*, 167.
- <sup>48</sup> A. Deshpande, R. Inman, G. Jursich, C. Takoudis, *Microelec. Eng.* **2006**, *83*, 547.
- <sup>49</sup> P. Dumas, Y.J. Chabal, P. Jakob, *Surf. Sci.* **1992**, *269/270*, 867.
- <sup>50</sup> Y. Caudano, P.A. Thiry, Y.J. Chabal, *Surf. Sci.* **2002**, *502-503*, 91.
- <sup>51</sup> Y.J. Chabal, K. Raghavachari, *Surf. Sci.* **2002**, *502-503*, 41.
- <sup>52</sup> G.F. Cerofolini, C. Galati, S. Reina, L. Renna, G.G. Condorelli, I.L. Fragal, G. Giorgi, A. Sgamellotti, N. Re, *Appl. Surf. Sci.* **2005**, *246*, 52.
- <sup>53</sup> J.E. Northrup, *Phys. Rev. B* **1991**, *44*, 1419.
- <sup>54</sup> M. Morita, T. Ohmi, E. Hasegawa, M. Kawakami, M. Ohwada, *J. Appl. Phys.* **1990**, *68*, 1272.
- <sup>55</sup> M.L. Green, M.Y. Ho, B. Busch, G.D. Wilk, T. Sorsch, T. Conard, B. Brijs, W. Vandervorst, P.I. Raisanen, D. Muller, M. Bude, J. Grazul, *J. Appl. Phys.* **2002**, *92*, 7168.
- <sup>56</sup> P. Mack, R.G. White, J. Wolstenholme, T. Conard, *Appl. Surf. Sci.* **2006**, *252*, 8270.
- <sup>57</sup> L.L. Chua, J. Zaumseil, J.F. Chang, E.C.W. Ou, P.K.H. Ho, H.R. Siringhaus, H. Friend, *Nature*, **2005**, *434*, 194.
- <sup>58</sup> G. He, Q. Fang, L.D. Zhang, *Materials Science in Semiconductor Processing*, **2006**, *9*, 870.
- <sup>59</sup> Kelly, M. J.; Han, J. H.; Musgrave, C.B.; Parsons, G. N. *Chem. Mater.* **2005**, *17*, 5305.
- <sup>60</sup> M.J. Ho, Y. Wang, R.T. Brewer, L.S. Wielunski, Y.J. Chabal, N. Moumen, M. Boleslawski, *Appl. Phys. Lett.* **2005**, *87*, 133103.
- <sup>61</sup> M.M. Frank, S. Sayan, S. Dörmann, T.J. Emge, L. S. Wielunski, E. Garfunkel, Y. J. Chabal, *Materials Science and Engineering B* **2004**, *109*, 6.

- 
- <sup>62</sup> M.A. Cameron, S.M. George, *Thin Solid Films*, **1999**, *348*, 90.
- <sup>63</sup> B.-C. Kan, J.-H. Boo, I. Lee, F. Zaera, *J. Phys. Chem. A*, **2009**, *113*, 3946.
- <sup>64</sup> W. Wang, T. Nabatame, Y. Shimogaki, *Jpn. J. Appl. Phys.* **2006**, *45*, L1183.
- <sup>65</sup> M.J. Biecuk, D.J. Monsma, C.M. Marcus, J.S. Becker, R.G. Gordon, *Appl. Phys. Lett.* **2003**, *83*, 2405.
- <sup>66</sup> L.H. Dubois, B.R. Zegarski, G.S. Girolami, *J. Electrochem. Soc.* **1992**, *139*, 3603.
- <sup>67</sup> J.P.A.M. Driessen, J. Schoonman, K.F. Jensen, *J. Electrochem. Soc.* **2001**, *148*, G178.
- <sup>68</sup> A. Soulet, L. Duquesne, G. Jursich, R. Inman, A. Misra, N. Blasco, C. Lachaud, Y. Marot, R. Prunier, M. Vautier, S. Anderson, R. Clancy, M. Havlicek, *Semiconductor Fabtech*, FT27, **2005**.
- <sup>69</sup> J. N. Musher, R.G. Gordon, *J. Mater. Res.* **1996**, *11*, 989.
- <sup>70</sup> S. Salim, C.K. Lim, K.F. Jensen, *Chem. Mater.* **1995**, *7*, 507.
- <sup>71</sup> H. Cai, X. Yu, S. Chen, H. Qiu, I.A. Guzei, Z.L. Xue, *Inorg. Chem.* **2007**, *46*, 8071.
- <sup>72</sup> J. N. Musher, R. G. Gordon, *J. Electrochem. Soc.* **1996**, *143*, 736.
- <sup>73</sup> C. Airoidi, D. C. Bradley, G. Vuru, *Transition Met. Chem.* **1979**, *4*, 64.
- <sup>74</sup> B.-C. Kan, J.-H. Boo, I. Lee, F. Zaera, *J. Phys. Chem. A* **2009**, *113*, 3946.
- <sup>75</sup> W. Chen, Q.Q. Sun, M. Xu, S.J. Ding, D.W. Zhang, L.K. Wang, *J. Phys. Chem. C* **2007**, *111*, 6495.
- <sup>76</sup> Rodriguez-Reyes, J. C. F.; Teplyakov, A. V. *J. Phys. Chem. C* **2007**, *111*, 4800.
- <sup>77</sup> N.J. Harrick, *J. Phys. Chem.* **1960**, *64*, 1110.
- <sup>78</sup> J. Fahrenfort, *Spectrochim. Acta*, **1962**, 698.
- <sup>79</sup> G. Lucovsky, G.B. Rayner Jr., Y. Zhang, C.C. Fulton, R.J. Nemanich, G. Appel, H. Ade, J.L. Whitten, *Appl. Surf. Sci.* **2003**, *212-213*, 563.
- <sup>80</sup> Surface analysis by Auger and X-ray photoelectron spectroscopy, ed. J.T. Grant and D. Briggs, IM publications, Chichester, U.K., **2003**
- <sup>81</sup> <http://www.wikipedia.com>
- <sup>82</sup> P. J. Cumpson, *Surf. Interface Anal.* **2000**, *29*, 403.

- 
- <sup>83</sup> P. J. Cumpson and M. P. Seah, *Surf. Interface Anal.* **1997**, 25, 430.
- <sup>84</sup> I.N. Levin, *Quantum Chemistry*, 5th Edition. Prentice-Hall, Inc.: New Jersey, **2000**.
- <sup>85</sup> M. Born and J.R. Oppenheimer, *Ann. Phys.* **1927**, 79, 361.
- <sup>86</sup> D.R. Hartree, *Proc. Cambridge Philos. Soc.* **1928**, 24, 328.
- <sup>87</sup> V.A. Fock, *Z. Phys.* **1930**, 15, 126.
- <sup>88</sup> S.F. Boys, *Proc. R. Soc. London*, **1950**, A200, 542.
- <sup>89</sup> C.C. Roothaan, *Rev. Mod. Phys.* **1951**, 23, 69.
- <sup>90</sup> D. Feller, E.R. Davidson, *In Reviews in Computational Chemistry*; K.B. Lipkowitz, D.B. Boyd, Ed; VCH: New York, **1990**; Vol. 1.
- <sup>91</sup> C.C.J. Roothaan, *Reviews of Modern Physics*, **1951**, 23, 69; G.G. Hall, *Proceedings of the Royal Society London A*, **1951**, 205, 541.
- <sup>92</sup> P. Hohenberg and W. Kohn, *Phys. Rev.* **1964**, 136, B864.
- <sup>93</sup> J.P. Perdew and W. Yue, *Phys. Rev. B* **1986**, 33, 8800.
- <sup>94</sup> C. Lee, W. Yang, and R.G. Parr, *Phys. Rev. B* **1988**, 37, 785.
- <sup>95</sup> J.P. Perdew, *Phys. Rev. B* **1986**, 33, 8822.
- <sup>96</sup> J.P. Perdew, *Phys. Rev. B* **1986**, 34, 046.
- <sup>97</sup> C.F. von Weizsacker, *Z. Physik*, **1935**, 96, 431.
- <sup>98</sup> A.D. Becke, *J. Chem. Phys.* **1993**, 98, 5648.
- <sup>99</sup> H. Vosko, L. Wilk and M. Nusair, *Canadian J. Phys.* **1980**, 58, 1200-1211.
- <sup>100</sup> K. Burke, J. P. Perdew and Y. Wang, *Electronic Density Functional Theory: Recent Progress and New Directions*, Ed. J. F. Dobson, G. Vignale and M. P. Das, Plenum, **1998**.
- <sup>101</sup> C.E. Dykstra, *Quantum Chemistry & Molecular Spectroscopy*, Prentice-Hall: New Jersey, **1991**.
- <sup>102</sup> Gaussian 03, Revision E.01, Frisch, M. J.; Trucks, G. W.; Schlegel, H. B.; Scuseria, G. E.; Robb, M. A.; Cheeseman, J. R.; Montgomery, Jr., J. A.; Vreven, T.; Kudin, K. N.; Burant, J. C.; Millam, J. M.; Iyengar, S. S.; Tomasi, J.; Barone, V.; Mennucci, B.; Cossi, M.; Scalmani, G.; Rega, N.; Petersson, G. A.; Nakatsuji, H.; Hada, M.; Ehara, M.; Toyota, K.; Fukuda, R.; Hasegawa, J.; Ishida, M.; Nakajima, T.; Honda, Y.; Kitao, O.; Nakai, H.; Klene, M.; Li, X.; Knox, J. E.; Hratchian, H. P.; Cross, J. B.; Bakken, V.; Adamo, C.; Jaramillo, J.; Gomperts, R.; Stratmann, R. E.; Yazyev, O.; Austin, A. J.; Cammi, R.; Pomelli, C.; Ochterski, J. W.; Ayala, P.

- 
- Y.; Morokuma, K.; Voth, G. A.; Salvador, P.; Dannenberg, J. J.; Zakrzewski, V. G.; Dapprich, S.; Daniels, A. D.; Strain, M. C.; Farkas, O.; Malick, D. K.; Rabuck, A. D.; Raghavachari, K.; Foresman, J. B.; Ortiz, J. V.; Cui, Q.; Baboul, A. G.; Clifford, S.; Cioslowski, J.; Stefanov, B. B.; Liu, G.; Liashenko, A.; Piskorz, P.; Komaromi, I.; Martin, R. L.; Fox, D. J.; Keith, T.; Al-Laham, M. A.; Peng, C. Y.; Nanayakkara, A.; Challacombe, M.; Gill, P. M. W.; Johnson, B.; Chen, W.; Wong, M. W.; Gonzalez, C.; and Pople, J. A.; Gaussian, Inc., Wallingford CT, 2004.
- <sup>103</sup> Halls, Mathew D.; Raghavachari, Krishnan; Frank, Martin M.; Chabal, Yves J. *Phys. Rev. B* **2003**, 68, 161302
- <sup>104</sup> J. Ren, Y.-T. Zhang, and D. W. Zhang, *J. Molecular Structure: THEOCHEM* **2007**, 803, 23.
- <sup>105</sup> K. Li, S. Dubey, H. B. Bhandari, Z. Hu, C. H. Turner, and T. M. Klein, *Journal of Vacuum Science & Technology A: Vacuum, Surfaces, and Films* **2007**, 25, 1389.
- <sup>106</sup> R. D. Fenno, M. D. Halls, and K. Raghavachari, *J. Phys. Chem. B* **2005**, 109, 4969.
- <sup>107</sup> Axel, D. B. *J. Chem. Phys.* **1993**, 98, 5648-5652.
- <sup>108</sup> C. Lee, W. Yang, R.G. Parr, *Phys. Rev. B*, **1988**, 37, 785.
- <sup>109</sup> C. Peng, P.Y. Ayala, H.B. Schlegel, M.J. Frisch, *J. Comp. Chem.* **1996**, 17, 49.
- <sup>110</sup> C. Peng, H.B. Schlegel, *Israel J. Chem.* **1993**, 33, 449.
- <sup>111</sup> Schlegel, H. B. *J. Comp. Chem.* **1982**, 3, 214.
- <sup>112</sup> W.R. Wadt, P.J. Hay, *J. Chem. Phys.* **1985**, 82, 284.
- <sup>113</sup> (a) Dunning, T.H. *J. Chem. Phys.* **1989**, 90, 1007. (b) Kendall, R.A.; Dunning, T.H.; Harrison, R.J. *J. Chem. Phys.* **1992**, 96, 6796. (c) Woon, D. E.; Dunning, T. H. *J. Chem. Phys.* **1993**, 98, 1358.
- <sup>114</sup> Figgen, D.; Peterson, K. A.; Dolg, M.; Stoll, H. *J. Chem. Phys.* **2009**, 130, 164108.
- <sup>115</sup> Y. Chabal, K. Raghavachari, *Phys. Rev. Lett.* **1985**, 54, 1055.
- <sup>116</sup> Y. Chabal, K. Raghavachari, *Phys. Rev. Lett.* **1984**, 53, 282.
- <sup>117</sup> G.S. Higashi, Y.J. Chabal, G.W. Trucks, R. Krishnan, *Appl. Phys. Lett.* **1990**, 56, 656.
- <sup>118</sup> M.D. Halls, K. Raghavachari, M.M. Frank, Y.J. Chabal, *Phys. Rev. B* **2003**, 68, 161302
- <sup>119</sup> D.B. Axel, *J. Chem. Phys.* **1993**, 98, 5648.
- <sup>120</sup> C. Lee, W. Yang, R.G. Parr, *Phys. Rev. B*, **1988**, 37, 785.
- <sup>121</sup> C. Peng, P.Y. Ayala, H.B. Schlegel, M.J. Frisch, *J. Comp. Chem.* **1996**, 17, 49.
- <sup>122</sup> C. Peng, H.B. Schlegel, *Israel J. Chem.* **1993**, 33, 449.

- 
- <sup>123</sup> H.B. Schlegel, *J. Comp. Chem.* **1982**, *3*, 214.
- <sup>124</sup> W.R. Wadt, P.J. Hay, *J. Chem. Phys.* **1985**, *82*, 284.
- <sup>125</sup> (a) T.H. Dunning, *J. Chem. Phys.* **1989**, *90*, 1007. (b) R.A. Kendall, T.H. Dunning, R.J. Harrison, *J. Chem. Phys.* **1992**, *96*, 6796. (c) D.E. Woon, T.H. Dunning, *J. Chem. Phys.* **1993**, *98*, 1358.
- <sup>126</sup> D. Figgen, K.A. Peterson, M. Dolg, H. Stoll, *J. Chem. Phys.* **2009**, *130*, 164108.
- <sup>127</sup> E.E. Ernstbrunner, J. Hudec, *J. Mol. Struct.* **1973**, *17*, 249.
- <sup>128</sup> H.D. Thomas, K.H. Chen, N.L. Allinger, *J. Am. Chem. Soc.* **1994**, *116*, 5887.
- <sup>129</sup> D.C. McKean, I.A. Ellis, *J. Mol. Struct.* **1975**, *29*, 81.
- <sup>130</sup> F. Bohlmann, *F. Angew. Chem.* **1957**, *69*, 641; D.C. McKean, I.A. Ellis, *J. Mol. Struct.* **1975**, *29*, 81; H.D. Thomas, K.H. Chen, N.L. Allinger, *J. Am. Chem. Soc.* **1994**, *116*, 5887.
- <sup>131</sup> D.M. Hausmann, E. Kim, J. Becker, R.G. Gordon, *Chem. Mater.* **2002**, *14*, 4350.
- <sup>132</sup> I. Stolkin, T.-K. Ha, Hs.H. Günthard, *Chem. Phys.* **1977**, *21*, 327.
- <sup>133</sup> J.Y. Yun, M.Y. Park, S.W. Rhee, *J. Electrochem. Soc.* **1998**, *145*, 2453.
- <sup>134</sup> M. Dai, Y. Wang, J. Kwon, M.D. Halls, Y.J. Chabal, *Nature Mater.* **2009**, *8*, 825.
- <sup>135</sup> Y.C. Liu, K. Furukawa, D.W. Gao, H. Nakashima, K. Uchino, K. Muraoka, *Appl. Surf. Sci.* **1997**, *121/122*, 233.
- <sup>136</sup> V.N. Khabashesku, S.E. Boganov, K.N. Kudin, J.L. Margrave, O.M. Nefedov, *Organomet.* **1998**, *17*, 5041.
- <sup>137</sup> C. Mui, J.H. Han, G.T. Wang, C.B. Musgrave, S.F. Bent, *J. Am. Chem. Soc.*, **2002**, *124*, 4027.
- <sup>138</sup> B. Stuart, *Infrared Spectroscopy: Fundamentals and Applications*, Wiley, **2004**.
- <sup>139</sup> K. Li, S. Dubey, H.B. Bhandari, Z. Hu, C.H. Turner, T.M. Klein, *J. Vac. Sci & Tech. A.* **2007**, *25*, 1389
- <sup>140</sup> P. Jakob, Y.J. Chabal, K. Raghavachari, S.B. Christman, *Phys. Rev. B* **1993**, *47*, 6839.
- <sup>141</sup> M.H. Chisholm, M.W. Extine, *J. Am. Chem. Soc.* **1977**, *99*, 792.
- <sup>142</sup> F. Quignard, C. Lecuyer, A. Choplin, J.-M. Basset, *J. Chem. Soc., Dalton Trans.*, **1994**, *7*, 1153.

- 
- <sup>143</sup> V. Vidal, A. Théolier, J. Thivolle-Cazat, J.-M. Basset, *Science*, **1997**, 276, 99.
- <sup>144</sup> G.V. Chertihin, L. Andrews, *J. Phys. Chem.* **1995**, 99, 15004.
- <sup>145</sup> M. Zhou, L. Zhang, J. Dong, Q. Qin, *J. Am. Chem. Soc.* **2000**, 122, 10680.
- <sup>146</sup> T. Shimanouchi, *Tables of Molecular Vibrational Frequencies Consolidated Volume I*, National Bureau of Standards, **1972**, 1-160.
- <sup>147</sup> D.A. Neumayer, E. Cartier, *J. Appl. Phys.* **2001**, 90, 1801.
- <sup>148</sup> C. Baldwin, M.F. Lappert, J.B. Pedley, J.S. Poland, *J. Chem. Soc. Dalton Trans.*, **1972**, 18, 1943.
- <sup>149</sup> X. Liu, S. Ramanathan, A. Longdergan, A. Srivastava, E. Lee, T.E. Seidel, J.T. Barton, D. Pang, R.G. Gordon, *J. Electrochem. Soc.* **2005**, 152, G213.
- <sup>150</sup> R. S. Mulliken, *J. Chem. Phys.* **1955**, 23, 1833-1840.
- <sup>151</sup> Meyerson, B.S. Himpfel, F.J. Uram, K.J. *Appl. Phys. Lett.* **1990**, 10, 1034.
- <sup>152</sup> Boland, J.J. *Phys. Rev. B*, **1991**, 44, 3.
- <sup>153</sup> J. Robertson, P.W. Peacock, *Microelectr. Eng.* **2004**, 72, 112.
- <sup>154</sup> J.I. Steinfeld, J.S. Francisco, W.L. Hase, *Chemical Kinetics and Dynamics*, 2<sup>nd</sup> edition, Prentice Hall: New Jersey, **1999**.
- <sup>155</sup> Y. Amatatsu, Y. Hamada, M. Tsuboi, *J. Mol. Spectrosc.* **1985**, 111, 29.
- <sup>156</sup> L.H. Dubois, B. R. Zegarski, G. S. Girolami, *J. Electrochem. Soc.* **1992**, 139, 3603.
- <sup>157</sup> T. Egawa, S. Konaka, *J. Phys. Chem. A* **2001**, 105, 2085.
- <sup>158</sup> M.A. Cameron and S. M. George, *Thin Solid Films* **1999**, 348, 90.
- <sup>159</sup> Y.J. Chabal, *Phys. Rev. B* **1984**, 29, 3677.
- <sup>160</sup> O. Sneh, M. L. Wise, A. W. Ott, L. A. Okada, and S. M. George, *Surf. Sci.* **1995**, 334, 135.
- <sup>161</sup> R.C. Mehrotra, D.C. Bradley, I.P. Rothwell, A. Singh, *Alkoxo and Aryloxo Derivatives of Metals*, Revised edition ed. Academic Press, **2001**.
- <sup>162</sup> M. M. Frank, S. Sayan, S. Dormann, T. J. Emge, L. S. Wielunski, E. Garfunkel, and Y. J. Chabal, *Materials Science and Engineering B* **2004**, 109, 6.
- <sup>163</sup> P. H. S. Koji Nakanishi, *Infrared Absorption Spectroscopy*, 2nd ed. Holden-Day, Inc., California, **1977**.

- 
- <sup>164</sup> G. A. Somorjai, *Introduction to Surface Chemistry and Catalysis* Wiley-Interscience, **1994**.
- <sup>165</sup> S. Brunauer, P. H. Emmett, and E. Teller, *J. Am. Chem. Soc.* **1938**, *60*, 309.
- <sup>166</sup> H. Setyawan, M. Shimada, K. Ohtsuka, K. Okuyama, *Chemical Engineering Science* **2002**, *57*, 497.
- <sup>167</sup> N.L. Privorotskaya, W.P. King, *Sensors and Actuators A: Physical*, (accepted manuscript) **2009**.
- <sup>168</sup> C.R. Kleijn, *J. Electrochem. Soc.*, **1991**, *138*, 2191.
- <sup>169</sup> H. Moffat, K.F. Jensen, *J. Cryst.l Growth*, **1986**, *77*, 108.
- <sup>170</sup> ITRS 2007 edition; <http://www.itrs.net>.
- <sup>171</sup> K.F. Jensen, *Chem. Eng. Sci.*, **1987**, *42*, 927.
- <sup>172</sup> K.F. Jensen, *J. Crystal Growth*, **1989**, *98*, 148.
- <sup>173</sup> D.J. Quiram, K.F. Jensen, M.A. Schmidt, P.L. Mills, J.F. Ryley, M.D. Wetzel, and D.J. Kraus, *Ind. Eng. Chem. Res.* **2007**, *46*, 8319.
- <sup>174</sup> The CRC Handbook of Thermal Engineering, **2002**.
- <sup>175</sup> S. Patnaik, R.A. Brown, C.A. Wang, *J. Cryst. Growth*, **1989**, *96*, 153.
- <sup>176</sup> Wadt, W. R.; Hay, P. J. *J. Chem. Phys.* **1985**, *82*, 284.
- <sup>177</sup> Clyde R. Metz, *Physical Chemistry*, McGraw-Hill: New York, NY, **1988**, p. 27-28.
- <sup>178</sup> Pijush K. Kundu, Ira M. Cohen, *Fluid Mechanics*, Academic, San Diego, CA, **2002**.
- <sup>179</sup> H. Moffat, K.F. Jensen, *J. Cryst. Growth*, **1986**, *77*, 108.
- <sup>180</sup> K.E. Grew, T.L. Ibbs, *Thermal Diffusion in Gases*, Cambridge University Press.: Cambridge U.K.,**1952**.
- <sup>181</sup> J.O. Hirshfelder, C.F. Curtis and R.B. Bird, *Molecular theory of gases and liquids*, 1<sup>st</sup> ed.,Wiley, **1964**.
- <sup>182</sup> K.Y. Lee, W.C. Lee, M.L. Huang, C.H. Chang, Y.J. Lee, Y.K. Chiu, T.B. Wu, M. Hong, R. Kwo, *J. Crystal Growth*, **2007**. 301-302, 378.
- <sup>183</sup> J.J. Gallegos, D.H. Triyoso, M. Raymond, *Microelectronic Eng.* **2008**, *85*, 49.
- <sup>184</sup> H.Y. Yu, N. Wu, M.F. Li, C. Zhu, B.J. Cho, D.L. Kwong, C.H. Tung, J.S. Pan, J.W. Chai, W.D. Wang, D.Z. Chi, C.H. Ang, J.Z. Zheng, S. Ramanathan, *Appl. Phys. Lett.* **2002**, *81*, 3618.

- 
- <sup>185</sup> G.D. Wilk, R.M. Wallace, J.M. Anthony, *Appl. Phys. Rev.* **2001**, *89*, 5243.
- <sup>186</sup> Y. Kim, A. Baunemann, H. Parala, A. Devi, R. A. Fischer, *Chem. Vapor. Dep.* **2005**, *11*, 294.
- <sup>187</sup> S. Panda, J. Kim, B.H. Weiller, D.J. Economou, D.M. Hoffman, *Thin Solid Films* **1999**, *357*, 125.
- <sup>188</sup> S.R. Kurtz, R.G. Gordon, *Thin Solid Films*, **1986**, *140*, 277.
- <sup>189</sup> M. Caymax, S. Van Elshocht, M. Houssa, A. Delabie, T. Conard, M. Meuris, M.M. Heyns, A. Dimoulas, S. Spiga, M. Fanciulli, J.W. Seo, L.V. Goncharova, *Mater. Sci. Eng. B* **2006**, *135*, 256.

## **Appendix A**

Experimental Configurations and Thermal Transfer Material Properties

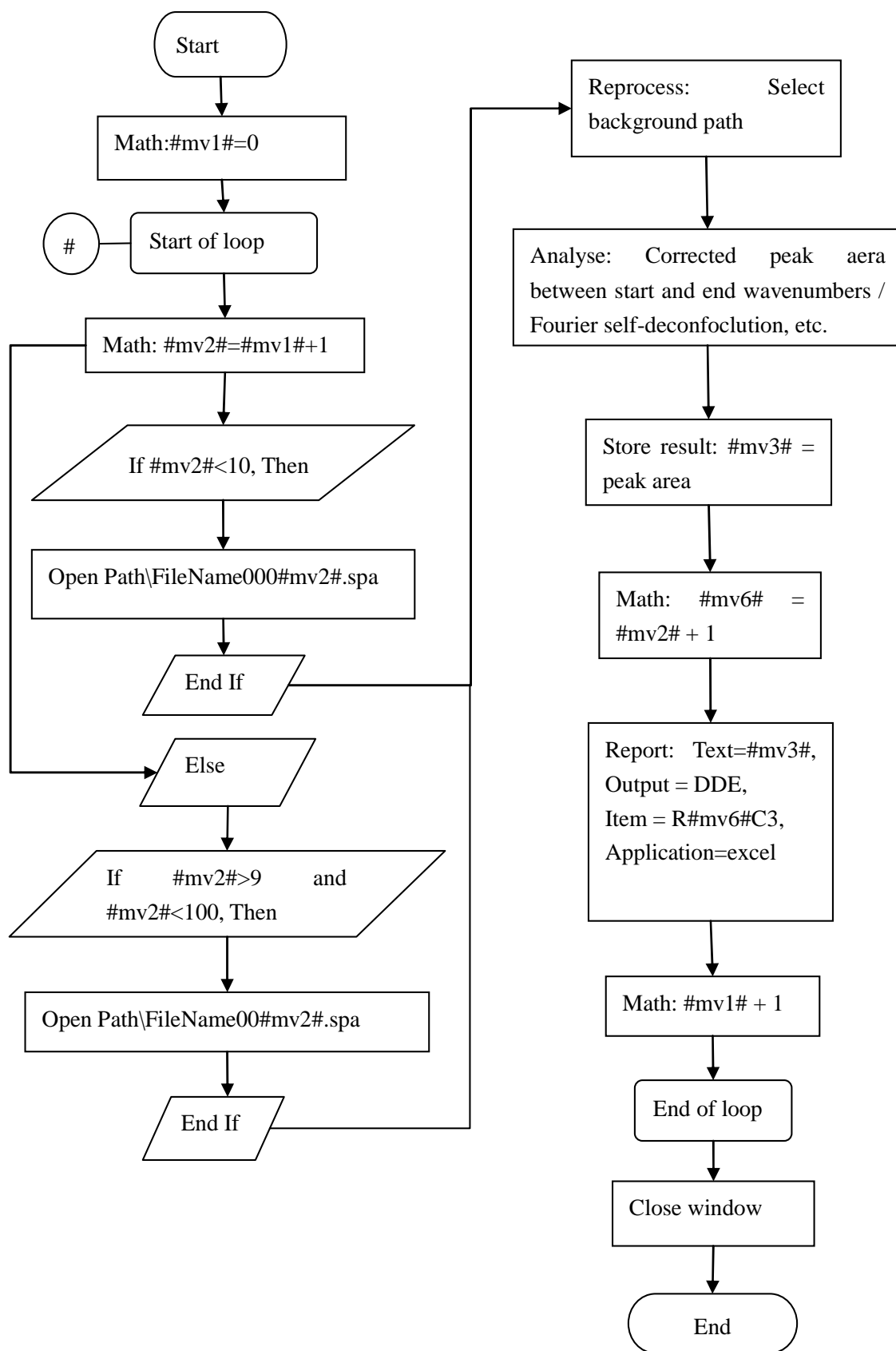


**Figure B-1.** Omnic Macro program for auto spectra processing and analysis.

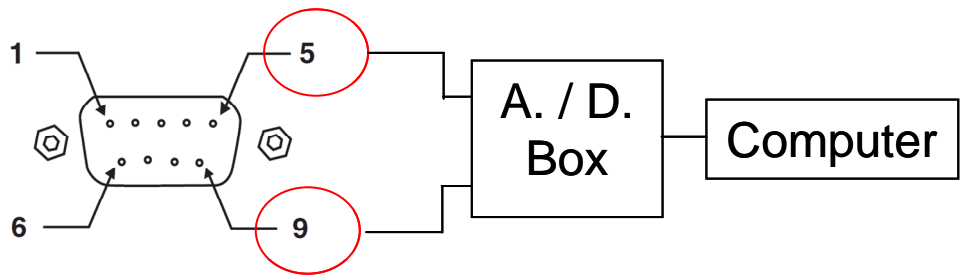


**Figure B-2.** The MKS Piani gauge readout electronic interfacing with an RS232 / serial port.

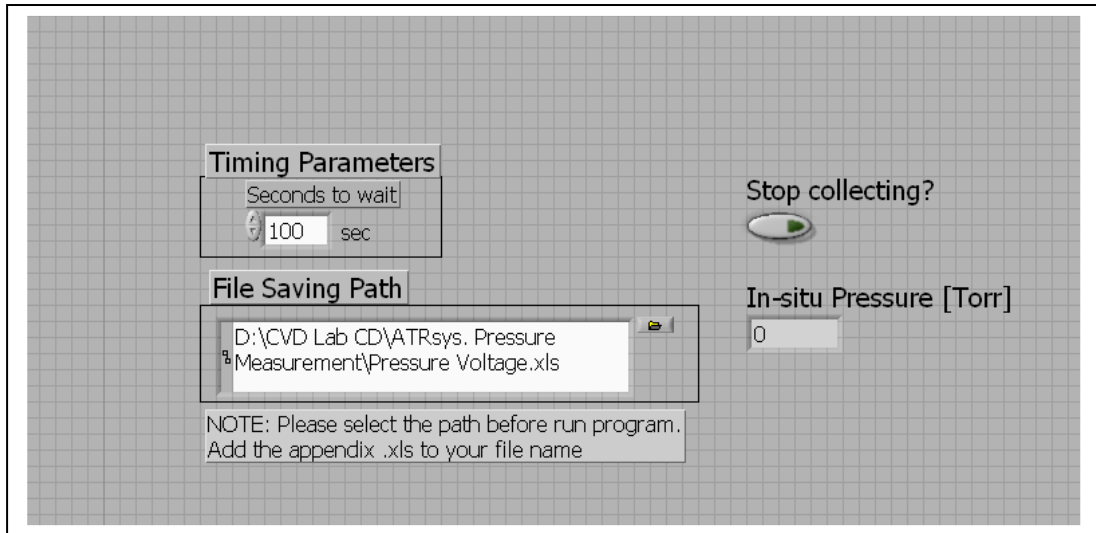


**Figure B-3.** Voltage-Pressure Measure LabView Front Panel

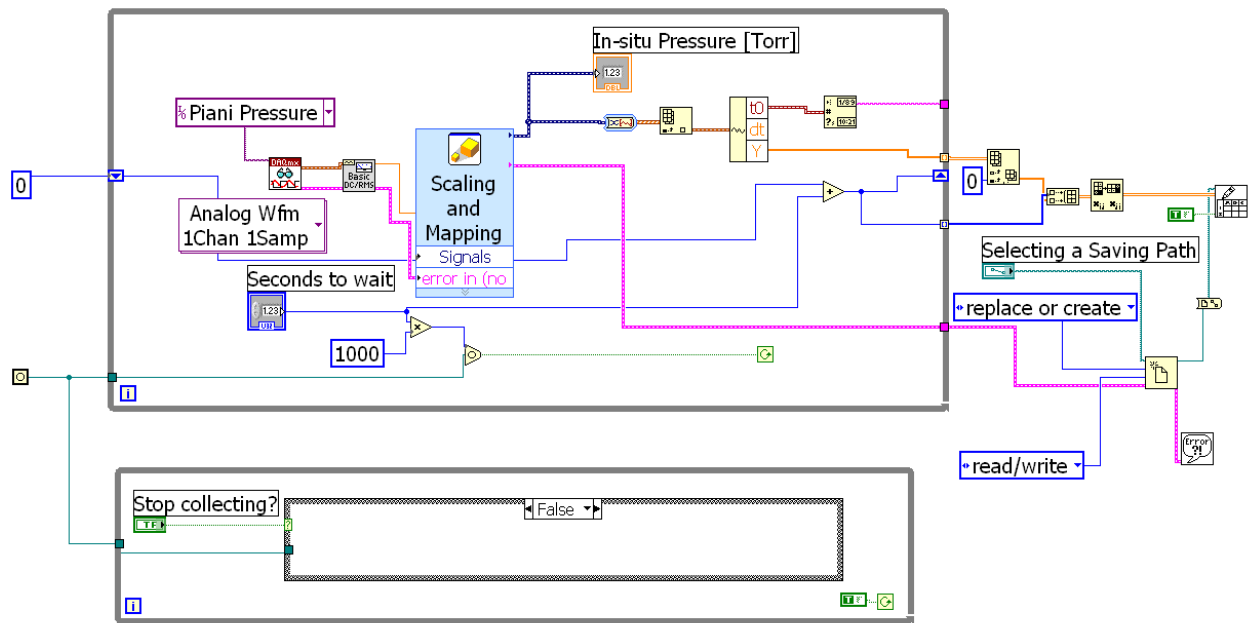


**Figure B-4.** Voltage-Pressure Measure LabView Block Diagram

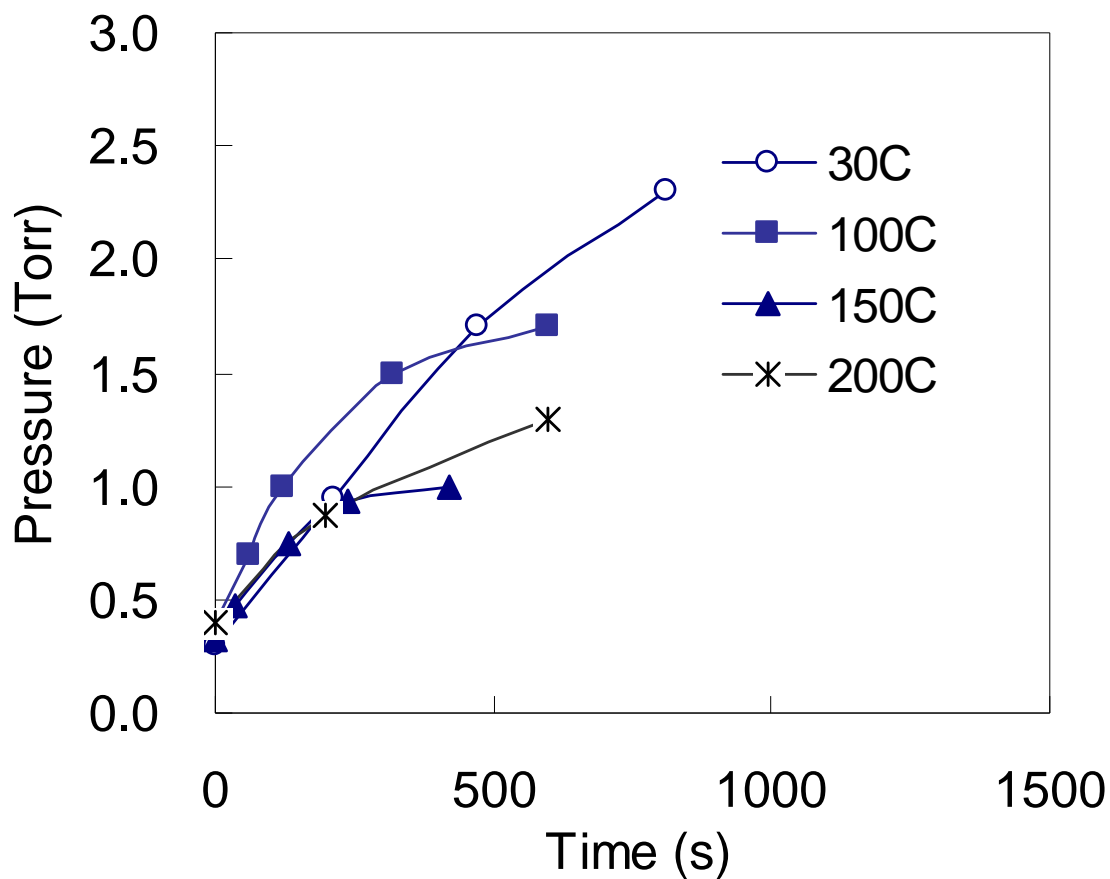


**Figure B-5.** Pressure recorded as a function of time at temperatures from 25 to 200°C for TDMAH in a closed cell.

At the initial stage at 25°C, the pressure increases nearly linearly with time, consistent with a unimolecular first order decomposition reaction to produce DMA. The slopes for the initial stages are 0.003, 0.005, 0.004, and 0.002 Torr/s for temperatures at 25, 100, 150, and 200 °C. More reactions occur at higher temperatures.

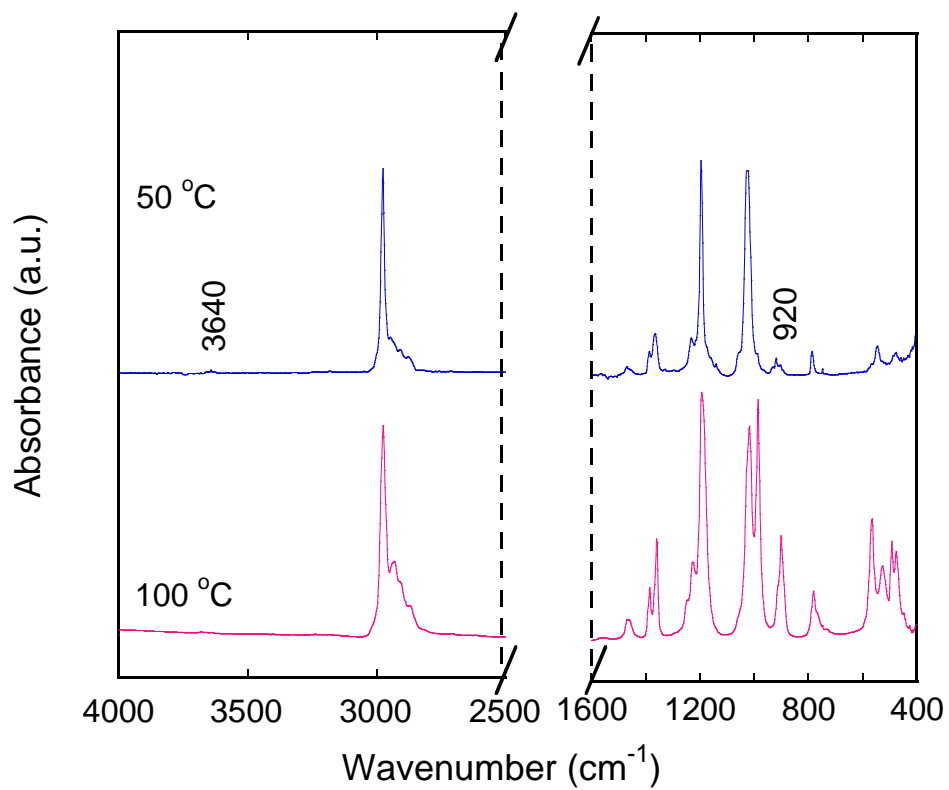


**Figure B-6.** Gas phase HTB at 5 min. after opening the bubbler in flow mode for 50 °C and 100 °C.

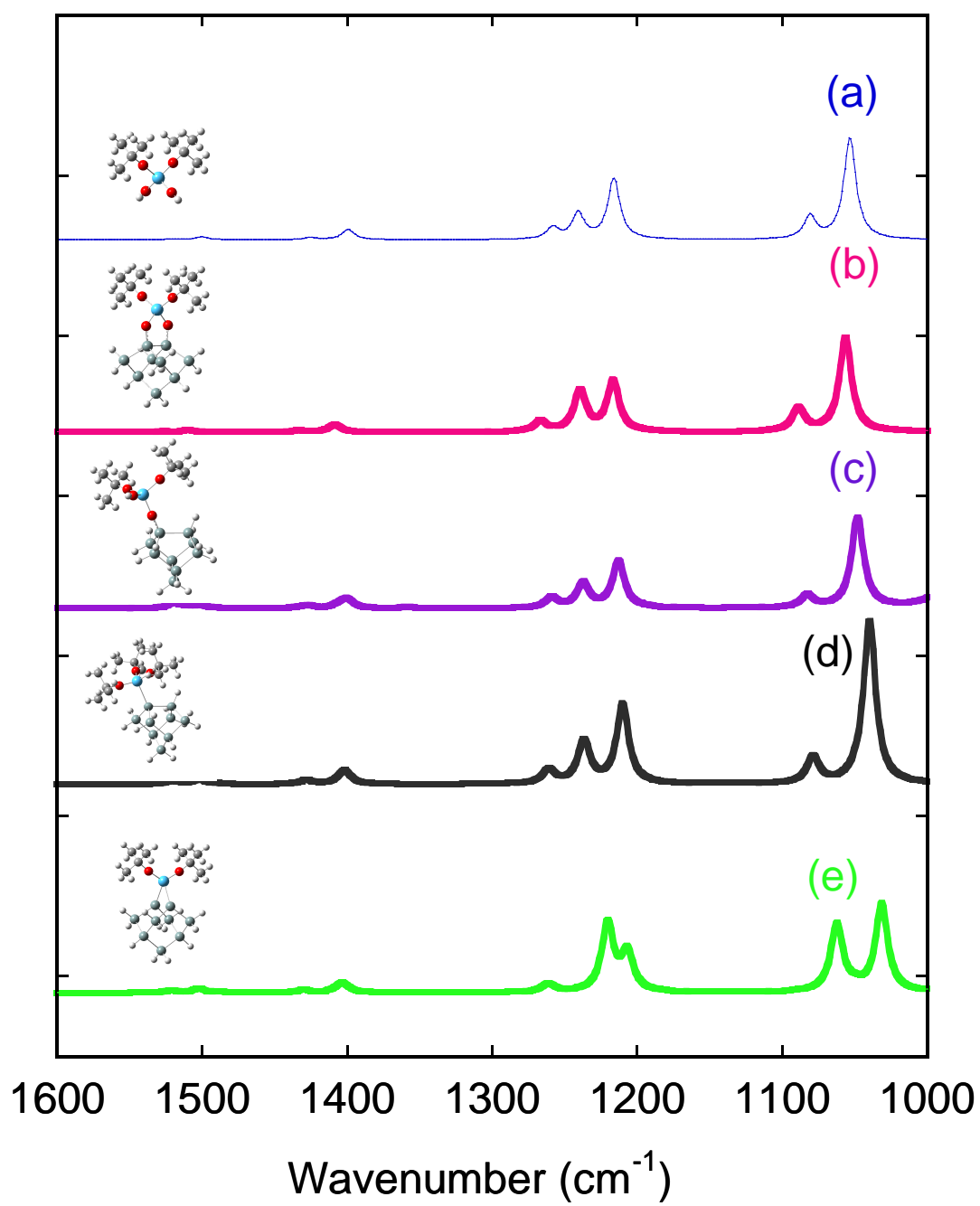


**Figure B-7.** Models that have triplet peaks around 1200  $\text{cm}^{-1}$ .

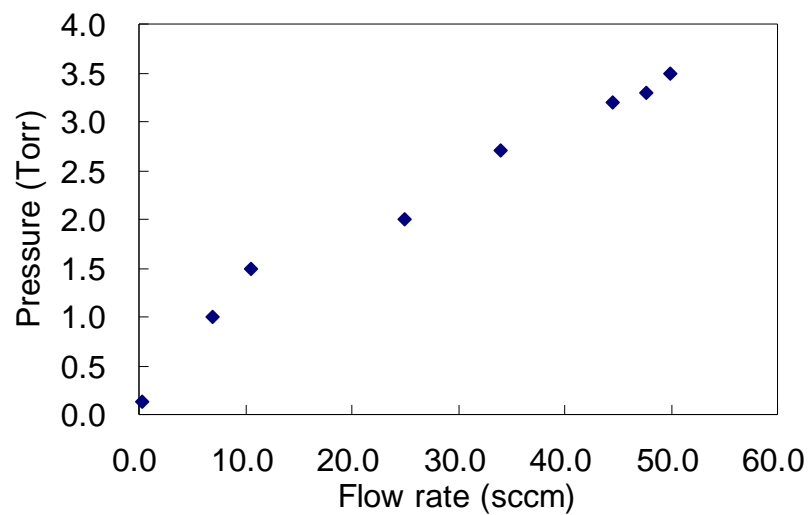


**Figure B-8.** MFC flow rate calibration from the reading of down stream piana gauge.

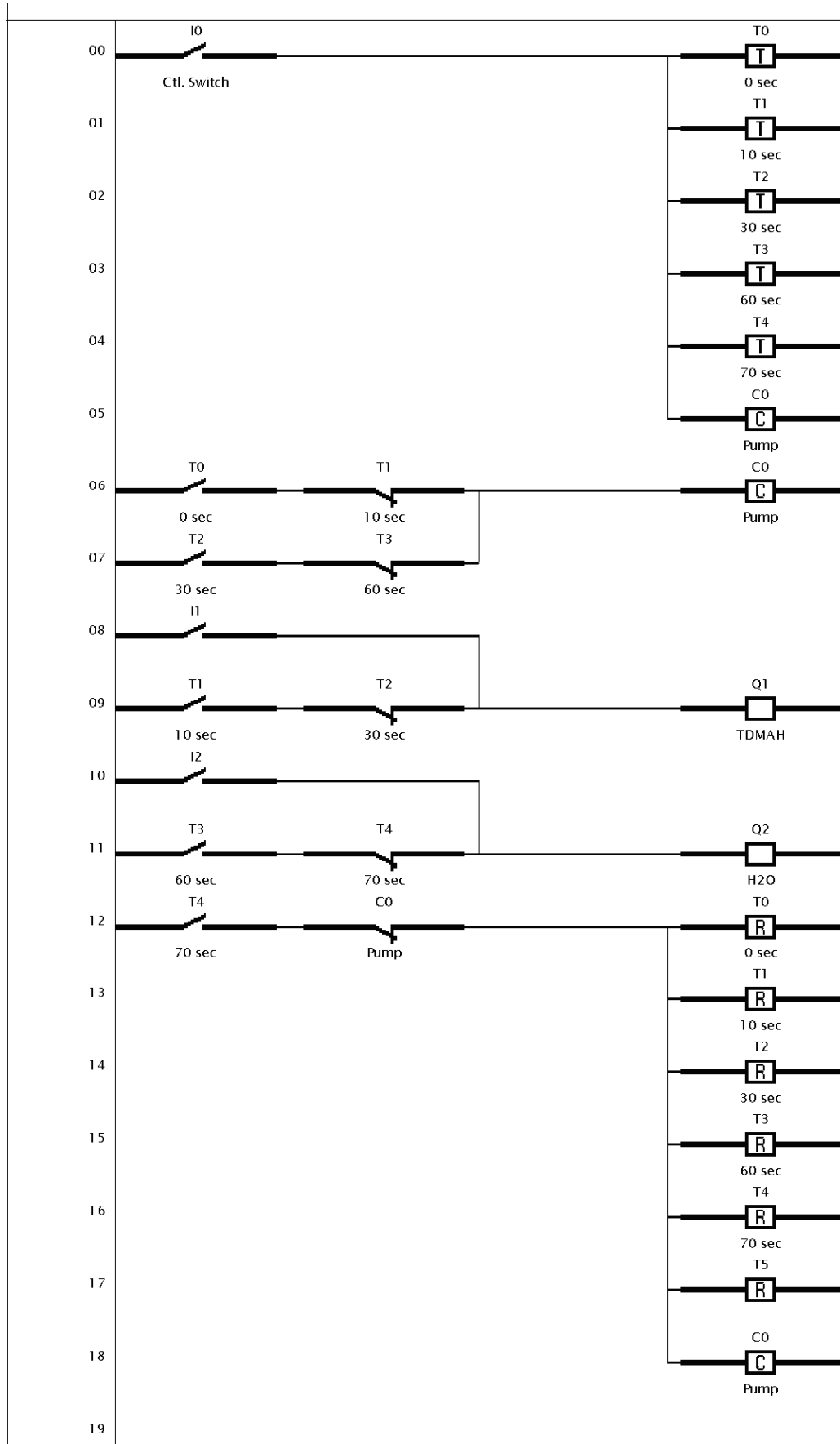


**Figure B-9.** ALD Programming Logic Design with Omron Zen 10 C1\*\*-A.

Notations for Figure B.1:

I0: The main control Switch on the panel

I1: Control Switch of precursor line

I2: Control Switch of water line

T: On-delay timer, trigger and reset modes for the up and bottom respectively

Q: Normal output relay

Co: Counter

The above design control configuration corresponds to the following ALD flow pattern:

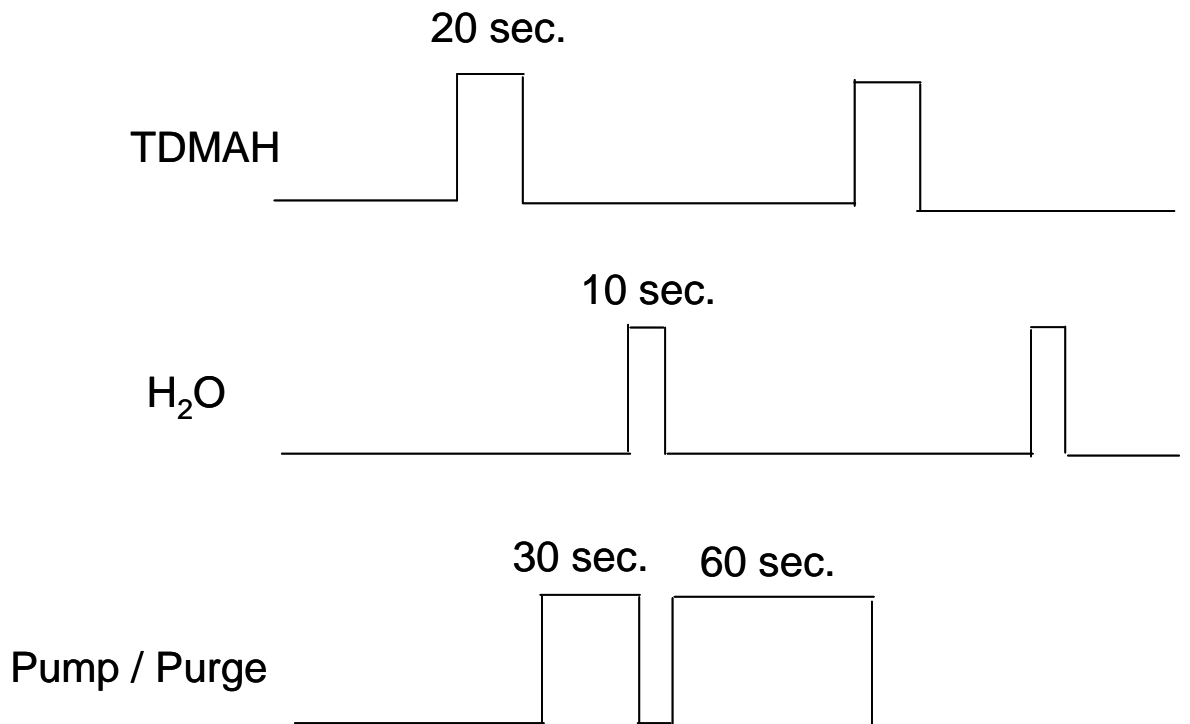


**Figure B-10.** TDMAH/H<sub>2</sub>O ALD process pattern.

**Table B - 1.** Thermal Conductivity of Flow Through Cell Component Materials

Temperature	Thermal Conductivity(W/m-K)				
	Si	Stainless Steel	aluminum	copper	Kalrez o-ring
60	2110		250	829	0.19
70	1680			647	
80	1340			557	
90	1080			508	
100	884	17		482	0.18
150	409			429	
200	264	19		413	
250	191	20	250	406	0.17

## **Appendix B**

DFT Calculated Geometries and Energies for Selected Models

Selected model structures are given below. The Cartesian coordinates are in Å and energies are in Hartree. The optimized structures are at the B3LYP/BS1 Level.

**TDMAH – Hf[N(CH<sub>3</sub>)<sub>2</sub>]<sub>4</sub>**

Hf	0.00194800	0.00617700	-0.00553600
N	-0.85718100	-1.31372900	-1.33321900
N	1.70313900	0.84752600	-0.80717400
N	0.49806700	-1.00960600	1.71189400
N	-1.35881500	1.47269600	0.46543700
C	-2.02026200	2.19033600	-0.61952300
H	-3.11625300	2.06798400	-0.58335600
H	-1.80852500	3.27270700	-0.58436200
H	-1.68506400	1.82223300	-1.59816500
C	-1.81630800	1.92557200	1.77087300
H	-1.31609900	1.36783200	2.56852100
H	-1.61007300	2.99867600	1.92455200
H	-2.90424800	1.78332800	1.89283900
C	-2.25343400	-1.72100800	-1.23145100
H	-2.35025700	-2.81031500	-1.08319600
H	-2.74546400	-1.22591600	-0.38575700
H	-2.82166400	-1.46415900	-2.14221700
C	-0.19998900	-1.93748200	-2.47402900
H	-0.20634300	-3.03829300	-2.39591700
H	-0.69697700	-1.67543600	-3.42429400
H	0.84348200	-1.61342400	-2.54846900

C	0.04274000	-2.32917400	2.12871700
H	-0.64270200	-2.75440000	1.38905900
H	0.88579300	-3.03218700	2.24610300
H	-0.48440700	-2.28961600	3.09733700
C	1.42835500	-0.43416000	2.67780300
H	2.31564400	-1.07457200	2.82215400
H	1.78319200	0.54841400	2.34423000
H	0.95779900	-0.29947600	3.66680200
C	2.91307900	0.04823400	-0.96233800
H	2.76425600	-0.96920200	-0.57862600
H	3.21662900	-0.03669400	-2.02011800
H	3.76395500	0.48453000	-0.41141800
C	1.89881200	2.21448700	-1.26873900
H	2.16183100	2.25022600	-2.33994400
H	0.98886700	2.80667000	-1.12662500
H	2.71196300	2.71730600	-0.71695600

Zero-point correction = 0.324405 (Hartree/Particle)

Thermal correction to Energy = 0.346188

Thermal correction to Enthalpy = 0.347133

Thermal correction to Gibbs Free Energy = 0.271279

Sum of electronic and zero-point Energies = -587.040601

Sum of electronic and thermal Energies = -587.018818

Sum of electronic and thermal Enthalpies = -587.017873

Sum of electronic and thermal Free Energies = -587.093727

**ТЕМАН – Hf[N(CH<sub>3</sub>)(C<sub>2</sub>H<sub>5</sub>)]<sub>4</sub>**

Hf	0.05450100	0.08809600	-0.13662100
N	-0.88172000	-0.60673500	1.55757300
N	-0.46786100	-1.07764800	-1.76549300
N	2.09149000	-0.01590500	0.16724100
N	-0.46771500	2.05106800	-0.55853800
C	-1.75399300	2.74036500	-0.47026600
H	-1.66774900	3.60132100	0.21782600
H	-1.99764400	3.17444700	-1.45768400
C	0.55670300	2.98834200	-1.02037400
H	1.53713700	2.50828100	-1.09046400
H	0.31106100	3.39798400	-2.01533700
H	0.66331300	3.84479000	-0.33233900
C	-0.70625300	0.20550800	2.76084000
H	-0.24068600	-0.37364000	3.57648300
H	-0.04974300	1.06338000	2.55901100
H	-1.65182000	0.61871000	3.14497400
C	-1.66708700	-1.81868000	1.78659100
H	-1.22025300	-2.39429300	2.61748200
H	-1.59219300	-2.45073700	0.89467400
C	2.78115400	-0.38641600	1.40239600
H	2.03187100	-0.71794200	2.13084800
H	3.43336200	-1.25902500	1.21348900
C	2.99976600	0.17217200	-0.96078300
H	3.65345800	-0.70645900	-1.10216900

H	2.43730400	0.30690400	-1.89358900
H	3.65286800	1.05188300	-0.84839400
C	-0.04701500	-2.44576100	-2.07341900
H	-0.94382800	-3.08190000	-2.18549700
H	0.45515300	-2.46431200	-3.05793500
C	-1.34006900	-0.58001900	-2.82961100
H	-2.25350400	-1.19205700	-2.92391600
H	-1.64153300	0.45354200	-2.63886100
H	-0.83361600	-0.60147000	-3.81011000
C	-2.92266800	1.86568600	-0.01813600
H	-3.08502800	1.02340200	-0.70073900
H	-2.75995800	1.46126300	0.98464500
H	-3.84465800	2.45734200	0.00030000
C	0.88226700	-3.08398100	-1.03963700
H	1.82093800	-2.53093300	-0.94353900
H	0.41697000	-3.13277100	-0.04844400
H	1.12137400	-4.10982500	-1.34077300
C	3.62442000	0.73354600	2.03452100
H	3.00190300	1.60613500	2.26226900
H	4.08282400	0.38485000	2.96777200
H	4.43329300	1.06008200	1.37244300
C	-3.15692500	-1.58820500	2.09083100
H	-3.64530400	-1.05938600	1.26572500
H	-3.66574400	-2.54948700	2.23038700
H	-3.30475800	-1.00379100	3.00501600

Zero-point correction=	0.438684 (Hartree/Particle)
Thermal correction to Energy=	0.465477
Thermal correction to Enthalpy=	0.466421
Thermal correction to Gibbs Free Energy=	0.380204
Sum of electronic and zero-point Energies=	-744.192489
Sum of electronic and thermal Energies=	-744.165696
Sum of electronic and thermal Enthalpies=	-744.164752
Sum of electronic and thermal Free Energies=	-744.250969

**HTB – Hf(OtBu)<sub>4</sub>**

Hf	0.00599100	-0.00123800	0.00082400
O	1.71851600	-0.61821900	0.65359900
O	-1.19442900	0.26508300	1.49327400
O	0.24089500	1.67008200	-0.94311900
O	-0.74089500	-1.31897200	-1.20169100
C	-1.28695700	-2.28807300	-2.07946300
C	0.40641300	2.90232900	-1.62247100
C	-2.10174000	0.45338300	2.56516000
C	2.97365700	-1.06599900	1.13523800
C	-0.96694400	3.35333400	-2.14639400
H	-1.66914300	3.47202200	-1.31468000
H	-0.89344900	4.30973400	-2.67620000
H	-1.37409100	2.60668200	-2.83609500
C	1.38494200	2.68448100	-2.78806300
H	1.54565000	3.61297500	-3.34752400
H	2.35230800	2.33626200	-2.41148100
H	0.99216700	1.92969200	-3.47722200
C	0.96975500	3.93040300	-0.62769600
H	1.93627700	3.59262300	-0.23932100
H	1.11107200	4.90668600	-1.10496200
H	0.28438200	4.05457200	0.21716400
C	-3.40400600	1.04330100	1.99910800
H	-4.14391200	1.20186200	2.79168900
H	-3.20633100	2.00512600	1.51458000

H	-3.83475200	0.36542600	1.25483000
C	-1.46337800	1.42139800	3.57456300
H	-2.13428600	1.60948200	4.42038000
H	-0.52803700	1.00431500	3.96199300
H	-1.23914500	2.37837500	3.09211700
C	-2.36655600	-0.91284500	3.21860700
H	-1.43136300	-1.34123700	3.59390600
H	-3.06610000	-0.82103600	4.05707400
H	-2.79326100	-1.60675800	2.48700400
C	3.52247000	-0.01046100	2.10907900
H	4.49806000	-0.30978000	2.50848600
H	3.63819100	0.95175100	1.59948600
H	2.83255500	0.12572100	2.94835900
C	2.76362200	-2.40818600	1.85514900
H	2.35146700	-3.14997200	1.16318000
H	3.70798700	-2.79510100	2.25434300
H	2.06167200	-2.28617300	2.68656800
C	3.91795300	-1.23760100	-0.06584100
H	4.90579600	-1.58809400	0.25384500
H	3.50484900	-1.96564600	-0.77174900
H	4.04289500	-0.28426200	-0.58969500
C	-1.45392900	-3.60381400	-1.30207700
H	-2.12402400	-3.45766500	-0.44847300
H	-1.87318900	-4.39006700	-1.93994000
H	-0.48516900	-3.94599000	-0.92344200

C	-2.64853200	-1.77581000	-2.57678300
H	-2.52552200	-0.82350300	-3.10296900
H	-3.11454500	-2.49224200	-3.26267500
H	-3.32564800	-1.61654000	-1.73118300
C	-0.31608900	-2.47422300	-3.25697000
H	-0.69321200	-3.21844400	-3.96748200
H	-0.17955300	-1.52707700	-3.78918900
H	0.66128300	-2.80809200	-2.89338800

Zero-point correction= 0.500025 (Hartree/Particle)

Thermal correction to Energy= 0.529152

Thermal correction to Enthalpy= 0.530096

Thermal correction to Gibbs Free Energy= 0.436547

Sum of electronic and zero-point Energies= -981.066330

Sum of electronic and thermal Energies= -981.037203

Sum of electronic and thermal Enthalpies= -981.036259

Sum of electronic and thermal Free Energies= -981.129808

**Si9H14**

Si	0.00032400	-0.00094300	2.48118800
H	0.00045600	-1.20353500	3.36315300
H	0.00042500	1.20060700	3.36456100
Si	1.96347400	-0.00043600	1.15135800
H	3.17592500	-0.00070300	2.02024000
Si	-1.96317600	-0.00022300	1.15185500
H	-3.17542400	-0.00018800	2.02101400
Si	1.88766400	1.80158600	-0.37592900
H	3.13456200	1.83265000	-1.19226300
H	1.72104300	3.13323700	0.27038900
Si	-1.88730800	1.80181300	-0.37542600
Si	-0.00003700	1.19839100	-1.67475400
H	-3.13428400	1.83283300	-1.19165400
H	-1.72057200	3.13353700	0.27070400
Si	-1.88794300	-1.80109800	-0.37683300
H	-1.72217800	-3.13347500	0.26818500
H	-3.13474700	-1.83060400	-1.19338000
Si	1.88731400	-1.80169200	-0.37684300
Si	-0.00023400	-1.19738900	-1.67536700
H	3.13416500	-1.83264000	-1.19324800
H	1.72041600	-3.13361000	0.26885100
H	-0.00036200	1.79115500	-3.04254200
H	-0.00052100	-1.78936500	-3.04350900

Zero-point correction=	0.126102 (Hartree/Particle)
Thermal correction to Energy=	0.142911
Thermal correction to Enthalpy=	0.143856
Thermal correction to Gibbs Free Energy=	0.083994
Sum of electronic and zero-point Energies=	-2613.809101
Sum of electronic and thermal Energies=	-2613.792292
Sum of electronic and thermal Enthalpies=	-2613.791348
Sum of electronic and thermal Free Energies=	-2613.851209

## **Appendix C**

Copyright Release

**Copyright release for Table 1-1:**

License Number: 2381371231543

License date: Mar 03, 2010

Licensed content publisher: Elsevier

Licensed content publication: Microelectronic Engineering

Licensed content title: On the scaling issues and high- $\kappa$  replacement of ultrathin gate dielectrics for nanoscale MOS transistors

Licensed content author: Hei Wong, Hiroshi Iwai

Licensed content date: October 2006

Volume number: 83

Issue number: 10

Pages: 38

Type of Use: Thesis / Dissertation

Portion: Figures/tables/illustrations

Number of Figures/tables/illustrations: 1

Format: Electronic

You are the author of this Elsevier article: No

Are you translating? No

Order Reference Number

Expected publication date: Mar 2010

Elsevier VAT number: GB 494 6272 12

**Copyright Release Letter for Figure 2-2.**

(E-mail release agreement by the editor and the author)

Dear Author,

I have received approval from one of the authors of the paper in question and have attached it to this email - I'm afraid this is the best resolution I can get as I do not have access to the original image file.

Please cite the following as the source of the image: "Image supplied by Air Liquide ALOHA, reproduced with permission from Semiconductor Fabtech (Edition 27, August 2005)."

The caption of the image is: Degradation of TEMAH during isothermal TGA (120°C and 150°C).

Please let me know if you have any further queries, and best of luck with your paper!

Síle Mc Mahon

Sub Editor & Content Manager

Photovoltaics International & Semiconductor Fabtech

**Copyright release For Figure 2-3:**

AMERICAN CHEMICAL SOCIETY LICENSE

TERMS AND CONDITIONS

Mar 03, 2010

This is a License Agreement between Kejing Li ("You") and American Chemical Society ("American Chemical Society") provided by Copyright Clearance Center ("CCC"). The license consists of your order details, the terms and conditions provided by American Chemical Society, and the payment terms and conditions.

All payments must be made in full to CCC. For payment instructions, please see information listed at the bottom of this form.

License Number: 2377150595716

License Date: Feb 27, 2010

Licensed content publisher: American Chemical Society

Licensed content publication: The Journal of Physical Chemistry A

Licensed content title: Thermal Chemistry of Tetrakis(ethylmethyamido)titanium on Si(100) Surfaces†

Licensed content author: Byung-Chang Kan et al.

Licensed content date: Apr 1, 2009

Volume number: 113

Issue number: 16

Type of Use: Thesis/Dissertation

Requestor type: Not specified

Format: Electronic

Portion: Table/Figure/Chart

Number of Table/Figure/Charts: 1

Author of this ACS article: No

Order reference number

Title of the thesis / dissertation: Metalorganic precursors adsorption and reaction on hydrogen terminated Si surfaces in a flow reactor.

Expected completion date: Mar 2010

Estimated size(pages): 200

**Copyright release for figures in Chapter 7:**

AMERICAN INSTITUTE OF PHYSICS LICENSE

TERMS AND CONDITIONS

Mar 03, 2010

This is a License Agreement between Kejing Li ("You") and American Institute of Physics ("American Institute of Physics") provided by Copyright Clearance Center ("CCC"). The license consists of your order details, the terms and conditions provided by American Institute of Physics, and the payment terms and conditions.

All payments must be made in full to CCC. For payment instructions, please see information listed at the bottom of this form.

License Number: 2381551348644

License date: Mar 03, 2010

Licensed content publisher: American Institute of Physics

Licensed content publication: Journal of Vacuum Science & Technology A

Licensed content title: In situ attenuated total reflectance Fourier transform infrared spectroscopy of hafnium (IV) tert butoxide adsorption onto hydrogen terminated Si (100) and Si (111)

Licensed content author: K. Li, S. Dubey, H. B. Bhandari, et al.

Licensed content date: Sep 1, 2007

Volume number: 25

Issue number: 5

Type of Use: Thesis/Dissertation

Requestor type: Author (original article)

Format: Electronic

Portion: Figure/Table

Number of figures/tables: 8

Title of your thesis / dissertation: Metalorganic precursors adsorption and reaction on hydrogen terminated Si surfaces in a flow reactor.

Expected completion date: Mar 2010

Estimated size (number of pages): 200